Synthesis, Characterization and Application of Graphene Based Materials

(Revised)

April 2026

Synthesis, Characterization and Application of Graphene Based Materials

(Revised)

A Dissertation Submitted to the University of Dhaka for the Partial Fulfillment of the Requirements of the Degree of Doctor of Philosophy in Applied Chemistry and Chemical Engineering

Submitted by
Registration No. 29
Session: 2018-2019

Department of Applied Chemistry and Chemical Engineering
University of Dhaka
Dhaka-1000, Bangladesh

April 2026

Dedication

This thesis is dedicated to my parents, wife, and daughters, without whom I would be unable to complete this journey.

Acknowledgements

I am profoundly indebted to my supervisor, **Dr. Md. Nurnabi**, a distinguished Professor and Chairman in the Department of Applied Chemistry and Chemical Engineering at the University of Dhaka, Dhaka-1000, Bangladesh. He has been a guiding force behind my academic and research journey. His role in my development as a researcher has been truly remarkable. His unwavering dedication to the pursuit of knowledge, along with his profound insights into the field, has not only shaped the direction of my research but has also transformed me into a more inquisitive and rigorous researcher. His commitment to fostering a culture of intellectual curiosity within our research group has been instrumental in my growth as a researcher. His encouragement of questions, explorations, and innovations has been a constant source of inspiration.

I extend my deepest appreciation to my co-supervisors, Professor **Dr. A. F. M. Mustafizur Rahman**, a renowned Professor in the Department of Applied Chemistry and Chemical Engineering at the University of Dhaka, Dhaka-1000, Bangladesh. Their exceptional expertise in the field of Applied Chemistry has played a pivotal role in shaping the direction and depth of my research. Their mentorships have been instrumental in expanding my understanding of complex chemical phenomena and research methodologies. Their willingness to invest time and effort in guiding my academic pursuits, especially during challenging moments, has been invaluable in my academic development. Their support has not only enriched my research but has also inspired me to explore new horizons in the field of applied chemistry.

I am profoundly grateful for the invaluable contributions and mentorships of **Dr. Mohammad Mahbubur Rahman**, Principal Scientific Officer**,** Fiber and Polymer Research Division, BCSIR Dhaka Laboratories, Bangladesh Council of Scientific and Industrial Research, Dhaka-1205, Bangladesh, throughout my Ph.D. journey. His extensive knowledge and expertise in the field of chemistry have been a beacon of guidance for me. I consider myself fortunate to have had the privilege of learning from scholars of this caliber.

I also extend my deepest appreciation to **all the Teachers and employees of the Department of Applied Chemistry and Chemical Engineering**, University of Dhaka, Dhaka-1000, Bangladesh. Their role in my research journey has been transformative. Their expertise in

the field of study and their commitment to pushing the boundaries of scientific knowledge have been a constant source of inspiration. I also acknowledge the **authority of the Bangladesh Council of Scientific and Industrial Research (BCSIR)**, Dhaka-1205, and the **authority of the Ministry of Science and Technology**, Government of the People's Republic of Bangladesh, for permitting me to complete my doctoral degree.

I would like to extend my heartfelt appreciation and acknowledgment to my fellow lab mates at the **Department of Applied Chemistry and Chemical Engineering**, University of Dhaka, Dhaka, and **Fiber and Polymer Research Division**, BCSIR Dhaka Laboratories, BCSIR, Dhaka. Our shared research journey has been a collaborative and enriching experience that has significantly contributed to my academic growth and the overall success of my research endeavors. I am deeply grateful for the support, both academic and personal, that I have received from my lab mates. I would also like to extend my gratitude to my colleagues at BCSIR for their immense support during the material analysis.

I express the heartiest thanks to my colleague, especially Dr. Shirin Akter Jahan, PSO, IGCRT, BCSIR; Dr. Nasir Uddin Ahamed, PSO, BCSIR Dhaka Laboratories; Aninda Nafiz Hasan, SE, PP&PDC, BCSIR; Dr. Dipa Islam, PSO, BTRI, BCSIR; Dr. Tushar Uddin, PSO, LRI, BCSIR; Saiful Kuddus, SSO, IGCRT, BCSIR; Md. Ashraful Islam, SSO, IGCRT, BCSIR; Dr. Shamima Akter Eti, SSO, BCSIR Dhaka Laboratories, BCSIR; Shabiba Parvin Shandhia, BCSIR Dhaka Laboratories, BCSIR; Mustafizur Rahman Naim, SO, BTRI, BCSIR; Tanvir Hossain, SSO, BCSIR Dhaka Laboratories of BCSIR for their continuous analytical support with sophisticated instruments and valuable discussions.

Finally, I would like to extend my heartfelt appreciation to my family. Their sacrifices and belief in my abilities have sustained me through the challenges of doctoral research. In conclusion, my Ph.D. thesis would not have been possible without the exceptional contributions, mentorship, and support of all these individuals. They have played an integral role in shaping my academic and research path, and I am sincerely grateful for their presence in my life and academic journey.

Declaration

Experiments described in this thesis were carried out by the author himself at the Department of Applied Chemistry and Chemical Engineering, University of Dhaka, Dhaka-1000, Bangladesh. This work has not been submitted and will not be submitted for any other degree.

Supervisor
Professor Dr. Md. Nurnabi
Professor
Department of Applied Chemistry
and Chemical Engineering
University of Dhaka
Dhaka-1000, Bangladesh

Co-Supervisor
Dr. A. F. M. Mustafizur Rahman
Professor
Department of Applied Chemistry
and Chemical Engineering
University of Dhaka
Dhaka-1000, Bangladesh

Ph.D. Student
Mohammad Amirul Hoque
Department of Applied Chemistry
and Chemical Engineering
University of Dhaka
Dhaka-1000, Bangladesh

General Abstract

Graphene is being exponentially utilized across diverse research fields due to its extraordinary ability to enhance material properties with its miraculous attributes. Still, the material is expensive due to difficulties in the production of high-quality graphene. In this study, a few initiatives were approached to reduce the production costs of graphene with improved properties. At first, Tour's modified Hummer's method was adopted to synthesize improved graphene with the feed acid liquor (FAL) recycling technique. About 90% of the FAL were recycled and reused five times as feed for successive production batches. Another focus was on the oxidation reaction to achieve graphene oxides (GOs) with higher oxygen to carbon ratios. The changes in recycled FAL and synthesized GOs properties due to repeated recycling were evaluated. The synthesized GOs were utilized for the removal of arsenic (As^{3+}) ions from water, showing a q_{max} of 343.14 mg/g with 98.4% removal efficiency from 300 ppm to 22 ppm. The GOs were then reduced thermally at various temperatures in water, kerosene, and kerosene followed by ascorbic acid methods and times. The major objective of the reduction was to achieve maximum reduction of GO. The synthesized reduced graphene oxides (rGO) were evaluated for the antimicrobial properties. Although the Hummer's method produces GO and rGO with improved properties, the method is difficult to carry out, very slow, and expensive. To obtain an easy and faster method for the production of graphene in bulk, a microwave assisted rapid exfoliation process of graphene exfoliation was examined along with the effect of variation of the intercalating agent ratio. All the products of FAL, GOs, rGOs, and microwave graphene (MG) were characterized using a Karl-Fischer moisture analyzer, IC, AAS, FT-IR (ATR), FT-Raman, UV-Visible Spectroscopy, PS-Zeta potential, XPS, XRD, STA, TGA, FE-SEM, and TEM analyzer. The FAL had increased moisture content with the successive recycling, but had no significant changes in properties and composition of GO. However, GO properties greatly changed with temperature and time of reaction, and the amount of oxidizing agent. The degree of reduction of GOs in N_2 atmosphere at 193.4 ^oC was 95% of its initial mass, even at a slow rate of heating, but at this temperature, GO explosively degraded. In water medium as well as in kerosene, the explosive degradation can be omitted, and even at 220 ^oC, affording 40% reduction, which was mainly due to the removal of oxygen atoms as evident from the XPS analysis. The extremely reduced rGO contained an oxygen-to-carbon ratio of only 2.49% based on its initial oxygen content. In this study, XRD data also supported the composition of rGO and showed that it contained a homogeneous amorphous or

nanocrystalline structure, as demonstrated by the 2θ = 24.91° peak in the (002) plane, which was shifted from the GO peak at 2θ = 12.86° in the (001) plane. The SEM image measured by ImageJ software showed that the obtained grain sizes were between 100 and 200 nm for both the GO and rGO. These rGO also showed strong activities against gram-positive and gram-negative bacteria, such as *B. subtilis*, *S. aureus*, *E. coli*, and *S. typhi.* In the case of MG, the degree of exfoliation was directly proportional to the intercalating agent ratios, and this method directly produces pristine graphene. This MG was highly thermo-stable up to 700-800 ºC with high crystallinity, having 2θ = 26.56° at the (002) plane. The crystalline graphene showed excellent adsorption of acid blue-25 dyes with q_{max} 472.8 mg/g and 94.56% removal efficiency in the case of a 300-ppm dye solution.

Table of Contents

List of Tables

List of Figures

List of Abbreviations

Sl. No.	Description
ABD	Acid blue dye
$(NH_4)_2SO_4$	Ammonium sulphate
ABC	Ammonium bicarbonate
AR	Analytical reagent
Å	Angstrom
AA	Ascorbic acid
AAS	Atomic absorption spectroscopy
BOD	Biological oxygen demand
BET	Brunauer–Emmett–Teller
COD	Chemical oxygen demand
°C	Degree centigrade
*n*D	Defect density
DI	De-ionized
DMF	Dimethyl formamide
DMSO	Dimethyl sulfoxide
DSC	Differential scanning calorimeter
C_e	Equilibrium concentration
q_e	Equilibrium sorption capacity
EG	Ethylene glycol
FAL	Feed acid liquor
FTIR-ATR	Furrier transforms infra-red attenuated total reflection
GPa	Giga pascal
GOs	Graphene oxides
HTT	Hardly thermal treatment

HT	Higher temperature
FWHM	Full width at half maximum
C_0	Initial concentration
I_D	Intensity of D peak
I_G	Intensity of G peak
ILs	Ionic liquids
K	Kerosene
KAA	Kerosene ascorbic acid
Lt	Long time
LT	Lower temperature
λ_{max}	Maximum absorption wavelength
MG	Microwave graphene
MWI	Microwave irradiation
MA	Mixed acid
MHA	Mueller Hinton agar
nm	Nano meter
HNO_3	Nitric acid
NO_X	Nitrogen oxides
H_3PO_4	Phosphoric acid
$K_2Cr_2O_7$	Potassium dichromate
K_2FeO_4	Potassium ferrate
$KClO_3$	Potassium perchlorate
$KMnO_4$	Potassium permanganate
rGO	Reduced graphene oxides
RT	Room temperature
SiO_2	Silicon dioxide
$NaBH_4$	Sodium borohydride
$NaNO_3$	Sodium nitrate
STT	Soft thermal treatment
H_2SO_4	Sulfuric acid
SEM	Scanning electron spectroscopy
SEM-EDX	Scanning electron microscopy-energy dispersive X-ray
STA	Simultaneous thermal analysis
STT	Softly thermal treatment
St	Short time
SD	Standard deviation
TC	Tetracycline
TPa	Tera pascal
TGA	Thermogravimetric analyzer
IC	Ion-chromatography
UV Vis.	Ultraviolet visible light
XPS	X-ray photoelectron spectroscopy
XRD	X-ray diffraction
W	Water

CHAPTER-1

General Introduction

General Introduction

1.1. Background

A monolayer of graphene is structurally constructed from one carbon-atom-thick, two-dimensional sheets of only carbon atoms, where every carbon atom is attached to three other carbon atoms with sp^2 hybridized orbitals, forming a hexagonal honeycomb lattice structure (Yang G., et al., 2018). Wallace P. R. theorized single-layer graphene in 1947, and Andre Geim and Konstantin Novoselov successfully isolated and identified it in 2004 using the "Scotch Tape technique" (Novoselov K. S., et. al., 2004). They credited Hanns-Peter Boehm for first identifying graphene in 1962 and coining its name in 1986. Graphene is the fundamental structure of all graphitic forms of carbon including carbon nanotubes and graphite, and gained

prominence in the mid-2000s due to its remarkable properties such as exceptional strength, cost-efficiency, unique electrochemical properties like stability, high adaptability due to its delocalized electrons, high visible light transparency, fascinating elasticity, excellent carrier mobility, thermal conductivity, extraordinary magnetic properties, large specific surface area, high surface charge, and charge transfer interactions with molecules. In addition, the presence of various defects and disorders, including corrugations, topological defects, vacancies, adatoms, and sp^3-defects, has a beneficial effect on electrical, thermal, chemical, and mechanical properties. These properties arise from graphene's intrinsic structural features, including its sp^2-hybridized lattice, unit-cell geometry, σ–π bonding framework, electronic band dispersion, edge configurations, and layer number. As an atomically thin carbon sheet, graphene possesses a quasi-metallic electronic structure, exceptionally high material quality, and remarkable environmental stability. The films are discovered to be a two-dimensional semimetal with a small overlap between the conductance and valence bands. They also show a strong ambipolar electric field effect, which allows gate voltage to induce electrons and holes in concentrations as high as $10^{13}/cm^2$ and with mobilities of about 10,000/cm^2-V-S square centimeters per volt-second at room temperature. Moreover, outstanding surface areas (2630 m^2/g), a high Young's modulus (1.0 TPa), high thermal conductivity (~5000 $W.M^{-1}.K^{-1}$), strong chemical durability, and high electron mobility ($2.5X10^5$ cm^2 $V^{-1}S^{-1}$) are among the remarkable properties of a highly ordered graphene sheet (Alimohammadzadeh E., et. al., 2024), (Brownson D. A., et. al., 2012), (Soldano C., et. al., 2010), (Geim A. K., et. al., 2007), (Novoselov K. S., et. al., 2005), (Novoselov K. S., et. al., 2012), ((Nair R. R., et. al., 2008), (Bolotin K. I., et. al., 2008), (Balandin A. A., et. al., 2008), (Stoller M. D., et. al., 2008), (Coroş M., et. al., 2018), (Abdelkader A. M., et. al., 2015), (Chabot V., et. al., 2014).

1.2. Structure and properties of graphene

Graphene's structure is characterized by its two-dimensional arrangement of carbon atoms, in which each carbon atom is sp^2-hybridized, forming three sigma bonds with neighboring carbon atoms. In contrast, the fourth p-orbital forms a delocalized π-bonding network as shown in (Figure-1.1) (Roberts M. W., et. al., 2010), (Ovsiienko I., et. al., 2018). This arrangement results in a planar structure with a bond length of approximately 1.42 Å between carbon atoms (Wang J. T., et. al., 2014), (Jakhar A., et. al., 2023). The unique electronic properties of graphene arise from its band structure, which features a linear dispersion relation near the Dirac points, leading to massless charge carriers known as Dirac fermions (Yankowitz M., et. al., 2012).

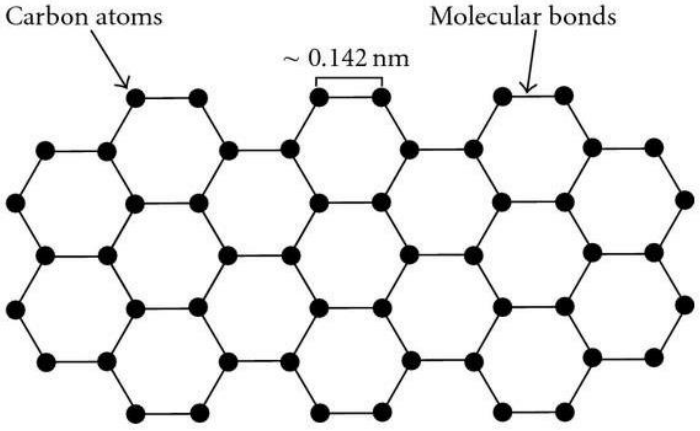

Figure-1.1: Structure of graphene with C-C Bond length (Roberts M. W., et. al., 2010).

The unique structure of graphene, characterized by its hexagonal lattice and sp^2 hybridization, significantly enhances its physico-chemical properties, making it a versatile material for various applications. The arrangement of carbon atoms allows for high charge mobility and exceptional electrical conductivity, attributed to the extended π-conjugation system, which facilitates electron transport (Cheng H., et. al., 2017). Additionally, the synthesis methods and conditions, such as the formation of σ and π bonds, influence the structural-morphological properties, thereby affecting electrochemical behavior and catalytic activity (Panteleimonov R. A., et. al., 2022). Graphene functionalization, through covalent and non-covalent bonds, further tailors' graphene's properties, improving its electrocatalytic performance and enabling applications in biosensors and energy storage devices (Vasilios G., et. al., 2012). Moreover, the presence of defects, such as vacancies and edge structures, can modify chemical reactivity, enhancing the utility in diverse fields (Sokrates T., et. al., 2012). Overall, the structural intricacies of graphene are pivotal in determining its remarkable properties and potential applications (Makhsin S. R., et. al., 2023).

The mechanical properties of graphene are equally impressive; it is known to be one of the strongest materials, with a tensile strength of over 130 GPa and a Young's modulus of approximately 1 TPa (Zhu C., et. al., 2016). Additionally, graphene exhibits excellent thermal conductivity, with values reaching up to 5000 W/mK, which is significantly higher than that of copper (Kawabata A., et. al., 2013). Its optical properties are also noteworthy, as graphene can absorb about 2.3% of incident light, making it a potential candidate for optoelectronic applications (Furchi M., et. al., 2012).

1.3. Synthesis of graphene oxides

There are two key approaches for synthesizing graphene oxide (GOs): top-down and bottom-up methods. Top-down strategies involve extracting GOs in bulk from graphite or a carbon source, whereas the bottom-up methods deal with the carbon molecules to create graphene (Abdelkader A. M., et. al., 2015), (Liu W. W., et. al., 2014), (Romero A., et. al., 2018). The majority of commercially available graphene is produced via top-down procedures because these methods are less expensive and easier to apply at larger scales (Lim J. Y., et. al., 2018). The chemical oxidation-reduction, exfoliation, arc-discharge, and irradiation of GOs are the methods involved in the typical top-down process for producing graphene/GOs (Dimiev A., et. al., 2012), (Eftekhari A., et. al., 2018), (Atta M. M., et. al., 2022). Amongst these top-down approaches, the chemical oxidation of graphite to GOs is the most often utilized one, which was proposed by Hummer's (Hummer's Jr. W. S., et. al., 1958) and eventually modified Hummer's method (Narasimharao K., et. al., 2016) and Tour method (Marcano D. C., et. al., 2010) emerged. Here we have conducted a precise outline on the synthesis of GOs following modified Hummer's method, especially modified by James M. Tour, called Tour's method. In this method, he eliminated nitric acid with phosphoric acid, which omitted the ice cooling step as well as the toxic NO_x gases evaluations.

1.3.1. Hummer's method

The most significant alternative technique for the oxidative chemical exfoliation of graphite was reported by Hummers and Offeman in 1958 (Hummer's Jr. W. S., et. al., 1958). This method is considered the safest and fastest strategy for developing GOs with a C/O ratio of around 2.25. This approach works with $KMnO_4$ in excess as oxidant, concentrated H_2SO_4 as intercalator, and a small amount of $NaNO_3$ with a synergistic effect. To date, there have been plenty of studies that used Hummer's method of GOs synthesis. GOs was synthesized by oxidizing the graphite via a simplified Hummer's method by our research group among many others (Mahmudunnabi D. M., et. al., 2024), (Kudus M. H., et. al., 2020), (Elhamid A. I., et. al., 2019), (Hou Y., et. al., 2020), (Chen X., et. al., 2022), (Kang J. H., et. al., 2016), (Liou Y. J., et. al., 2015), (Lv S., et. al., 2013), (Sun L., et. al., 2013), (Peng K. J., et. al., 2016), (Zhang B., et. al., 2016). El-Khodary et al. also proposed the modification of Hummer's method by using hydrogen peroxide as an oxidizing agent without affecting the yield of the product (El-Khodary S. A., et al., 2014). Highly oriented industrially expandable pyrolytic graphite was used as a precursor for mass production of GOs using Hummer's method after a slight modification of the spontaneous expansion process, which enabled it to become facile (Sun L., et al., 2013).

Various GOs samples were synthesized under different working conditions following Hummer's method (Wu T. T., et al., 2013). In terms of safety, time, and quality, Hummer's method is considered superior as this method offers benefits compared to the oxidation methods mentioned earlier (Hou Y., et al., 2020), (Chen X., et al., 2022). Nevertheless, the release of harmful gases and enhanced reaction temperature in Hummer's method restricts its feasibility for widespread application. Consequently, coordinated efforts had been initiated to enhance and/or modify Hummer's method to address concerns regarding safety, reaction duration, reaction temperature, oxidation level, and expenses.

1.3.2. Modified Hummer's method

Numerous alterations and variants of Hummer's approach have been created to enhance the yield and characteristics of GOs while minimizing the drawbacks (Zaaba N. I., et. al., 2017). GOs with different structures, oxygen contents, and carbon/oxygen (C/O) ratios were developed by conducting a second study on GOs synthesis using several modifications to Hummer's methodology (Guerrero C. J., et. al., 2015). By altering the amounts of $NaNO_3$ and $KMnO_4$, GOs with various structures, oxygen contents, and carbon/oxygen (C/O) ratios were produced. In a similar approach, oxidation of graphite using $K_2Cr_2O_7$ was made with many adjustments to Hummer's technique (Muzyka R., et. al., 2017). A traditional 24-hour reaction was necessary to produce GOs in Hummer's method with a comparable oxygen concentration (~41%), while the GOs made using $K_2Cr_2O_7$ had the same oxygen content with a 2-hour reaction time. GOs were synthesized with a high degree of oxidation by varying the reactant compositions and oxidation temperatures using modified Hummer's method (Alkhouzaam A., et. al., 2020), (Heidarizad M., et. al., 2016), (Kong S., et. al., 2020), (Ramesha G. V., et. al., 2011), (Yang D., et. al., 2009). GOs were also developed using the same method, and the reaction mechanism was revealed (Elhamid A. I., et. al., 2018). Microwave-assisted expanded graphite was used to synthesize GOs using modified Hummers' method (Algamdi M. S., et. al., 2019). Optimization of the synthesis process was performed with chemical adjustment to optimize the use of H_3PO_4 (Olorunkosebi A. A., et. al., 2021). The synthesized GOs by this method were applied to reveal their catalytic property (Lin C., et. al., 2016), (Quitain A. T., et. al., 2018). GOs nanosheets were produced from natural graphite flakes via this method (Zarrin H., et. al., 2011). Aqueous suspensions of GOs were also prepared by this method (Wilson N. R., et. al., 2009).

1.3.3. Improved Hummer's method/ Tour's method

In 2010, the methodology used by Hummer's group was enhanced by Tour and his team (Marcano D. C., et. al., 2010) for the production of GOs with a high level of oxygen. A small proportion of phosphoric acid was added in place of $NaNO_3$, which acts as an etching and dispersive agent to carry out the oxidation of graphite in the presence of a greater amount of $KMnO_4$, a 1:6 ratio with graphite, and a 9:1 mixture of H_2SO_4 and H_3PO_4. The GOs developed by Tour's technique exhibited a higher yield, an enhanced level of oxidation, and a more organized structure with fewer imperfections in comparison to the GOs synthesized by other methods. In the basal plane, the development of five-membered cyclic phosphate groups between two adjacent diols and phosphoric acid was associated with the construction of an ordered structure. In comparison to Hummer's technique, the enhanced method provides a greater number of hydrophilic groups on the oxidized graphene. Similarly, GOs was produced by the oxidation of natural graphite powder using an improved version of Hummer's method by replacing the $NaNO_3$ with $KClO_3$ and fuming HNO_3 with concentrated H_2SO_4 from the reaction formula (Chen J., et. al., 2013).

In another study, graphite flakes sized between 3–20 μm were fully changed into single-layer GOs with a remarkable yield of 171 ± 4% using concentrated H_2SO_4 and 3 times extra $KMnO_4$ in Hummer's method (Chen J., et. al., 2015). Eco-friendly oxidant K_2FeO_4 was utilized for the synthesis of GOs from graphite flakes (Romero A., et. al., 2018). A series of GOs nanosheets were synthesized with different lateral sizes and oxidation degrees by using Nafion (5% perfluorinated resin in water) solution (Li P., et al., 2018). Acidic group functionalized GOs were prepared using Nafion to develop improved GOs which could provide a higher amount of active oxygenated moieties on the GOs surface (Barik B., et. al., 2023). Since the Tour process just requires low-temperature heating (50 ºC) and doesn't create any harmful gases, it is safer than other oxidation techniques. It has been determined that the improved Hummer's approach offers greater benefits due to its reduced toxicity and a number of other benefits of the synthesized product (Jilani A. I., et. al., 2018), as well as adding advantages to large-scale GO production (Marcano D. C., et. al., 2010).

1.3.4. Electrochemical exfoliation of graphite to GOs

Graphene sheet produced in the electrochemical exfoliation process is more hydrophilic because of the existence of various types of oxygen functional groups that make it more dispersible in water as well as more stable as a colloidal substance (Sevilla M., et. al., 2016).

However, it is time-consuming and makes some defects because of existing foreign particles (Coroş M., et. al., 2018).

Electrochemical processes for the preparation of GOs involve the use of an aqueous solution (Yang S., et. al., 2016) because of availability, good dispersibility in water, and an electrical biasing DC current to the graphite electrode, either cathodic or anodic. It is generally known that the electrolyte is essential to the quality and yield of graphene produced by the electrochemical exfoliation process. Ionic liquid (Liu N., et. al., 2008), high molecular polymer (Lee S. H., et. al., 2010), polar solvents (Wang J., et. al., 2011), surfactants (Alanyalıoğlu M., et. al., 2012), and inorganic solutions are among the several types of electrolytes that had been employed (Morales G. M., et. al., 2011) (Su C. Y., et. al., 2011) (Parvez K., et. al., 2013) (Wu L., et. al., 2014) (Parvez K., et. al., 2014).

Electrochemical exfoliation has become a straightforward method for producing graphene from various graphite forms, such as powders, foils, and flakes (Kovtun A., et. al., 2019) (Su C. Y., et. al., 2011). By applying either cathodic (negative) or anodic (positive) bias, ions in electrolytes facilitate exfoliation (Abdelkader A. M., et. al., 2015) (Wei D., et. al., 2012) (Low C. T. J., et. al., 2013). Electrochemical exfoliation shows significant advantages over other processing methods because of simple operation and easy control under ambient conditions at room temperature, and takes place in a solo route (Coroş M., et. al., 2018) (Abdelkader A.M., et. al., 2015).

The electrochemical exfoliation of graphite to graphene was examined using potassium chloride as an electrolytic medium (You X., et. al., 2011). The chloride ions are gasified during electrolysis between the layer of graphite, which produces an electrostatic force between the layers to overcome the van der Waals force between the graphite layers and the exfoliated graphene layers. A monolayer, bilayer, and trilayer of exfoliated GOs on a SiO_2 substrate had average spin-coated thicknesses of 1.9, 2.8, and 3.9 nm, respectively. Controlling factors like electrical potential, electrolyte composition, and processing time allow tailoring graphene's defect density, oxygen content, and layer size. Additionally, functionalizing agents can chemically modify graphene during exfoliation (Yang S. L. M., et. al., 2016) (Yu P., et. al., 2015) (Paredes J. I., et. al., 2017) (Huang X., et. al., 2015; Parvez K. W. Z., et. al., 2014).

Common electrolytes include sulfuric acid (H_2SO_4), which enables the SO_4^{2-} ion to fit well in graphite's structure, expanding it and forming gases that aid exfoliation. Pretreating graphite in NaOH can further enhance graphene yield by reducing oxidation (Liu J., et. al., 2013) (Wu L., et. al., 2014).

Sodium halides must also be taken into consideration. At low salt concentrations, graphite electrodes were not sufficiently intercalated, but at high concentrations, the intercalation process was incredibly dynamic and quick, causing the electrodes to disintegrate. For NaCl, NaBr, and NaI, the ideal absorption is 0.05 M, 0.1 M, and 0.1 M, respectively (Munuera J. M. P. J., et. al., 2017). By adding NaCl or KCl as an electrolyte to Na_2SO_4. Munuera et. al. was able to prevent graphene from oxidizing more effectively than using NaBr, NaI, Na_2SO_3, sodium citrate, ascorbic acid (Anaya I. O., et. al., 2023), $NaBH_4$, and ethanol. This resulted in graphene materials with one of the highest C/O proportions (33.3-50) ever recorded (Munuera J. M. P. J., et. al., 2018). In another publication, he shows that the structural flaws in graphite foils, such as crowding, voids, and wrinkles, would help exfoliate graphite and lessen damage (Munuera J. M. P. J., et. al., 2015). Other electrolytes, including inorganic and organic salts, including ionic liquids (ILs), sulfates, halides, and transition metals, were used in graphene synthesis, impacting graphene properties by interacting with oxidative radicals during exfoliation. Besides salts, organic compounds have been explored to reduce oxidation and improve graphene quality. For example, Yang et. al. used inorganic reducing agents in $(NH_4)_2SO_4$, and Yoshimura et al. utilized glycine-HSO_4 complexes to aid ion intercalation in graphite electrodes (Yang S., et. al., 2015).

1.3.5. Microwave exfoliation of graphite

Recently, as one kind of mechanical exfoliation method to produce graphene, microwave-assisted exfoliation of graphite nanoplatelets has attracted extensive attention for its many advantages (Janowska I., et. al., 2010). Graphene produced under MWI had been reported earlier (Li Z., et. al., 2010) (Long J., et. al., 2011) (Xu Z., et. al., 2011) (Murugan A. V., et. al., 2009). For instance, Pirzado A., et. al., have obtained the electrical property of large few-layer graphene flakes by microwave-assisted exfoliation of expanded graphite (Pirzado A., et. al., 2016). Specifically, the few-layer graphene was synthesized by microwave-assisted exfoliation of expanded graphite in toluene with an overall yield of 7% to 20%. Typically, the previous

studies have mainly been proposed to effectively reduce the oxidation of graphene by MWI (Shen J., et. al., 2012).

Most of these reduction methods assisted by MWI used pretreated graphite oxide as the precursor or were synthesized in liquid phase, which cause the pretreatment process inevitably involves the use of chemical reagents. Moreover, the MWI methods have some limitations for rapid preparation of graphene at present, such as generating unwanted structural defects, uncontrolled sizes, shapes, uncontrolled layer numbers, poor absorption capacity, fast electron–hole recombination, low photocatalytic quantum, etc. (Ajay K., et. al., 2024) (Tung T. T., et. al., 2023). The adsorption process is one of the most significant processes in the field of dye removal, and it is better than other methods due to its low cost, ease of operation, and insensitivity to toxic substances (Malik P.K., 2004).

Compared with previous methods, the preparation method via peeling from bulk graphite assisted by MWI in the solid state shows many advantages, like maneuverability, time-saving, and scalable, which may find practical applications in the preparation of graphene-based materials (Dubey A., et. al., 2024).

1.4. Method of reduction of GOs to rGO

The reduction of GOs to rGO involves the removal of –OH and other functional groups from GOs, resulting in the restoration of the carbon backbone in a layered structure. Various methods for the reduction of GOs to rGO are reported in the literature, some of which are discussed below-

1.4.1. Thermal reduction methods

GOs were reduced thermally under different conditions in different media such as atmospheric air, N_2, water, solvent, etc. A general method to synthesize graphene nanosheets by thermal reduction of GOs at 350 °C for varying durations, and most of the reduction was completed in one hour. An increase in reduction time improved exfoliation, surface area, and graphitization (I_D/I_G ratio of 1.34) (Mokhtar M. M., et. al., 2017). The main function of the reduction procedure of GOs to rGO is the removal of oxygen, which contains several functional groups. This action provides a more hydrophobic characteristic of the material with improved electrical conductivity. The most commonly used reducing agents are hydrazine, ascorbic acid, sodium

borohydride, and thermal annealing. Additionally, the effects of the reduction condition on the generation of photocurrent in GOs/rGO-based large-area thin film photodetectors were evaluated. RhB (cationic dye) has a strong affinity for GOs due to its vast surface area and high concentration of negatively charged exogenous groups, which aid in the fast adsorption of RhB (Poulomi D., et. al., 2024). Thermally reduced GOs film (r-GOF) was made by annealing GOs films, showing improved thermal conductivity and mechanical properties as the temperature rises. At 1200 °C, r-GOF achieves 1043.5 W/m·K (Jing S. N., et. al., 2014). Solar-reduced GOs (SRGO) were synthesized under solar radiation and were coated on a polyurethane sponge for oil adsorption from water. Green reduced graphene oxide (GrGO) was synthesized using jute leaf extract and graphite from waste batteries for efficient tetracycline (TC) removal from water (Kabir M. H., et al., 2024). An environmentally friendly method using *Chlorella sp.* UMACC 313 suspensions produced rGO (Tee J. Y., et. al., 2024) (Peng C., et. al., 2011). A new reducing agent system using hydroiodic acid and trifluoroacetic acid can convert GOs into reduced GOs at subzero temperatures in solution. Investigate the electrical conductivity of rGO from GO using sodium borohydride ($NaBH_4$) as a reducing agent for 2 min to 24 hrs. at a temperature of 20–80 °C (Guex L. G., et. al., 2017).

1.4.2. Reduction of GOs under solvothermal and hydrothermal conditions

The thermal reduction of GOs in solvents (H_2O, DMF) at 100 and 150 °C enhances reduction rates compared to dry conditions. This process is also known as the solvothermal process. DMF accelerates GOs reduction, while DMSO and Ethylene glycol show less impact (Lin Z., et. al., 2010). Refluxing GOs in NMP deoxygenates and reduces with a color change from light brown to black. Commercial graphite was oxidized using modified Hummer's method, exfoliated in water via ultrasound (Farazas A., et. al., 2018), and reduced by stirring in hot distilled water at 95 °C, replacing toxic hydrazine and producing graphene or rGO without hazardous chemicals (Vorrada L., et. al., 2013). Hydrothermal reduction of GOs at 200 °C is an eco-friendly and cost-effective method. A detailed study shows that GOs reduced after 4 hours, yielding rGO with low oxygen content, smaller interlayer spacing, and wrinkled structures, suitable for various applications (Hui H. H., et. al., 2018).

A green approach to synthesizing rGO using palm oil leaf extract as a reducing agent, replacing hazardous chemicals. The method demonstrated successful oxidation, reduction, and restoration of its properties, with rGO showing enhanced electrochemical performance, ideal

for industrial applications (Faiz M. S., et. al., 2020). Reduced GOs, synthesized via a hydrothermal method from GOs, were done by Mei X. et. al., and showed the temperature-dependent reduction (Xiufeng M., et. al., 2015). Raman analysis confirms higher temperatures enhance GOs reduction, impacting interlayer spacing, I_D/I_G ratio, and conductivity (Xiufeng M., et. al., 2015). Thermal reduction of GOs with and without carbon suboxide (C_3O_2). Where lower activation energy, increasing GO's reactivity, while reducing the energy released during thermal decomposition compared to pure GOs (Rūta A., et. al., 2021). Water-dispersible rGO using pH-tuned liquid-phase photoreduction without stabilizers to afford defect-free GOs, maintaining stability and water dispersion, offering potential for future rGO applications. (Kazuto G., et. al., 2017).

1.4.3. Reduction of GOs in kerosene

Graphite was exfoliated into graphene sheets by high-energy wet milling in kerosene and 2-ethylhexanol to provide good morphology and structure. Graphene from 2-ethylhexanol had many layers, larger crystals, and fewer defects, while kerosene produced fewer layers, smaller crystals, and more defects (Al-Sherbini A., et. al., 2017). Graphene oxide synthesized from kerosene soot showed nanostructure, high conductivity with a large band gap, and frequency-independent conductivity (Mashiath K., et. al., 2018).

1.4.4. Reduction of GOs in water with ascorbic acid

GOs were synthesized from natural graphite and reduced using ascorbic acid (AA) as a green reductant rapidly in 30 minutes, where natural graphite proved superior for GOs synthesis, providing a cost-effective, eco-friendly method for producing GOs and rGO (De Silva K. K., et. al., 2017). GOs were reduced using ascorbic acid (vitamin C), a low-cost, eco-friendly agent, replacing toxic reducers like hydrazine. The reduction process preserved key properties of rGO, making it suitable for various applications (Sharma T. K. A., et. al., 2021). An eco-friendly method was developed to reduce GOs using carbonic acid, synthesized from dry ice and deionized water or acetic acid and sodium bicarbonate (Wadekar P. H., et al., 2018). The resulting rGO shows excellent water dispersibility, high specific capacitance (350.3 F/g), and stable electrochemical performance, suitable for application in supercapacitors. A large-scale and cost-effective, green method for synthesizing GOs and rGO using natural graphite and ascorbic acid as a reductant was also demonstrated (De Silva K.K., et. al., 2017).

A green method to synthesize GOs by the Tour method was successfully reduced to rGO using ascorbic acid, offering an eco-friendly approach (Habte A. T., et. al., 2019). The individual graphene oxide sheets can be readily reduced under mild conditions using L-ascorbic acid (L-AA), and through this simple approach, a partially of water-soluble graphene was obtained on a large scale (Zhang J., et. al., 2010). This study afforded high surface area rGOs. A graphene oxide reduction method using ascorbic acid produced a chitosan/graphene modified electrode, which showed excellent electrocatalytic activity for dopamine and ascorbic acid detection, with low detection limits and successful application in human serum samples (Xu Z., et. al., 2012). A scalable one-pot method for producing rGO via sonication-assisted oxidation of graphite, followed by ascorbic acid reduction (Abdolhosseinzadeh S. H., et. al., 2015). This process simplifies washing, reduces production time, and enhances yield, facilitating large-scale graphene production. Vitamin C, as an effective, non-toxic alternative to hydrazine, achieves similar deoxygenation and conductivity restoration, enabling stable GOs suspensions in water and organic solvents for large-scale applications (Merino M. J. F., et. al., 2010). A low-cost, environmentally friendly reduced graphene nanosheets (rGNS) with L-AA for multifunctional coatings in the aeronautical industry was also demonstrated (Markus O., et. al., 2023).

1.5. Characterization of graphene materials

1.5.1. UV-Visible light absorbance properties

GOs showed good absorbance in the UV region, and the absorbance is linear with the concentration. So, this technique can be utilized for the measurement of GOs concentration in solution (Abele C. D., et. al., 2022). It was also observed that there is a small change in UV light absorbance due to a change in the particle size of GOs, and the variation occurs due to the chemical compositional change in the functional groups during size reduction activities. Chemical reduction of GOs provides excellent rGO properties using hydrazine as a reducing

agent, showing a red shift from 238 to 279nm in UV-Visible absorption band (Hidayah N. M., et. al., 2017).

1.5.2. FT-IR spectroscopic analysis

Fourier Transform Infrared (FT-IR) spectroscopy is a powerful analytical technique widely used for the characterization of graphene-based materials such as GOs, rGO, and microwave-assisted graphene. This technique provides valuable insights into the functional groups present on the material's surface, which play a crucial role in determining their properties and applications.

For GOs, FT-IR spectra typically reveal the presence of oxygen-containing functional groups, such as hydroxyl (–OH), epoxy (>c^Oc<), and carbonyl (>C=O). The peak at 1288 cm^{-1} is attributed to (C-O) bond bending in >c^Oc<, while C-OH bending is observed at 1587 cm^{-1}. The carbonyl group shows a peak at 1724 cm^{-1} as (>C=O) stretching, and a broad peak at 3448 cm^{-1} is attributed to O-H stretching vibration, respectively. These groups are introduced during the oxidation process. These functional groups significantly enhance the hydrophilicity and chemical reactivity of GOs but also disrupt its conjugated π-electron system (Andrijanto E., et. al., 2016).

In the case of rGO, the FT-IR spectra demonstrate a significant reduction or elimination of these oxygen-containing groups, indicating the partial restoration of the conjugated carbon network. This transformation highlights the efficiency of the reduction methods used and correlates with the improved electrical and mechanical properties of rGO (Ghorbani M., et. al., 2015).

1.5.3. FT-Raman spectroscopic analysis

It can be observed that GOs exhibit two distinct Raman features at approximately 1353 cm^{-1} and approximately 1598 cm^{-1}, which correspond to the D and G bands (Kaushal A., et. al., 2019). The C-C stretching, which was constant across all sp^2 Carbon systems, contributed to the G peak. Disordered regions in C-C with sp^3 carbons coupled to out-of-plane vibrations were the cause of the D peak. In addition, GOs showed a higher wavenumber of the 2D peak at about 2686 cm^{-1}. The location of GOs verified that the GOs that were generated were multilayered. The combination of the D and G peaks, which were distinguished at 2938 cm^{-1}, was assigned the S3. For rGO, it has been noted that as the relative intensity rises, the G and D peaks have

grown wider and narrower, while the S3 and 2D peaks have gotten narrower. GOs main are reduced to shifting D, G, 2D, and S3 peaks to approximately 1349 cm^{-1}, 1596 cm^{-1}, 2714 cm^{-1}, and 2947 cm^{-1}. As of the restoration of the sp^2 carbon and the reduction in the average size of the sp^2 region, the I_D/I_G ratio for GOs increases to 1.16 after reduction. Using the following equations, the I_D/I_G ratio is used to estimate the in-plane size of sp^2 domains (Lsp^2) were determined using (equation-1), average defect distance (LD) using (equation-2), and defect density (nD, cm^{-2}) using (equation-3): -

$$L\text{sp}^2 = \frac{560\ \text{IG}}{\text{EL4 ID}} \quad \ldots\ldots\ldots\ldots\ldots\ldots\ldots\ldots\ldots\ldots \text{(1)}$$

$$L^2_{\text{D}}\ (nm^2) = 2.4 \times 10^{-9}\ \lambda^4_{\text{L}}\ \text{I}_{\text{G}}/\text{I}_{\text{D}} \ldots\ldots\ldots\ldots\ldots\ldots\ldots \text{(2)}$$

$$nD = 2.4 \times 10^{22}\ \text{I}_{\text{D}} / \lambda^4_{\text{L}}\ \text{I}_{\text{G}} \ldots\ldots\ldots\ldots\ldots\ldots\ldots\ldots \text{(3)}$$

where E_L and λ_L stand for the laser source's energy and wavelength, respectively. For intercalants, equations (6) and (7) are valid for charging impurities and defects. The calculated values for the crystallite size in both the in and out planes (i.e., D and L values) and the observed I_D/I_G ratio showed that rGO had more formed sp^2 domains in smaller sizes than GOs. As a result, the rGO computed defect density (nD) was enormous, which encouraged the emergence of additional defects.

Following the transformation of GOs to rGO, the average number of graphene layers and average sp^2 crystallite size (L) drop from 15 to 3 and 17.33 nm to 14.75 nm, respectively (Kaushal A., et. al., 2019). Following reduction, the increased I_D/I_G ratio showed an increase in the number of sp^2 domains along with an increase in defect density.

1.5.4. X-Ray diffraction analysis

For graphite, a single, sharp peak has been observed at $2\theta = 26.34°$. This peak determined the orientation at (002) and (FWHM = 0.34368) as well as the fine arrangement of the layered structure with 0.334809 nm d-spacing. The 2θ shifted to 10.24° for GOs, indicating that graphite had fully oxidized to become GOs (Kaushal A., et. al., 2019). Additionally, the interlayer distance of GOs was increased by 0.863 nm, with a d-spacing and (001) orientation. Inter-layer spacing was calculated using the following (equation 4):

$$2d \sin\theta = n\lambda \ldots\ldots\ldots\ldots\ldots\ldots\ldots\ldots\ldots\ldots \text{(4)}$$

Where d = Interlayer spacing, θ= Diffraction angle, n= Wavenumber, and λ= Wavelength of X-ray source.

The presence of a broad peak for rGO at 2θ = 24.10 suggested that the crystal phase was arranged at (002). The d-spacing of rGO was decreased by the elimination of functional groups that contained oxygen. The band of disordered carbon materials, visible at 2θ = 42.60° with (100) orientation, was revealed by a second, less intense peak.

The Debye-Scherer equation (equation-5) provides the average crystallite width (D) within the graphene maintenance: -

$$D = k \lambda / \beta \cos \theta \quad \text{.....(5)}$$

where, for spherical crystals with cubic unit cells, K=0.89 (a parameter associated with crystallite shape), θ = half diffraction angle, and β = full peak width of the diffraction peak at half maximum height (FWHM).

Similarly, the size of an in-plane crystallite (L) can be obtained from (equation 6)

$$L = 1.84 \lambda / \beta \cos \theta \quad \text{.....(6)}$$

It has been observed that the average crystallite size in rGO is smaller than in GOs (D ~ 118 Å; L ~ 301.3 Å). This demonstrated the foundation of more lateral defects and the shrinkage of graphene regions, which were caused by the exclusion of graphene layers during reduction. Debye-Scherer and Bragg's equations can be combined to get the expression for n (equation 7), which can be used to determine the average number of graphene layers (n) per region from the broadening of the peak by XRD.

$$n = D / d + 1 = 2k \tan \theta + 1 \quad \text{..... ...(7)}$$

1.5.5. Morphology analysis using TEM

The morphology of chemically oxidized-reduced graphene was analyzed using Transmission Electron Microscopy (TEM), and it was found that there were defect-free areas where carbon atoms are chemically sp^2 bonded with three neighboring carbon atoms to form a nanoscale graphene sheet (Navarro G. C., et. al., 2010). TEM image can explain the area percentage of graphene, defect-free sp^2 graphene, and defective area occurred during oxidation reduction process in GOs and rGO (Erickson K., et. al., 2010).

1.5.6. Scanning tunneling spectroscopy (STS) study

According to the Scanning Tunneling Spectroscopy (STS) investigation of GOs and rGO, the GO sheets are 1-1.2 nm thick and get thinner upon reduction. The rGO revealed a spectrum of band structures, whereas the GO's band gap was discovered to be in the region of 0.8 eV. Because rGO possesses a non-zero band gap, unlike graphene, it opens up a new area of research on atomically thin layers of carbon (Kumar P., 2019).

1.6. Application of GOs and rGOs

The applications of GOs and rGOs are vast and diverse due to their unique chemical, electrical, and physical properties. In spite of huge unexplored field of application, a short but very important fields of application are explained here with an overview across various fields-

1.6.1. Removal of organic dyes

The textile industry uses a lot of extremely harmful chemicals for sizing, softening, desizing, whitening, dyeing, and finishing at different points in the process (Kishor R., et. al., 2021). Apart from the textile industry, other industries that can release dyes and heavy metals include mining, food additives, papers, plastics, pharmaceuticals, paints, electroplating, batteries, and other industrial, medical, and agricultural sectors (Adel M., et. al., 2022). Among the textile chemicals, dyes are considered one of the most toxic chemicals (Lellis B., 2019). The majority of dyes are long-lasting, and do not decompose spontaneously (Forgacs E., et. al., 2004). Treatment with roughly 2% of the untreated dyes gets into the effluent, which seriously pollutes the environment (Foo K. Y., et. al., 2010). Human health is impacted by wastewater that contains dyes because the textile industry produces a lot of wastewaters that is brightly colored and contains a variety of persistent contaminants (Al-Tohamy R., et. al., 2022).

Dye staffs are extremely stable to light and other environmental factors and do not break down, penetrate waterbodies, lower dissolved oxygen levels, have an impact on aquatic ecosystems, and ultimately endanger life. In addition to causing sneezing, asthma, and skin irritation, dyes damage the human immune system. Therefore, it is crucial to remove these compounds from wastewater before disposal (Hassaan M. A., et. al., 2017). According to Uddin M. T., et. al., about 10% of the dyes, which are extremely poisonous and carcinogenic, are released into water (Uddin M. T., et. al., 2009). Additionally, dyes alter the color of water, preventing sunlight from reaching aquatic plants, disrupting their ability to photosynthesize, and resulting in an unbalanced aquatic ecosystem (Thakur K., et. al., 2019). Thus, these dyes ought to be

eliminated in light of the potential for environmental toxicity and harm to public health. But without any prior treatment, textile dyes are released as wastewater and effluent into aquatic habitats such as lakes, rivers, streams, and ponds, constituting a major ecotoxicological risk and having toxic effects on living things (Parmar S., et. al., 2022).

Therefore, one of the main areas of applied science study has been finding a practical and efficient way to remove dyes from wastewater. One crucial area of fundamental and applied study is the adsorption of different dyes to reduce industrial effluent contamination. It is crucial to find new, affordable, and effective materials for dye removal. Over the years, a number of dye removal methods have been developed, including membrane separation, ion exchange, coagulation/ flocculation, and even biological procedures (Mahmoudian M., et. al., 2021). Numerous of these methods have drawbacks, including high energy usage, intricate designs, and lengthy operating procedures. Among these techniques, adsorption stands out as one that may be helpful because it is inexpensive, straightforward, and simple to use (Gisi D. S., et. al., 2016). Researchers have discovered a new method to enhance the existing solutions in wastewater treatment processes as a result of advancements in nanotechnology and the use of nanomaterials (Ali M. E., et. al., 2020).

Many outstanding evaluations that have been published to date demonstrate that graphene-based nanoparticles can be used to remove toxic pollutants from wastewater. Nevertheless, most of these evaluations focus on a single pollutant class or are limited to a certain type of material or adsorbent.

The application of graphene-based materials has spurred studies at the nexus of various sectors, particularly environmental restoration, with an emphasis on the basic studies of graphene-based nanoparticles for wastewater management, by focusing on the challenges facing future research. Multiple fields of study have experienced a revolution as a result of the multiple uses of graphene-based nanomaterials. Because of its many benefits, including a very high theoretical surface area and special physical characteristics (like high mechanical strength and electrical and thermal conductivity), graphene, a novel carbon-based nanomaterial, is attracting a lot of attention (Novoselov K. S., et. al., 2012), (Hossain M. N., et. al., 2017). Like graphene, GOs are a monolayer of carbon atoms arranged in a honeycomb pattern. Its two-dimensional planar structure aids in the processes of charge transfer (Amiri M., et. al., 2017).

A large number of oxygen-containing functional groups, including carboxyl, hydroxyl, and epoxide groups, are also present in GOs, giving it a generally hydrophilic and negatively charged surface (Björk J., et. al., 2010). Because of its special qualities, graphene is a great option for organic pollutants removal from water through adsorption and catalysis (Khaliha S., et. al., 2021), (Mantovani S., et. al., 2021), (Lombardi L., et. al., 2022). Because of their functional groups and huge specific surface area, GOs and rGO, which are derivatives of graphene, have enhanced adsorption capabilities (Mantovani S., et. al., 2021), (Mantovani S., et. al., 2023). Organic pollutants can be efficiently captured by these nanomaterials via hydrogen bonding, π-π stacking, and other interactions.

Additionally, GOs can be readily functionalized by a variety of treatments to change the functional groups and achieve the required surface characteristics. Because of their physical and chemical characteristics, graphene and other carbon materials can be employed to create membranes. For instance, because of its high surface area, oxygen-containing groups, and mechanical durability, GOs are used as a membrane material (Zeng H., et. al., 2020). In recent years, GOs and rGOs, two graphene-related materials, have been widely produced and employed in a wide range of applications (Sanchez V. C., et. al., 2012). In addition to cationic and anionic dyes, Wang et al. studied the adsorption of a neutral dye called acridine orange (AO) (Wang H., et. al., 2016). They created an MGSi/GOs composite by coating a GOs sheet with calcium silicate, following the deposition of Fe_3O_4 nanoparticles. Up to 193.05 mg/g may be adsorbed by these nanocomposites.

A different study (Wanag A., et. al., 2017) demonstrated that when the number of C=O groups decreased, magnetic graphene nanoparticles (Fe_3O_4@GNs) had a greater capacity for MB adsorption. As anticipated by the pseudo-second-order model, the kinetics data showed that MB dye and Fe_3O_4@GNs underwent chemisorption through π-π interactions (Hartono T., et. al., 2009). The adsorption behavior of cationic dyes on GOs has only been reported twice recently (Bradder P., et. al., 2011), (Yang S. T., et. al., 2011), and the interactions between the adsorbent and the adsorbate have not been thoroughly examined.

The functional groups and the multilayer structure of EGO (Jeong H. K., et. al., 2008) might help the dye adsorption. In their 2020 study, Mao B., et. al., found that employing GOs, the dye

(Methylene blue) removal efficiency by almost 99.0% was achieved (Mao B., et. al., 2020). Additionally, their investigation has demonstrated that GOs is the most effective adsorbent among the materials examined in this study; its maximum adsorption capacity for MB and RhB was 403.3 mg/g and 686.6 mg/g, respectively, demonstrating its exceptional adsorption ability. rGO is a promising material for the removal of 1-naphthol from water, according to (Ali M. M., et. al., 2014).

It was reported in their study that EGO and rGO can act as good adsorbents for cationic and anionic dyes from aqueous solutions, respectively (Ramesha G. V., et. al., 2011). While EGO shows removal efficiency of up to 95% for cationic dyes, the removal efficiency is negligible for anionic dyes. This is in parallel with the charge-based interactions between EGO and the adsorbates. The removal efficiency in the case of rGO is 95% for anionic dyes, while it is 50% for cationic dyes. According to a study by Mahmudunnabi (Mahmudunnabi D. M., et. al., 2024), produced rGO that showed a high adsorption ability towards anionic dye Tarques Green-N (TGN) with a q_{max} of 588.24 mg/g at a pH of 7.0. The adsorption of TGN on rGO was found to follow pseudo-second-order kinetics and the Langmuir model. A study demonstrated a powerful nano-adsorbent photocatalyst for the effective degradation of organic dyes by rGO 250 (Sha S. M., et. al., 2024). Then, rGO-250 obtained the best photocatalytic degradation (36.28% for IC and 25.73% for NR) and adsorptive removal (29.26% for IC and 25.23% for NR) of dyes, demonstrating that the primary causes were narrowing of the band gap and increased surface area. After performing the reaction up to five times, rGO-250 was able to destroy over 90% of dyes, demonstrating its great stability and reusability.

Thus, GOs have proven to be an extremely effective adsorbent for the removal of cationic dyes as well as for the separation and recycling of mixed cationic and anionic dyes. Additionally, it implies that GOs may be utilized in the treatment of industrial wastewater to successfully eliminate dangerous dyes, which are frequently connected to the food, paper, cosmetic, and textile industries (Shirazi E.K., et. al., 2020).

1.6.2. Removal of heavy metals using GOs and rGOs

Numerous studies have demonstrated the effectiveness of GOs and rGO in removing various heavy metals from wastewater. The following sections highlight key findings from recent research. Copper is a common heavy metal pollutant found in industrial wastewater. Previous

researchers showed that rGO exhibited a high adsorption capacity for Cu^{2+} ions, achieving removal efficiencies of up to 97.94% (Wang B., et. al., 2012), (Ahmed S., et. al., 2023). The study emphasized the importance of pH, with higher adsorption capacities observed at lower pH levels due to increased electrostatic attraction.

Lead is another toxic heavy metal that poses serious health risks (Guo T., 2023). A study by Pourbeyram, S., et. al., demonstrated that a GO-Zirconium Phosphate nanocomposite effectively removed Pb^{2+} ions from aqueous solutions, achieving high adsorption rates due to the synergistic effects of both materials (Pourbeyram S., et. al., 2016). The functional groups on GOs played a crucial role in binding lead ions, highlighting the importance of material design in enhancing adsorption performance. Cadmium is known for its toxicity and persistence in the environment. Research conducted previously revealed that GOs could efficiently adsorb Cd^{2+} ions, with the adsorption process being influenced by factors such as contact time, initial concentration, and temperature (Ahmed S., et. al., 2023), (Guo T., et. al., 2021). The study also noted the potential for magnetic separation, which could simplify the recovery of the adsorbent after treatment.

Mercury is a highly toxic heavy metal that requires effective remediation strategies. A study by Awad et al. demonstrated that partially rGO functionalized with 2-Imino-4-thiobiuret exhibited high selectivity and efficiency for the removal of Hg^{2+} ions from polluted water (Awad F., et. al., 2017). The functionalization process significantly enhanced the binding affinity of the adsorbent for mercury, showcasing the potential of tailored graphene-based materials for specific applications. In conclusion, the application of GOs and rGO for the removal of heavy metals from wastewater represents a promising approach to addressing water pollution. Their unique properties, including high surface area, ease of functionalization, and recyclability, make them effective adsorbents for various heavy metals. Ongoing research continues to explore the optimization of these materials and their integration into practical wastewater treatment systems, paving the way for sustainable and efficient solutions to heavy metal contamination. GOs were synthesized through the pyrolysis of biomass, and Cr^{3+} was efficiently removed with a q_{max} of 74.79 mg/g with 54.21% efficiency (Zohra F. T., et. al., 2022).

1.6.3. Supercapacitor application

Supercapacitor behavior of GOs with ionic liquid was also investigated, and it was found that the GOs exhibit the greatest supercapacitor performance in an ionic liquid (Jadhav S. T., et. al., 2013). The specific capacitance of GOs in ionic liquid was 290F/g, and the CV curves were not changed with increased scan rate, which indicated the good high-rate capability. The supercapacitance of the areal GOs and rGOs is 99.3 μF/cm^2 and 556.7 μF/cm^{2,} respectively, at the scan rate of 0.1 V/s. Therefore, rGO shows a better capacitive behavior than GOs (Rai S., et. al., 2018). With the increase of scan rate, the capacitance of GOs increases, but that of rGO decreases.

1.6.4. Nanomedical applications

Graphene and GOs toxicity and biocompatibility have shown several aspects that affect how they behave in biological systems. The toxicity of these nanomaterials has been demonstrated to be size- and dose-dependent in both in vitro and in vivo investigations (Aleksandrzak M., et. al., 2016). The quantity of oxygen-containing functional groups on the surface of GOs or rGO is another important factor. Because of the interaction between O-groups and blood cells, graphene is more biocompatible than GOs according to blood toxicity studies. Enhancing GO's biocompatibility by functionalization has been accomplished using a variety of compounds, including PEG, PVK, dopamine, heparin, and amine modifiers. Because GOs increase the cytotoxic effect of medications. Biocompatible polymers like PEG, chitosan, dextran, and poly (ethylene imine) are the most often utilized materials, particularly for targeted drug delivery systems. By functionalizing the nanocarrier with receptors like peptides, antibodies, and other ligands, this is made possible. Nanocarriers smaller than 100 nm have the potential to improve anticancer activity and the therapeutic effect.

1.6.5. Carbocatalytic activity of GOs and rGO

Because of their wide availability, ease of surface modification, non-toxicity, various surface features, ease of purification, and financial benefits, carbon nanomaterials, particularly GOs and carbon dots, are crucial for heterogeneous catalysis (Majumdar B., et. al., 2018). The π-π* network allowed GOs to exhibit Carbocatalytic activity towards several organic conversions, and the presence of oxygenated functional groups on the GOs surface also increased catalytic activity. Additionally, GO's oxygenated functional groups increase the reaction's analyzability. For a number of oxidation and acid-catalyzed processes, oxygenated functional groups served as the active site. Other active catalysts for the reduction of metal and metal oxide nanoparticles could be anchored by different oxygenated functionalities on the GO's surface.

1.6.6. GOs and rGO nano-composites with polymers

GOs and rGO were made composite with poly(3-hydroxythiophene), and the optoelectronic properties of both the composites were measured to understand the charge transfer process. The energy gap between HUMO and LOMO of the composites was diminished by the reduction process (Zheng F., et. al., 2015). rGO-polymer nanocomposites were prepared using thermal annealed rGO with polyazomethine by the solvent casting method in dimethylformamide (Kostromin S. V., et. al., 2019). The solution conductivity dependence on rGO composition at different temperatures, and in both cases, the conductivity increased with rGO composition and solution temperature.

GOs were used to make a nanocomposite with Hytrel, a kind of polyester-based thermoplastic polymer, and their effect on its thermos-mechanical and physicochemical properties was studied (Pandey N., et. al., 2021). The thermal stability and mechanical properties of GO/HTL nanocomposites were increased with increasing GO content. The composites have a valuable improvement in tensile strength (139%) and storage modulus (72%) for the HTL composite containing 5 wt% GOs. The incorporation of GOs into HTL polymer shows enhancement in thermal and mechanical properties due to the presence of the strongest noncovalent interaction (π–π^* stacking) between the interface of the nanocomposite.

The impact of functionalized-GOs or GOs on the manufactured copolymer product and on the in-situ bulk radical copolymerization method of their nanoscopic materials based on n-butyl methacrylate and styrene was investigated. Lower initiator efficiency was the initial observation attributed to side reactions between the hydroxyl groups on the surface of GOs and the initiator primary radicals (Tsagkalias I. S., et. al., 2019). Composites of linear low-density polyethylene (LLDPE) polymer were formed with higher surface area (C-GNP, 300-500 m^2/g) and lower surface area (M-GNP, 120-150 m^2/g) graphene nanoplates to observe the effect of their surface area on composite properties (Khanam P. N., et. al., 2016). Due to higher surface area C-GNP composite acquired a more brittle morphology than the M-GNP, resist a melt flow index 43% to 35%, a low increase in thermal conductivity 31% to 92%, higher increase in electrical conductivity of 4.28 X 10^{-5} S/cm than 1.1X10^{-7} S/cm, respectively.

1.6.7. GOs and rGOs in polymer membranes

Polysulfone-GOs mixed matrix membranes were prepared using GOs, which showed enhanced performance of the nanofiller of mixed matrix membranes with polysulfone (PSf). Composite membrane exhibited improved water flux (up to 2.7 times) and oil rejection than the control PSf sample. Composite with GOs produced by Staudenmaier methods showed better performance than the Hummer's and Tour methods in the separation of oil-water emulsion (Yu Y., et. al., 2020). (Sali S., et. al., 2019).

1.6.8. Antimicrobial activity of GOs and rGOs

GOs and rGO have garnered significant attention due to their remarkable physicochemical properties, including large surface area, tunable surface chemistry, and biocompatibility. These features make GOs and rGO particularly attractive for various applications, including antimicrobial agents. Given the rise in antimicrobial resistance, developing novel materials like graphene derivatives to combat bacterial, fungal, and viral infections is a pressing need. This review explores the antimicrobial mechanisms of GOs and rGO, compares their effectiveness against various pathogens, and discusses the influence of surface modifications and nanocomposites in enhancing their antibacterial performance.

One of the most well-documented mechanisms of antimicrobial activity in GOs and rGO is the physical disruption of microbial cell membranes. The sharp edges of GOs nanosheets can penetrate and disrupt bacterial cell walls, leading to cell death. In a study by it was demonstrated that direct contact with GOs and rGO nanosheets caused membrane damage in *Escherichia coli*, resulting in cell lysis (Liu S., et. al., 2011). The study proposed a three-step antimicrobial mechanism involving initial cell deposition, membrane stress due to the interaction with the sharp edges of graphene sheets, and subsequent cell death due to membrane disruption. Similarly, GOs exhibited strong antimicrobial activity against both bacterial and fungal pathogens, causing local perturbation of the cell membrane and leakage of cellular contents (Chen J., et. al., 2013). The study showed that GOs wrap around the pathogens, causing significant membrane disruption, ultimately leading to cell death. In addition to physical damage, oxidative stress plays a crucial role in the antimicrobial action of GOs and rGO. GOs sheets can generate reactive oxygen species (ROS), which damage cellular components such as lipids, proteins, and DNA, leading to microbial death. Gurunathan et. al. demonstrated that GOs and rGO induce the production of superoxide anions in *Pseudomonas aeruginosa*, which contributed to oxidative damage and cell death (Gurunathan S., et. al., 2012). Interestingly,

some studies suggest that oxidative stress mechanisms may not always involve ROS. For instance, Alayande et. al. reported that the antimicrobial activity of rGO-CuO nanocomposite films was not dependent on ROS production. Instead, the bacterial inactivation was attributed to direct interactions with the bacterial cell membrane and the inherent properties of copper oxide combined with rGO (Alayande A. B., et. al., 2019).

In addition to physical and oxidative damage, graphene-based materials can entrap bacterial cells, preventing their proliferation. Perreault F., et. al., showed that larger GO sheets trapped bacteria, preventing their replication and effectively inactivating them (Perreault F., et. al., 2015). While the cell entrapment was reversible by mechanical means such as sonication, it still provided a temporary antimicrobial effect. The study emphasized that smaller GO sheets are more effective when applied as surface coatings due to their higher defect density and greater oxidative potential.

GOs and rGOs are particularly effective against gram-negative bacteria, including *Escherichia coli* and *Pseudomonas aeruginosa*. The outer membrane of gram-negative bacteria makes them more susceptible to the physical disruption caused by graphene sheets. Studies have consistently demonstrated significant antibacterial activity of GOs and rGO against *E. coli*, with membrane damage being the primary mechanism (Wanag A., et. al., 2017). *Pseudomonas aeruginosa*, a pathogen known for its resistance to many antibiotics, is also highly susceptible to GOs and rGO. Gurunathan et. al. demonstrated that both GOs and rGO exhibited dose-dependent antibacterial activity against *P. aeruginosa*, with increased production of ROS and loss of cell viability (Gurunathan S., et. al., 2012).

Though gram-positive bacteria possess a thicker peptidoglycan layer, GOs and rGO still exhibit significant antimicrobial effects against these microorganisms. Studies have shown that *Staphylococcus aureus*, a common Gram-positive bacterium, is effectively inactivated by GOs and rGO, particularly when combined with other materials like copper oxide or titanium dioxide. In a study by Wanag et. al., rGO-modified TiO2 showed enhanced photocatalytic activity against *S. aureus*, leading to complete bacterial inactivation within 75 minutes of exposure to artificial solar light (Wanag A., et. al., 2017). The antimicrobial activity of graphene-based materials is not limited to bacteria. Chen J., et. al., demonstrated that GOs could inhibit the reproduction of fungal pathogens such as *Fusarium graminearum* and *Fusarium oxysporum*. The study found that GOs caused partial cell swelling and lysis in fungal conidia,

suggesting that the material interacts with fungal pathogens similarly to its interaction with bacteria (Chen J., et. al., 2013). In light of growing antibiotic resistance, one promising avenue for the application of GOs and rGO is in combination with antibiotics. Studies have shown that graphene derivatives can enhance the efficacy of conventional antibiotics. Butler et. al. demonstrated that GOs, when combined with ciprofloxacin, showed additive antimicrobial effects against multidrug-resistant pathogens such as *Enterococcus faecium* and *Klebsiella pneumoniae* (Butler J. A., et. al., 2020). This synergistic effect is highly promising for the development of new antimicrobial therapies to overcome resistance.

1.6.9. Biocompatible graphene

The effects of GOs on mice and human fibroblast cells were investigated in order to determine the biocompatibility of GOs (Kiew S. F., et. al., 2016). GOs with low dose administration less than 20 μg/mL did not exhibit toxicity to human fibroblast cells, but the doses of more than 50 μg/mL exhibited obvious cytotoxicity. In the case of mice dose of 0.25 mg did not exhibit obvious toxicity high dose of 0.4 mg/mL exhibited chronic toxicity, such as 4/9 mice died and lung granuloma formation, mainly located in the lung, liver, spleen, and kidney, almost could not be cleaned by the kidney. The biodegradation of GO sheets was experimented with using myeloperoxidase (hMPO) produced from human neutrophils in the presence of a small amount of hydrogen peroxide (Kurapati R., et. al., 2015). hMPO fails in degrading the most aggregated GOs, but succeeds in completely metabolizing GOs that were highly dispersed due to hydrophilicity, negative surface charge, and colloidal stability of the aqueous GOs in their biodegradation by hMPO catalysis.

1.6.10. Environmental applications

The potential of GOs and rGO in environmental remediation is particularly notable. Their high surface area and reactivity allow for effective adsorption of heavy metals and organic pollutants from water. For instance, GOs have been shown to effectively adsorb heavy metals such as lead and arsenic, with studies indicating that they can be regenerated for multiple cycles, retaining a significant portion of their adsorption capacity (Felshia S. C., et. al., 2023). GOs have been shown to effectively remove high concentrations of formaldehyde in alkaline media. Notably, GOs can adsorb 411 mg of formaldehyde per mg of material. After this process, the used GOs can be reduced to rGO and further reutilized as an energy storage material, showing high double-layer capacitance for supercapacitors (Liang H., et. al., 2014). Moreover, GOs can serve

as a support material for catalysts in environmental remediation. When combined with iron oxide (Fe_3O_4), GOs is used to create composite microjets that are effective in catalyzing the degradation of methylene blue dye. These microjets offer a magnetically recoverable and reusable option for organic dye degradation, making them an efficient tool for water purification (Shi H., et. al., 2020).

Similarly, rGO composites have demonstrated effective reuse in removing contaminants, maintaining structural integrity and adsorption capacity even after several cycles of use (Zhang Y., et. al., 2011). In the context of organic pollutant removal, reported that GO-based aerogels could retain over 90% of their initial adsorption capacity after five cycles of methylene blue dye removal, showcasing the economic and environmental benefits of reusing these materials (Jin Y., et. al., 2022). Additionally, rGO's hydrophobic properties make it suitable for oil spill cleanup, with studies indicating that rGO-based membranes can be regenerated with minimal loss of adsorption capacity (Felshia S. C., et. al., 2023), (Zhang Y., et. al., 2011).

1.6.11. Application in energy storage devices

The reusability of GOs and rGO is also critical in energy storage applications. rGO, in particular, has been extensively studied for its application in supercapacitors and lithium-ion batteries. rGO derived from GOs via thermal reduction shows improved performance as an anode material in lithium-ion batteries and supercapacitors. A study demonstrated that rGO annealed at 400 °C exhibited a reversible charge capacity of 1220 mAh/g, making it ideal for high-capacity energy storage (Kim J. M., et. al., 2014). Zhu Y., et. al., demonstrated that rGO-based supercapacitor electrodes could be reused after regeneration, showing minimal degradation in capacitance even after 1000 charge-discharge cycles (Zhu Y., et. al., 2010), (Zhang Y., et. al., 2011). Similarly, rGO-coated anodes in lithium-ion batteries could be reused effectively, maintaining excellent capacity retention after multiple cycles were found (Zhang Q., et. al., 2023). Also, rGO shows promise for hydrogen storage, a critical factor in the development of clean energy technologies. When reduced thermally, rGO demonstrates an optimal pore size for hydrogen storage, with capacities reaching 5 wt%. This performance is comparable to advanced hydrogen storage materials, making rGO a viable candidate for future energy applications (Kim J. M., et. al., 2014).

1.6.12. Application in catalysis

In catalysis, GOs and rGO serve as effective catalysts or supports for various reactions. GO's functional groups enable it to act as a catalyst in oxidation reactions, retaining most of its catalytic activity after multiple cycles (Felshia S. C., et. al., 2023). rGO, on the other hand, is often used as a support material for metal nanoparticles, enhancing catalytic efficiency (Gupta V. K., et. al., 2009). Reported that an rGO-supported palladium catalyst shows activity and selectivity after five reuse cycles, underscoring the durability of rGO in catalytic applications (Zhang Y., et. al., 2011).

1.6.13. Biomedical applications

In biomedical fields, the ability to reuse GOs and rGO is crucial for reducing waste and costs associated with medical treatments. GO's functionalization capabilities make it an ideal candidate for drug delivery systems, where it can be regenerated for multiple cycles of drug loading and release without significant loss of efficiency (Zhang Y., et. al., 2011). Furthermore, rGO-based biosensors show the ability to be washed and reactivated for multiple uses, retaining sensitivity and specificity, which is essential for sustainable diagnostic tools (Felshia S. C., et. al., 2023).

1.7. Challenges and future directions

Despite the promising applications of GOs and rGO, challenges remain regarding their long-term reuse. Material degradation over multiple cycles can lead to reduced performance, particularly in energy storage and catalytic applications (Dreyer D. R., et. al., 2010). Studies have reported that rGO's performance might degrade due to incomplete reduction or defect formation during regeneration processes (Long J., et. al., 2012). Techniques such as microwave-assisted reduction and green reduction methods are pushing the boundaries of scalable production. However, further advancements are needed to reduce production costs and environmental impact while maintaining the high quality of rGO (Xie X., et. al., 2019). As the functionalization of GOs and rGO evolves, future research should focus on tailoring the oxygen functional groups to optimize material properties for specific applications. This would further enhance the performance of GOs and rGO in energy storage, catalysis, and environmental remediation (Kuo S., et. al., 2013). Future research should focus on developing robust regeneration techniques that minimize these issues while maintaining the functional integrity of GOs and rGO.

1.8. Limitations for the synthesis of GOs and rGOs

The synthesis of GO and reduced rGO has been a subject of extensive research due to their unique properties and potential applications. However, several limitations exist in the synthesis processes that affect the quality, scalability, and functionality of these materials. This literature review discusses the key challenges associated with the synthesis of GOs and rGO. One of the critical limitations in the synthesis of rGO is the use of toxic reducing agents, particularly hydrazine, which is efficient but harmful to both human health and the environment. Hydrazine has been the preferred choice due to its ability to restore the properties of graphene effectively. Still, its toxicity makes it unsustainable for large-scale production (De Silva K. K., et. al., 2017). Consequently, alternative green reductants, like ascorbic acid, have been explored. However, they tend to be less effective, leaving behind more oxygen functional groups, which negatively affects the electrical conductivity and other key properties of rGO (Khan J., et. al., 2021) (Khan J., 2021).

Another major challenge in rGO synthesis is the incomplete reduction of GOs. Despite the use of various chemical or thermal reduction methods, oxygen-containing functional groups often remain attached to the graphene sheets. These functional groups prevent the material from fully regaining its pristine electrical and mechanical properties. Studies suggest that even mild thermal treatment followed by chemical reduction can only remove around 47% of the oxygen functional groups (Lopez M. L, et. al., 2017). This partial reduction affects the material's performance in applications such as supercapacitors and other electronic devices, where the electrical properties of the graphene are critical.

One of the primary limitations in the synthesis of GOs and rGO is the introduction of impurities during the oxidation process. Jalili R., et al, highlight that the oxidation of graphite can introduce various contaminants, which can adversely affect the performance of graphene-based devices (Jalili R., et. al., 2018). The presence of silicon, as identified in their study, is a common contaminant that arises from the reagents used during synthesis. This contamination can lead to significant deviations in the expected electronic and mechanical properties of the resulting graphene derivatives. Furthermore, the synthesis methods often rely on high-purity graphite, which may not always be feasible or cost-effective for large-scale production (Jalagonia N., et. al., 2022). Traditional methods of producing GOs, such as Hummer's method, involve the use of potassium permanganate ($KMnO_4$), sulfuric acid (H_2SO_4), and sodium nitrate ($NaNO_3$).

While efficient, this method produces hazardous byproducts, including toxic gases like nitrogen dioxide (NO_2). Improved synthesis methods aim to eliminate these toxic emissions by modifying the reaction parameters (Daniela C. M., et. al., 2010), such as using a mixture of sulfuric acid and phosphoric acid, which is less hazardous but still produces waste that must be carefully managed (Marcano D. C., et. al., 2010). Hofmann et al. argue that existing methods, such as chemical vapor deposition (CVD) and chemical reduction of GOs, often yield graphene with limited functionalization and structural characteristics (Hofmann M., et. al., 2015). This restricts the applicability of the synthesized graphene in diverse applications.

The inability to control the degree of reduction and the resultant properties of rGO is particularly concerning, as it can lead to inconsistencies in performance across different batches (Chua C. K., et. al., 2014). Moreover, control over the oxidation level remains a challenge, as over-oxidation can damage the graphene structure, while under-oxidation leads to poor exfoliation. Scaling up the production of GOs and rGO while maintaining consistent quality poses another limitation. Parameters such as reaction time, temperature, and chemical concentrations need to be tightly controlled to ensure that large batches of graphene exhibit uniform properties. For example, studies have shown that reaction conditions, such as a temperature of 40 °C and a reaction time of 12 hours, result in a better oxidation degree of graphite into GOs (Emiru T. F., et. al., 2016). However, these conditions must be optimized for each specific application, which adds complexity to the manufacturing process. Moreover, (Kotsyubynsky V., et. al., 2021) note that while rGO can serve as a more affordable alternative to pure graphene, the large-scale production of high-quality graphene remains complex and expensive.

The synthesis processes often require specialized equipment and conditions, which can be prohibitive for smaller companies or research institutions. Additionally, the methods employed, such as the modified Hummer's method, can be hazardous and environmentally unfriendly due to the use of strong oxidizing agents (Nandakumar P., et. al., 2022). The reduction process itself also presents challenges. Discuss the various reducing agents available for the reduction of GOs, noting that while there are over 50 types, the choice of reducing agent can significantly affect the quality of the resulting rGO (Chua C. K., et. al., 2014). Inconsistencies in reduction can lead to variations in electrical conductivity and structural integrity, which are critical for applications in electronics and energy storage.

The reduction process may not completely restore the original properties of graphene, leading to materials that do not meet the desired specifications for high-performance applications (Eigler S., et. al., 2014). Chemical reduction often leaves behind chemical residues that affect the purity of the rGO. Thermal reduction requires high temperatures, which can damage the graphene structure. A combination of methods, such as chemical and thermal reduction, has been shown to improve efficiency, but achieving full reduction while retaining the material's integrity remains a challenge (Gu C., et. al., 2013).

CHAPTER-2

Synthesis of Graphene Oxides with Higher Oxygen to Carbon Ratios using Feed Acid Liquor Recycling Technique and Its Application for the Removal of Arsenic (III) from Aqua Solution

Abstract

Graphene has recently drawn exponential attention due to its surprising physicochemical properties and diversified field of applications. Although GO itself is an exclusive material, it is also an intermediate product for the production of rGO, graphene, and their derivatives, which are more superficial materials. In this study, GOs with higher oxygen to carbon ratios were synthesized following the Tour method, where the excess feed acid liquor (FAL) of mixed concentrated sulfuric and orthophosphoric acids at a ratio of 90:10 was recovered from the reaction slurries by applying the centrifugation technique. About 80-90 % of the FAL was recycled and reused as feed for the subsequent batches. The changes in the properties of FAL

for the five consecutive recycling and reuse were studied. The properties of recycled FALs were investigated by measuring density, moisture content, pH, and ion concentration. The consecutive recycling of FALs tends to increase the moisture content by about 0.5% in each recycles. Ion chromatography (IC) was used to measure the variation in SO_4^{2-} and PO_4^{3-} ions in the FALs. The H_2SO_4 reacts with $KMnO_4$ and crystallizes out from the recovered FAL faster than the phosphoric acid. So, sulfuric acid content in the makeover FALs must be greater than primary FAL. The product GOs were characterized using FT-IR, FT-Raman, UV-Vis, STA, SEM, XPS, Zeta-potential, and particle size analyzers. The variation of the properties of GOs with the changes in the reaction parameters, such as temperature and time, was investigated and correlated with the product yield. It was observed that the effect of temperature on the reaction rate was found to be negative and positive with the reaction time. The oxygen-to-carbon atomic ratio from XPS analysis was found to be 66.7%, which supported the increase in product yields of 66.9% in the experimental results. The effect of acid concentration, reaction temperature, and time on the GOs properties was satisfactory, correlated, and easily controllable with the reaction conditions. A higher extent of oxidation and enhanced product yields of 65-70% were observed at 60-70 ℃ and 14-18 h. A mixture of nano- and macro-molecular GOs was obtained, and their compositions were easily controllable and separable by controlling the reaction conditions. A correlation was made among the properties of synthesized GOs, FAL, and recycled FAL and reaction conditions. The synthesized GOs were applied for the removal of As(III) ions from water at pH 7.0. As the GOs contain 67% oxygen, they can adsorb 343.14 mg/g of As(III) with 97.9% efficiency.

Objectives

From the literature review, it is clear that the main purpose of the chemical oxidation and reduction process is to exfoliate graphite layers into graphene sheets, and the degree of exfoliation is proportional to the degree of oxidation. The main objective of this research is to achieve higher oxygen containing GOs with lower production costs. So, the objectives are-

i) to synthesize Graphene oxide (GOs) with enhanced oxygen-to-carbon ratios following Tour's method. The effects of reaction temperature and time will also be evaluated, and

the optimum reaction conditions for the higher oxygen to carbon ratios will be established.

ii) to study the effect of recycling and reusing of feed acid liquor (FAL) in GO synthesis, and the changes in the properties of recovered FAL, and the synthesized GO will be studied.

iii) Application of GOs for the removal of Arsenic (III) from aqueous solution.

2.1. Introduction

The term “graphene” was first introduced by A. Geim and K. Novoselov, and they were awarded the Nobel Prize in 2010 for their revolutionary contribution to discovering one carbon atom-thick two-dimensional materials that exhibit high crystal quality. They first obtained single-layer and few-layer transferable graphene nanosheets by mechanical exfoliation from graphite samples (Geim, et. al., 2007), (Novoselov, et. al., 2004). Chemically, graphene was observed as a two-dimensional nanomaterial, and it contains single and multi-layers of carbon atoms arranged as a honeycomb lattice that is held together by σ bonds, where most of the

carbon atoms preserve sp^2 hybridization (Zhu Y., et. al., 2010), (Ray S., 2015). Generally, 2D graphene sheets are rolled into a 3D graphite structure. Thus, graphene sheets need to be separated from the graphite structure. Synthesizing GOs is one of the effective ways to separate graphene from graphite lattices. The typical process of graphene separation is done by oxidizing the graphene sheets to introduce oxygen into its lattice structure, followed by reduction of the GOs either thermally or chemically. Moreover, GOs are an excellent starting material for the synthesis of various derivatives of graphene, such as Fluorographene, graphol, graphene acid, etc. (Chronopoulos D. D., et. al., 2017), (Pumera M., et. al., 2017), (Jankovský O., et. al., 2016).

GOs have a wide variety of applications owing to their tunable properties and relatively easy modification techniques than other conventional materials. Generally, graphite has been used as a very efficient material for energy storage devices such as batteries, capacitors, etc. (Zhang X., et. al., 2016). Recently, reduced GOs / rGOs are extensively used as a replacement for graphite owing to their enhanced charge storage properties and large surface area compared to graphite (Mao S., et. al., 2011), (Trung T. Q., et. al., 2014). GOs are also suitable for making transparent conductive films (Liu L., et. al., 2017), strong conducting papers (Yan J. X., et. al., 2019), and ultra-light elastic aerogels (Pei S., et. al., 2018), (Peng L., et. al., 2015).

Numerous fascinating applications based on the electronic, optical, thermal, mechanical, and chemical nature of graphene and GOs have been adopted as solid electrolyte or proton conductors, electronics devices ferromagnetism, electrodes or electron mediators for enzyme biosensors, biomedical applications, surface coating technology, composites, dye-sensitized solar cells (Ghann W. E., et. al., 2019), paper-like materials, filters for water and purification (Xu P., et. al., 2023), and as an ingredient of hybrid photo-catalysts in water splitting, nano-filtration membrane (Han R., et. al., 2019) (Sali S., et. al., 2019), (Al-Gaashani R., et. al., 2019), (Poh H. L., et. al., 2012). Recently, GOs have been used to avoid friction in mechanical devices due to their self-lubricating properties (Hua Y., et. al., 2022).

To eliminate difficulties in the synthesis of graphene in bulk, various chemical methods were introduced. The procedure involves the chemical oxidation of graphite to form GOs and is followed by a reduction process (Ruoff R., et. al., 2008). The Hummer's method, which is extensively employed for the chemical conversion of graphite to GOs, entails an initial oxidation step utilizing $KMnO_4$, $NaNO_3$, and H_2SO_4 at a significantly reduced temperature to

mitigate the risk of explosion (Offeman R. E., et. al., 1958). Subsequently, over a period of several hours, the resulting mixture is subjected to high temperatures. The Hummer's method was modified further to improve the synthesis of GOs by replacing $NaNO_3$ with K_2FeO_4 (Hummers W. S., et. al., 2015).

The modified Hummer's method provides comparatively better-desired properties in GOs than the Hummer's method (Paulchamy B., et. al., 2015). The properties of the synthesized GOs were found to be the same as those of the preferred method. In addition, the evolution of toxic gases is minimized in this process; hence, it is termed as a facile synthesis approach (Hou, et. al., 2018), (Khan F. U., 2019). Notable progress has been made in enhancing Hummer's technique for synthesizing GOs, with a focus on cost-effectiveness and efficiency. The improvement of the method is to eliminate $NaNO_3$ and replace $KMnO_4$ with K_2FeO_4. The method also reduced the use of concentrated sulfuric acid without affecting the yields, properties, or applications of GOs (Yu H., et. al., 2016). Synthesizing GOs in polar solvents enhances the conductivity of the GOs sheets (Zaaba N. I., et. al., 2017).

This method was further improved by James M. Tour and is termed Tour's method. This process excludes the use of $NaNO_3$ with the increase in the amount of $KMnO_4$ in the presence of mixed acid (MA), H_2SO_4:H_3PO_4, with a ratio of 9:1. The presence of orthophosphoric acid improves the efficiency of the oxidation process. This method yields more hydrophilic GOs compared to other methods. Moreover, this method does not generate toxic gas, and the temperature is moderately higher than room temperature, making it easy to control (Marcano D. C., et al., 2018). A higher amount of oxygen-containing GOs can be obtained by this method than by other chemical methods (Al-Gaashani R., et. al., 2019). The roles of SO_4^{2-} ions in GO synthesis were investigated, and it was found that the formation of the epoxy bridge between the nearby carbon atoms increases with ion concentration (De Mendonça J. P. A., et. al., 2018). The Tour method underwent further enhancements with the incorporation of a pre-treatment procedure applied to the graphite raw materials before the oxidation stage. This modification led to notable enhancements in the properties of the synthesized GOs (Benzait Z., et. al., 2021). An effective condition for the preparation of few-layered GOs and rGO was thoroughly investigated, and the properties of the prepared products were evaluated. The degree of oxidation was controlled by varying reaction times and temperatures, and the interlayer distances of few-layer graphene were found to increase with increasing time and temperature

(Xu S., et. al., 2017). In another study, GOs were alternatively synthesized from graphite using a low concentration of ozone at high temperature, which produced GOs with enhanced properties (Webb M. J., et. al., 2011). Moreover, the material is highly stable at slightly elevated temperatures. The exposure of GO materials and composites to very high temperatures initiated a degradation process that results in a change in color shade (Zhou S, et. al., 2013), (Khanam N. P., et. al., 2016).

However, notable limitations are associated with the various chemical techniques employed in the synthesis of GOs. These include high costs, time-consuming reactions, difficulties in controlling process parameters, the risk of explosions, environmental pollution, the generation of numerous byproducts, the inclusion of contaminants requiring further purification, and imprecise control of the degree of oxidation and particle size (Capaz R. B., 2022), (Zare P., et. al., 2021). To mitigate these difficulties, an effective method for electrochemical exfoliation of graphite was established (Liu F., et. al., 2019). This method reports a scalable, safe, and environmentally friendly approach with a high yield (Liu F., et. al., 2019), (Parvez K., et. al., 2014). The reactions of graphite to GOs are based on electrolytic oxidation conditions in water. In the electrochemical oxidation method, the graphite lattice is fully oxidized within a few seconds, making it a speedy process (Parvez K., et. al., 2014). The GOs obtained by this method have similar properties to those of the other methods. The synthesis method is continuous and easily controllable. Another approach to reduce the difficulties of the production of GOs from graphite was to use $KFeO_4$ instead of $KMnO_4$ with concentrated H_2SO_4. This method not only minimizes environmental pollution but also reduces reaction times from several days/hours to only 1 hour. The products GOs powders are highly water-soluble, from which GOs liquid crystals can be formed, and thus macroscopic graphene fibers, films, and aerogels can be produced. This method produces 100% of single-layered GOs and their macroscopic materials without applying any ultrasonic treatment. Thus, the large-scale commercial production of graphene becomes ultra-low-cost (Sofer Z., et al., 2016), (Sabbaghan M., 2018). GOs are also synthesized by applying ultrasonication to reduce cost and impurities (Soltani T., et. al., 2017), (Ickecan D., et. al., 2017). GOs can be reduced using several reducing chemicals, such as ascorbic acid and hydrazine (Karim M. R., et. al., 2014).

Economical and environmentally friendly synthesis methods of GOs are essential for industrial applications. Several studies have focused on developing economical and green synthesis

techniques for GOs and rGO. Green synthesis involves the use of natural and biochemicals such as plant extracts and biomass for the reduction and stabilization of rGO (Parthipan P., et. al., 2021), (Chandu B., et. al., 2020). Although these methods are environmentally friendly, they are impractical in an industrial setting. Synthesis of GOs in the Hummer's method, modified by the Tour method, is highly effective and applicable in an industrial environment. Among these methods, the Tour method of synthesizing GOs is industrially favorable, energy efficient, and eco-friendly (Ikram R., et. al., 2020), (Habte A. T., et. al., 2019). Moreover, oxygen the oxygen-to-carbon ratio of GOs are much higher in Tour's method than in any other synthesis techniques. However, recycling and reusing the reagents for successive synthesis of GOs can increase their sustainability and add more value as an eco-friendly technique. To this date, very few studies have been reported on the successive use of chemical reagents for producing GOs with a high oxygen to carbon ratio.

In this research, GOs have been synthesized by the oxidation of graphite using Tour's method. The unreacted feed acid liquors (FAL) have been recycled and reused for five consecutive cycles. The recycled FAL and synthesized GOs have been characterized using state-of-the-art instruments. A correlation has been established between the properties of recycled FAL and synthesized GOs.

2.2. Materials and methods

2.2.1. Materials

2.2.1.1. Materials used for the synthesis experiment of GOs

The chemicals used for the experiment were collected from the following sources: Extra pure graphite fine powder of purity 98% with particle size 60 mesh was collected from Loba Chemie Pvt. Ltd., Mumbai, India; reagent grade potassium permanganate with purity 99.8%; AR grade sulfuric acid with purity 97%; reagent grade hydrochloric acid with purity 37%; and AR grade hydrogen peroxide with purity 35% were from Merck KGaA, Darmstadt, Germany; and AR

grade orthophosphoric acid with purity 85% from Active Fine Chemicals Ltd., Dhaka, Bangladesh.

2.2.1.2. Materials used for the application of synthesized GOs

All reagents used in this study were of analytical grade to ensure precision and reliability. Sodium metaarsenite ($AsNaO_2$, ≥99% purity, Sigma-Aldrich, USA) was employed for preparing simulated arsenic-contaminated water. A stock solution of 2000 mL at a concentration of 100 ppm As(III) was prepared by diluting 200 mL of 1000 ppm of $AsNaO_2$ standard solutions to 2000 mL of deionized water, and the solution was stabilized using Nitric acid (HNO_3, analytical grade), 10.0mL 0.5 (M) solution before storing at 4 °C for subsequent experiments. The adsorption experiments were conducted using GOs, which were synthesized previously in the laboratory according to the published article (Hoque M. A., et. al., 2024) following a modified Hummer's method. The material had a particle size range of 100 - 500 nm. The pH of the solutions was carefully adjusted using Hydrochloric acid (HCl with purity 37%), NaOH (≥97.0% ACS-grade pellets), reagent grade and AR grade hydrogen peroxide with purity 35% including Nitric acid, which were collected from Merck, Germany. These reagents ensured accurate control of the pH conditions necessary for the experiments. All experimental conditions and material specifications were selected to optimize the reliability and reproducibility of the results, thereby facilitating the evaluation of arsenic removal under controlled laboratory conditions.

2.2.2. Instrumental methods

The following instruments were used for the quantification and characterization of the samples.

2.2.2.1. Karl-Fischer moisture analyzer

Water content in raw concentrated sulfuric acid, phosphoric acid, fresh MA, and recovered acid liquors after every reaction was measured by using a Karl-Fischer moisture analyzer (Metrohm, USA). For each measurement, 0.20 mL of sample was added to a moisture-free Karl-Fischer reagent. The acquired data were expressed as percentages (Scholz E., 1984).

2.2.2.2. Measurement of anion content using ion chromatography

Ion chromatography (Thermo Scientific, Germany) was utilized for the measurement of SO_4^{2-} and PO_4^{3-} ion concentrations in concentrated sulfuric acid, phosphoric acid, fresh MA, and recovered FAL after each reaction. After adjusting the concentration to the calibration range, 0.10 mL of the acids was diluted to 100 mL with distilled DI water and investigated for SO_4^{2-} and PO_4^{3-} ion concentrations. The results obtained are based on ppm units (Smith R. E., et. al., 1987).

2.2.2.3. Atomic absorption spectroscopy

In the synthesis experiment, an atomic absorption spectroscopy (AAS) instrument was used for the determination of K^+ and Mn^{2+} ion concentrations in H_2SO_4, H_3PO_4, fresh FAL, and recovered acid liquors, directly inserting the samples into the atomic absorption spectroscopy (Shimadzu, modes-7000, Japan). After adjusting the concentration to the calibration range, 0.10 mL of the acids was diluted to 100 mL with distilled DI water and tested for K^+ and Mn^{2+} ion concentrations. This instrument was also used for the quantification of Arsenic ions in water before and after adsorption by the GOs samples. It is a highly precise and accurate method for the quantification of metal ions in solutions. The solutions were made slightly acidic using a few drops of Nitric acid to prevent precipitation in the solutions. At first, a calibration curve is essentially made using the standard reference material, and the solution concentration is measured on the basis of the calibration curve. Install an arsenic-specific hollow cathode lamp and set the wavelength to 193.7 nm. Optimize lamp current, burner height, and slit width according to the manufacturer's guidelines. Configure the hydride generation system with sodium borohydride ($NaBH_4$) as the reducing agent for producing arsine gas (AsH_3).

2.2.2.4. FT-IR spectroscopic analysis

The structural characterization of the G and synthesized GOs was carried out by attenuated total reflectance-fourier transform-infrared spectroscopy FTIR-ATR (Frontier, PerkinElmer, USA). The FT-IR spectra were captured using an ATR module with a diamond crystal. Acetone was used to polish the diamond crystal, and a background scan was taken before every measurement. The spectra were recorded in the 650–4000 cm^{-1} range at 4 cm^{-1} spectral resolution with 12 scans per spectrum.

2.2.2.5. FT-Raman spectroscopic analysis

The structural characterization of the G and synthesized GOs was carried out by attenuated total reflectance-fourier transform-Raman (FT-Raman) spectroscopy (MacroRAM, Horiba, France). The FT-Raman spectra were captured using a solid sampling prob module with a diamond crystal. Acetone was used to polish the diamond crystal, and a background scan was taken before every measurement. The spectra were recorded in the 0-3500 cm^{-1} range at 4 cm^{-1} spectral resolution with 6 scans per spectrum.

2.2.2.6. UV-Visible spectroscopic analysis

The absorbance of UV-visible light and the determination of the maximum absorbance (λ max) were carried out through the utilization of a PerkinElmer Lambda 35 instrument (USA) in the process of ultraviolet-visible spectroscopy (UV-Vis). The powder samples were dissolved in distilled and deionized (DI) water at a concentration of approximately 1.5 mg/mL. Subsequently, the aforementioned solutions were transferred into sample cuvettes in order to conduct absorbance measurements.

2.2.2.7. Particle size analysis using DLS measurement

Particle size and zeta-potential value of the samples were measured in a particle size analyzer (Malvern, UK). Powder samples were scattered in distilled and DI water in a 0.5% ratio and placed in sample cells to measure their particle size and zeta potential.

2.2.2.8. Image analysis using SEM-EDX

A Scanning Electron Microscopy-Energy Dispersive X-Ray (SEM-EDX) analyzer was used for imaging purposes (JEOL, Japan). A very small sample, about 1 mg, was placed in the sample holder and placed in the vacuum dryer at 55 ºC for 12 hours, and then it was placed inside the instrument for capturing the images using Scanning Electron Microscopy. The localized composition of the analyzed samples was found in Energy Dispersive X-Ray analysis. The images were analyzed using the ImageJ software.

2.2.2.9. Composition analysis using XPS measurement

The X-ray photoelectron spectroscopic analysis of the samples were measured using XPS spectroscopy (K-Alpha, Bruker, USA). Properly dried powder samples were dispersed in isopropyl alcohol and dried on the copper plate to form a film. Then the sample was placed under ultrahigh vacuum in a nitrogen environment to remove atmospheric oxygen and volatile components. Then the sample was analyzed to measure the binding energy of the elements.

2.2.2.10. Thermal properties analysis using STA measurements

The thermal properties of graphene and GOs were determined using a simultaneous thermal analyzer (Brand: Netzsch GmbH, Model: Jupiter 449 F3, USA). The perfectly vacuum dried samples were undergone the thermal treatment experiment. Approximately 3.0 mg of the samples was loaded into an alumina crucible and then positioned in the furnace. The samples were subjected to heating from RT (25^{o}C) to 950^{o}C at a heating rate of 10 ℃ per minute, and the resulting thermogram were recorded along with TG simultaneously.

2.2.3. GOs synthesis method

There are several methods to synthesize GOs from graphite, among them Hummer's method is very popular. Because this method provides GOs with a higher degree of oxygen. Modified Hummer's method is becoming more popular by improving the properties and reducing the disadvantages. Here, the modified Hummer's method, especially modified by Tour's method, was carried out. The process is hassle-free, very safe, less toxic, and provides GOs with very high oxygen-to-carbon ratios.

2.2.3.1. Synthesis of GOs using FAL recycling technique

GOs were synthesized using a sequential methodology. A flat-bottom flask with a capacity of 1000 mL was initially filled with a concentrated MA solution, which was termed feed acid liquor (FAL), approximately 1000 mL in volume. The FAL was prepared by combining concentrated H_2SO_4 and ortho H_3PO_4 in a ratio of 90:10. In order to establish a regulated environment, the flask was subjected to a cooling process, resulting in a temperature lower than 50 ℃. Following that, a quantity of 10.0 g of G powder was added to the flask under constant stirring at a rate of 500 rpm. This stirring was done to prevent the formation of lumps and to ensure thorough and uniform mixing. The flask was immersed in a water bath to facilitate heat dissipation and control the temperature of the reaction vessel at the desired level. Following that, a total of 60.0 g of $KMnO_4$ was slowly added to the mixture with constant stirring. Subsequent to obtaining the condition, the temperature of the reaction media was gradually raised by 10 ℃/h until 95 ℃. The processes of heating and stirring were then stopped. After being cooled to room temperature, the unreacted acid solution was separated from the solid reaction mass by a centrifugation process at a speed of 6000 rpm for 20 min. The reaction mass was allowed to oxidize in air overnight. To obtain the diluted mass, 400 g of distilled deionized water ice was added to the cake. Then, a solution containing 15-30 mL of H_2O_2 with a concentration of 36% was gradually added to the mixture while maintaining a constant stirring. Upon completion of the oxidation process, the GOs underwent a purifying step. The procedure entailed filtration utilizing Whatman filter paper number 1, followed by multiple rinses with distilled deionized water and further filtration. The filter cake thus obtained is a crude GOs product.

2.2.3.2. Purification of crude GOs using acid wash

The crude GOs product, containing a substantial quantity of salts generated during the reaction between $KMnO_4$ and FAL, underwent a purification process to recover potassium and manganese salts as potential by-products. The GOs filter cakes, primarily composed of these salts, were also subjected to purification. Initially, the crude GO was washed with a 10% HCl solution while being stirred and heated to a temperature below 50 °C for 2 hours. Following this, the filter cakes were extensively rinsed with distilled, deionized water and centrifuged 8–10 times to achieve a final solution with a neutral pH of approximately 7.0. This process effectively removed residual impurities, enhancing the quality and purity of the GOs product.

2.2.4. Application of synthesized GOs for the Adsorption of Arsenic (III) from aqua solution

The synthesized GOs demonstrated effective adsorption of As(III) from water, owing to their high surface area and abundant oxygen-containing functional groups. Batch experiments revealed significant removal efficiency under optimized conditions, highlighting its potential as an eco-friendly and efficient adsorbent for arsenic remediation in water treatment applications.

2.2.4.1. The adsorption principle

The concentrations of As^{3+} ions in water were quantified using an AAS instrument, ensuring precise and reliable analysis. The Arsenic acceptable limit according to the WHO (the World Health Organization) guideline in drinking water is 5 µg/L. So, the calibration curve of standards was prepared with concentrations ranging from 0.05 to 5.0 mg/L by serial dilution of the As(III) stock solution using deionized water. The deionized water was prepared in the laboratory immediately before the experiment using a membrane technology-based instrument. To ensure all measurements fell within the calibration range, samples were appropriately diluted before analysis, and an internal standard with a concentration of 5 µg/L was incorporated to enhance analytical accuracy and reproducibility.

The calibration curve and its linearity had to be obtained. This internal standard facilitated the monitoring and correction of potential variations during measurement. The optimized AAS method provided consistent and reproducible data, crucial for assessing arsenic removal efficiency in adsorption experiments under varying experimental conditions. By ensuring strict control of preparation and analysis procedures, this approach enabled the generation of reliable data to evaluate the performance of adsorbents and to understand the dynamics of arsenic adsorption in aqueous solutions.

At a constant pH and constant temperature of the solution, for a certain amount of adsorbent, the rate of adsorption is directly proportional to the initial concentration and the contact time of the adsorption. To determine the adsorption rate of As(III) ions by the synthesized GOs adsorbent at different initial concentrations of As ions in water, the contact time was varied.
The percentage removal of As(III) (%R) was calculated using Equation (8):

$$R(\%) = \frac{Co - Cf}{Co} \times 100 \quad \text{----------(8)}$$

Where C_o is the initial As(III) concentration (µg/L), and C_f is the final concentration (µg/L) after treatment.

This equation provided a direct measure of the adsorbent's performance in removing arsenic. The adsorption capacity of the adsorbent (Q_e) at equilibrium, expressed in µg/g, was determined using Equation (9):

$$Q_e = \frac{(Co - Ce) \times V}{m} \text{----------(9)}$$

Where, C_e is the equilibrium concentration of As(III) (µg/L), V is the volume of the solution (L), and m is the mass of the adsorbent used (g). These calculations enabled the evaluation of the adsorbent's effectiveness under varying experimental conditions.

The experimental setup and methodology were designed to provide detailed insights into the adsorption dynamics and equilibrium behavior of GOs. The study evaluated the impact of critical variables, including pH, initial As(III) concentration, contact time, and adsorbent dosage, on arsenic removal efficiency. By employing rigorous analytical techniques and ensuring replicability, the results offer a comprehensive understanding of the adsorption process, which can inform the optimization of conditions for effective arsenic remediation.

2.2.4.2. Determination of calibration curve

The data from Table 2.3 form the basis for the calibration curve, which plots the measured concentrations against the known concentrations of arsenic in the standard solutions. This calibration curve serves as a reference to quantify unknown arsenic concentrations in test samples. A linear relationship is observed in the data, as evidenced by the proportional increase in measured concentration with increasing standard concentration. The calibration curve for As(III) adsorption by GOs from water was determined using an atomic absorption spectrophotometer (AAS). The calibration data provide the relationship between known arsenic

concentrations in standard solutions and the measured concentrations obtained through the AAS instrument.

The calibration curve of standards was prepared with concentrations ranging from 0.05 to 5.0 mg/L by serial dilution of the As(III) stock solution using deionized water. The curve demonstrates a linear relationship between the known and measured concentrations, expressed by the equation:

$$Y = mX + C \text{ ----------(10)}$$

Here, Y represents the measured concentration of As(III), X is the known concentration from the standard solution, and m is the slope of the calibration line.

The regression analysis yielded an excellent linear fit, with R^2 =0.9999

For As(III) adsorption in water, the slope (m) is 0.9999, and since the line passes through the origin, the C is the y-axis intercept (C) is zero. Thus, the calibration equation simplifies to:

$$Y = 0.9999X \text{ ----------(11)}$$

This equation allows the determination of unknown As(III) concentrations in solution based on absorbance measurements obtained through AAS.

2.2.4.3. Adsorption experimental procedure

The adsorption rate of arsenic using GOs is evaluated by measuring the contact time between the absorbent and absorbate. A certain amount of absorbate in a liquid medium with the non-concentration was absorbed on the adsorbent surface in a certain time, and the rate of adsorption was calculated. Here, an Arsenic solution of 350 mL at a concentration of 100 ppm was adsorbed on the surface of the synthesized GO samples, and 10 mL of the solution was collected every 30 minutes. The solutions were collected for 12 hours, and the equilibrium concentrations were measured for 24 hours. The concentrations of As^{3+} ions in collected samples were

determined using AAS, a highly sensitive technique for quantifying metal ions. Initially, a calibration curve was established using standard solutions to ensure accurate quantification. The instrument automatically measured the concentrations of As^{3+} ions in water samples before and after adsorption onto the adsorbent, with the results interpreted based on the calibration curve. This approach facilitated precise monitoring of adsorption efficiency in artificially contaminated water and appropriate agitation in a vortex rotator before measurement.

Research indicates that the optimal pH for arsenic adsorption by GOs is approximately 7, as this pH provides a favorable surface charge for electrostatic interactions with arsenic species, thereby maximizing adsorption capacity (Shanmugaraj K., 2023). Based on this, the experiments were designed to investigate the effects of initial arsenic concentrations and GOs dosages on adsorption performance. These parameters were systematically varied to evaluate their influence on arsenic removal efficiency under controlled conditions, providing insights into the adsorption dynamics of GOs.

Adsorption experiments were conducted to evaluate the efficiency of GOs in removing As(III) from aqueous solutions. A predetermined quantity of the adsorbent was introduced into a 500 mL beaker containing 350 mL of arsenic solution with specified initial concentrations of 100 ppm. The amount of GO dosages for the adsorption experiment was calculated based on 3.0 g GOs/1000 mL of 1050 ppm As(III) solution, so that 1.0 g of the GOs sample can adsorb a maximum of 350 mg of As(III). All experiments were carried out under controlled temperature conditions to maintain consistency.

The suspensions were agitated using a magnetic stirrer at a constant stirring speed of 80 rpm. At the beginning of the experiment, the concentration of the As(III) in the solution was 100 ppm, and the adsorbent dosages were 0.1 g GOs for 350 mL of 100 ppm solution, which were charged and contact time ranged from 30 to 720 minutes for kinetics studies, and for the equilibrium studies, it was 1440 minutes. After every 30 minutes, a portion of the solution (20 mL) was sampled in a Falcon tube and filtered using a 0.45 μm nylon syringe filter. The adsorption experiments were continued for 12 hours, and equilibrium was reached at 24 hours as measured by the concentration in the AAS instrument.

2.2.4.4. Adsorption experiment at variation of contact times

To observe the effect of variation in contact time on adsorption, following the above-mentioned procedure (Please see- 2.2.4.2). The samples were collected at 30-minute intervals, and the corresponding concentration reflects the variation of contact times. All experiments were performed in duplicate to ensure reproducibility, and the results were presented.

2.2.4.5. Equilibrium adsorption experiments at different initial concentrations of solution

The adsorption of As on G.2Os surface not only depends on GOs properties but is also influenced by several variable parameters, such as temperature, agitation, initial concentration, pH, etc.

2.3. Results and discussion

2.3.1. Synthesis of GOs

The flow diagram for the synthesis of GOs has been presented in Figure 2.1. The synthesis method of GOs was followed by modified Hummer's method, which reused the feed acid liquor recycling technique. The method was especially modified by Tour, called Tour's method, which was followed with some modification (Sohail, et. al., 2017). The purpose of this modification was to mitigate the creation of lumps, prevent abrupt temperature rise, which can lead to an explosion, maximize utilization of the oxidizing agents, and employ the FAL recycling

techniques. Tour's modification technique was applied to produce GOs with higher oxygen to carbon ratios with minimal drawbacks.

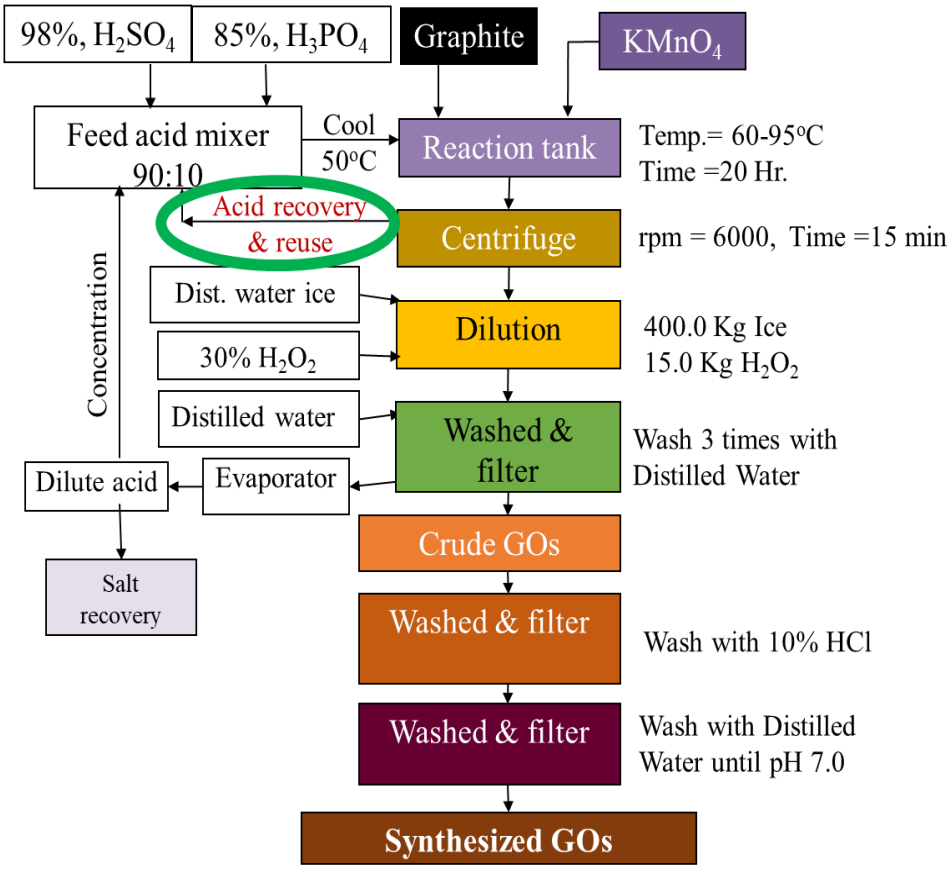

Figure-2.1: Synthesis of GOs and reuse of feed acid liquor recycling technique following Tour's method.

The reaction continued until the color of the mixture changed from a dark violet in Figure 2.2 (a) to a chocolate brown color in Figure 2.2 (b). This change of the mixture color indicates the complete consumption of $KMnO_4$. The reaction temperature was gradually raised to facilitate the maximum use of the oxidizing agents. Solids and FALs were separated from the slurry using a filter press and centrifugation for further synthesis cycles. Solid reaction mass oxidized under air and moisture, forming a pinkish-violet color as depicted in Figure 2.2 (c). To minimize the heat generated during the dilution process, ice can be used to minimize the heat of dilution. The careful incorporation of H_2O_2 was conducted to mitigate the occurrence of excessive foam generation resulting from the release of gases. H_2O_2 was stopped adding upon the attainment of a persistent, brilliant orange-yellow color in Figure 2.2 (d). From Figure 2.2, the GOs were

successfully oxidized, and the extent of the oxidation was indicated by the change in color intensity of the mixture.

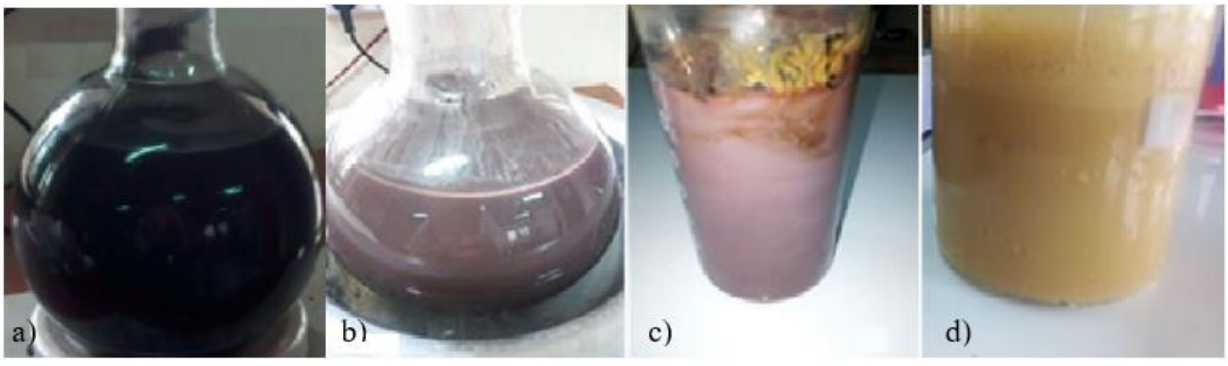

Figure-2.2. Images of color changes at different stages of graphite to GOs conversion. a) starting of the reaction (dark violet), b) end of the reaction (chocolate brown), c) centrifuged cake (pinkish brown), d) addition of hydrogen peroxide (golden orange).

The slurry derived from the manufacturing process of GOs contains different metal salt impurities, which underwent a purifying step. The purpose of the purification is to convert the metal salts into soluble chloride salts. These salts were easily removed by filtration. The produced GOs were freeze-dried to obtain fine pure GO powder.

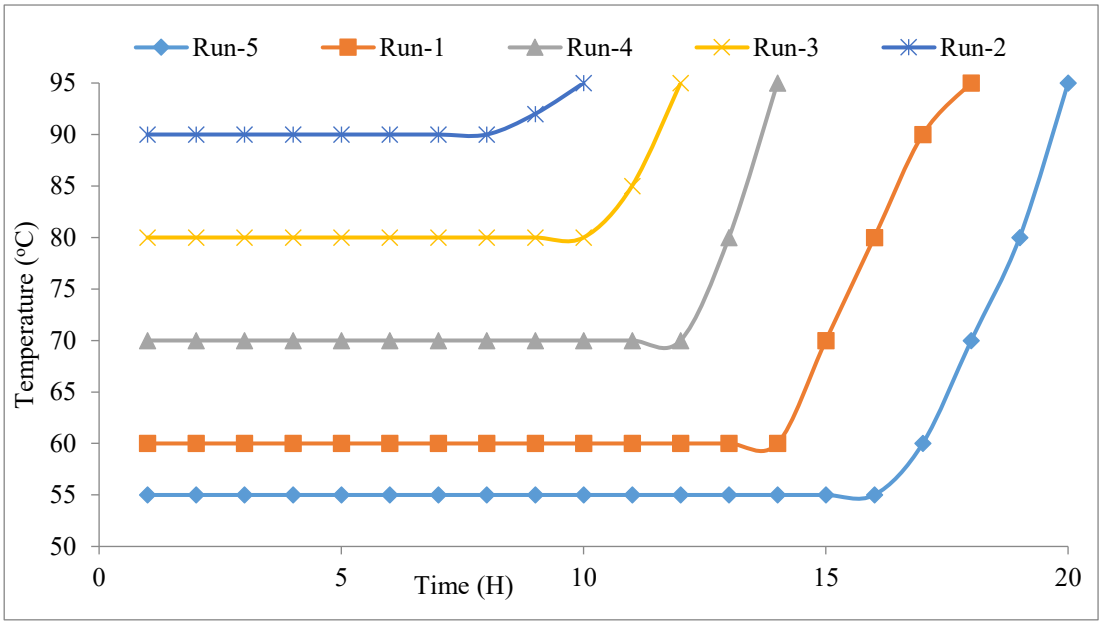

Figure-2.3: Temperature profile of the experiments of Run-1, Run-2, Run-3, Run-4, and Run-5 for the synthesis of GOs with respect to time.

During the synthesis process, particularly for Run-1, the initial temperature and the temperature primarily maintained ranged between 55 and 60 ℃. Over the course of 16 h, the temperature gradually increased, reaching 95 ℃ within 4 h, as shown in Figure 2.3. The reaction was terminated after a total of 20 h. Similarly, for subsequent reactions, denoted as Run-2, Run-3, Run-4, and Run-5, the initial temperature and main temperature conditions were set at 60–65, 70–75, 80–85, and 90–95 ℃, respectively. The reaction durations were reduced progressively to 14, 12, 10, and 8 h for these runs, respectively.

The synthesis was carried out until the oxidizing agent was fully consumed. At 55 ℃, the oxidizing agent underwent a reaction for a period of 20 h, resulting in the production of 17.05 g of GOs from an initial quantity of 10.0 g of graphite, as shown in Table 2.1 and Figure 2.3. Comparably, when subjected to 60, 70, 80, and 90 ℃, the reactions exhibited reaction times of 18, 14, 12, and 10 h, respectively. Consequently, these reactions resulted in the production of 16.91 g, 16.69 g, 15.54 g, and 14.39 g of GOs, respectively.

Table-2.1: Properties of synthesized GOs (GOs), reaction temperature, reaction time, moisture content, particle size, and zeta potential value

Experiments	Reaction temperature (ºC)	Reaction time (h)	Prepared GOs (g)	Moisture content (%)	Particle Size (nm)	Zeta potential (mV)
Run-1	55	20	17.05	6.07	851	-19.7
Run-2	60	18	16.91	7.39	892	-24.1
Run-3	70	14	16.69	7.9	1013	-26.2
Run-4	80	12	15.54	8.48	1063	-29.5
Run-5	90	10	14.39	9.95	1661	-19

The yield of GOs production is substantially influenced by the reaction temperature and time. The oxygen content in GOs is shown to be higher when longer processes are conducted at lower temperatures, as opposed to shorter processes at higher temperatures, while maintaining the same quantity of reactants. As a consequence, there is a notable enhancement in the yields of the product inside the sediment volume, as seen from Figure 2.4. As a result, decreased temperature and increased reaction time have been observed to increase the overall production

yields. The most favorable reaction conditions were determined to occur within a temperature range of 65–70 ℃ with a reaction duration of 14–15 h.

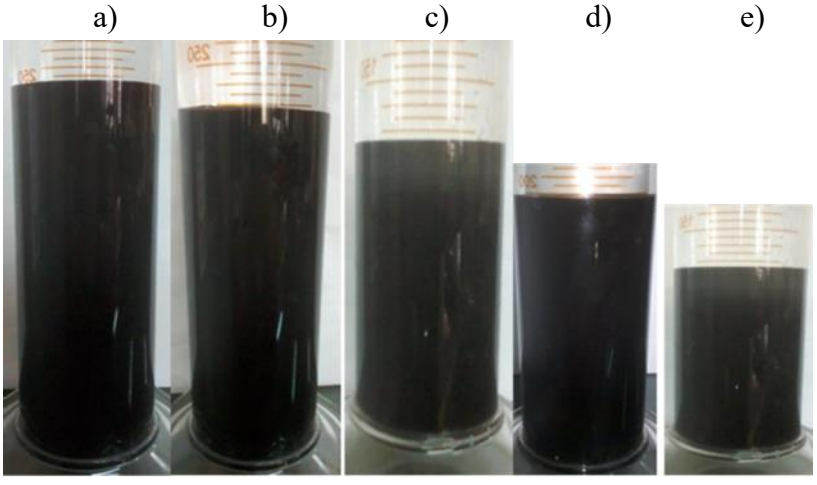

Figure-2.4. Images of the sediment volume of GOs products from different reaction runs a) Run-1, volume-242 mL, b) Run-2, volume-228 mL, c) Run-3, volume-202 mL, d) Run-4, volume-187 mL, and e) Run-5, volume-126 mL.

2.3.2. Regression analysis for GO synthesis process

A regression study was undertaken to establish the correlation among reaction time, temperature, and the product yield of GOs in g. The analysis yielded a regression model that exhibited a high level of fit, as shown by an adjusted R^2 value of 1.00. The regression model exhibits a high level of significance ($p = 0.00$) at a significance level of 0 percent.

2.3.3. Regression model

The regression model obtained from the analysis is shown in equation (12)

$$\text{Product (in g)} = 37.281 - 0.204 \times \text{Temperature} + 0.450 \times \text{Time} \text{----------(12)}$$

The regression model follows the linear straight-line equation, $Y = mX + C$. According to the model, temperature harms product yield. With every 1 ℃ increase in temperature, the product yield decreases by 0.204 g. In contrast, reaction time has a positive effect on the production of GOs, contributing to a 0.45-g increase for each additional hour of reaction time, as shown in Equation 12.

The reactions involved in the oxidation process are-

$$2KMnO_4 + H_2SO_4 \longrightarrow K_2SO_4 + 2HMnO_4$$

$$2HMnO_4 \longrightarrow Mn_2O_7 + H_2O$$

$$Mn_2O_7 \longrightarrow 2MnO_2 + 3\,[O] \quad \text{(Explosive step)}$$

$$MnO_2 + H_2SO_4 \longrightarrow MnSO_4 + H_2O + [O]$$

$$[\text{Graphite}]\ C + [O] + H_2O \longrightarrow -\overset{|}{\underset{|}{C}}-OH\ /\ >C=O\ /\ -\overset{O}{\overset{\|}{C}}-OH\ /$$

Figure-2.5: Reaction mechanism for the oxidation of graphite to GOs using potassium permanganate in a strong acid mixture.

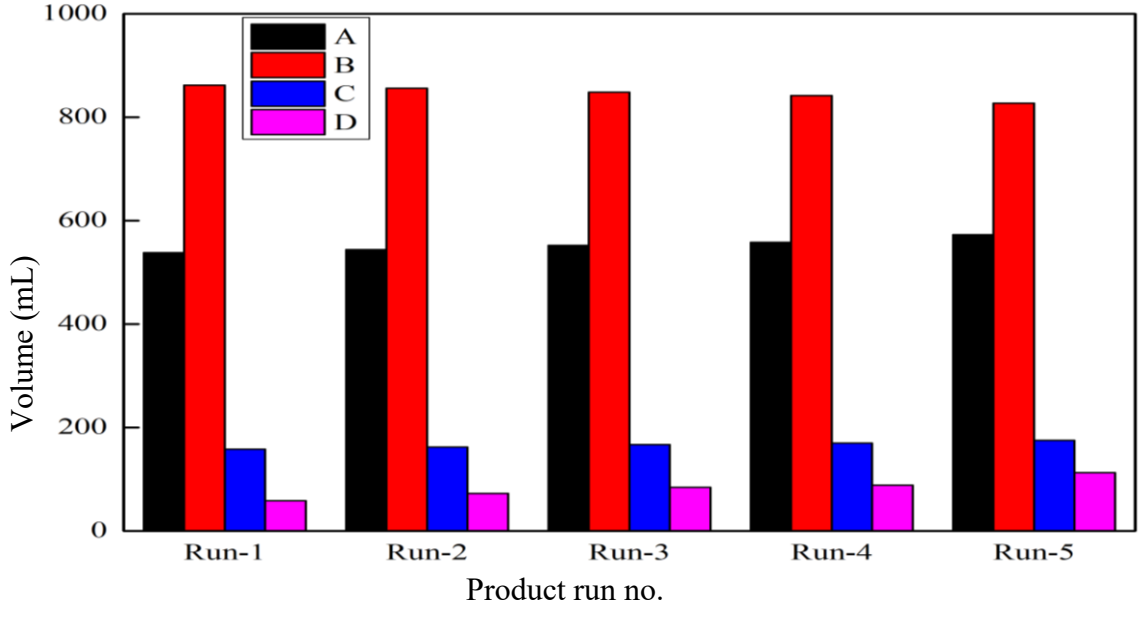

Figure-2.6. Amount of consumed and recovered acid at different reaction runs (A) MA consumed (mL), (B) recovered MA (mL), (C) recovered dilute acid (mL) and (D) recovered salt (g)

2.3.4. Recycling of feed acid liquor

The chemical pathway involved in the synthesis of GOs increased the ratio of oxygen to carbon (Figure 2.5). The roles of SO_4^{2-} were explained by De-Mendonça J. P. (De-Mendonça J. P., et. al., 2018). In the context of the oxidation reaction as a whole, it is evident that the stoichiometry indicates a 1:1 molar ratio between $KMnO_4$ and H_2SO_4. Hence, a total of 60.0 g of potassium permanganate ($KMnO_4$) with a purity level of 99.8% is required to react with 39.09 g of H_2SO_4, which has a concentration of 95%. Alternatively, this can be expressed as 21.11 mL of the H_2SO_4. Nevertheless, the initial acid recovery rate remained at 86.2% during the initial run, but

a progressive decline in subsequent reaction cycles was observed. The observed acid consumption exceeded the anticipated theoretical value, and the quantity of concentrated acids recovered exhibited a decline in successive recovery and reuse cycles. The observed phenomenon can be attributed to the absorption of acids by the solid cakes obtained by centrifugation of the reaction slurry. The quantity of solid cakes exhibited a gradual increase in conjunction with subsequent reactions. The cakes contained GOs as well as K, Mn, and SO_4^{2-} or PO_4^{3-} salts that precipitated from the reaction slurry as a result of saturation. As a result, there was a progressive increase in both the quantity of acid consumed and the volume of dilute acid obtained from the washing process as the number of recovery and reuse cycles increased (Figure 2.6).

2.3.5. Moisture analysis of recycled FAL

The moisture content of the recovered MA was determined using the initial moisture content of the fresh MAs using a Karl Fischer moisture analyzer. The moisture content initially was found to be 3.77% in fresh feed acid liquor, and in recovered feed acid liquor, it gradually increased with the increasing number of recoveries and reuses. After the first recovery, it increased to 6.07% and gradually increased with the increasing number of successive recoveries and reuses, reaching 9.95% at the fifth recovery (Figure 2.6). The concentration of salts in recovered FALs is also influenced by the level of moisture present in the recovered acids. The salt recovery was 58.44 g in the first recovery and gradually increased to 112.57 g in the fifth recovery. As a result, the reaction medium becomes slightly diluted but increases in density with each successive recovery and reuse (Figure 2.6).

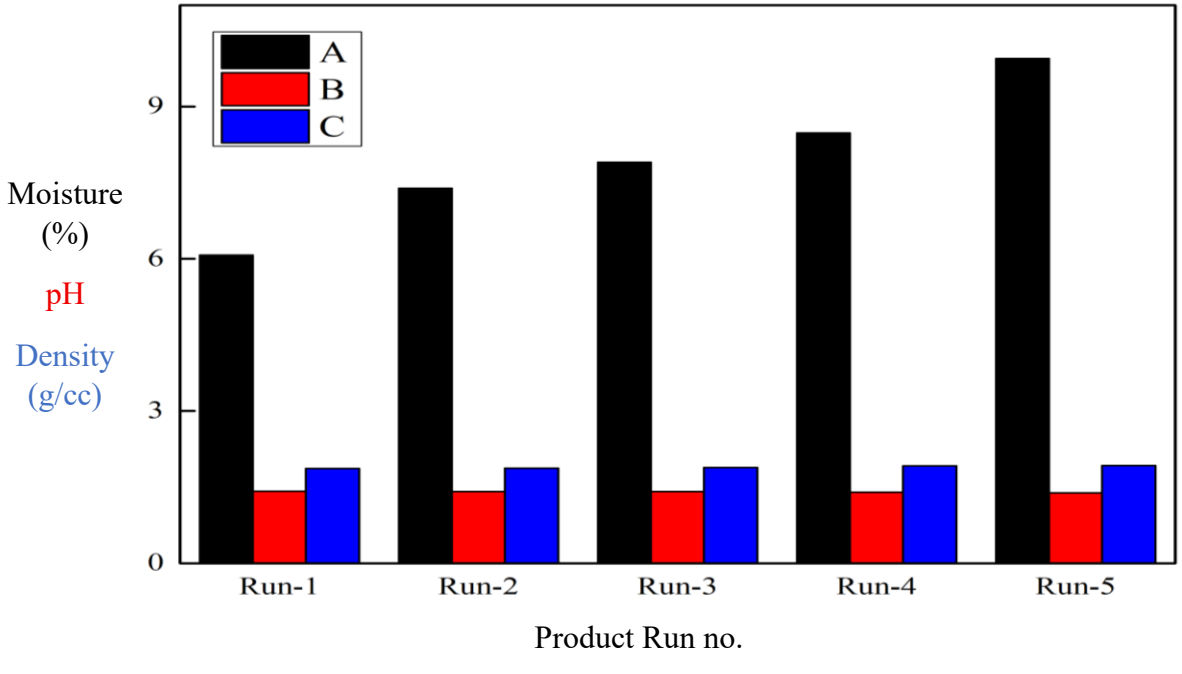

Figure-2.7: Recovered acid properties (A) moisture (%), (B) pH of 0.1% water solutions, and (C) density (g/cc).

2.3.6. pH and density of recycled FAL

The pH of the recovered MA after dilution with water to 1:1000 also decreases, which supports the dilution of the acid. However, the density of the recovered acid increases with the number of recovery cycles, as shown in Figure 2.7. This is due to the increase in water content in recovered acids, which significantly affects the solubility of salts produced in the reaction medium. Overall, the amount of recovered concentrated MA decreases with the number of runs, and the number of recovered salts gradually increases. The absorbed acids were also collected by washing the solid cakes with a small amount of distilled water. Thus, the amount of dilute acid solutions also increased with the increasing number of solid cakes and salts in different reaction runs (Figure 2 .6).

2.3.7. Atomic absorption spectroscopic analysis of FAL

The atomic absorption spectroscopic analysis of fresh and recycled FAL was conducted for the measurement of K^+ and Mn^{2+} concentration in them according to the method described by Ieggli C. V. S., et. al., 2010, and the results obtained from the experiment were presented in Figure 2.8. The amounts of K^+ and Mn^{2+} concentrations were measured from the samples after their dilution to a 1:1000 ratio. Initially, the K^+ ion was about 1 ppm for FAL, which increased to 11.67 ppm after the first recovery, and slowly increased for successive recovery and reuse. In the case of the Mn^{2+} ion, it was 0.1 ppm for FAL and 0.53 ppm after the first recovery and increased with successive recovery and reuses (López-García I., et. al., 1999). After reaching around 2 ppm, it becomes saturated and does not further increase substantially.

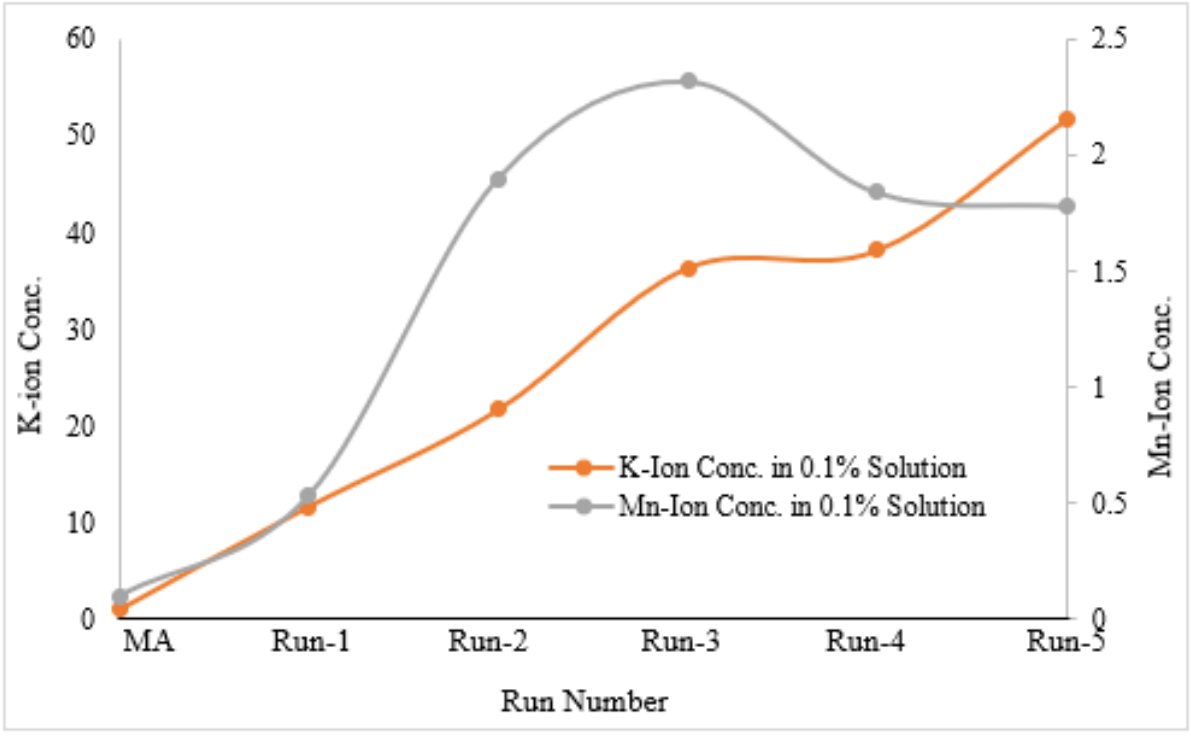

Figure-2.8: K^+ and Mn^{2+} ion concentration in recovered acids after dilution to 0.1% in water.

2.3.8. Ion chromatographic analysis of fresh and recycled FAL

The SO_4^{2-} and PO_4^{3-} ion concentrations of the fresh and recycled FAL were measured using ion chromatography after dilution it to 1:1000 ratio, and the result obtained were graphically presented in Figure 2.9. FAL contains 834 ppm SO_4^{2-} and is diluted after successive recovery and reuse. But in the case of phosphoric acid, it contains 110 ppm, and after the first recovery, it was increased to 144 ppm, and the values were increased with the number of recovery and reuse cycles, because most of the $KMnO_4$ reacts with sulfuric acid to produce atomic oxygen, K_2SO_4, $MnSO_4$ salts, and water. Formation of PO_4^{3-} salts is prevented because of the lower affinity of K and Mn for PO_4^{3-} ions than SO_4^{2-} ions (Paull B., 2005).

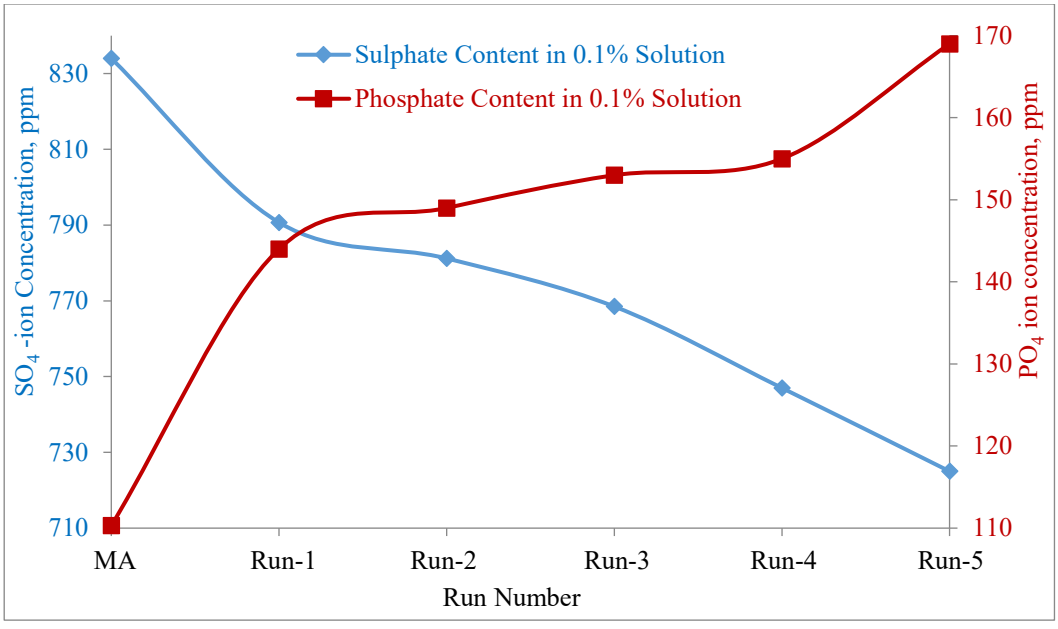

Figure-2.9: Amount of recovered salt and product of GOs in the synthesis process.

2.3.9. Synthesis of GOs with a higher oxygen to carbon ratio

The synthesis of GOs from G was carried out at varying temperatures and times. At higher reaction temperatures, the reactions were completed in a shorter period of time. This was because the reactant $KMnO_4$ dissociates very fast at higher temperatures to generate atomic oxygen. So, $KMnO_4$ was consumed rapidly, leading to faster oxidation of the G material. On the other hand, at lower reaction temperatures, reactions take more time to complete using the same amount of feed materials, as shown in Figure 2.3. On the contrary, the lower temperatures show a higher degree of oxidation of G to GOs. This process splits the G layers, which results in a reduction in particle size. The product yield is highly dependent on the reaction temperature and time, as observed from the sediment volume of the product under water, presented in Figure 2.4. The optimum reaction condition should be between 60 and 70 °C, as seen from Figure 2.10. depicting the relationship between product yield, reaction time, and temperature. The amount of GOs has been directly related to reaction temperature and time. It could be observed that the amount of synthesized GOs

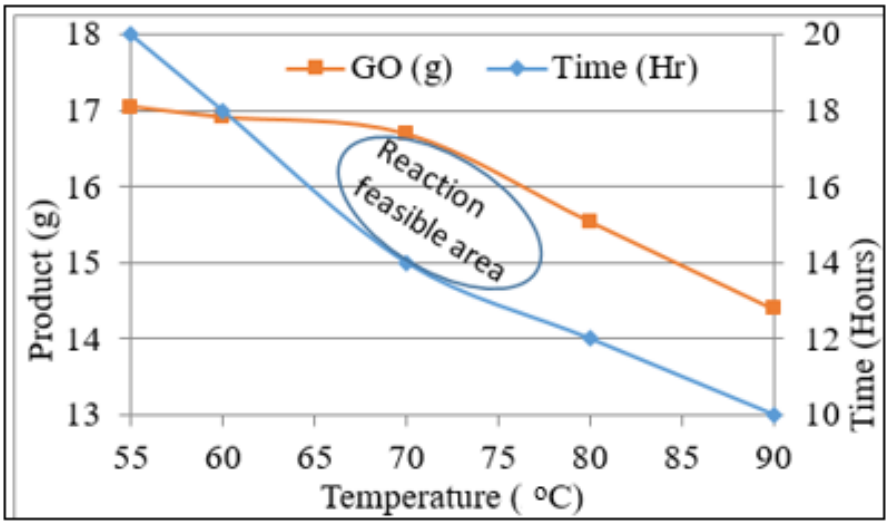

Figure-2.10. Reaction times and temperature relationship, and the amount of GOs products at various times and temperatures.

Lower temperatures and longer reaction times yield higher amounts of GOs products with smaller particle sizes, while the reverse conditions yield lesser amounts of GOs products with larger particle sizes. The optimum conditions for the synthesis of GOs were found to be 65–70 ℃ and 14–15 h (Figure 2.10). The particle size of the synthesized GOs was measured using both a particle size analyzer and SEM analysis. Particle sizes of the synthesized GOs completely depended on the reaction conditions such as the reaction temperature, the reaction time, and the moisture content (leading to an increase in the pH of the reaction media), affects the size of GOs particles substantially. Specifically, lower reaction temperatures, longer reaction times, and lower moisture content tend to produce smaller GO particle sizes, as evidenced by the data presented in Table 2.1. Conversely, altering these conditions in the opposite direction results in larger GO particle sizes. The particle size of the generated GOs exhibits significant variation based on factors such as the extent of the temperature of oxidation reaction, duration, and pH, which greatly affect the yield of GOs, particle size, and degree of oxidation, i.e., the oxygen to carbon ratio (Prodan D., et al., 2021).

The zeta-potential values of the GOs were determined by employing a particle size and zeta-potential analyzer. This study revealed that the measured values were dependent on the reaction conditions, specifically temperature and duration of the reaction. The zeta-potential values of the produced GOs increased as lower temperatures and longer reaction periods were employed (Figure 2.11). Lower values of zeta potential were obtained at higher temperatures and shorter reaction periods. Nevertheless, once the temperature exceeded 80 ℃, the Zeta-potential value

experienced a significant decline as a result of charge deactivation induced by partial reduction (Figure 2.12). The zeta potential was influenced by the pH of the reaction fluid and temperature.

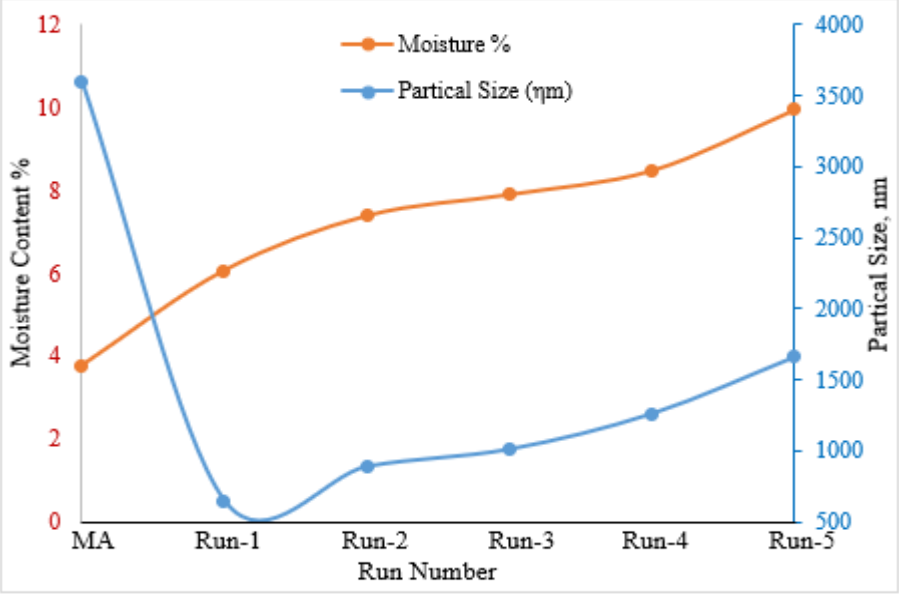

Figure-2.11: Relation between particle size and moisture content of produced GOs.

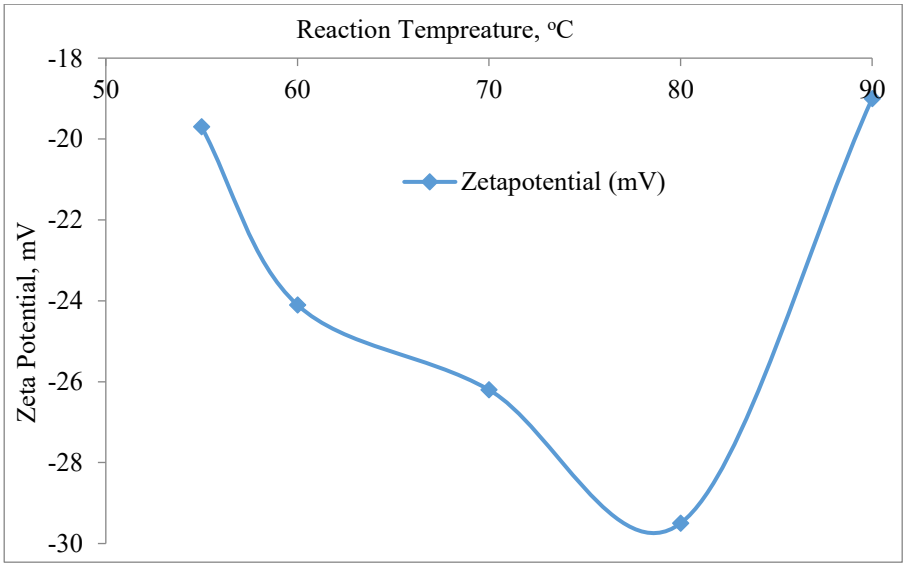

Figure-2.12: Relation between Zeta potential and reaction temperature of produced GOs.

2.4. Characterization of synthesized GOs

2.4.1. FTIR-ATR spectroscopic analysis

The FTIR-ATR spectra of the purified and freeze-dried GOs samples revealed several significant absorption peaks, as depicted in Figure 2.13. A broad absorption peak was observed around 3175–3230 cm^{-1}, indicating the formation of hydroxyl groups (-OH) during the

oxidation of graphite. This peak was absent in the spectrum of graphite in Figure 13. Additionally, there was a sharp absorption peak at around 1704–1720 cm^{-1}, which is attributed to the formation of carboxyl groups (-CO-), and another sharp peak at around 1591–1620 cm^{-1}, corresponding to the stretching and bending vibration modes of groups (-OH). Two shorter absorption peaks were observed around 1354–1394 cm^{-1} and 1237–1262 cm^{-1}, indicating the formation of etheric oxygen (C-O-C) bond stretching modes. Finally, there was a sharp and intense absorption peak at around 1048–1057 cm^{-1}, which corresponds to the vibrational mode of the C–O bond. These FT-IR absorption peaks confirmed the formation of the oxidized form of the synthesized GO products (Prodan D., et al., 2021), (Çiplak Z., et. al., 2015), (Sahoo P., et. al., 2022).

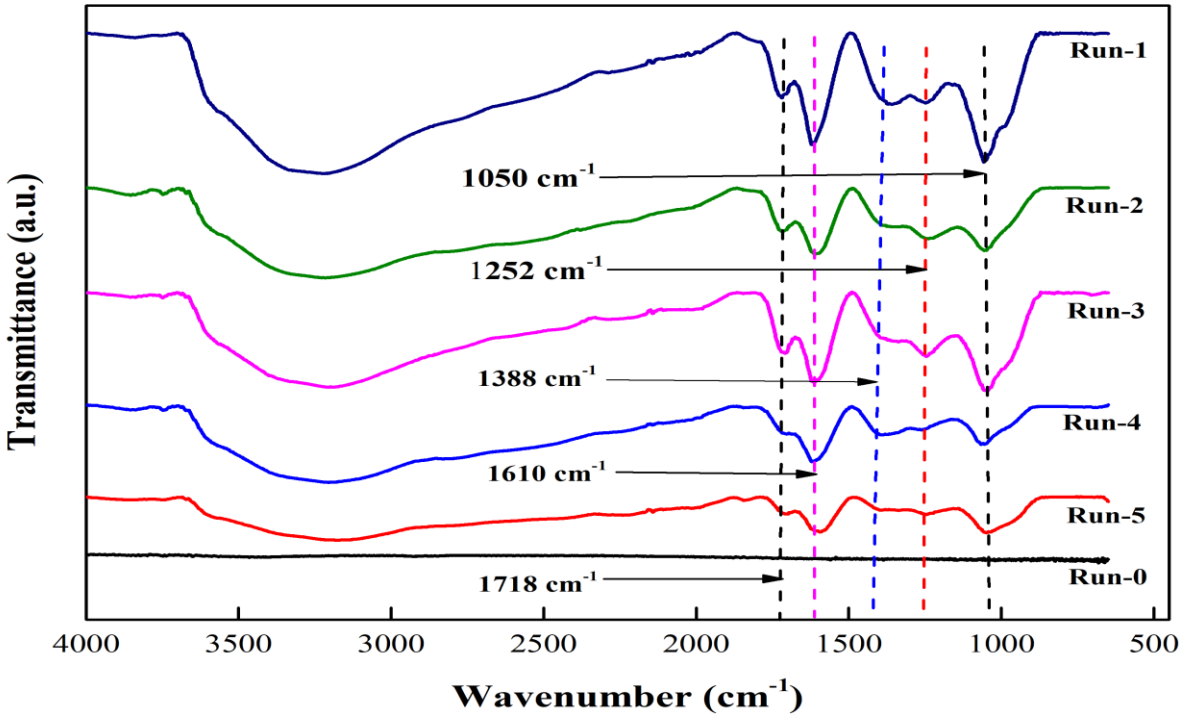

Figure-2.13: FT-IR spectroscopic analysis of different GOs products from different runs: (Run-1) GOs @ 55 ºC for 20 hours, (Run-2) GOs @ 60 ºC for 18 hours, (Run-3) GOs @ 70 ºC for 14 hours, (Run-4) GOs @ 80 ºC for 12 hours, (Run-5) GOs @ 90 ºC for 10 hours and (R-0) raw graphite represents.

2.4.2. UV-Visible spectroscopic analysis of GO nanoparticles

Figure 2.14 depicts the UV-visible spectra of the raw graphite and prepared GO nanoparticles that remained in the supernatant solutions of different reaction Runs. The spectrum corresponding to the graphite showed no absorption peaks, as expected. All spectra of GO nanoparticles exhibited an absorption peak at around 242-253 nm, along with other minor peaks. The absorption peak was centered at λ_{max}= 243 for Run-1, which resembles the $\pi \rightarrow \pi^*$

transition of C=C of the graphene layer. Similar peaks were observed for the samples from Run-2 to Run-5 at wavelengths closer to the λ_{max} of Run-1. The intensity of the $\pi \rightarrow \pi^*$ transition depends on two types of conjugative effects: one is related to the nanometer-scale sp^2 clusters, and the other is related to the number of chromophore units, such as C-O, C=O, and C=C bonds (Lai Q., et. al., 2012). In addition to the broad peak, a shoulder was observed in the GO nanoparticle samples for Run-3 and Run-4. This shoulder was related located in the 300–400 nm range to the $\pi \rightarrow \pi^*$ transition involving the C-O and >C=O groups present on the graphene nanoparticle sheet (Chen G., et. al., 2013).

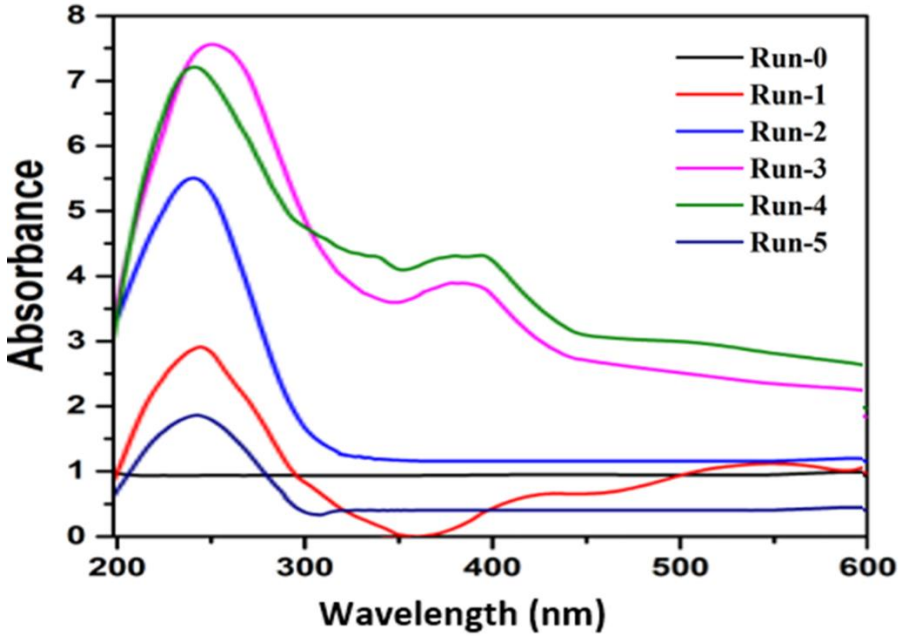

Figure-2.14. UV Visible spectroscopic analysis of different GO nanoparticles obtained from supernatant collected in different runs: (a) Run-0, raw graphite, GOs of (b) Run-1, (c) Run-2, (d) Run-3, (e) Run-4, and (f) Run-5.

GO nanoparticles of Run-1 displayed the presence of absorption peaks in the range of 600–800 nm, which were related to the presence of impurities on the surface of the GO nanoparticle layer (Gupta V., et. al., 2017). Absorption spectra of the GO nanoparticles also addressed the size distribution in the dispersed medium. According to the quantum confinement principle, the small particle sizes in the microscopic scale tend to show absorption edges around lower wavelengths or higher energy, and GOs with larger particle sizes showed absorption edges around higher wavelengths or lower energy (Arefi-Rad M. R., et. al., 2020) (Kafashan H., et. al., 2024).

2.4.3. FT- Raman spectroscopic analysis of GOs dried samples

The Raman spectra of the purified graphite of Run-0 and synthesized GOs, obtained from reaction Runs 1-5, are shown in Figure 2.15. This figure depicted the prepared GO samples. Raman spectroscopy was widely used to gain insight into the structural information of carbon-based materials (Claramunt S., et al., 2015), (López-Díaz D., et. al., 2017), (Dennison J. R., et. al., 1996), (Wang Y., et. al., 1990). The presence of C=C bonds and their conjugation led to high Raman intensities. The graphite spectrum showed no Raman bands, as expected, because it had a similar structure to Graphene. But, in the case of GOs of different reaction runs, a very noisy spectra were observed. However, the most prominent and sharp bands were distinguished from these spectra at around ~1355 cm^{-1}, which corresponded to the disordered band caused by graphitic edges and were also denoted as the D band. Another prominent but less sharp peak at around ~1575 cm^{-1}, which was formed due to the phase vibration of the graphite lattice and was denoted as the G band (Coccato A., et. al., 2015). The intensity of the G and D bands was highly dependent on the structure of the GOs. As disorder in the graphene lattice was increased due to exfoliation, the D band's relative intensity increased compared to the G band. Moreover, the G band becomes broader with the increased disorder in the structure of the GOs. For this reason, the GOs of Run-1 showed a relatively higher intensity of both the G and D bands, were indicates the presence of disorder in the structure of GOs than the other runs (Adar F., 2022), (Tuinstra F., et. al., 1970). The G and D bands were absent in the product of Run-0, as it was pure graphite. These phenomena were not shown in any type of blue or red shifts and were progressive from GOs of Run-2 to Run-5, which suggested the absence of amorphous graphene (Ferrari A. C., et. al., 2000).

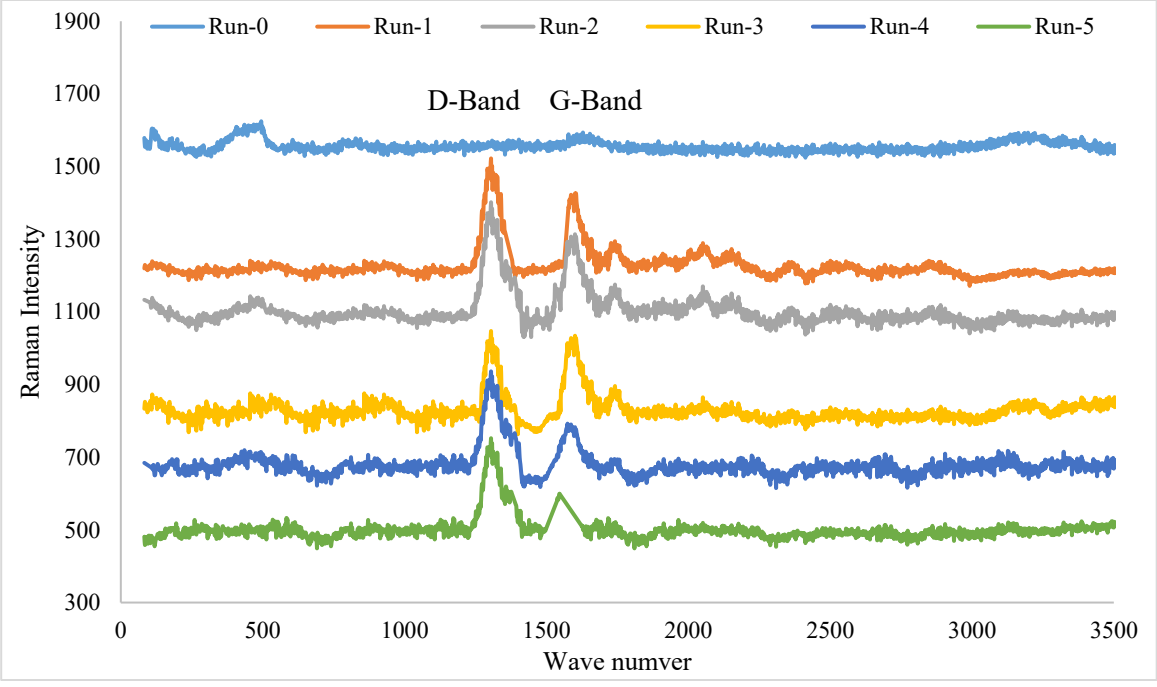

Figure-2.15. FT-Raman spectroscopic analysis of different GOs products from different runs- (a) Run-0, raw graphite, (b) GOs of Run-1, (c) GOs of Run-2, (d) GOs of Run-3, (e) GOs of Run-4, and (f) GOs of Run-5.

2.4.4. SEM image analysis of GOs

The FE-SEM micrographic images are shown in Figure 2.16, and it was found that the GOs showcased the surface morphology at different magnifications. FE-SEM micrographs indicated that different forms and sizes of GOs were formed. GOs showed a layered structure, and the layer thickness was found to be 200–260 nm, as seen from Figure 2.16 (C). GOs generally have well-defined and interlinked three-dimensional graphene sheets, forming a porous network that resembles a loose sponge-like structure (Paulchamy B., et. al., 2015). The wrinkled and layered flakes seen on the surface imply that the graphene layers were fully oxidized to GOs (Hidayah, et al., 2017).

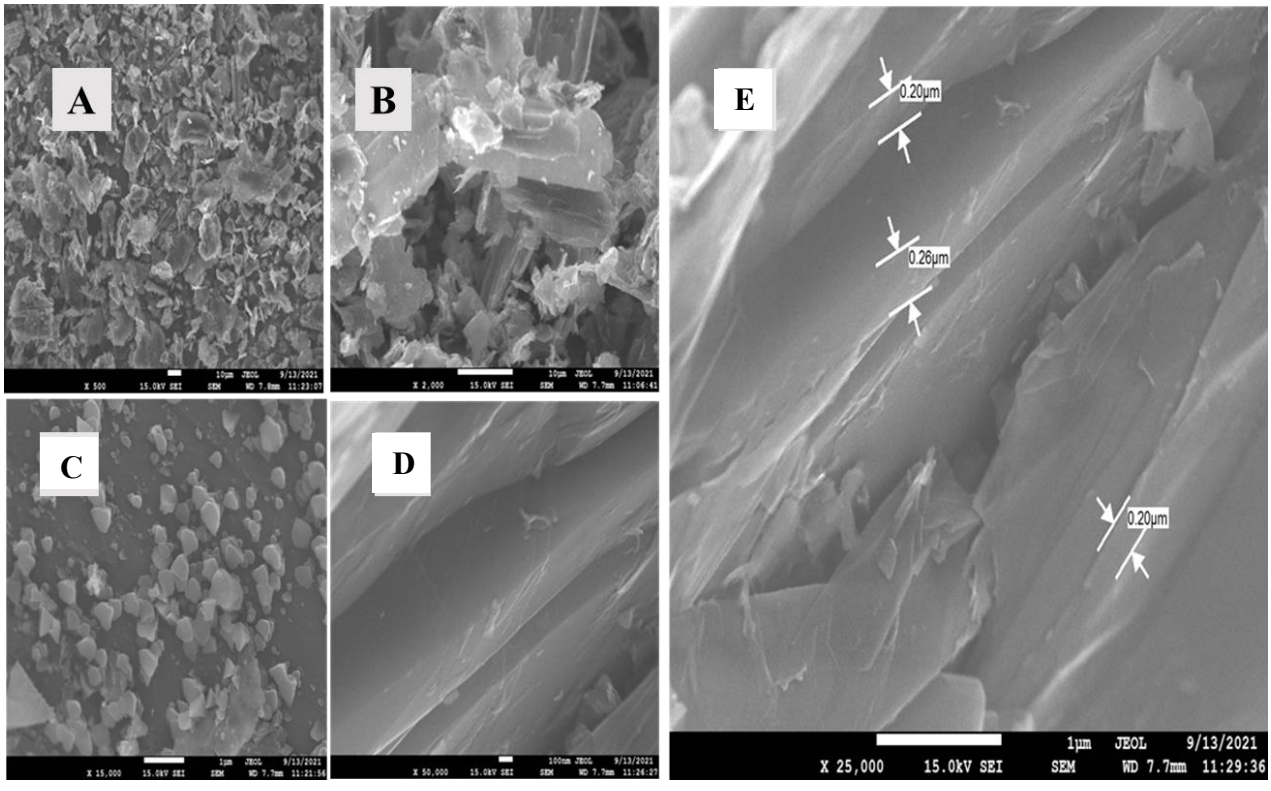

Figure-2.16. Scanning Electron Microscopic Image of R-3 GOs [A), B), and C) Random image at different resolutions, D) Stacked layers of GOs nano sheets, E) Layer thickness].

2.4.5. XPS analysis of GOs

XPS is a readily accessible and efficient quantitative technique employed for the determination of the oxidation state of the surface of the materials. The XPS analysis conducted on the produced GOs provides insights into the degree of oxidation in relation to the presence of organic functional groups incorporated into the structure of GOs (Marcano D. C., et al., 20180), (Zhang, et al., 2013). The synthesized GOs from Run-3 and Run-5 underwent XPS analysis and are presented in Figure 2.17–2.20.

The XPS survey scan analysis of the synthesized GOs from Run-3 was presented in Figures 2.17 and 2.18. In the survey scan analysis, presented in Figure 2.17, it was observed that the produced GOs samples contain two distinct peaks corresponding to carbon and oxygen atoms. Substantial peaks were observed in the survey scan of the XPS analysis. The observed peak, with a center at around 287.08 eV, was attributed to the C1s peak, indicating the presence of carbon atoms. At the same time, the primary peak observed at around 533.08 eV was assigned to the O1s peak, suggesting the presence of oxygen atoms (Figure 2.17). Based on the area percentage calculation, the atomic carbon content in GOs was 57.75%, and the atomic oxygen

was 38.55%. The results in an atomic oxygen-to-carbon ratio were 66.7%. After deconvolution of the Carbon peak exhibited five distinct sub-peaks were presented in the spectrum in Figure 2.18 (A), which indicated the inclusion of both sp^3 and sp^2 carbon types, C-C/C=C bonds in GOs, observed at 284.18 eV. These bonds accounted for approximately 15.838% of the material. The peak observed at 284.99 eV in the C1s spectrum was assigned to the sp^3/σ-bond of carbon-oxygen (C-O) in C-OH bonds, which represented approximately 18.718% of the overall carbon content in the composition. The peak observed at 286.78 eV in the C1s spectrum was attributed to the presence of sp^3/σ-bonds between carbon and oxygen atoms in the C-O-C epoxide and C=O functional groups. These peaks accounted for roughly 39.771% of the total spectral intensity. This observation of a C1s peak at 288.78 eV suggests the existence of sp^2/π-bonds associated with the C=O moiety in the COOH compound, which accounted for approximately 17.645% of the analyzed specimen. Another carbon satellite peak was observed at 290.98 eV, which accounted for about 8.025% of the total carbon composition. The analysis of the oxygen peak demonstrated the existence of three distinct sub-peaks, which were shown in Figure 2.18 (B). The major peak observed at 532.88 eV in the O1s spectrum was identified as originating from the sp^3/σ-bonds of carbon-oxygen (C-O) from several chemical groups, namely C-O-C epoxide, C-OH, and COOH carboxylic groups. These particular types of bonds were collectively accounted for around 61.723% of the overall oxygen composition. The peak observed at 534.68 eV in the O1s spectrum corresponds to the presence of sp^2/π-bonds in the C=O functional group, which accounted for approximately 15.096% of the total signal intensity. The presence of sp^2/π-bonds of C=O in COOH carboxylic groups, which accounted for approximately 23.18% of the total oxygen bonds, was confirmed by the O1s signal observed at 536.08 eV. (Johra F. T., et. al., 2014), (Priante F., et. al., 2018).

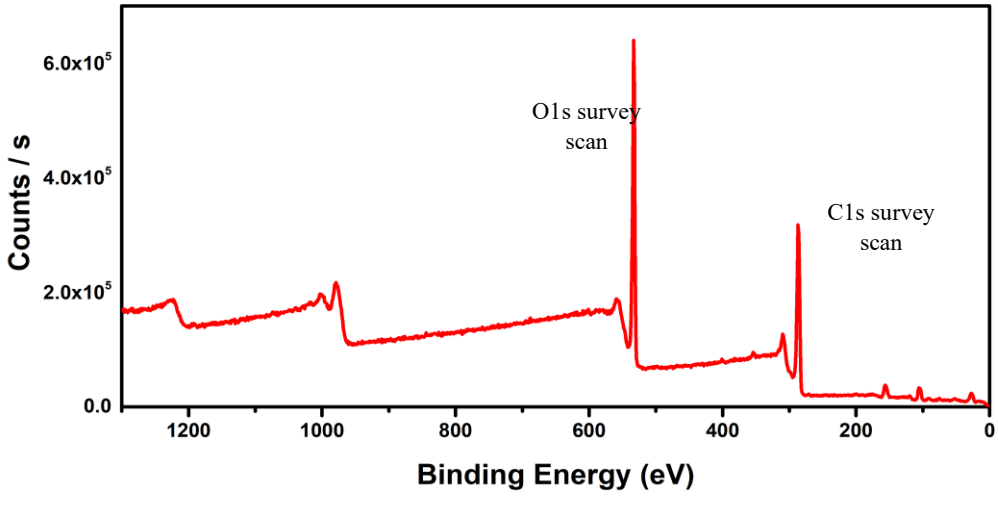

Figure-2.17. XPS survey scan binding energy of Run-3 of GOs.

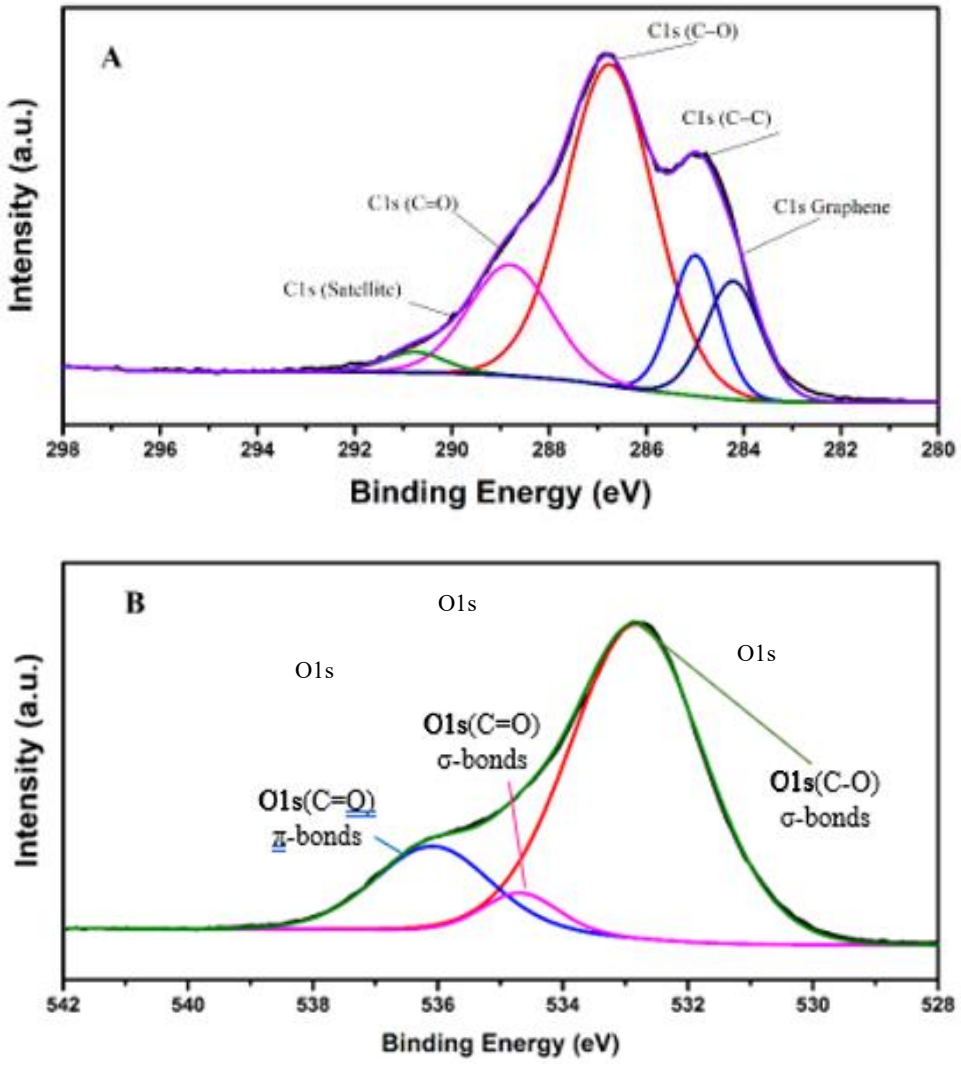

Figure-2.18. XPS survey scan analysis of deconvoluted bonding energy of binding energy of (A) C-1s scan peak deconvolution of Run-3 GOs and (B) O-1s scan peak deconvolution of Run-3 GOs.

The XPS survey scan analysis of the synthesized GOs from Run-5 has been presented in Figures 2.19 and 2.20, respectively. In the survey scan analysis presented in Figure 2.19, the GOs showed two distinct peaks corresponding to carbon and oxygen atoms. The peak at approximately 287.08 eV represents the C1s peak for carbon atoms, while the peak at around 533.08 eV represents the O1s peak for oxygen atoms. Based on the area percentage calculation, the atomic carbon content in the GOs was 63.88% and the atomic oxygen content was 32.69%, which were resulted in an oxygen-to-carbon atomic ratio of 51.17%. Following the process of deconvolution, a total of five sub-peaks were obtained from the carbon peak shown in Figure 2.20 (A). The peak observed at 283.88 eV in the C1s spectrum corresponds to the presence of C-C bonds in graphitic carbon. These bonds were found in both aromatic and aliphatic carbons,

indicating a mixture of sp^3 and sp^2 hybridization. The C-C bonds accounted for approximately 4.36% of the overall composition. The peak at 284.78 eV in the C1s spectrum, which were corresponded to the sp^3/σ-bonds of carbon-oxygen (C-O) inside the C-OH functional groups, constituted approximately 40.40% of the total spectrum. Similarly, the peak at 286.88 eV in the C1s spectrum corresponded to the sp^3/σ-bonds of carbon-oxygen (C-O) in C-O-C epoxides and carbon-oxygen double bonds (C=O). This peak accounted for roughly 37.658% of the total spectral intensity. The C1s spectrum consisted of a peak at 288.78 eV, indicating the presence of sp^2/π-bonds of carbon-oxygen (C=O) in the carboxylic acid (-COOH) functional group, representing approximately 12.019% of the overall composition. Furthermore, there existed an additional peak in the C satellite spectrum at 290.58 eV, which contributed to about 5.56% of the whole carbon spectrum. Three sub-peaks were obtained from the deconvolution of the spectra of O1s corresponding to oxygen peaks in Figure 2.20 (B). O1s spectrum exhibited a peak at 532.68 eV, which was attributed to the sp^3/σ-bonds of carbon-oxygen (C-O) was present in C-O-C epoxides, C-OH groups, and carboxylic (-COOH) groups. These functional groups collectively make up around 76.05% of the overall composition (Rathnayake R. M. N. M., et. al., 2017), (Dreyer D. R., et. al., 2014). At 534.68 eV in the O1s spectrum, the peak corresponded to the sp^2/π-bonds of the carbon-oxygen (C=O) functional group, constituting approximately 11.97% of the total spectrum. The peak at 531.08 eV in the O1s spectrum corresponded to the sp^2/π-bonds of carbon-oxygen (C=O) in carboxylic groups (-COOH). This peak accounted for approximately 11.98% of the whole spectrum.

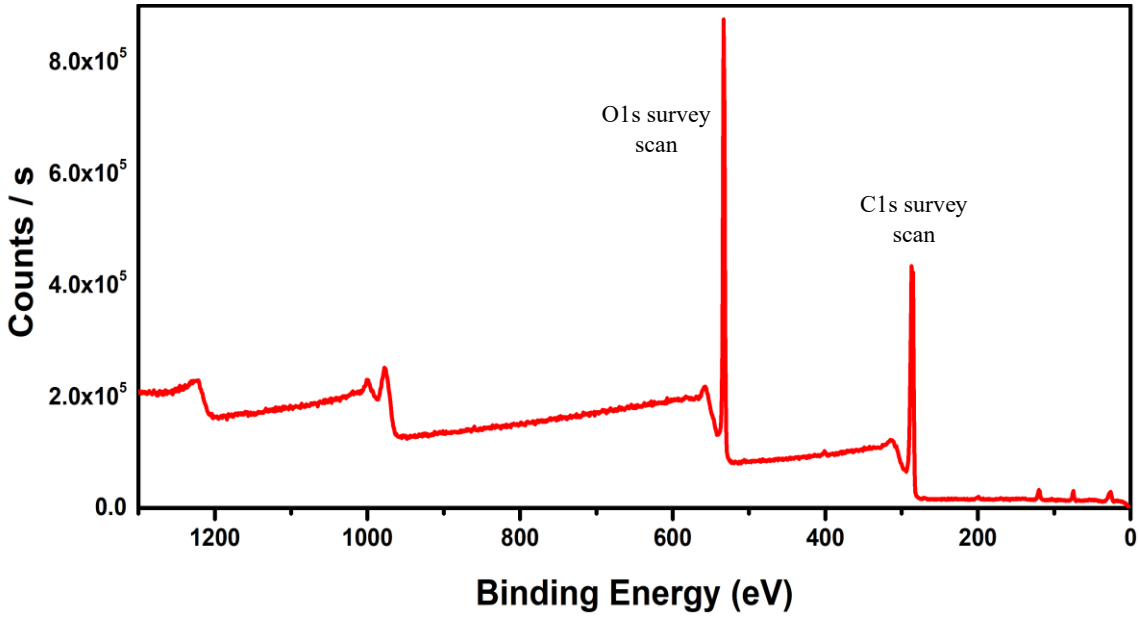

Figure-2.19. XPS survey scan binding energy of Run-5 GOs.

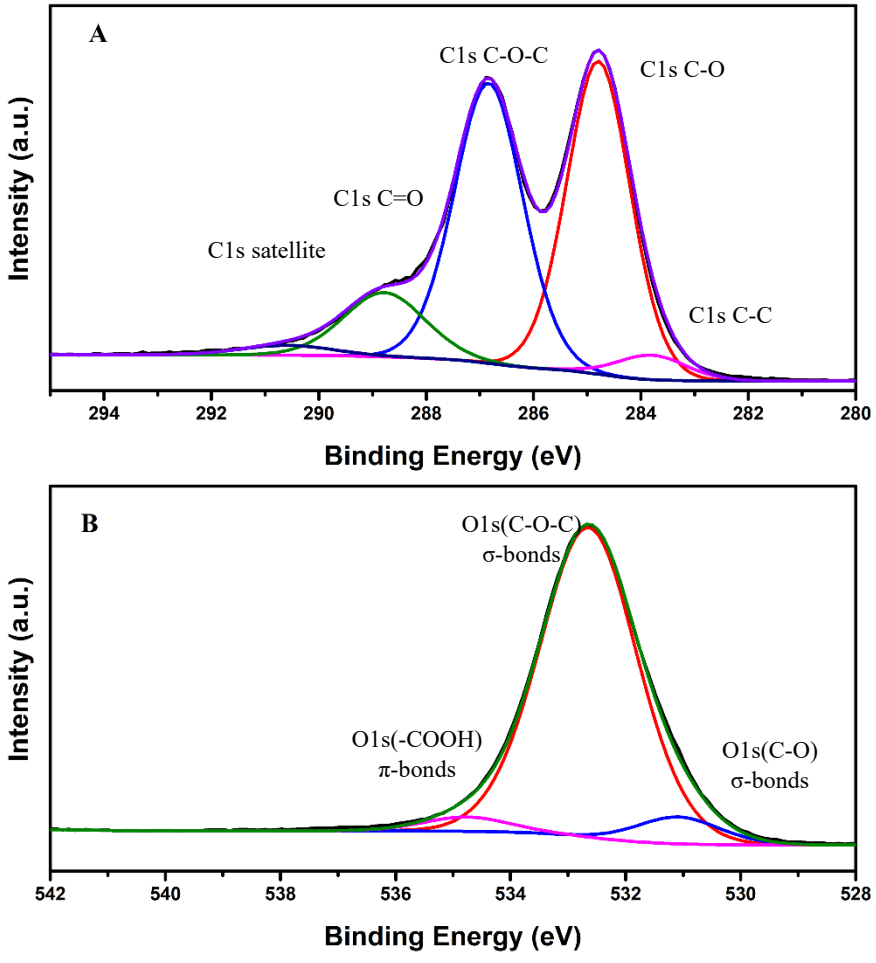

Figure-2.20. XPS survey scan analysis of the deconvoluted bonding energy of binding energy of Run-5 GOs. (A) C1s Scan peak deconvolution of Run-5 GOs and (B) O1s Scan peak deconvolution of Run-5 GOs.

2.4.6. Thermal properties of GOs

The thermal properties of the GO samples were measured and demonstrated in Figure 2.21. The GOs were stable up to 75 ℃. The mass loss due to thermal treatment was initiated beyond this temperature, and continues up to around 193.4 ℃. At this temperature, the total mass loss was about 18.99%, and an endothermic peak was observed in the DSC curve. This loss of mass was due to the loss of water molecules trapped inside the nanolayer of GOs (Sengupta I., et. al., 2018). At 193.4 ℃, a sharp loss of huge mass, about 73.28% of the total mass, with an exothermic peak was observed, and it occurred due to the thermal decomposition of hydroxyl functional groups along with the breakdown of carbon ring framework structures (Dreyer D. R., et. al., 2014). After that, the mass loss was not so significant but steady up to the temperature 425 ℃, and there was no change in energy observed. But at the temperature between 425 ℃

and 500 °C, a third mass loss of about 8% was observed, with an exothermic peak again. This mass loss indicated the burning of the carbon skeletons (Xing B., et al., 2017).

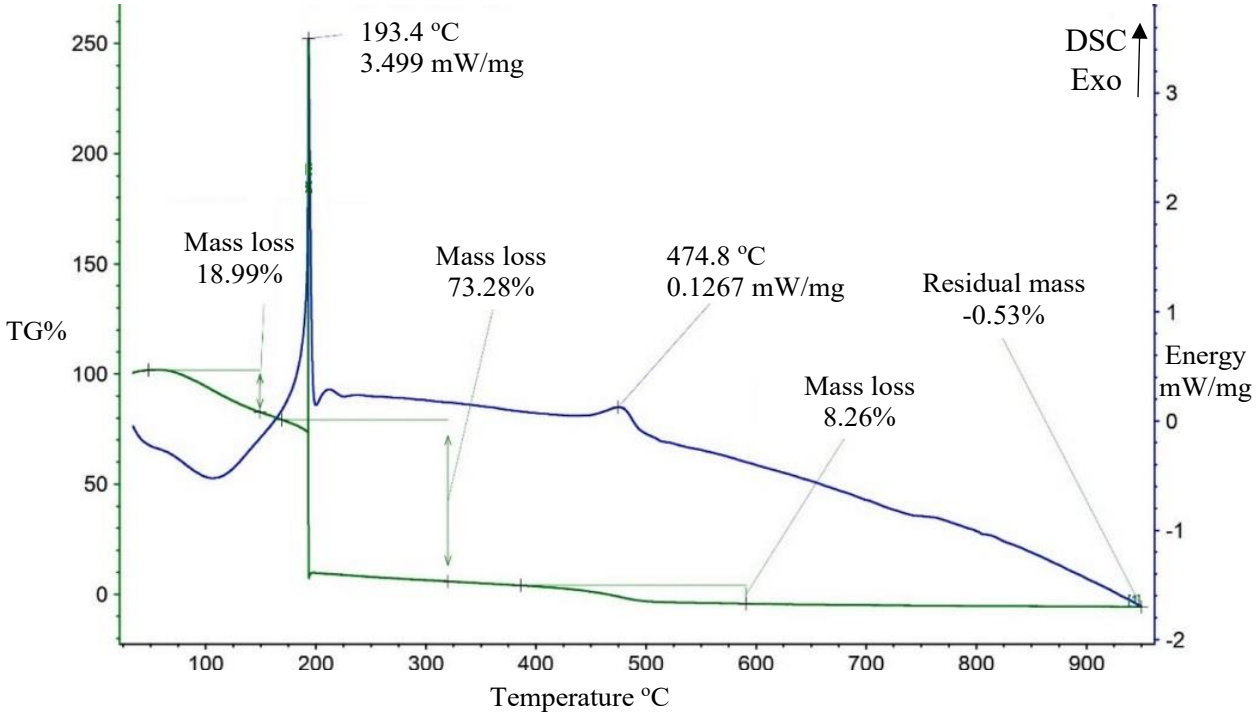

Figure-2.21. Simultaneous thermal analysis (STA) of GOs products of Run-3.

2.4.7. Correlation between the properties of GOs

Correlation analysis was performed to evaluate the relationship between the properties of the synthesized GOs with time, temperature, and yields, which were evaluated using the SPSS software. The correlation also found a significant effect of FAL recovery on GOs and the recovered FAL of different reaction Runs. The correlation matrix reveals a coherent set of interdependent physicochemical behaviors among the recovered acids, salts, and particle characteristics. The results of these analyses were displayed in Table 2.2.

The correlation analysis revealed several distinct interaction patterns among the physicochemical properties of the generated graphene oxide (GO) samples. The particle size exhibited strong and positive correlations with multiple key variables, including salt recovery (0.933), dilute acid recovery (0.944), recovered acid density (0.827), moisture content (0.906), phosphate ion concentration, PO_4^{3-} (0.977), and potassium ion concentration, K^+ (0.868). These relationships suggested that larger GO particle performances were improved.

Table-2.2: Correlation among the different reaction conditions for different reaction runs and properties of different produced GOs

	Particle size	Zeta potential	Acid recovery	Salt recovery	Dilute acid recovery	Recovered acid density	Moisture %	SO_4^{2-}	PO_4^{3-}	K^+	Mn^{2+}
Particle Size	1	0.372 (0.538)	0.944* (0.016)	0.933* (0.021)	0.944* (0.016)	0.827 (0.084)	0.906* (0.034)	0.916* (0.029)	0.977** (0.004)	0.868 (0.057)	0.266 (0.665)
Zeta potential	0.372 (0.538)	1	-0.046 (0.942)	0.031 (0.960)	0.046 (0.942)	-0.173 (0.781)	-0.034 (0.956)	0.011 (0.986)	0.169 (0.786)	-0.112 (0.858)	-0.559 (0.327)
Acid recovery	0.944* (0.016)	-0.046 (0.942)	1	-0.992** (0.001)	-1.000** (0.000)	-0.953* (0.012)	-0.984** (0.002)	0.990** (0.001)	-0.991** (0.001)	-0.974** (0.005)	-.478 (0.415)
Salt recovery	0.933* (0.021)	0.031 (0.960)	-0.992** (0.001)	1	0.992** (0.001)	0.922* (0.026)	0.994** (0.001)	-0.969** (0.007)	0.986** (0.002)	0.983** (0.003)	0.565 (0.321)
Dilute acid recovery	0.944* (0.016)	0.046 (0.942)	-1.000** (0.000)	0.992** (0.001)	1	0.953* (0.012)	0.984** (0.002)	-0.990** (0.001)	0.991** (0.001)	0.974** (0.005)	0.478 (0.415)
Recovered acid density	0.827 (0.084)	-0.173 (0.781)	-0.953* (0.012)	0.922* (0.026)	0.953* (0.012)	1	0.935* (0.020)	-0.982** (0.003)	0.913* (0.031)	0.929* (0.022)	0.445 (0.453)
Moisture %	0.906* (0.034)	-0.034 (0.956)	-0.984** (0.002)	0.994** (0.001)	0.984** (0.002)	0.935* (0.020)	1	-0.970** (0.006)	0.973** (0.005)	0.976** (0.004)	0.596 (0.288)
Sulphate	-0.916* (0.029)	0.011 (0.986)	0.990** (0.001)	-0.969* (0.007)	-0.990** (0.001)	-0.982** (0.003)	-0.970** (0.006)	1	-0.973** (0.005)	-0.953* (0.012)	-0.429 (0.472)
PO_4^{3-}	0.977** (0.004)	0.169 (0.786)	-0.991** (0.001)	0.986** (0.002)	0.991** (0.001)	0.913* (0.031)	0.973** (0.005)	-0.973** (0.005)	1	0.946* (0.015)	0.423 (0.478)
K^+	0.868 (0.057)	-0.112 (0.858)	-0.974** (0.005)	0.983** (0.003)	0.974** (0.005)	0.929* (0.022)	0.976** (0.004)	-0.953* (0.012)	0.946* (0.015	1	0.641 (0.243)
Mn^{2+}	0.266 (0.665)	-0.559 (0.327)	-.478 (0.415)	0.565 (0.321)	0.478 (0.415)	0.445 (0.453)	0.596 (0.288)	-0.429 (0.472)	0.423 (0.478	0.641 (0.243)	1

*Correlation is significant at the 0.05 level (2-tailed)
**Correlation is significant at the 0.01 level (2-tailed)

In contrast, particle size showed significant negative correlations with acid recovery (–0.944) and sulphate ion concentration (SO_4^{2-}, –0.916), indicating that smaller particles more efficiently associated with acid recovery and greater sulphate retention.

The acid recovery displayed a negative correlation with salt recovery (–0.992), dilute acid recovery (–1.000), recovered acid density (–0.953), moisture content (–0.984), PO_4^{3-} concentration (–0.991), and K^+ concentration (–0.974). However, strong positive correlations were observed between acid recovery and SO_4^{2-} concentration (0.990), suggesting that acid recovery favored phosphate and potassium ions over sulphate ions.

Salt recovery, dilute acid recovery, and recovered acid density were tightly interlinked in a cluster. Salt recovery correlated strongly and positively with dilute acid recovery (0.992), recovered acid density (0.922), moisture content (0.994), PO_4^{3-} (0.986), and K^+ (0.983), while it showed a notable negative correlation with SO_4^{2-} (–0.969). Similarly, dilute acid recovery shared strong positive correlations with recovered acid density (0.953), moisture (0.984), PO_4^{3-} (0.991), and K^+ (0.974), but displayed a strong negative correlation with SO_4^{2-} (–0.990). The recovered acid density follows this trend, correlating positively with moisture (0.935), PO_4^{3-} (0.913), and K^+ (0.929), and negatively with SO_4^{2-} (–0.982).

Moisture content is strongly aligned with the enrichment of PO_4^{3-} (0.973) and K^+ (0.976), and inversely associated with SO_4^{2-} (–0.970). The ionic relationships are particularly pronounced: SO_4^{2-} shows strong negative correlations with PO_4^{3-} (–0.973) and K^+ (–0.953), whereas PO_4^{3-} and K^+ exhibit a robust positive intercorrelation (0.946), indicating co-mobility or co-enrichment during the recovery process.

Finally, manganese demonstrates uniformly weak correlations with all variables, suggesting minimal influence from the recovery conditions that drive the behavior of other species.

2.5. Application of the synthesized GOs

2.5.1. Removal of Arsenic (III) from aqueous solution using GOs

The adsorption of arsenic (III) by synthesized GOs offers several advantages over other methods, including high removal efficiency with a higher adsorption rate, because GOs have large surface area and versatile oxygen functional groups. This method is environmentally friendly, cost-effective, and scalable, providing a sustainable solution for water purification while avoiding the generation of hazardous by-products commonly associated with conventional methods.

2.5.2. Determination of calibration curve

The role of the calibration curve is very important for the measurement of As^{3+} ions in water. It is considered the main scale of measurement. If the calibration curve can't be drawn properly, the whole measurement technique will be in doubt. It expresses the accuracy of measurement. The significance of the calibration curve can be understood from the R^2 value and its linearity. It should be almost a straight curve, and the R^2 value should come approximately 1 or at least 0.999 for the chemical measurement.

Table 2.3 and Figure 2.22 showed the absorbance and R^2 value of the experimental data obtained from the absorbance measurements using an AAS instrument at the variation in concentration of As^{3+} ions in aqueous solutions, and the R^2 value obtained was 0.999.

Table-2.3: Calibration data for As(III) adsorption using the AAS instrument

Sample No.	Used Arsenic Concentration (ppm)	Measured Arsenic Concentration (ppm)
1	0.05	0.06
2	0.10	0.09
3	0.50	0.51
4	1.00	0.98
5	2.00	2.03
6	5.00	4.97

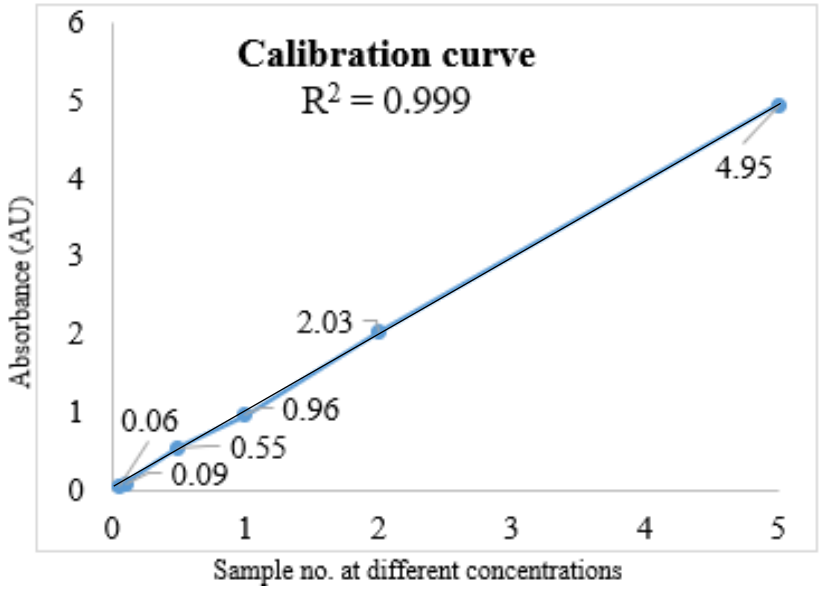

Figure-2.22: The calibration curve obtained for the As^{3+} ions from the AAS instrument.

From Table 2.4, the expression of the As^{3+} ions removal Capability (q_e), Adsorption Efficiency (E), and Adsorption Kinetics (R). The provided dataset outlines the experiment of adsorption behavior of As^{3+} ions in water using GOs as an adsorbent was measured over 24 hours. The key parameters included in the solution concentration, adsorption capability (q_e), and removal efficiency (R), with a constant adsorbent mass of 0.1 g and an initial arsenic concentration of 100 ppm, and a total volume of 400 mL solution were examined. During the initial stages, a rapid decline in the solution's arsenic concentration was observed. Figure 2.23 illustrates the increase in As^{3+} ion Adsorption efficiency with changes in concentration over time.

Within the first 1.0 hours, the concentration decreased from 100 ppm to 13.27 ppm, achieving a removal efficiency of 86.73% and an adsorption capability of 346.92 mg/g. After 2 hours, the solution concentration dropped to 1.98 ppm, corresponding to an adsorption capability of 392.08 mg/g and a removal efficiency of 98.02%. This rapid initial adsorption phase was attributed to the high availability of active adsorption sites on the GOs surface, which strongly interact with arsenic ions via mechanisms such as electrostatic attraction, complexation, and π-π interactions. Between 0 and 1 hours, the adsorption rate slowed as the remaining active sites on the GOs surface became saturated. The solution concentration decreased steadily, from 13.27 ppm at 1 hour to 1.95 ppm at 2 hours. Correspondingly, at 12 hours, the adsorption capacity reaches 392.96 mg/g, with a removal efficiency of 98.24%.

2.5.3. Measurement adsorption capability (qe), adsorption efficiency (E), and adsorption kinetics (R) study

Table-2.4: Variation in concentration with contact time

Time (Minute)	Amount of adsorbent (g)	Solution Concentration (ppm)	Adsorption capability (mg/g)	Removal Efficiency (%)
0.0	0.1	100	0	0
5.0	0.1	82.84	68.64	17.16
10.0	0.1	69.95	120.20	30.05
15.0	0.1	51.83	192.68	48.17
20.0	0.1	42.04	231.84	57.96
25.0	0.1	36.53	253.88	63.47
30.0	0.1	31.26	274.96	68.74
35.0	0.1	28.62	285.52	71.38
40.0	0.1	25.24	299.04	74.76
45.0	0.1	22.93	308.28	77.07
50.0	0.1	19.01	323.96	80.99
55.0	0.1	15.56	337.76	84.44
60.0	0.1	13.27	346.92	86.73
65.0	0.1	10.91	356.36	89.09
70.0	0.1	8.49	366.04	91.51
75.0	0.1	6.03	375.88	93.97
80.0	0.1	4.01	383.96	95.99
85.0	0.1	2.99	388.04	97.01
90.0	0.1	2.33	390.68	97.67
95.0	0.1	1.99	392.04	98.01
100.0	0.1	1.98	392.08	98.02
105.0	0.1	1.97	392.12	98.03
110.0	0.1	1.96	392.16	98.04
115.0	0.1	1.95	392.20	98.05
120.0	0.1	1.95	392.20	98.05
720.0	0.1	1.76	392.96	98.24

The gradual reduction in adsorption rate was explained by the decreased availability of unoccupied sites and the increased competition among arsenic ions for the remaining active areas. Additionally, the diffusion of arsenic ions to the surface became rate-limiting due to the decreased concentration gradient.

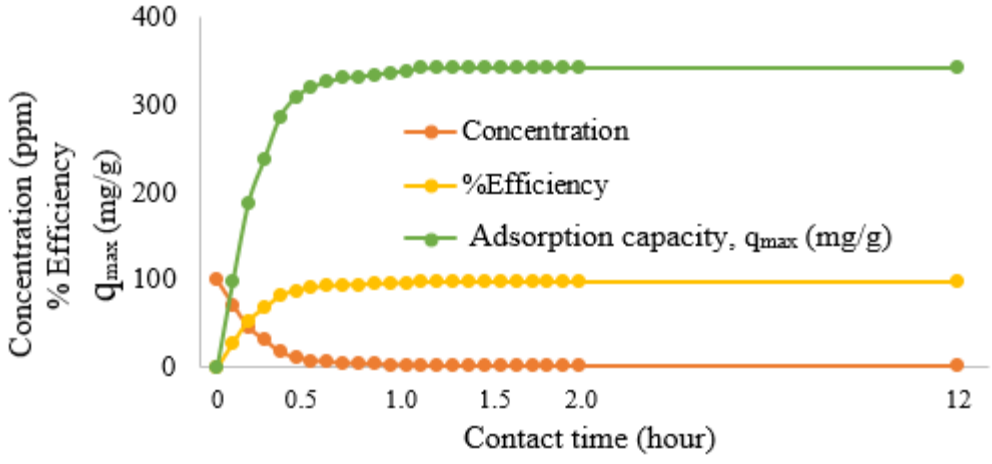

Figure-2.23: As(III) Adsorption efficiency with the concentration changes with time

After 1 hour, the system reached near-equilibrium conditions, as indicated by minimal changes in solution concentration, adsorption capacity, and removal efficiency. At the removal efficiency consistently exceeded 95% before 1 hour, indicating that GOs is highly effective even at a lower adsorbent dose. The high equilibrium adsorption capacity (343.14 mg/g) underscored the potential of GOs for treating arsenic-contaminated water, especially in regions where arsenic pollution is a significant concern. The data provide a comprehensive understanding of the adsorption process and kinetics of As(III) by GOs.

Furthermore, after 2 hours, the concentration stabilized at 1.95 ppm, with an adsorption capacity of 392.20 mg/g and a removal efficiency of 98.05%. At the end of the experiment (12 hours), the solution concentration reached 1.76 ppm, and the adsorption capacity slightly increased to 392.96 mg/g, with a removal efficiency of 98.24%. These results confirmed the high adsorption efficiency of GOs for As(III), demonstrated their potential for water treatment applications. The data in Figure 2.23 demonstrated the real-time efficiency % and solution concentration of As(III) adsorption by GOs. The rapid initial adsorption phase highlighted the strong affinity of GOs for arsenic ions, making it an effective material for rapid wastewater treatment. The plateauing of adsorption capability at equilibrium reflected the finite number of active sites available for arsenic binding.

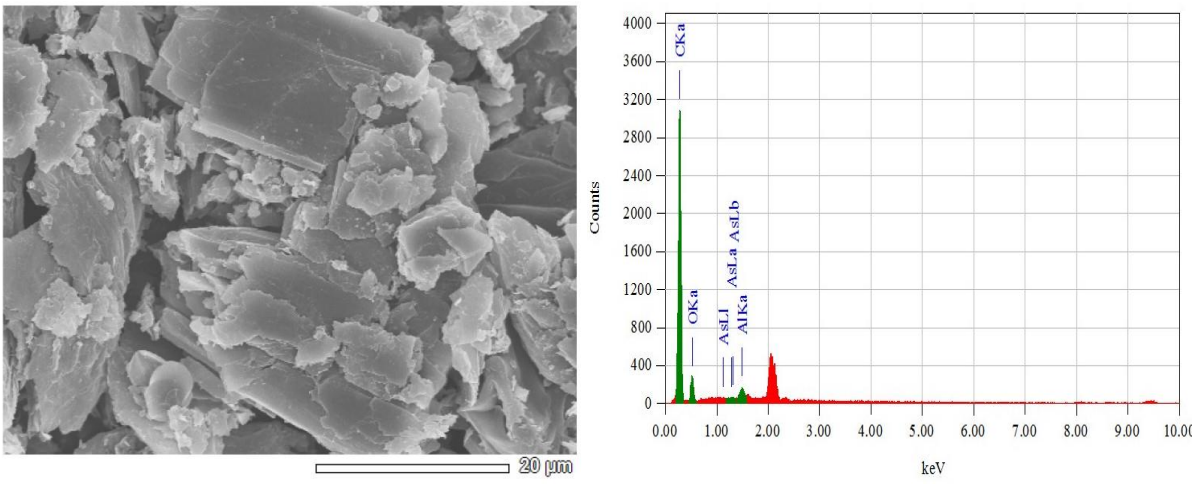

Figure-2.24: EDX analysis of the As (III) adsorption in GOs, A) EDX Image and B) Elements in of adsorbed GOs.

Figure 2.24 provided evidence of As^{3+} ions adsorption found in EDX analysis of the GOs after adsorption of As (III). The rapid adsorption rate, high removal efficiency, and substantial adsorption capacity affirmed the suitability of GOs as an advanced adsorbent for water purification. Future studies could focus on optimizing adsorbent dosage, evaluating multi-component adsorption systems, and scaling up the process for practical applications.

2.5.4. Effect of the initial concentration

Table-2.5: Adsorption kinetics of As(III) solution passed through adsorbent

Experiment No.	Amount of GOs (g)	Initial As(III) concentration of solution (ppm)	As(III) adsorption capability (mg/g)	As(III) adsorption efficiency (%)
01.	0.1	100	388.12	97.88
02.	0.1	100	390.84	97.92
03.	0.2	200	392.04	98.06
04.	0.2	200	394.36	97.64
05.	0.3	300	398.00	98.28
06.	0.3	300	394.40	98.66
07.	Average		392.96	98.24

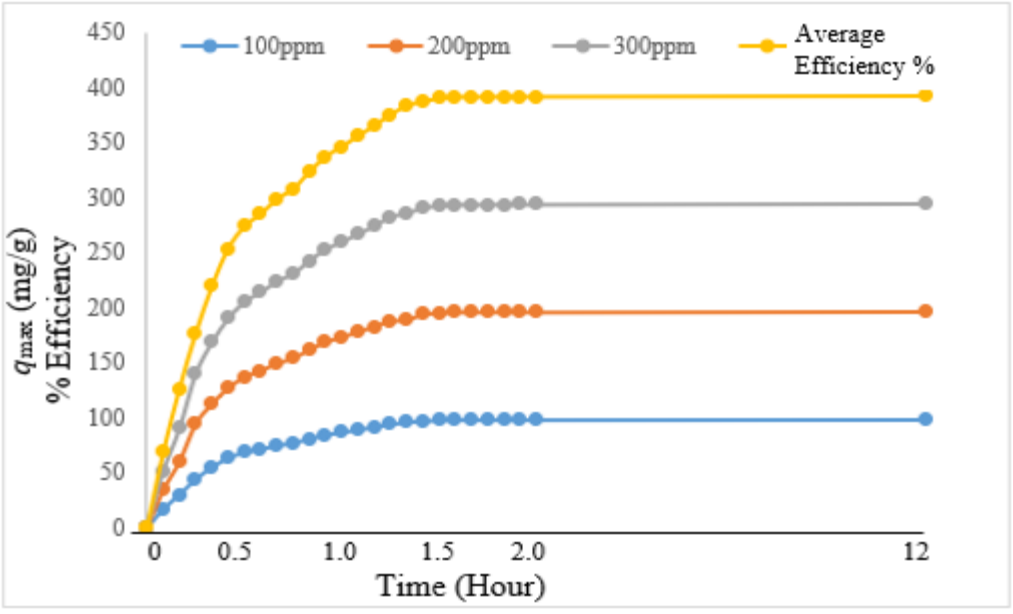

Figure-2.25: As(III) Adsorption capability of GOs with the concentration changes with time, Equilibrium adsorption

The experimental evaluation of GOs for As(III) adsorption demonstrated high performance across varying conditions. Table 2.5 and Figure 2.25 illustrate the effects of the initial As(III) concentration on the adsorption process. Three experiments were conducted using 0.1 g, 0.2 g, and 0.3 g of GOs with initial arsenic concentrations of 100 ppm, 200 ppm, and 300 ppm, respectively. The adsorption capability (q_e) remained consistent, ranging from 342.86 mg/g to 343.14 mg/g, indicating saturation of GOs adsorption capacity. Adsorption efficiency exceeded 97.9% in all experiments, highlighting GOs strong binding affinity for arsenic ions. The proportional ratio between GO dosage and arsenic concentration ensured consistent evaluation, confirming GOs reliability as an effective and efficient adsorbent.

2.7. Conclusions

This method has effectively produced GOs with increased carbon-to-oxygen ratios, reaching a maximum of 57.75%:38.55%. The effect of reaction temperature and duration on the extent of oxidation was considered significant. The best oxidation reaction conditions were 60-70 ℃ and 14-18 h, with respect to product yield and quality. 65-70% GOs were produced at the mentioned conditions. In contrast, elevated temperatures and shorter reaction times led to reduced oxidation and lower product yield. The unreacted feed acid liquor (FAL) was successfully recycled and reused for five consecutive cycles. In each recycled experiment, 80-90% of FAL was recycled and reused successfully. The properties of recycled FALs were investigated by measuring density, moisture content, pH, and ion concentration. The consecutive recycling of FALs tends to increase the moisture content by about 0.5% in each recycles. Ion chromatography (IC) was used to measure the variation in SO_4^{2-} and PO_4^{3-} ions in the FALs. The H_2SO_4 reacts with $KMnO_4$ and crystallizes out from the recovered FAL faster than the phosphoric acid. So, sulfuric acid content in the makeover FALs must be greater than the primary FAL. However, the recovered acid slurry underwent slow dilution of 0.5% in each recycle due to water production in the oxidation reaction. The alteration in the concentration of the acid slurry has an impact on the size of the GO particles. The particle size of GOs was increased from 900 to 1660 nm due to the increase in moisture in the FAL. During the reaction process, SO_4^{2-} exhibits a higher degree of participation with K^+ and Mn^{2+} ions compared to PO_4^{3-} ions. The zeta potential of GOs exhibits an upward trend when the reaction temperature is increased up to 80–85 ℃. The study examined how the characteristics of GOs change in response to variations in reaction parameters, including temperature and time, and how these changes are related to the product yield. The impact of temperature on the reaction rate was determined to have both negative (–0.204 g/℃) and positive (+0.450 g/h) effects on the reaction time. The XPS examination revealed an oxygen-to-carbon atomic ratio of 57.75%: 38.55%, which correlated with the 66.9% rise in product yields observed in the experimental data. The G and D band at ~1355 cm^{-1} and ~1575 cm^{-1} in Raman spectra confirms the conversion of graphite to GOs. SEM images of GOs showed a layered structure of 200–260 nm thickness. TGA showed the stability of GOs up to 75 ℃. 75% of GOs were decomposed at 193℃. As it can be removed very efficiently by the synthesized GOs. It can remove about 343 mg/g As(III) with 98% efficiency.

CHAPTER-3

Study on the Reduction of GOs to rGOs and Its Antimicrobial Activity Study

Abstract

This chapter focuses on the synthesis of nano graphene sheets using chemical oxidation and reduction methods to optimize graphene's properties. GOs with high oxygen-to-carbon ratios were produced from graphite powder using Tour's method and reduced through eco-friendly techniques to maximize the reduction of GO to afford rGO. The effects of soft, hard, and extreme thermo-chemical reduction treatments were investigated. First, GOs were synthesized using an acid liquor recycling technique to lower costs and enhance oxidation, followed by thermogravimetric analysis to study their thermal behavior. Soft thermal treatment (STT) of GOs in a polar solvent, water, at 95-98 °C for 48 hours (STT-St) and 96 hours (STT-Lt) yielded hydrophilic rGO. Hard thermal treatment (HTT) was then performed in a nonpolar solvent, kerosene, at 180 °C (HTT-LT) and 220 °C (HTT-HT) for 1 hour, resulting in hydrophobic rGO. For extreme reduction, HTT-HT rGO was further treated with ascorbic acid, reversing its hydrophobicity to hydrophilicity. Characterization techniques, including FT-IR, UV-Vis, FT-Raman, XRD, TEM, SEM, BET, and XPS, confirmed the formation of rGO. Upon stepwise reduction, the oxidation levels of the GOs decreased stepwise from 66.7% to 45.39%, 32.68%, 17.77%, 8.83% and finally 2.43% in the extremely reduced rGO-KAA. Structural analysis from XRD also supports the stepwise reduction compositions and showed broad peaks at 2θ at around 25° at the plane (002) for the rGO, which increases stepwise, whereas other broad peaks at 2θ around 10-13 for the (001) plane of GOs decrease consecutively, but a short peak around 43° for (100) plane remains same. BET analysis revealed a high surface area of 27.15 m^2/g. and 32.60 m^2/g respectively for rGO-K220 and rGO-KAA. The degradation mechanism was studied, and found that the lower temperature thermal reduction influenced non-destructive degradation only, but the higher temperature thermal reduction accomplished both non-destructive and destructive degradation consecutively. The antimicrobial activity of highly and extremely reduced rGO was tested, and the test results showed that highly reduced rGO showed activity against both B. subtilis, S. aureus, E. coli, and S. typhi compared to hydrophobic rGO, while GOs exhibited no activity. The highest zone of inhibition was 19.5 mm at 20 μg/mL after 24 hours, compared to 27.5 mm for standard tetracycline.

Objectives

According to the literature review, the maximum chemical oxidation of graphite provides the highest degree of exfoliation, but it suppresses some of the graphene properties, e.g., reduces transparency, electrical and thermal conductivity, crystallinity, etc. To reactivate these properties, GOs should be reduced. To reveal the rGO properties, the synthesized GOs were thermally treated under several conditions to achieve maximum reduced rGO, and it was the main objective of this research. So, the objectives are-

i. Thermal degradation of GOs at different conditions to achieve the maximum reduced condition phenomena, and to obtain optimum reduction temperature, time, and medium of reduction
ii. Optimized the thermal treatment using water and kerosene and their effect on oxygen to carbon ratios to understand the reduction mechanism.
iii. The effect of combined thermal and chemical reduction on the reduction of GOs to rGO.
iv. Application of rGO for the evaluation of antimicrobial properties.

3.1. Introduction

Research on Graphene materials has drawn enormous attention due to its extreme electromechanical properties and diversified application fields (Geim A. K., et. al., 2007). It has the basic building block of other carbon allotropes, and graphene has been wrapped to create 0D fullerenes, rolled up to form 1D carbon nano tubes (CNTs), atomically thin sheet form 2D, graphene, and stacked to make 3D graphite (Georgakilas V., et. al., 2015). Its superior mechanical, optical, and thermal properties offer its diversified fields of utilization (Banerjee A. N., 2018), (Sur U. K., 2012). It achieved a very high planar surface (2,630 m^2/g) (Stoller M. D., et. al., 2008), ultrahigh electron mobility (2,00,000 $cm^2\ V^{-1}S^{-1}$) (Bolotin K. I., et. al., 2008), superior thermal conductivity (about 5,000 W/m/K), (Balandin A. A., et. al., 2008), exceptional mechanical strength (Young's modulus, ~1,100 GPa) (Lee C., et. al., 2008), (Farazas A. A. M., et. al., 2018), and exceptional electronic characteristics (Timochenco V., et. al., 2018), (Arthi G., et. al., 2015).

GOs were synthesized chemically by applying various methods (Timochenco V., et. al., 2018), (Benzait Z., et. al., 2019). The most popular method for producing GOs was Hummer's method, where graphite powder was oxidized using $KMnO_4$ in the presence of $NaNO_3$ in H_2SO_4 in an ice bath (Offeman R. E., et. al., 1958), (Dimiev A. M., et. al., 2012). The most effective modification to this method was to eliminate the ice bath and remove $NaNO_3$, which increased the amount of $KMnO_4$. The reaction was conducted in a 9:1 mixture of H_2SO_4:H_3PO_4 to enhance the oxidation process and produce a significant amount of hydrophilic GO material. Since the temperature could be readily adjusted to produce a significant amount of GOs, this adjustment prevented the production of harmful gases (Marcano D. C, et. al., 2010), (Habte A. T., et. al., 2019). Due to its versatile properties, such as high mechanical strength, electrical conductivity, chemical properties, molecular barrier abilities, and optical properties of a single-layered 2-dimensional carbon sheet of sp^2 carbon atoms arranged in a honeycomb structure has gained a giant research interest (Kurian M., et. al., 2021). These synthesized GOs were also reduced to achieve rGO by applying plenty of physical and chemical methods (Ayele D. W., et.al., 2019) (Kurian M., et. al., 2021), (Zhi M., et. al., 2019). The hydrothermal method for the production of rGO at pH 11 using NaOH with stirring for 6.0 hrs. at 140 °C (Kurian M., et. al., 2021). Microwave conversion of GOs to rGO provides a fast and easy process for direct pristine graphene (Rahayu E. F., et. al., 2022).

rGO was considered a pivotal material in the realm of nanotechnology, characterized by its exceptional properties and diverse applications across various fields (Kar K. K., 2020). This unique derivative of graphene, a single layer of carbon atoms arranged in a two-dimensional honeycomb lattice, undergoes a process of reduction from GOs, enhancing its electrical conductivity and mechanical strength while preserving its remarkable flexibility and high surface area.

The formation of rGO involves a multi-step process, typically commencing with the oxidation of graphite flakes to produce GOs (Ghulam A. N., et. al., 2022), (Liu W., et. al., 2021). This precursor material exhibits abundant oxygen-containing functional groups such as hydroxyl, epoxy, and carboxyl groups, rendering it hydrophilic and facilitating its dispersion in various solvents. The subsequent reduction step involves the removal or reduction of these oxygen functionalities, leading to the restoration of sp^2 carbon networks akin to pristine graphene.

Reduction of GOs provides improvement of some physicochemical properties of rGO, aiming at some specific and sophisticated applications. Several methods were employed for the reduction of GOs, including thermal, chemical, and electrochemical approaches (Agarwal V., et. al., 2021). Thermal reduction methods involve annealing GOs at high temperatures under inert atmospheres or vacuum conditions to eliminate oxygen groups. Chemical reduction utilizes reducing agents such as hydrazine, hydroiodic acid, or various metal nanoparticles to achieve the reduction of GOs to rGO. Electrochemical reduction involves the use of an electric current to induce the reduction of GOs.

Applications of biomass rGO include bioengineering, electronics, nanotechnology, and other industries (Ansari M. Z., et. al., 2019), (Shubha P., et. al., 2018). The air annealing of GOs produced rGO with reduced and exfoliated pristine GOs into fluffy and wrinkled rGO, and the product also shows six times higher sorption capacity to remove the atmospheric pollutants than N_2 annealed rGO (Giang T. T., et. al., 2018). The thermal reduction of GOs plays an important role in the high purity of the product and the maximum exfoliation of GOs flakes, and the optimum temperature is 350 ^oC to obtain the maximum product without the least defects (Sengupta I., et. al., 2018).

The resulting rGO exhibits superior electrical conductivity, excellent mechanical properties, and high thermal stability, making it highly desirable for a myriad of applications (Yan J. X., et. al., 2019). In the field of electronics, rGO finds utilization in flexible and transparent conductive films, energy storage devices like supercapacitors and batteries, due to its high surface area, and as a promising material for next-generation sensors and actuators, owing to its sensitivity and responsiveness.

Moreover, in biomedical applications, rGO biocompatibility, large surface area, and ease of functionalization have garnered attention for drug delivery systems, bio-sensing platforms, and tissue engineering scaffolds (Papaefthymiou G., et. al., 2015). Additionally, its incorporation in composite materials enhances their mechanical strength (Wang J., et. al., 2020), thermal conductivity (Chen J., et. al., 2020), and electrical properties (Leow C., et. al., 2023), making rGO an attractive additive for enhancing the performance of polymers, ceramics, and metals. rGOs were prepared from GOs using green nontoxic chemical of caffeine, and the I_D/ I_G value of GOs was raised from 0.93 to 1.11 in FT-Raman analysis (Vu T. H. T., et. al., 2015). The versatility and promising characteristics of rGO continue to propel its exploration and adoption across various disciplines, fostering innovation and driving advancements in numerous technological domains. The synthesis, functionalization, and application potential of rGO remains boundless, offering a pathway to revolutionize diverse industries and pave the way for the next generation of advanced materials and composites (Tarcan R., et. al., 2020).

rGO was made composite with polyaniline (PANI) in-situ and ex-situ methods, and it was found that in-situ composites were more thermally stable, but had pore electrical conductivity (0.01 $S \cdot cm^{-1}$) compared to neat PANI (0.11 $S \cdot cm^{-1}$), but that in ex-situ PANI (280 $S \cdot cm^{-1}$). To stabilize the nanocomposite in dispersion, an emulsifier was effective (Bautkinová T, et. al., 2020). rGO was used as a material for the development of electrochemical sensors, and the sensors were utilized for sensing a huge number of chemicals in gas chromatographic analysis techniques (Rowley-Neale S. J., et. al., 2018). Though rGO properties resemble those of true graphene, it differs from the original in pore conductivity, defects, layers, electronic, and optoelectronic characteristics. The properties of rGO varied selectively in the degree of reduction in different techniques (Khan M. A., et. al., 2021). Cracks and wrinkles are frequently created during the transfer of graphene from one substrate to another, which lowers the product quality (Yang G., et. al., 2018).

Tannic acid stabilizes graphene, affecting concentration and exfoliation efficiency. It acts as a dispersant and regulator, forming uniformly integrated graphene polymer matrices for high-performance nanocomposites (Zhao S., et. al., 2018). Ascorbic acid-rGO contains 33% oxygen atomic percentage due to the removal of hydroxyl and epoxy groups at basal planes, while edge carbonyl groups contribute to a small extent. This reduces epoxy and hydroxyl functional groups, allowing better solution processing (De Silva K. K. H., et. al., 2018).

RGO was produced from coconut trash using a straightforward catalytic oxidation process utilizing ferrocene catalyst and was used as a high-performance electric double-layer capacitor with excellent cyclic stability (Tamilselvi R., et. al., 2020). Chitosan-graphene nanocomposites were synthesized using in situ chemical reduction of GO sheets with l-ascorbic acid, resulting in improved mechanical and electrical properties. These nanocomposites showed strong hydrogen bonding interactions with polyvinyl alcohol, making them potential drug delivery carriers (Cobos M., et. al., 2018). 100 ml of deionized water was mixed with 0.5 g of prepared GOs. 5.0 grams of ascorbic acid were added to the mixture, and while the temperature was kept at 60 ºC, the reaction was agitated at 600 rpm. The sample was filtered and cleaned with deionized water after 12 hours (Ali I., et. al., 2019), (Tewatia K., et. al., 2021), (Habte A. T., et. al., 2019). A significant waste product of the sugar production process, sugarcane bagasse, was subjected to green reduction of GOs to rGO. A promising adsorbent for the removal of methylene blue was rGO/bagasse (Gan L., et. al., 2019).

In another interesting study, sugarcane bagasse-rGO demonstrated good cyclic stability and conductivity and could be used to remove Cd(II) with an adsorption capacity of 24.47 mg/g (Li B., et. al., 2018). The lignin-rGO composite electrode, which was made using ascorbic acid and hydrazine, demonstrated a high capacitance of 90 F g^{-1} at 0.5 A g^{-1} and 133.9 F g^{-1} at 10 A g^{-1}, and it was able to maintain 86.5% of its specific capacitance even after 10,000 continuous cycles of galvanostatic charge/discharge (Ye W., et. al., 2017). The utilization of graphene and polypyrrole as the electrodes exploits the surface of graphene for charge storage while also facilitating oxidation and reduction reactions between the electrolyte and polypyrrole (Li Y, et. al., 2016). A 40% PPy content supercapacitor shows the best electrochemical performances, with a very large capacitance per weight (326 F g^{-1} at 0.5 A g^{-1} and 250 F g^{-1} at 2 A g^{-1}).

Recent advances in catalytic applications of GOs have led to the development of metal/metal oxide nanohybrids, metal-free catalysis, and electrocatalysis successfully achieved for green synthesis of different bioactive and other chemicals (Sachdeva H., et. al., 2020). Numerous heterogeneous catalytic systems, such as metal-free carbon nanomaterials including fullerene, carbon nanotubes (CNTs), graphite, graphene, and carbon nanodots, have been investigated for their potential as metal oxide supports or as effective carbocatalysts for a range of catalytic applications (Machado B. F., et. al., 2012), (Chen Q., et. al., 2019). rGO shows concentration-dependent effects on Escherichia coli. At high concentrations (200–400 μg/mL), rGO exhibits antibacterial activity, while lower concentrations (10–50 μg/mL) enhance bacterial growth. This growth may result from bacterial interactions with rGO, as evidenced by changes in surface chemistry, including C-N bond formation (Mann R., et. al., 2021), (Zhou Y., et. al., 2023). X-ray diffraction (XRD) analysis of thermally rGO (rGO) reveals significant structural transformations, particularly in the removal of oxygen functionalities and changes in crystallinity. Studies indicate that thermal reduction at temperatures ranging from 200 °C to 700 °C enhances the C/O atomic ratio, with values increasing from approximately 2.0 to 4.5, leading to a denser and more compact rGO structure (Torrisi L., et. al., 2023), (Ramamoorthy, et. al., 2021). The XRD patterns demonstrate a decrease in interlayer spacing, correlating with the reduction of oxygen-containing groups and the formation of a more graphitic structure (Priyadarshani M., et. al., 2024), (Singh P. K., 2023). Additionally, the analysis highlights the emergence of vacancy-type defects at higher temperatures, which can affect the material's electrical properties (Ramamoorthy H. et. al., 2021). Overall, XRD serves as a crucial tool in understanding the microstructural changes during the thermal reduction process (Afanas'ev V. P., et. al., 2020).

Transmission Electron Microscopy (TEM) has emerged as a pivotal technique for analyzing the thermal reduction of GOs, providing real-time insights into structural transformations. In-situ heating experiments reveal that as GOs is thermally treated, oxygen-containing functional groups are progressively removed, leading to the reordering of the graphitic structure, which is observable through Selected Area Electron Diffraction (SAED) patterns (Ceniceros-Reyes M. A., et. al., 2022). Additionally, studies on rGO-based platinum nanocatalysts demonstrate that the thermal stability of metal nanoparticles is enhanced on flat rGO surfaces, highlighting the importance of surface morphology during thermal processes (Ying Z., et. al., 2021). The combination of high-resolution TEM imaging and Electron Energy-Loss Spectroscopy (EELS)

allows for detailed tracking of functional group transformations and water desorption, providing a comprehensive understanding of GO's thermal behavior (Pelaez-Fernandez M., et. al., 2021). Furthermore, the impact of high-temperature treatments on microstructure and crystallinity has been confirmed through various characterization techniques, emphasizing the effectiveness of thermal reduction methods (Singh P. K., et. al., 2023). Lastly, Joule heating techniques have shown significant improvements in conductivity during the reduction process, indicating a highly localized reduction mechanism (Hettler S., et. al., 2021).

The thermal degradation of GOs is a function of temperature and the environment where the heating takes place. The optimum temperature for the thermal reduction of GOs is 350 °C, where the maximum possible reduction, carbon–oxygen ratio, and minimum lattice defect are achieved (Sengupta I., et. al., 2018). Some GOs samples can undergo explosive decomposition when heated slowly in an inert gas environment. This is due to the exothermicity of GOs reduction, which can cause a local temperature rise and thermal runaway reaction (Qiu Y, et. al., 2014). As GOs is heated, its oxygen functional groups decompose, releasing CO_2, H_2O, and CO. This process can begin at temperatures as low as 373 ^oK, but higher temperatures are required to remove more resistant groups (Menezes I. R., et. al., 2023), (Wang C., et. al., 2022).

Different reduction method produces different rGO with different defect densities, and hence their mechanisms also greatly differ depending on the reduction conditions. Two types of mechanisms were proposed depending on defect density. Reduction process releases only oxygen-containing functional groups, produces fewer defects in rGO, and in the case of destructive degradation, releases oxygen-containing groups along with parts of the carbon backbone in graphene, increasing the defects (Rosanna L., et. al., 2011). The long-term aging effect on GOs properties was studied, where GOs changed, with the C/O ratio rising from 1.96 to 2.76 and interlayer spacing decreasing from 0.660 to 0.567 nm due to desorption of oxygen groups. Defect density fell (I_D/I_G value increased from 0.87 to 0.92). Thermal decomposition showed a lower peak temperature (195 °C vs. 216 °C), with less CO, CO_2, and H_2O released, and activation energy decreased from 150 to 134 kJ/mol (Li C., et. al., 2021). This study uses in-situ thermal TEM to analyze GOs reduction, examining the transformations of oxygen functional groups, water desorption, and graphitization from 70 to 1200 °C. Combining HRTEM and EELS, it is a model for water and oxygen group removal, providing insights into GO’s thermal behavior relevant to its application stability under heat (Hettler S., et. al., 2021).

Graphene materials show antimicrobial activities, and as rGO contains some different oxygen functional groups so it also possesses some of these properties. Graphene-based materials exhibit varying antibacterial effects against *E. coli,* with GO being most effective. Antimicrobial mechanisms include membrane disruption by nanosheets and oxidative stress. Optimizing graphene's properties can enhance its antibacterial activity while mitigating environmental impacts (Liu S., et. al., 2011).

The microbiological effects of rGO on Escherichia coli. At high concentrations (200 and 400 μg/mL), rGO showed antibacterial activity, but at lower concentrations (10 and 50 μg/mL), it enhanced bacterial growth. X-ray photoelectron spectroscopy indicated changes in the rGO surface, suggesting possible interactions with bacterial cell components. These findings highlight the concentration-dependent effects of rGO, influencing both antibacterial applications and environmental impact (Mann R., et. al., 2021). Bio-reduced GOs (B-rGO) showed strong antibacterial activity against E. coli, evidenced by high LDH release, ROS levels, and morphological damage observed via SEM. Despite these effects, its antibacterial performance was inferior to commercial rGO. B-rGO's potential for environmental remediation is promising (Zhou Y., et. al., 2023).

Graphene-based materials, with unique properties, show promise as antibacterial agents. This review highlights advancements in functionalization, biosafety concerns, and the need for deeper research into mechanisms and effectiveness (Kumar P., et. al., 2019). GOs nanosheets exhibit significant antimicrobial activity against multidrug-resistant (MDR) Gram-negative and Gram-positive hospital superbugs such as *E. coli*, *K. pneumoniae*, and *S. aureus*. GO's bactericidal effect. It outperforms commonly used antibiotics and shows promise for future antibacterial applications. GOs disrupt bacterial cell walls, dissolve genomes, and prevent biofilm formation on medical implants, highlighting its potential for antibiofilm surface coatings in healthcare to combat implant-related infections (Aunkor M. T. H., et. al., 2020). At relatively high concentrations (200 and 400 μg/mL), rGO exhibited antibacterial activity on the model bacterium *Escherichia coli*, while at lower concentrations (10 and 50 μg/mL), interestingly, no antibacterial effect was observed. Increasing the concentration to 200 μg/mL, rGO saw a ~50% less viable cells after 3 h, and only about a third of the cells were viable in the 400 μg/mL rGO system. The results indicate the antibacterial effect at the higher rGO concentration exposures (Mann R., et. al., 2021).

3.2. Materials and methods

3.2.1. Materials

The materials and methods used for the experiment are-

3.2.1.1. Materials used for thermal reduction of GOs to rGOs

The chemicals used to perform this experiment were collected from the following sources: Extra pure graphite fine powder of purity 98% with particle size 60 mesh was collected from Loba Chemie Pvt. Ltd., Mumbai, India; reagent grade ascorbic acid with purity 98%, potassium permanganate with purity 99.8%, AR grade sulfuric acid with purity 97%, reagent grade Hydrochloric acid with purity 37%, and AR grade hydrogen peroxide with purity 35% were from Merck KGaA, Darmstadt, Germany; AR grade orthophosphoric acid with purity 85% from Active Fine Chemicals Ltd., Dhaka, Bangladesh; locally available commercial Kerosene from Meghna Petroleum Pvt. Ltd. Bangladesh were redistilled before use.

3.2.1.2. Materials used for the antimicrobial activity study of rGOs

In vitro antibacterial activity was assessed using the agar-well diffusion method. Briefly, 20 ml of sterile Mueller-Hinton Agar (MHA) was poured into Petri dishes and allowed to solidify. A 50 µl aliquot of freshly cultured bacterial suspensions (approximately 105cells/100ml, OD600 = 0.05) was then evenly spread across the agar surface. Using a sterile cork borer, wells measuring 6 mm in diameter were created on the agar surface. Subsequently, 100 µl of 4 differently concentrated sample solutions (0.5, 1.0, 2.5, and 5.0 mg/ml) were added to the wells. A tetracycline solution (Sigma, USA) at a concentration of 0.5 mg/ml in 10% DMSO (w/v) served as a positive control, while a solution of 10% DMSO alone was used as the negative control.

3.2.2. Methods

The major instrumental and experimental methods used for the conduction of the research are described below-

3.2.2.0. Instrumental methods for the analysis of rGOs

3.2.2.1. Simultaneous thermal analysis (STA)

The GOs and rGO samples underwent STA analysis to understand their thermal properties. The STA analysis was carried out in a STA analyzer (Simultaneous Thermal Analyzer, Beand-Netzsch, Model-Jupiter F3, Germany) from 30-900 ^{o}C. A 3-5 mg sample was placed in the sample carrier of the instrument and heated up at the rate of 10 ^{o}C/minute in a Nitrogen atmosphere. The mass loss, i.e., TGA, along with DSC/DTA data, was recorded with temperature in a graph.

3.2.2.2. Measurements of thermal properties with thermogravimetric analyzer (TGA)

The thermal properties of GOs and rGO were determined using a Thermogravimetric analyzer (TGA, Brand: PerkinElmer, Model: Syntrea). Approximately 2.3 mg of the samples was loaded into a Platinum crucible and then hung in the balance ring. The samples were subjected to heating from RT - 850 ^{o}C at a rate of 10 °C per minute with a nitrogen gas flow of 40mL/minute, and the resulting mass loss was recorded as Tg-curve against Temperature.

3.2.2.3. FT-IR spectroscopic analysis

The detailed description of this instrument, including operating conditions of the samples are same as the instrumental method described in Chapter 2 (section 2.2.2.4)

3.2.2.4. FT-Raman spectroscopic analysis

The detailed description of this instrument, including the operating condition of the samples are same as the instrumental method described in Chapter 2 (section 2.2.2.5)

3.2.2.5. X-Ray photoelectron spectroscopy (XPS) analysis

The detailed description of this instrument, including the operating condition of the synthesized GOs samples are same as the instrumental method described in Chapter 2 (section 2.2.2.9)

3.2.2.6. X-Ray diffraction (XRD) analysis

The structural characterization of the Gf, prepared GOs, and different rGOs was carried out by X-Ray Diffraction (XRD) Analysis. XRD works on the principle of Bragg's equation, which can be described in terms of the reflection of a collimated X-ray beam incident on a crystal plane of the sample to be characterized. A beam of X-rays is passed through the specimen and is scattered, or diffracted, by the atoms in the path of the X-rays. A small amount of sample was vacuum dried and ground using a mortar to achieve a homogeneous fine powder. The powder sample was placed in the sample holder and pressed to obtain a smooth surface. To ensure the compactness and smoothness of the sample surfaces. The X-ray diffraction analysis of the samples was measured using an XRD (XRD, Rigaku, Japan) instrument. Well-dried powdered samples were mounted on the sample holder and the sample surface so that the surface became smooth and evenly distributed. Then the sample was placed on the instrument and started to measure the X-ray diffraction value in 2θ was measured. The sample was run to obtain values from 5^{o} to 90^{o} at the rate of 3^{o}/min, and the XRD data obtained were recorded and analyzed.

3.2.2.7. Measurements of the surface area and pore size distribution using the BET analyzer

The specific surface area of the prepared rGO-K220 and rGO-KAA was determined with the aid of a BET (Brunauer–Emmett–Teller) Sorptometer (Porous Materials Incorporation, USA). 0.4066 g sample was placed in a vacuum dryer under 20 microns vacuum at 130 ^{o}C then, then nitrogen gas flow was passed through the sample holder, and the absorbed gas amount. Pore size distribution was estimated using the Barrett–Joyner–Halenda (BJH) method. The micro-pore surface area values were estimated using the t-plot method.

3.2.2.8. Image analysis using SEM-EDX

The detailed description of this instrument, including the operating conditions of the synthesized rGO samples are same as the instrumental method described in Chapter 2 (section 2.2.2.8).

3.2.2.9. Antibacterial activity test

The antibacterial activity was evaluated using 2 Gram-positive bacteria (Bacillus subtilis ATCC 11774 and Staphylococcus aureus ATCC 9144) and 2 Gram-negative bacteria (Escherichia coli ATCC 11303 and Salmonella typhi ATCC 1331).

3.2.3.0. Experimental methods for the analysis of rGOs

3.2.3.1. Synthesis of GOs from graphite following FAL recycling technique

GOs were synthesized from GP with higher oxygen to carbon ratios using modified Hummer's method, especially modified by Tour, called Tour's method. In this method, GP was first purified by treating it using 5% Hydrochloric acid solution at 98 ºC for one hour. After washing and drying under vacuum, the GP was oxidized using $KMnO_4$ in feed acid liquor (FAL), which was a mixture of Conc. Sulphuric acid and Conc. Phosphoric acid at a ratio of 90:10. A series of products were prepared by recycling and reusing the FAL at the optimized reaction conditions, and the synthesis procedure was fully described in the article (Hoque M. A., et. al., 2024) (Xu C., et. al., 2015). The temperature and time of reaction were maintained according to the optimized conditions of 70 ºC for 14 hours.

Table-3.1: Synthesis of GOs from graphite following modified Tour's method, adding the recycling and reusing the feed acid liquor at a temperature of 70 ºC for 14 hours.

Experiments No.	Graphite (g)	$KMnO_4$ (g)	Product GOs (g)
Run-1	20.0022	120.0011	16.9485
Run-2	20.0012	120.0026	16.9109
Run-3	20.0015	120.0038	16.8901

3.2.3.2. Evaluation of thermal properties to find suitable reduction conditions of GOs

Synthesized GO samples were first subjected to Simultaneous Thermal Analysis (STA) (Figure 3 .1) to evaluate their degradation pattern of the product. From the thermogram, it is observed that the GOs are stable below 75 ºC and beyond this temperature, a slow and uniform rate of mass loss starts. Then a vigorous mass-loss was observed around 193 ºC. Up to the slow degradation, total mass losses were about 19%, but at 193.4 ºC the GOs degraded vigorously with an explosion and showed a sharp mass loss of about 73% showing an exothermic enthalpy change. After that, the product remains stable up to 450 ºC, and at 474.8 ºC, another exothermic degradation was observed with mass loss of about 8%.

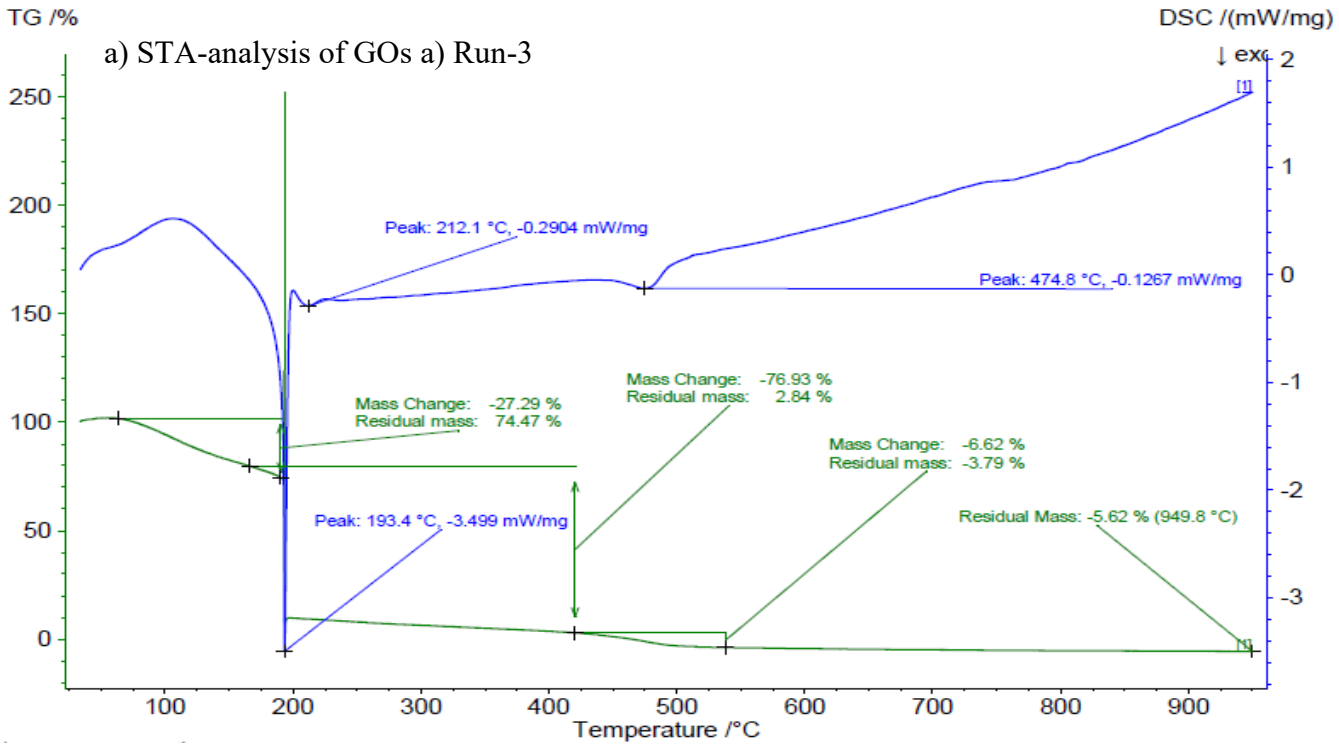

Figure-3.1: Simultaneous thermal analysis (STA) of the GOs product of a) Run-3.

3.2.3.3. Thermal reduction of GOs to rGO in water at 95-98 °C

From the STA degradation study of the products, it was found that the GOs start to degrade over 80 °C. So, to investigate the lower temperature thermal degradation, the products were heated in a lower boiling solvent, water, for several days. The degradation reactions were carried out on GOs at different time intervals. At first, the GOs were Softly Thermal Treatment (STT) at 95-98 °C for a short time (St) = 48 hours and then for long time (Lt) = 96 hours' periods, and the products obtained are Softly reduced rGO (Figure 3.2). To perform these operations, about 2.00 g of GOs were treated with STT-St and STT-Lt. The products were then cooled to room temperature, centrifuged at 10,000 rpm for 30 minutes, and fridge dried to obtain finished partially rGOs rGO-W48 and rGO-W96. The mass losses obtained from the STT reduction of the rGO are shown in Table 3.2.

Table-3.2: Lower temperature reduction of GOs in water medium

Exp. ID	Sample ID	Graphite (g)	Initial XPS C:O_2 ratio	Reaction temp. (°C)	Reaction time (hrs.)	Product (g)	Product Yield (%)	Expected C:O_2 ratio
STT-St	rGO-W48	2.0023	59.97:40.03	95-98	48	1.6958	84.69	70.81:29.19
STT-Lt	rGO-W96	2.0027	59.97:40.03	95-98	96	1.5517	77.48	77.40:22.60

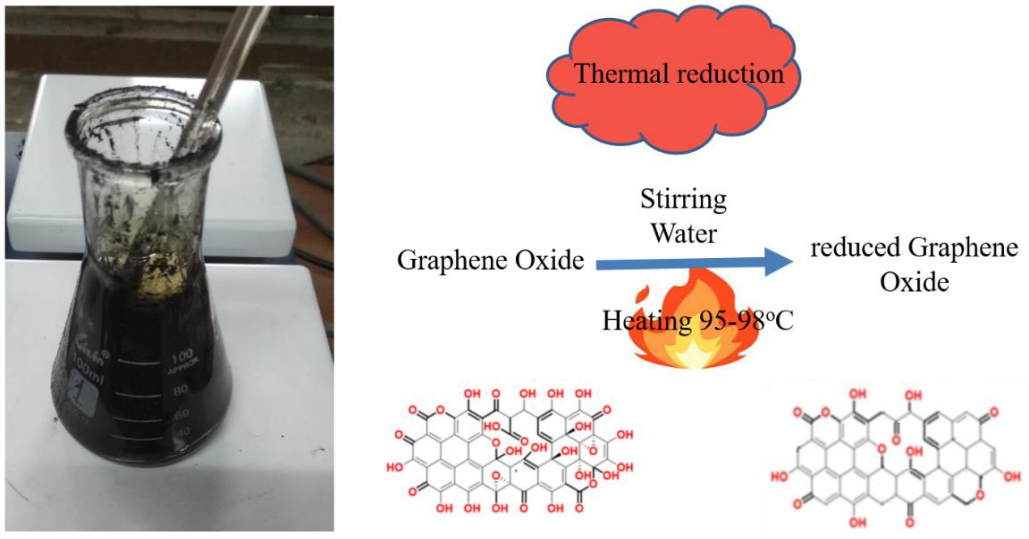

Figure-3.2: Lower temperature thermal degradation of GOs in water medium for several days.

3.2.3.4. Thermal reduction of GOs to rGO in the kerosene medium

Considering the thermal degradation pattern in STA analysis from Figure 3.1, an inert solvent of a higher boiling point was selected as a hard thermal treatment (HTT) medium is Kerosene. This mixture of hydrocarbon solvents possesses higher temperature boiling fractions from 150-300 ºC. From this wide range of boiling fractions, a selective boiling fraction range was collected by fractional distillation.

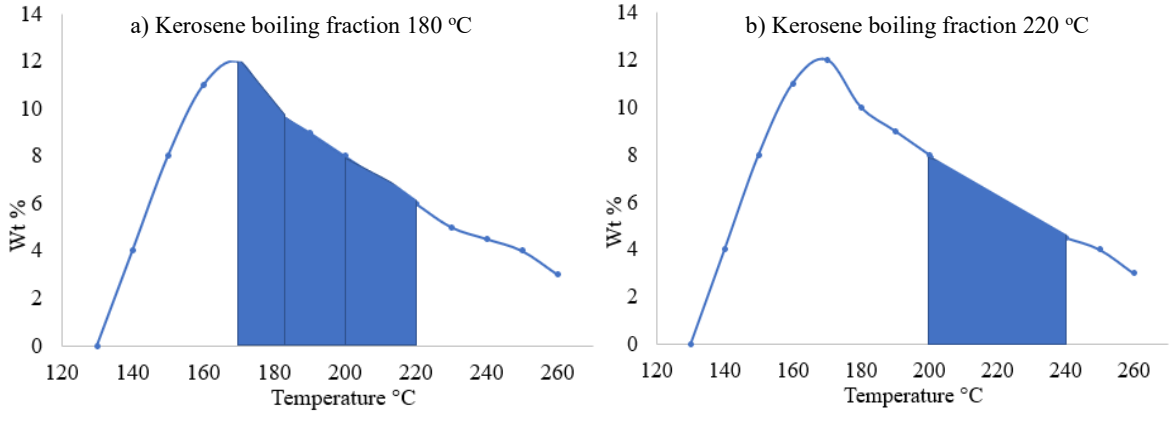

Figure-3.3: The fractional distribution of kerosene solvent at different boiling temperature ranges, and the portion (marked as blue) was selected as a suitable solvent for thermal reduction of GOs. a) Kerosene boiling fraction for 180 ºC fraction 170-220 ºC was collected. b) Kerosene boiling fraction for 220 ºC fraction 200-240 ºC was collected.

To maintain the reflux bath at a lower temperature (LT), were chosen below 180 ºC and for Higher Temperature (HT) were chosen 220 ºC. To ensure LT, the solvent Kerosene distilled fractions between 170-220 ºC (Figure-3.3a) were collected, and for the HT fractions between 200-240 ºC (Figure-3.3b) were collected. Figure 3.3 (a) and (b) shows the selective fractional distillation of Kerosene for temperatures of 180 ºC and 220 ºC. The HTT operation was carried out on GOs for 1.0 hour only.

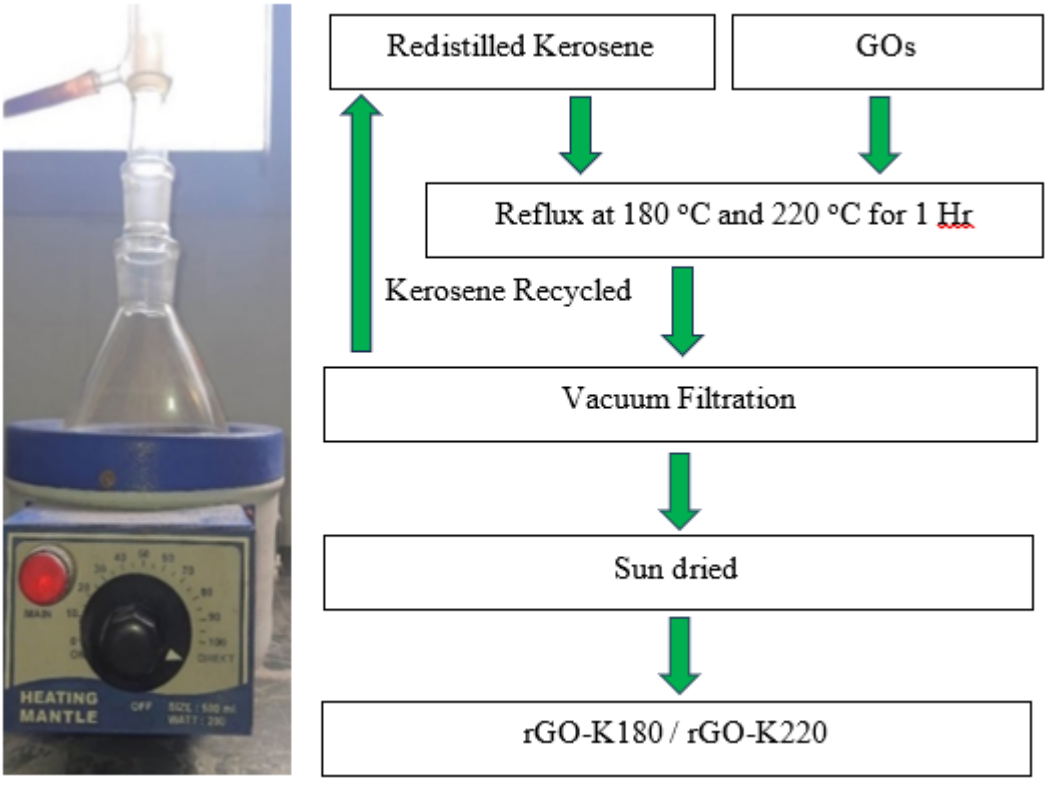

Figure-3.4: High temperature thermal treatment of GOs at 180 ºC and 220 ºC in Kerosene for 1.0 hour.

Figure 3.4 illustrates the higher temperature thermal degradation in inert solvent media, which were collected for the thermal degradation of GOs to highly rGO. For conducting the HTT-LT operation, about 2.0 g GOs were refluxed under 200 mL of redistilled kerosene in a round-bottom reflux and heated in a heating mental. After 1 hr. thermal treatment, the reaction mass was cooled to room temperature, vacuum filtered, and sun dried for several hrs. to remove traces of Kerosene to obtain the product rGO-K180.

In the same way, the HTT-HT operation, also carried out on a 2.0 g GOs sample, was refluxed under 200 mL of redistilled kerosene in a round-bottom reflux and heated in a heating mental. After 1 hr. thermal treatment, the reaction mass was cooled to room temperature, vacuum filtered, and sun dried for several hrs. to remove excess kerosene to obtain the product rGO-K220. The mass losses obtained from the higher temperature thermal degradation of the products, GOs to rGO were recorded in Table 3.3.

Table-3.3: High temperature reduction of GOs at different time periods

Exp. ID	Product ID	Graphite (g)	Initial XPS $C:O_2$ ratio	Reaction Temp. (ºC)	Reaction time (hrs.)	Product rGO (g)	Product Yield (%)	Expected $C:O_2$ ratio
HTT-LT	rGO-K180	2.0014	59.97:40.03	180	1.0	1.3791	68.91	87.03:12.97
HTT-HT	rGO-K220	2.0032	59.97:40.03	220	1.0	1.2842	64.11	93.54:6.46

3.2.3.5. Extreme reduction of GOs to rGO using a two-step reduction

Figure 3.5 illustrates the higher temperature thermal degradation of GOs to obtain extremely rGO. At first, GOs underwent HTT-HT according to the procedure described in Figure 3.4.

Then, after removing kerosene, the product was again treated with ascorbic acid in a water medium. The RB flask was again charged with rGO-K220 and ascorbic acid, maintaining the ratio about 1:1, and then 100 mL DI water was added, shaken vigorously, and refluxed for 4.0 hours. After reduction, the products were washed 8-10 times with distilled water followed by centrifugation to remove all the chemical remains in it, and then were fridge dried to obtain extremely rGO and termed as rGO-KAA.

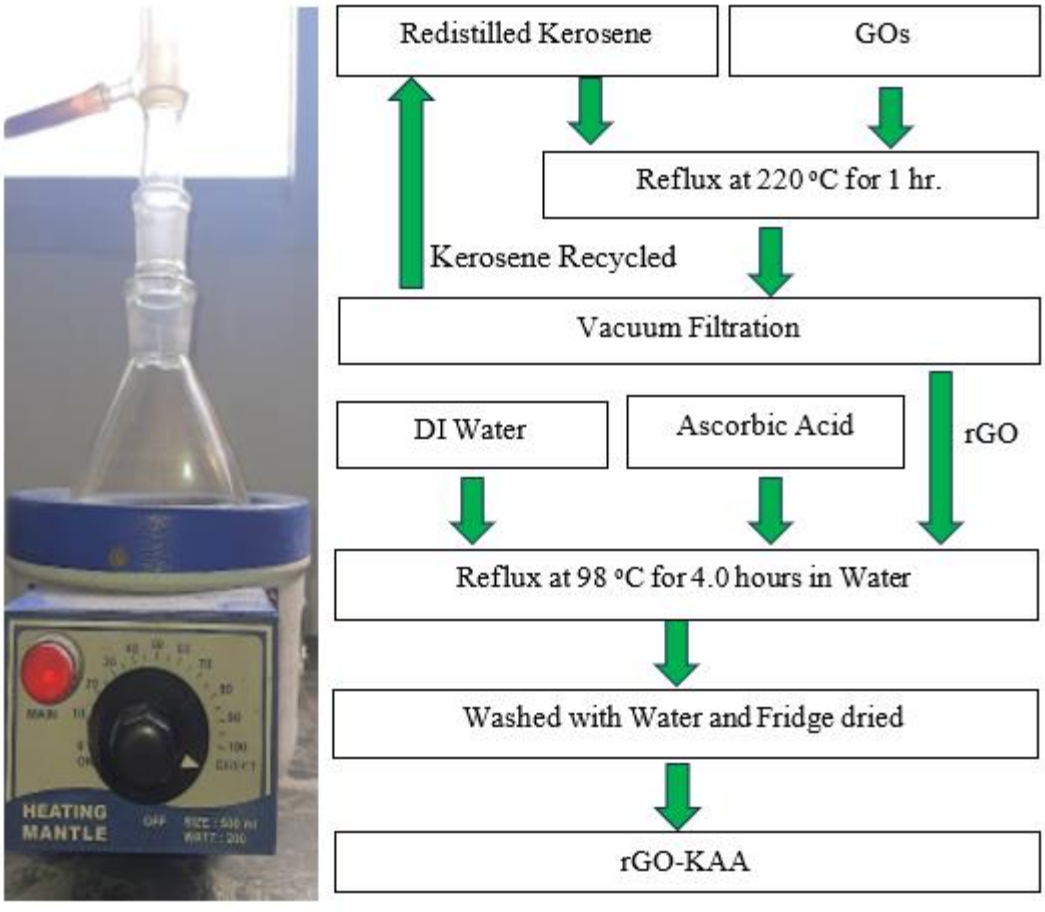

Figure-3.5: Extreme reduction of GOs by higher temperature thermal degradation, and then with ascorbic acid in water.

Table-3.4: Extreme reduction of GOs by the double reduction system.

Experiments ID	GOs (g)	Initial XPS C:O_2 ratio	Ascorbic acid (g)	Reaction Time (hrs.)	Reaction Temp. (°C)	Product (g)	Product Yield (%)	Expected C:O_2 ratio
rGO-KAA1	2.0029	59.97:40.03	2.0028	1 + 4	220 & 98	1.2217	60.99	98.32:1.68
rGO-KAA2	2.0024		2.0022	1 + 4	220 & 98	1.2199	60.92	98.44:1.56

The above two samples produced a similar percentage of products, so they were mixed for characterization and named as rGO-KAA.

3.2.3.6. Antibacterial activity assessment of rGO-K220 and rGO-KAA

In vitro antibacterial activity was assessed using the agar-well diffusion method. Briefly, 20 ml of sterile Mueller-Hinton Agar (MHA) was poured into Petri dishes and allowed to solidify. A 50 µL aliquot of freshly cultured bacterial suspension (approximately 10^5 cells/100 mL, OD600 = 0.05) was then evenly spread across the agar surface. Using a sterile cork borer, wells measuring 6 mm in diameter were created on the agar surface. Subsequently, 100 µL of four differently concentrated sample solutions (0.5, 1.0, 2.5, and 5.0 mg/mL) were added to the wells. A tetracycline solution (Sigma, USA) at a concentration of 0.5 mg/ml in 10% DMSO (w/v) served as a positive control, while a solution of 10% DMSO alone was used as the negative control. The plates were incubated for 24 hours at 37 °C, after which the zones of inhibition were measured in millimeters. Each experiment was conducted in triplicate for both the rGO dispersions and controls, with results reported as mean ± standard deviation (SD).

3.3. Results and discussion

3.3.1. Effect of different thermal reduction procedure

The GOs were synthesized following Tour's method, where the reaction conditions were maintained at 70 ^{o}C for 12 hours provides which was the optimized reaction condition (Hoque MA, 2024). All the products GOs were produced in similar yields between 168.5-169.5% and all of them are hydrophilic in nature (table-1). The product's uniformity was assured by controlling the reaction conditions by applying the feed acid liquor recycling technique. So, all the products were mixed, named as GOs, and used as a feed material for different reduction experiments. In case of STT-St operation, the product rGO-W48 yield was 87.24% but in STT-Lt the product rGO-W96 yield was 79.53%. So, the thermal reduction in water degradation increases with time with retaining their hydrophilic properties due to the polar medium. In the case of HTT-ST, the product rGO-K180 yield was 70.53% in 1.0 hour, but in HTT-LT, the product rGO-K220 was 65.51% in 1.0 hour.

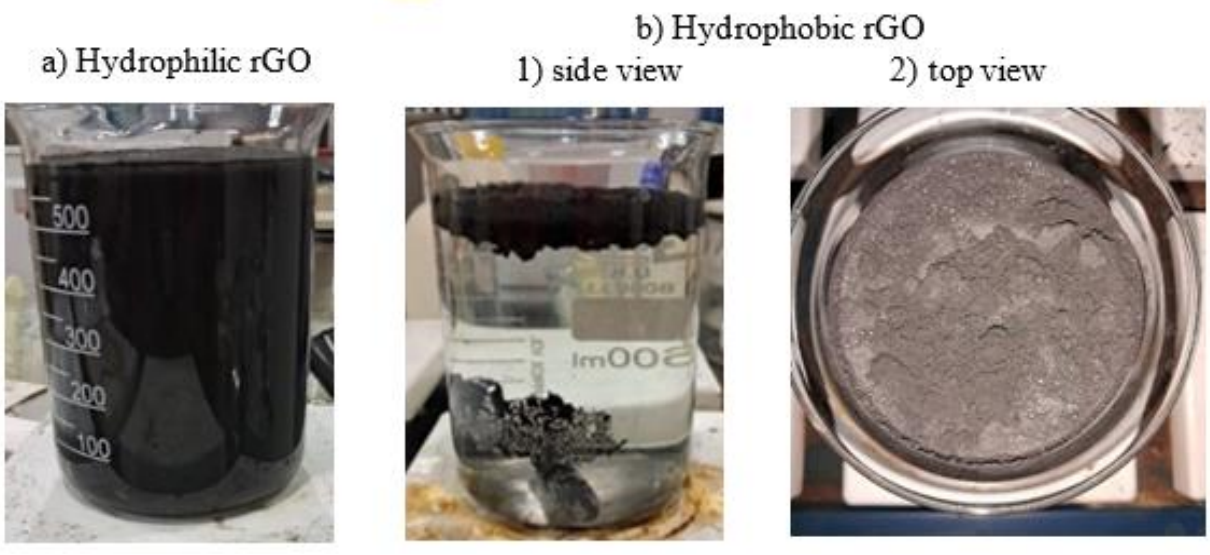

Figure-3.6: a) Hydrophilic rGO and b) Hydrophobic rGO [1) side view, 2) top view]

So, the thermal reduction in Kerosene degradation increases with temperature. The hydrophilic nature of the kerosene-reduced rGO was converted to hydrophobic due to the removal of plenty of oxygen-containing groups on the surface. As it was not removed completely, it was soaked after prolonged exposure to water.

In case of extreme reduction of GOs, the products were thermally treated in two different methods in two stages consecutively to have the extremely reduced GOs product rGO-KAA, and the product yield was 60.95%. The thermal treatment with Kerosene converts the product to a hydrophobic character from hydrophilic, but due to the Ascorbic Acid treatment, it becomes hydrophilic again. Figure 3.6 shows the hydrophilic and hydrophobic nature of rGO (Faisal S, et. al., 2023).

3.3.2. Characterization of synthesized rGOs

The characterization of thermally and thermos-chemically reduced rGO was carried out using the following state-of-the-art instruments-

3.3.2.1. FT-IR spectroscopic analysis

The Fourier-transform infrared (FT-IR) spectra were recorded for synthesized GOs and rGOs obtained under different soft thermal treatment (STT) and hardly thermal treatment (HTT) conditions, as well as various reduction parameters, including time, temperature, and medium variations. The FT-IR analysis revealed significant variations in the absorption spectra, highlighting the chemical transformations of functional groups during the reduction processes. As shown in Figure 3.7, fresh GOs exhibited a broad and intense absorption peak within the range of 3175–3530 cm^{-1}, corresponding to hydroxyl (-OH) functional groups (Xu C, et. al., 2015) (Xu C, 2015) (Khalili D., et. al., 2016) (Khalili D., 2016) (Faniyi IO, et. al., 2019) (Faniyi IO, 2019). These groups are characteristic of functionalized hydroxyl moieties introduced during the oxidation process. However, upon thermal treatment for reduction, the hydroxyl absorption peak diminished progressively. Specifically, under STT conditions, prolonged exposure to heat resulted in a gradual disappearance of this peak, whereas at HTT conditions, the peak was nearly eliminated, reflecting the removal of hydroxyl groups. Additionally, a sharp absorption peak observed around 1704–1720 cm^{-1} was attributed to carboxyl (>C=O) functional groups, while another prominent peak at 1591–1620 cm^{-1} corresponded to the stretching and bending vibrations of conjugated carbon-carbon double bonds (C=C). These two peaks demonstrated high thermal stability, as they persisted under STT conditions even after extended heating durations, although significant reductions in intensity were observed under HTT, with the carboxyl peak almost completely removed. Two shorter absorption peaks, identified at approximately 1354–1394 cm^{-1} and 1237–1262 cm^{-1}, corresponded to etheric oxygen (C-O-C) and hydroxyl (-OH) stretching modes, respectively. These peaks also showed

tendencies to diminish during prolonged heating, particularly under HTT. The etheric oxygen peak, in particular, became undetectable under high-temperature conditions, indicating the loss of oxygen functionalities. Furthermore, a sharp and intense absorption peak located around 1048–1057 cm^{-1} was attributed to the vibrational modes of the C–O bond. This peak exhibited notable reductions in intensity with increasing temperature or extended heating duration, though it was not eliminated under STT conditions, suggesting some structural resistance. Continuous heating of the GOs led to a gradual decrease in the intensity of all oxygen-associated functional groups, confirming their thermal instability. Notably, the peaks at 3175–3230 cm^{-1} and 1048–1057 cm^{-1} diminished more rapidly compared to others, indicating that hydroxyl (-OH) groups are particularly susceptible to thermal decomposition, even at lower temperatures, likely due to the weaker bond formation between hydroxyl groups and the graphenized carboxylic carbon atoms. The next weakest groups, namely ketone (>C=O) and epoxy (=C–O–C=) bonds, also displayed tendencies to disappear during prolonged heating at lower temperatures, with complete removal observed under HTT. The products obtained under HTT conditions exhibited a dramatically altered spectral pattern, with most oxygen functionalities removed. Specifically, the broad absorption peak for hydroxyl groups at 3175–3230 cm^{-1} shifted to 3400–3550 cm^{-1}, reflecting changes in the remaining hydroxyl groups. The sharp carboxyl absorption peak at 1704–1720 cm^{-1} was eliminated under HTT, indicating complete decarboxylation. Meanwhile, the C=C peak at 1591–1620 cm^{-1} shifted to approximately 1650 cm^{-1} and became shorter and sharper, suggesting structural modifications in the graphene lattice. Another significant change was observed in the C–O absorption peak, which shifted from 1050 cm^{-1} to 1150 cm^{-1} and transformed into a sharper peak, indicative of a new vibrational mode or structural rearrangement. Other spectral peaks, including those corresponding to etheric oxygen (C-O-C) and hydroxyl (-OH) bonds, were absent under HTT conditions, confirming their complete thermal decomposition. These findings reveal that HTT induces more extensive reduction and structural transformation than STT, resulting in rGO with minimal oxygen-containing groups. The progressive reduction of functional groups observed in FT-IR spectra provides insights into the thermal stability and reduction pathways of GOs. Hydroxyl (-OH) and C–O groups exhibited the highest susceptibility to thermal degradation, while carboxyl (>C=O) and epoxy (=C-O-C=) groups demonstrated greater stability under moderate thermal conditions but were eventually removed at higher temperatures. Comparative analysis of STT and HTT products revealed similar trends in the reduction of oxygen-containing groups, albeit with varying extents of transformation. Under HTT conditions, the

majority of functional groups were removed, and the resulting rGO exhibited sharper and more defined spectral features, indicative of a more graphenized structure. This analysis highlights the importance of optimizing thermal reduction parameters to achieve the desired balance between the removal of oxygen functionalities and the preservation of graphene's structural integrity, offering valuable insights for tailoring rGO for specific applications in areas such as energy storage, catalysis, and electronics. These observations are consistent with previous studies on the thermal reduction of GOs, which also reported the removal of hydroxyl, carboxyl, and etheric oxygen groups at elevated temperatures (Ickecan D., et. al., 2017), (Gensheimer J., et. al., 2015), (Jiao X, et. al., 2017). Furthermore, the results confirm that chemically converted GOs produced under different conditions share similar spectral characteristics, underscoring the reproducibility and scalability of the reduction process for rGO synthesis. By systematically analyzing the FT-IR spectra, this study provides a comprehensive understanding of the chemical transformations and thermal stability of GOs under varying treatment conditions, contributing to the broader field of graphene-based material research.

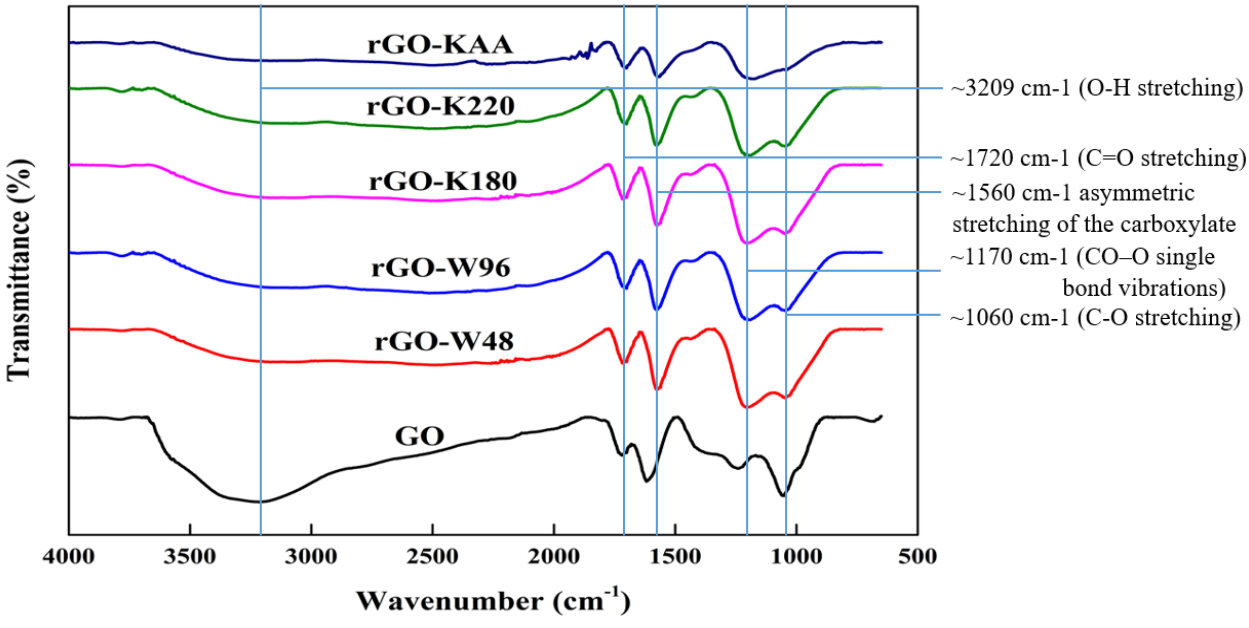

Figure-3.7: FT-IR spectral analysis of the products GOs and different rGO obtained by different thermal reductions with various conditions: (a) Fresh GOs, (b) rGO-W48, (c) rGO-W96, (d) rGO-K180, (e) rGO-K220, and (f) rGO-KAA.

The effect of continuous heating of the GOs results in all the oxygen-associated functional groups tending to decrease gradually with time. Especially, the peaks at 3175–3230 cm^{-1} and 1048–1057 cm^{-1} tend to disappear faster than the other peaks, which means a typical form of

functionalized hydroxyl (-OH) groups is very weak to split rapidly even at STT heating due to weaker bond formation with graphenized carboxylic carbon atom. Then other weaker bones in GOs are ketone >(C=O) and epoxy >c^Oc< oxygen bond, which also has a tendency to show disappearance on longer time, lower temperature heating. Similarly, at the HTT operation, the products were completely changed, and the products showed a similar type of spectral pattern in Figure 3.7. A broad absorption peak at 3175–3230 cm^{-1} corresponding to different functionalized hydroxyl (-OH) groups changes shifted to 3400-3550 cm^{-1}. A sharp absorption peak at around 1704–1720 cm^{-1}, which is attributed to the formation of carboxyl groups (>C=O), was completely removed. But another peak at 1591–1620 cm^{-1} was shifted to 1650 cm^{-1} and changed to a shorter and sharper peak. Another significant change in the absorption peak at 1050 cm^{-1} was shifted to 1150 $cm^{-1,}$ and a change to a sharp peak also. Other spectral peaks were completely disappeared in all cases. From this analysis, it can be concluded that different forms of chemically converted GOs were produced, similar to types of rGO.

3.3.2.2. FT-Raman spectroscopic analysis

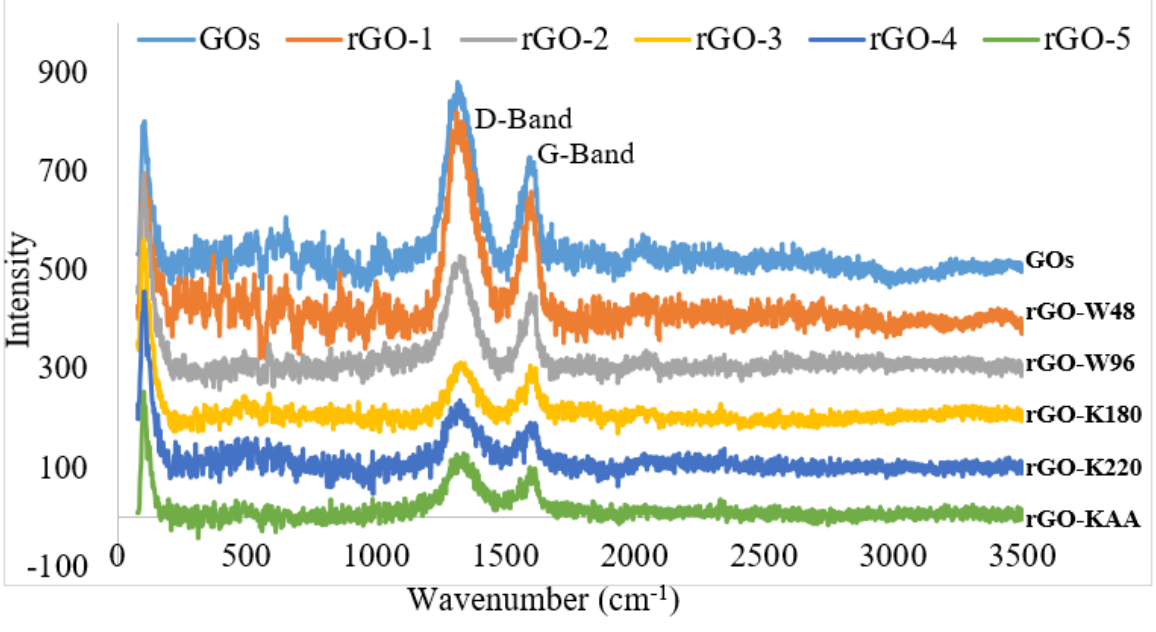

Figure-3.8: FT-Raman spectrum of GO and different rGOs.

The reduced rGO samples were characterized using FT-Raman spectroscopy (Figure 3.8), revealing two prominent bands in the spectra, located at approximately 1345 cm^{-1} and 1605 cm^{-1}. The band at ~1345 cm^{-1}, referred to as the D band, originates from structural defects and imperfections, including graphitic edges and disordered carbon structures. Conversely, the band

at ~1605 cm^{-1}, known as the G band, is associated with the in-plane vibrational modes of sp^2-hybridized carbon atoms within the graphite lattice. Together, these bands serve as critical indicators of the structural integrity and composition of the material. The intensity ratio of the G band to the D band (I_G/I_D) provides valuable insights into the degree of structural order in the rGO samples. This ratio varies substantially with the extent of reduction, offering a measure of changes in defect density and the re-establishment of graphitic domains. Specifically, higher (I_G/I_D) values indicate an enhanced graphitic order, which is typically attributed to the removal of oxygen-containing functional groups and the repair of structural defects during the reduction process. In contrast, lower I_G/I_D values signify a higher degree of disorder, reflecting increased defect density or incomplete restoration of graphitic regions (David L. D., et. al., 2017). Analyzing the spectral features and the I_G/I_D ratio enables a comprehensive understanding of the reduction process and its impact on the structural evolution of rGO. This approach provides crucial insights into the relationship between the chemical and structural properties of rGO, facilitating its optimization for specific applications. Such characterizations are essential for tailoring the material properties to meet the demands of various advanced technologies, including energy storage, catalysis, and environmental remediation. The detailed analysis of Raman spectra thus plays a pivotal role in understanding and improving the performance of rGO-based systems (Farah S., et. al., 2020).

3.3.2.3. Thermogravimetric analysis (TGA)

Figure-3.9. shows the thermogravimetric analysis (TGA) graph of all the synthesized products as GOs, rGO-W48, rGO-W96, rGO-K180, rGO-K220, and rGO-KAA. TGA graph of pure GOs shows a steady mass loss of GOs with the increase in temperature up to 200 ºC. Total mass loss at this point is about 25%. At 200 ºC, a sudden sharp fall of the graph with an upward notch indicates the explosive degradation of the GOs and the mass loss of about 60%. As the synthesized GOs contain a higher percentage of Oxygen and at higher temperatures, this Oxygen influences the graphenized carbon to degrade explosively. The rest 5% graphitic carbon degrades steady state way up to the temperature 600 ºC, and at 850 ºC, the incombustible matter content up to 850 ºC was about 1.475% (Feng H., et. al., 2013), (Machado P. B., et. al., 2024).

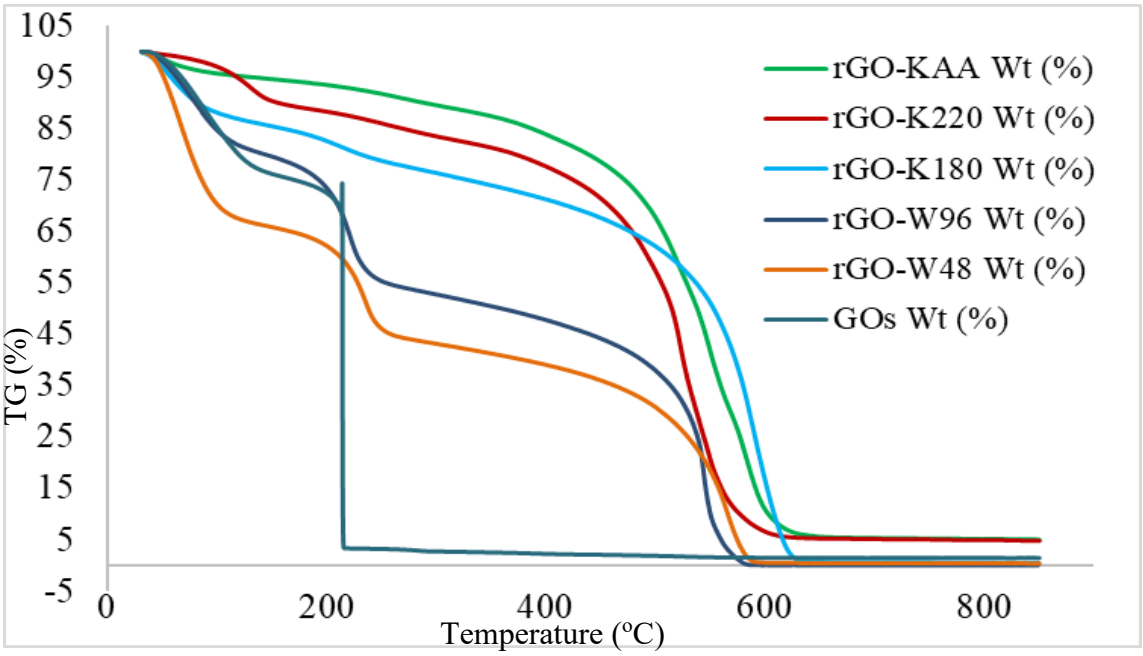

Figure-3.9: The thermogravimetric analysis (TGA) of synthesized GOs and five rGO samples.

In the case of rGO-W48, the initial mass loss pattern was similar to GOs, but the loss rate and percentage were increased to about 35%. This is because of the conversion of some carbonyl (>C=O) or epoxy (C-O-C) groups to hydroxyl groups, which tends to degrade rapidly, and the phenomenon was also observed and supported by FT-IR analysis. Then another mass loss is observed about 20% between 215-250 °C, which was supposed to be -O- and -OH functionalized graphene. The rest 40% mass, which was supposed to be graphenized carbon and was stable up to a temperature of 480 °C, then another mass loss was observed between 480-615 °C, which was about 5%. After this portion, the residual incombustible matter content up to 850 °C was about 0.431%. In the case of rGO-W96, the initial mass loss pattern was similar to rGO-W48. The initial steady-state mass loss up to 200 °C was approximately 25%, followed by a regular mass loss at 200-230 °C of about 30%. Then a slow degradation was observed between 230-495 °C, a mass loss of about 5%, then another significant mass loss at 495-595 °C mass loss of about 40% which was supposed to be graphenized carbon, and then the residual incombustible matter content up to 850 °C was about 0.25%. In the case of rGO-K180, the initial mass loss pattern was changed from rGO-W48 or rGO-W96. The initial steady-state mass loss up to 90 °C was about 12% then a slow and steady mass loss from 90-440 °C was about 28% occurred, which was supposed to be -O- and -OH functionalized graphene. Then a massive degradation was observed between 510-625 °C, a mass loss of about 60%, which was supposed to be graphenized carbon, and then the residual incombustible matter content up to

850 ºC was about 0.25%. In the case of rGO-K220, the initial mass loss pattern was similar to rGO-K180. The initial steady-state mass loss up to 120 ºC was about 5%, then a short mass loss from 120-150 ºC up to 5 %, then a slow and steady mass loss from 150-450 ºC was about 18% occurred, which was supposed to be -O- and -OH functionalized graphene. Then a massive degradation was observed between 450-615 ºC, a mass loss of about 67%, which was supposed to be graphenized carbon, and then the residual incombustible matter content up to 850 ºC was about 4.5%. In the case of rGO-KAA, the initial mass loss pattern was similar to rGO-K220. The initial steady-state mass loss up to 120 ºC was about 5%, then a slow and steady mass loss from 120-460 ºC was about 18% occurred, which was supposed to be -O- and -OH functionalized graphene. Then a massive degradation was observed between 460-635 ºC, mass loss of about 72%, which was supposed to be graphenized carbon, and then the residual incombustible matter content up to 850 ºC was about 5.0%.

3.3.2.4. X-ray photoelectron spectroscopic (XPS) analysis

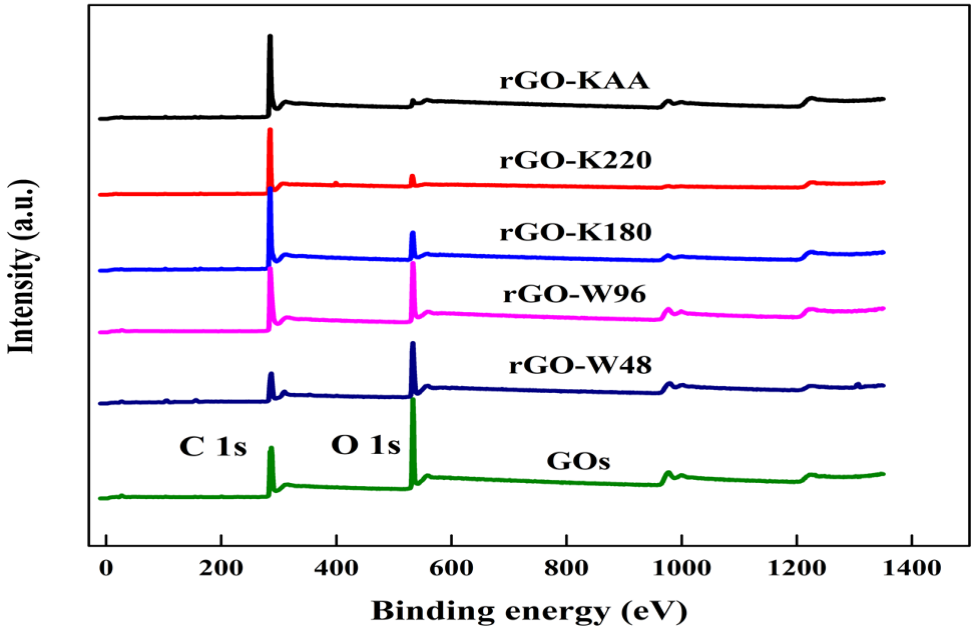

Figure-3.10: XPS survey scan spectral peak analysis of GO3, rGO-W48, rGO-W96, rGO-K180, rGO-K220, and rGO-KAA.

Figure 3.10. illustrates the Competitive XPS Spectrum analyses of all the synthesized products as GOs, rGO-W48, rGO-W96, rGO-K180, rGO-K220, and rGO-KAA. From Figure 3.11, it was found that the initial composition of the pure GOs sample contains carbon-59.97% and oxygen-40.03%, i.e., the initial oxygen to carbon ratio was 66.75% (Table 3.5). After STT-St

treatment of the product, GOs were reduced partially in water to rGO-W48, and the composition of the reduced product was obtained as carbon- 68.78% and oxygen- 31.22%; i.e., the oxygen to carbon ratio in the product was 45.39%. So, the STT-St treatment reduces more than 32% of the oxygen content. Then that STT-Lt treatment of the product GOs was also reduced partially in water to rGO-W96, and the composition of the reduced product was obtained as carbon- 75.37% and oxygen- 24.63%; i.e., the oxygen to carbon ratio in the product was 32.68%. STT-St treatment of the GOs with 66.75% Oxygen reduced more than 51% of the oxygen content were reduced.

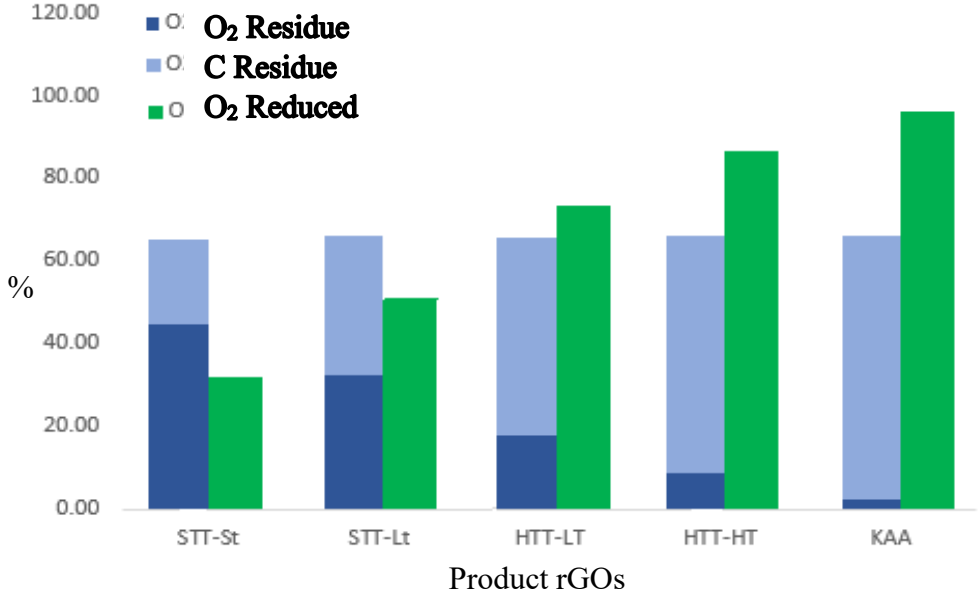

Figure-3.11: O_2 content in the rGO after treatment and O_2 % reduction

After the HTT-LT treatment, GOs product of 66.75% oxygen was highly reduced to rGO-K180 with a composition of carbon- 84.91% and oxygen- 15.09%; i.e., the oxygen to carbon ratio in the product was 17.77%. So, the treatment procedure reduced more than 73% of the oxygen content. Then the HTT-HT treatment GOs product of 66.75% oxygen was highly reduced to rGO-K220 with composition carbon- 91.86% and oxygen- 8.14%; i.e., the oxygen to carbon ratio in the product was 8.86%. So, the treatment procedure reduced more than 86% of the oxygen content. Finally, the double reduction methods reduce the product GOs from 68.78% oxygen content to product rGO-KAA with composition carbon- 97.57% and oxygen- 2.43%; i.e., the oxygen to carbon ratio in the product was 2.49%. So, the treatment procedure reduced more than 96% of the oxygen content.

Table-3.5: XPS survey scan spectral peak analysis of GOs, rGO-W48, rGO-W96, rGO-K180, rGO-K220, rGO-KAA.

Sample ID	Treatment Method	Binding Energy eV		Response Peak Area (N) TPP-2M		Composition Atomic %		Oxygen to Carbon ratio %
		C1s	O1s	C1s	O1s	C1s	O1s	
GOs	Tour's	287.08	533.08	317489	639510	59.97	40.03	66.75
rGO-W48	STT-St	286.56	533.17	32729.89	14854.4	68.78	31.22	45.39
rGO-W96	STT-Lt	285.93	533.20	35683.09	11658.46	75.37	24.63	32.68
rGO-K180	HTT-LT	285.03	532.73	33942.62	6032.44	84.91	15.09	17.77
rGO-K220	HTT-HT	284.92	532.21	23349.67	2067.71	91.86	8.14	8.86
rGO-KAA	Double reduction	285.09	532.80	356281.23	8856.58	97.57	2.43	2.49

From the narrow-spectrum analysis of the above XPS spectrum of GOs, rGO-W48, rGO-W96, rGO-K180, rGO-K220, and rGO-KAA samples were found after deconvolutions of the respective spectra. Deconvolution of the carbon and oxygen peaks of the products is listed in Table 3.6.

The deconvolution of the Carbon peak of GOs sample about five different functional carbon atoms (including satellite peak) were obtained (Table-3.6 and 3.7), in which C1s peak at BE 284.21 represents Graphene Carbon- 12.67%, at BE 284.99 represents C-C functional group- 12.85%, at BE 286.75 represents C-O functional group- 54.49%, at BE 288.80 represents >C=O functional group- 17.57% and at BE 290.76 a Carbon Satellite peak of 2.41%. On the other hand, the deconvolution of the Oxygen peak of the GOs sample about three different functional Oxygen bonds was obtained, in which the O1s peak at BE 532.81 represents >c  c< bonds- 76.74%, at BE 534.68 represents C=O functional group- 5.50% and at BE 536.08 represents (H-O-C=O) functional group- 17.76%.

Similarly, the deconvolution of the Carbon peak of the rGO-W48 sample about four different functional carbon atoms was obtained, in which the C1s peak at BE 284.16 represents Graphene Carbon- 2.58%, at BE 285.07 represents C-C functional group- 40.42%, at BE 287.32 represents C-O functional group- 43.44% and at BE 289.06 represents C=O functional group- 8.92%. On the other hand, the deconvolution of the Oxygen peak of the GOs sample about two different functional Oxygen bonds was obtained, in which the O1s peak at BE 531.08 represents C-O/O-H bonds- 3.98% and at BE 533.08 represents >c 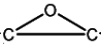 c< functional group- 96.02%.

In the same, the deconvolution of the Carbon peak of the rGO-W96 sample about four different functional carbon atoms peaks (including satellite peak) were obtained, in which the C1s peak at BE 284.8 represents Graphene Carbon- 51.27%, at BE 286.76 represents C-O functional group- 24.17% and at BE 288.75 represents C=O functional group- 13.75%. On the other hand, the deconvolution of the Oxygen peak of the GOs sample about three different functional Oxygen bonds was obtained, in which the O1s peak at BE 531.27 represents C-O/O-H bonds- 9.18%, at BE 532.94 represents >c 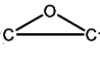 c< bonds- 85.22% and at BE 536.28 represents H-O-C=O functional group- 5.60%.

Again, the deconvolution of the Carbon peak of rGO-K180 sample about five different functional carbon atoms (including satellite peak) were obtained, in which C1s peak at BE 284.61 represents Graphene Carbon- 89.97%, at BE 285.52, represents C-C functional group- 1.51%, at BE 286.47 represents C-O functional group- 0.86%, at BE 288.77 represents >C=O functional group- 4.02% and at BE 290.67 a Carbon Satellite peak- 4.64%. On the other hand, the deconvolution of the Oxygen peak of the GOs sample about two different functional Oxygen bonds was obtained, in which the O1s peak at BE 531.63 represents C-O/O-H bonds- 63.38% and at BE 533.12 represents >c 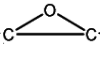 c< functional group- 36.62%.

Further, the deconvolution of the Carbon peak of the rGO-K220 sample about four different functional carbon atoms was obtained, in which the C1s peak at BE 284.54 represents Graphene Carbon- 51.28%, at BE 284.91, represents C-C functional group- 47.51%, at BE 288.26 represents C=O functional group- 1.02% and at BE 290.92 a Carbon Satellite peak- 0.19%. On the other hand, the deconvolution of the Oxygen peak of the GOs sample about two different functional Oxygen bonds was obtained, in which the O1s peak at BE 531.70 represents C-O/O-H bonds- 52.22% and at BE 533.18 represents >c 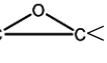 c< functional group- 47.78%.

Table-3.6: XPS narrow spectrum of GO3, rGO-W48, rGO-W96, rGO-K180, rGO-K220 and rGO-KAA

Sample ID: GOs					
C1s			O1s		
Graph	eV*	Area %	Graph	eV*	Area %
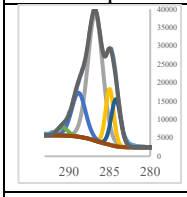	284.21, Graphene Carbon	12.67	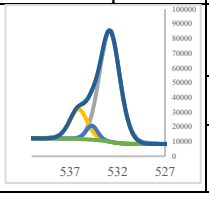	532.81, >C(O)C<	76.74
	284.99, C-C	12.85			
	286.75, C-O	54.49		534.68 C=O	5.50
	288.80, C=O	17.57		536.08, (H-O-C=O)	17.76
	290.76, Satellite	2.41			
Sample ID: rGO-W48					
C1s		Area %	O1s		Area %
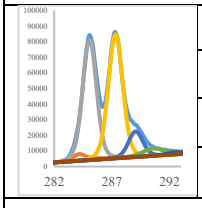	284.16, Graphene Carbon	2.58	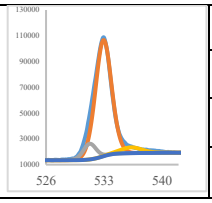	531.27, (C-O/O-H)	9.18
	285.07, C-C	40.42		532.94, >C(O)C<	85.22
	287.32, C-O	43.44		536.28 (H-O-C=O)	5.60
	289.06, C=O	8.92			
Sample ID: rGO-W96					
C1s		Area %	O1s		Area %
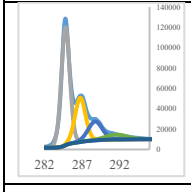	284.8 Graphene Carbon	51.27	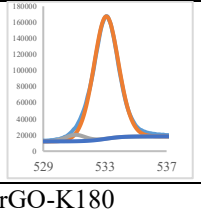	531.08, (C-O/O-H)	3.98
	286.76 (C-O)	24.17		533.08, >C(O)C<	96.02
	288.75, (C=O)	13.75			
	291.58, Satellite	10.81			
Sample ID: rGO-K180					
C1s		Area %	O1s		Area %
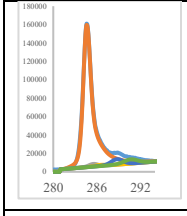	284.61, Graphene Carbon	89.97	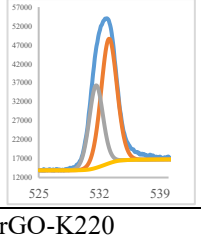	531.63, (C-O/O-H)	63.38
	285.52, C-C	1.51		533.12, >C(O)C<	36.62
	286.47, C-O	0.86			
	288.77, C=O	4.02			
	290.67, Satellite	4.64			
Sample ID: rGO-K220					
C1s		Area %	O1s		Area %
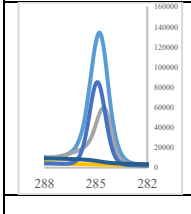	284.54, Graphene Carbon	51.28	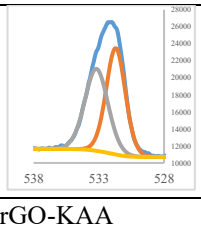	531.70, (C-O/O-H)	52.22
	284.91, C-C/C-H	47.51		533.18, >C(O)C<	47.78
	288.26, C=O	1.02			
	290.92, Satellite	0.19			
Sample ID: rGO-KAA					
C1s		Area %	O1s		Area %
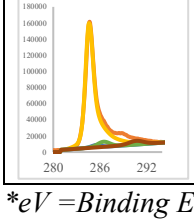	284.61, Graphene Carbon	92.36	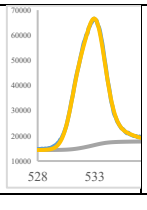	533.10, >C(O)C<	100.00
	285.52, C-C/C-H	1.18			
	286.47, C-O	3.33			
	290.67, Satellite-1	2.84			

**eV =Binding Energy in eV, *Gr=Graphenized carbon.*

Table-3.7: XPS narrow spectrum analysis of GO3, rGO-W48, rGO-W96, rGO-K180, rGO-K220 and rGO-KAA and deconvoluted table

	GOs			rGO-W48			rGO-W96			rGO-K180			rGO-K220			rGO-KAA		
	BE, eV	Bond Type	%	eV	B. Type	%	eV	B. Type	%	eV	B. Type	%	eV	B. Type	%	eV	Type	%
C1s	284.21	Graphene Carbon	12.7	284.2	GC	2.58				284.6	GC	89.97	284.5	GC	51.28	284.6	GC	92.36
	284.99	C-C/C-H	12.9	285.1	C-C	40.42	284.8	C-C	51.27	285.5	C-C	1.51	284.9	C-C	47.51	285.5	C-C	1.18
	286.75	C-O	54.5	287.3	C-O	43.44	286.8	C-O	24.17	286.5	C-O	0.86				286.5	C-O	3.33
	288.8	C=O	17.6	289.1	C=O	8.92	288.8	C=O	13.75	288.8	C=O	4.02	288.3	C=O	1.02			
	290.76	Satellite	2.41				291.6	Sat.	10.81	290.7	Sat.	4.64	290.9	Sat.	0.19	290.7	Sat.	2.84
O1s				531.1	C-O	3.98	531.3	C-O	9.18	531.6	C-O	63.38	531.7	C-O	52.22			
	532.81	C-O-C	76.7	533.1	C-O-C	96.02	532.9	C-O-C	85.22	533.1	C-O-C	36.62	533.2	C-O-C	47.78	533.1	C-O-C	100
	534.68	C=O	5.5															
	536.08	H-O-C=O	17.8	536.3	O-C=O	5.6												

At last, the deconvolution of the Carbon peak of Kerosene and Ascorbic acid reduced rGO-KAA sample about four different functional carbon atoms were obtained, in which C1s peak at BE 284.61 represents Graphene Carbon- 92.36%, at BE 285.52, represents C-C functional group- 1.18%, at BE 286.47 represents C-O functional group- 3.33% and at BE 290.67 a Carbon Satellite peak- 2.84%. On the other hand, the deconvolution of the Oxygen peak of the GOs sample about one type of Oxygen functional bonds was obtained, in which the O1s peak at BE 533.10 represents >C=O bonds- 100.00%.

3.3.2.5. XRD analysis

The XRD analysis of five samples, presented in Figure 3.12 and Table 3.8, reveals that the graphite sample displays a sharp peak at $2\theta = 26.39°$, corresponding to an interplanar distance of $d = 3.35$ Å. This indicates that the sample is highly crystalline, with its structure aligned along the (002) plane, representing the ideal interlayer spacing for graphite. The sharpness of the peak and the precise interplanar spacing confirm the presence of 100% graphitic carbon in the sample. These characteristics highlight the sample's excellent structural order, which is essential for applications requiring high thermal, electrical, and mechanical performance. For GOs (GOs-7014), the sharp XRD peak observed for graphite at $2\theta = 26.39°$ disappears entirely, and it is replaced by two broad spectra. The first, a prominent broad peak, is observed at $2\theta = 11.76°$ with an interplanar spacing of $d = 7.55$ Å. The second, a smaller broad peak, appears at $2\theta = 42.97°$ with an interplanar spacing of $d = 3.07$ Å. The area composition of these two peaks is 92.13% and 7.87% respectively. These peaks correspond to the (001) and (100) planes,

respectively, and indicate an amorphous-like structure with diversified nano-crystallinity. This behavior reflects the inhomogeneous and disordered characteristics typical of GOs. The absence of sharp peaks confirms that the sample is entirely composed of 92% GOs, with no crystalline graphite present (Saini B., et. al., 2021), (Leonardi A, et. al., 2020), (Hidayah N. M., et. al., 2017), (Das P, et. al., 2021), (Johra F. T., et. al., 2014).

The thermal reduction of the GOs sample (GOs-7014) in water to rGO-W48 and rGO-W96 resulted in a significant reduction of the characteristic peaks of GOs-7014, with the graphenized carbon peak around the (002) plane reappearing. For the rGO-W48 sample, three distinct peaks were observed. Two prominent peaks, corresponding to the GOs-7014 sample, remained unchanged, one at $2\theta = 10.67°$ with an interplanar distance of d = 8.64 Å representing the (001) plane, and another at $2\theta = 42.67°$ with d = 2.14 Å, associated with the (100) plane. The area composition of these three peaks is 63.02% and 6.21% respectively.

Additionally, a new broader peak appeared at $2\theta = 30.98°$ with an interplanar distance of d = 4.32 Å. This peak corresponds to the (002) plane, indicating the partial formation of rGO in the rGO-W48 sample. The analysis of these peaks suggests that the composition of the sample includes 30.77% rGO. The area composition of these three peaks is 63.02%, 30.77% and 6.21% respectively. That means the 48 hours thermal treatment of GOs in water, 30.77 % rGO was formed. These findings highlight the inhomogeneous and disordered amorphous structure characteristic of partially rGO, with contributions from both GOs and rGO phases, reflecting the intermediate stage of reduction (Leonardi A, et. al., 2020), (Hidayah N. M., et. al., 2017).

After prolonged reduction of the GOs-7014 sample to form rGO-W96, notable changes were observed in the XRD peaks, reflecting the transition from GOs to rGO. The characteristic GOs peak at $2\theta = 11.34°$, corresponding to the (001) (Ruzhenu X., 2025) plane with an interplanar distance of d = 8.29 Å, became shorter and significantly broader, indicating a decrease in the order of the GOs structure. Similarly, the smaller broad peak at $2\theta = 43.12°$, associated with the (100) plane with d = 2.12 Å, remained consistent with the GOs-7014 sample.

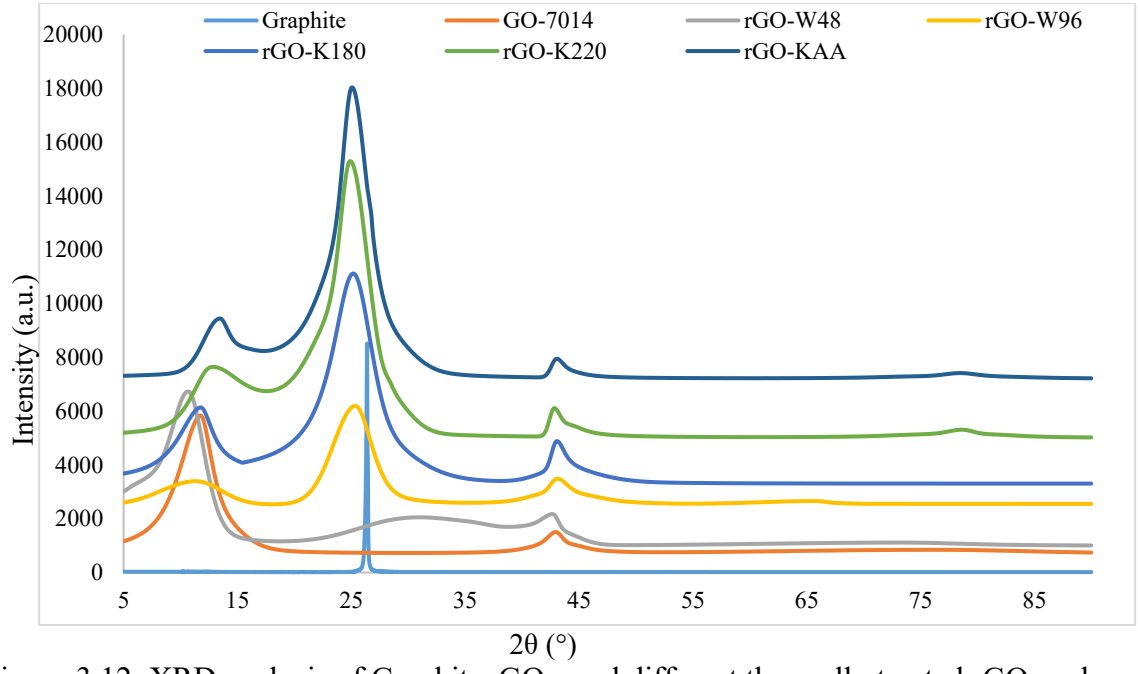

Figure-3.12: XRD analysis of Graphite, GOs, and different thermally treated rGO peaks.

In contrast, the rGO characteristic peak at 2θ = 25.36°, corresponding to the (002) (Ruzhenu X., 2025) plane with an interplanar distance of d = 3.58 Å, became more pronounced, increasing in both height and breadth. This change signifies enhanced conversion of GOs to rGO. The composition of the rGO-W96 sample was determined to be 24.38% GOs, 65.77% rGO, and 9.85% Satellite peaks of carbon residue, reflecting the substantial progress of the reduction process (Das P., et. al., 2021). During the high-temperature thermal reduction of the GOs sample to form rGO-K180, significant changes in the XRD peaks were observed, indicating the transformation from GOs to rGO. The pronounced GOs peak at 2θ = 11.77°, corresponding to the (001) (Ruzhenu X., 2025) plane with an interplanar distance of d = 7.55 Å, became shorter, reflecting a reduction in the structural order of the GOs. Meanwhile, the smaller broad peak at 2θ = 43.08°, associated with the (100) (Ruzhenu X., 2025) plane and an interplanar distance of d = 2.105 Å, remained similar to that of the original GOs sample.

In contrast, the rGO characteristic peak at 2θ = 25.17°, corresponding to the (002) (Ruzhenu X., 2025) plane with an interplanar distance of d = 3.56 Å, became significantly more pronounced, with increased height and broadness. This observation indicates a substantial increase in the conversion of GOs to rGO. The composition of rGO-K180 was determined to be 15.88% GOs, 77.81% rGO, and 6.31% Satellite peaks of carbon residue with enhanced structural properties (Johra F. T., et. al., 2014).

Table-3.8: XRD pattern of different GOs and softly and hardly treated rGO peaks from in water and kerosene medium.

Sample ID	2 θ (2 Theta)		
	At (001) plane	At (002) plane	At (100) plane
Graphite	-	26.39 100% 3.35	-
GO	11.76 92.13% (7.55)	-	42.97 7.87% (3.07)
rGO-W48	10.67 63.02% (8.64190)	30.98 30.77% (4.32000)	42.67 6.21% (2.13903)
rGO-W96	11.34 24.38% (8.29)	25.36 65.77% (3.58200)	43.12 9.85% (2.12478)
rGO-K-180	11.77 15.88% (7.55)	25.17 77.81% (3.56198)	43.08 6.31% (2.105)
rGO-K220	12.86 12.66% (6.590)	24.91 84.00% (3.555)	42.85 3.3% (2.105)
rGO-KAA	13.46 9.81% (6.590)	25.07 88.16% (3.53300)	43.06 2.03% (2.105)

At a higher temperature, the thermal reduction of the GOs sample to rGO-K220 led to significant transformations in the XRD peaks, indicative of the conversion from GOs to rGO. The characteristic GOs peak at 2θ = 12.86°, corresponding to the (001) (Ruzhenu X., 2025) plane with an interplanar distance of d = 6.59 Å, became shorter and broader, signifying further disruption of the GOs structure. Similarly, the small, broad peak at 2θ = 42.85°, associated with the (100) plane and an interplanar distance of d = 2.105 Å, remained consistent with the original GOs sample.

In contrast, the rGO characteristic peak at 2θ = 24.91°, corresponding to the (002) plane with an interplanar distance of d = 3.555 Å, showed a substantial increase in height and breadth. This reflects enhanced conversion of GOs into rGO, showing improved structural regularity of the reduced material. The composition of the rGO-K220 sample was determined to be predominantly rGO (84.00%), indicating a high degree of reduction and excellent structural refinement (Siburian R, et. al., 2018). The residual GOs were 12.66% and 3.34% Satellite peaks of carbon residue.

The thermochemical double degradation reduction of the GOs sample to rGO-KAA resulted in changes in the XRD peaks, highlighting the conversion from GOs to rGO. The characteristic GOs peak at 2θ = 13.46°, corresponding to the (001) plane (Ruzhenu X., 2025) with an interplanar distance of d = 6.59 Å, became shorter and less broad, indicating a reduction in the structural order of the GOs. The small, broad peak at 2θ = 43.06°, associated with the (100) plane (Ruzhenu X., 2025) an interplanar distance of d = 2.105 Å, remained largely unchanged, reflecting the persistence of GOs characteristics.

Conversely, the rGO characteristic peak at 2θ = 25.07°, referring to the (002) plane with an interplanar distance of d = 3.533 Å, showed a significant increase in both height and broadness, indicating a high conversion of GOs to rGO. This confirms that the composition of the rGO-KAA sample includes both GOs and rGO, with the exact proportion depending on the thermal condition. The results underscore the critical role of thermal treatment in achieving the desired reduction of GOs to rGO. The composition of rGO-K180 was determined to be 9.81% GOs, 88.16% rGO, and 2.03% Satellite peaks of carbon residue with enhanced structural properties.

3.3.2.6. SEM image analysis of different GO and rGOs products

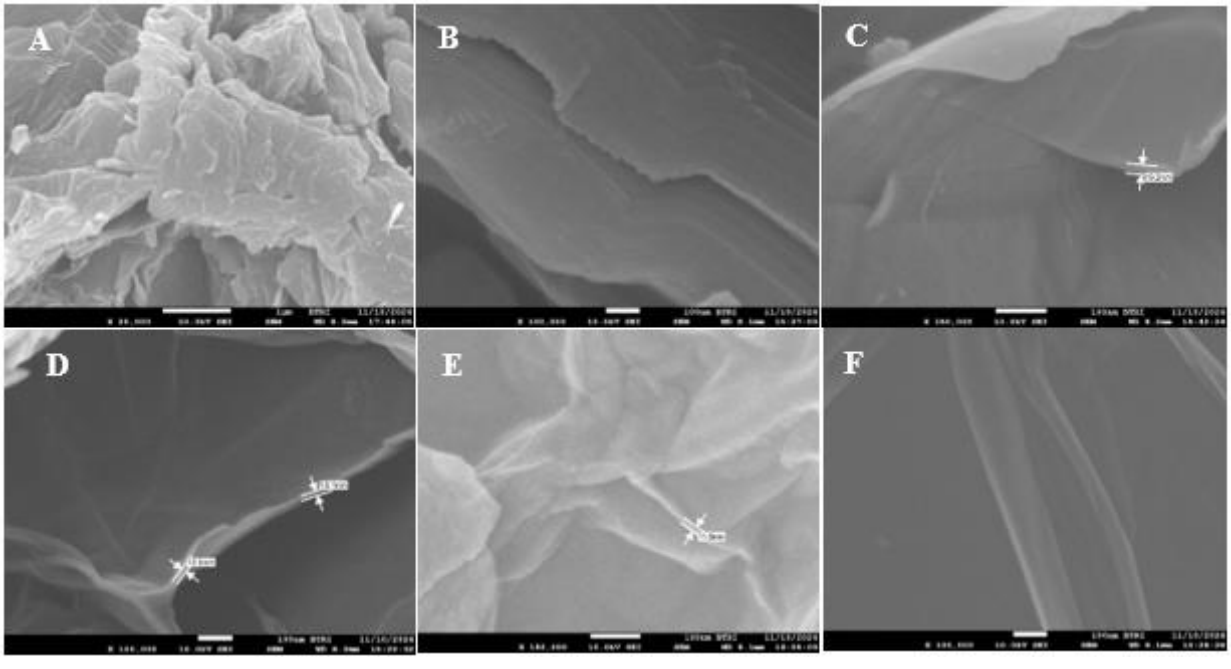

Figure-3.13: SEM Image analysis of different Soft and Hard treated GOs and rGO: A) GOs, B) rGO-W48, C) rGO-W96, D) rGO-K180, E) rGO-K220, F) rGO-KAA.

Figure 3.13 shows the microstructure of precursor graphite particles before and after chemical processing, as observed by FE-SEM. The as-received graphite powder exhibits an irregular, flaky morphology typical of graphite. The accompanying XRD analysis in Figure 3.12 shows only a carbon peak, confirming the purity of the starting graphite powder. Quantitative analysis revealed that the precursor graphite contains up to 98% carbon, aligning with the XPS results. The thickness measured in the images was 9-19 nm. These findings suggest that the commercial-grade graphite powder does contain impurities, though minimal. While these impurities could extend the processing time required to remove them, they are unlikely to negatively impact the quality of the resulting graphene. This indicates that, despite the impurities, the graphite used is of sufficiently high quality for graphene production, and the chemical processing can effectively purify the material without compromising the final product (Khan Q. A., et. al., 2017), (Wilson N., et. al., 2009), (Zhang W, et. al., 2022), (Abdolhosseinzadeh S. H., et. al., 2015), (Viswanathan A., et. al., 2024).

3.3.2.7. TEM image analysis of different GOs and rGO products

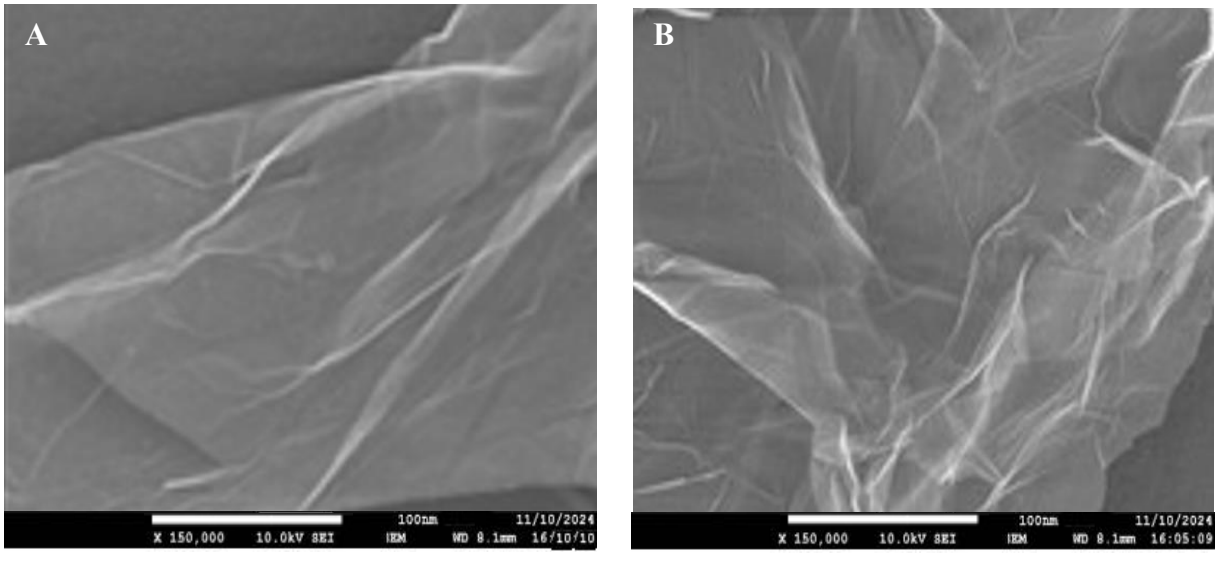

Figure-3.14: TEM Image of different rGOs in A) Kerosene medium rGO-K220, and B) Ascorbic acid in water rGO-KAA.

TEM analyses of rGO (rGO-K220 and rGOK-AA) provide detailed insights into its structural and morphological features. TEM images revealed ultrathin, sheet-like rGO structures, typically consisting of a few layers with minimal wrinkles and folds, were shown in Figure 3.14. At higher magnifications, lattice fringes become visible, indicating crystalline domains with an interplanar distance (d002) of approximately 3.508 Å. TEM images confirm rGO's

crystallographic structure, showing partial restoration of the sp^2 carbon network with some residual defects (Chuah R, et. al., 2020).

Comparative TEM studies highlight differences among graphite, GOs, and rGO. Graphite exhibits elongated, platelet-like structures with folds, while GOs show crumpled edges and less dense dark regions. Exfoliated GOs appear flatter and less contrasted, indicating fewer layers. Thermally reduced rGO is characterized by a crumpled morphology due to oxygen removal and graphene lattice reorganization. Edges appear smooth, reflecting reduced oxygen groups, although some uneven edges suggest localized thermal distortions. Additionally, TEM studies of synthesized rGO reveal significant differences in their morphology found in literature (Chuah R., et. al., 2020). They appear as elongated, platelet-like structures with dark regions, along with pronounced folding and wrinkling. Upon oxidation and reduction, rGO forms on the edges and corners of graphene layers, with larger internal gaps. rGO-K220 shows less visible dark regions and crumpled edges than rGO-KAA. Exfoliated rGO displays a flat structure with low contrast, indicating only a few graphene layers and sharp edges. rGO sheets exhibit lattice fringes, smooth edges, and a transparent, flat morphology with reduced folding and wrinkling. This highlights the structural transformation through oxidation and reduction processes (Kumar D, et. al., 2023), (Aliyev E., et. al., 2019).

3.3.2.8. Surface area analysis using the BET sorptometer

The (Brunauer-Emmett-Teller) BET sorptometer analysis of rGO-K220 and rGO-KAA samples was conducted using nitrogen adsorption at cryogenic temperatures. Adsorption-desorption isotherms with hysteresis loops confirmed the mesoporous structure of both samples. Figure 3.15 highlights their cumulative surface areas, with higher surface areas and pore volumes enhancing electrochemical reactivity and energy storage capacities. This study underscores the significance of mesoporous features in optimizing material performance, as supported by previously explained. (Brunauer S., et. al., 1938), (Rouquerol J., et. al., 1994).

Adsorbate and experimental conditions

Nitrogen, a standard adsorbate in BET measurements, was used for characterizing the surface area and pore structure of rGO-K220 and rGO-KAA. Measurements occurred at 29.22 °C, with cryogenic testing at -195.76 °C ensuring effective nitrogen adsorption (Zhao J., et. al., 2010).

Sample preparation and outgassing

The samples were outgassed at 130 °C under a 20-micron vacuum, removing adsorbed moisture and volatile contaminants, ensuring accurate BET results. Weight differences before and after outgassing (rGO-K220: 0.4066 g to 0.3812 g; rGO-KAA: 0.4498 g to 0.4351 g) confirmed successful impurity removal.

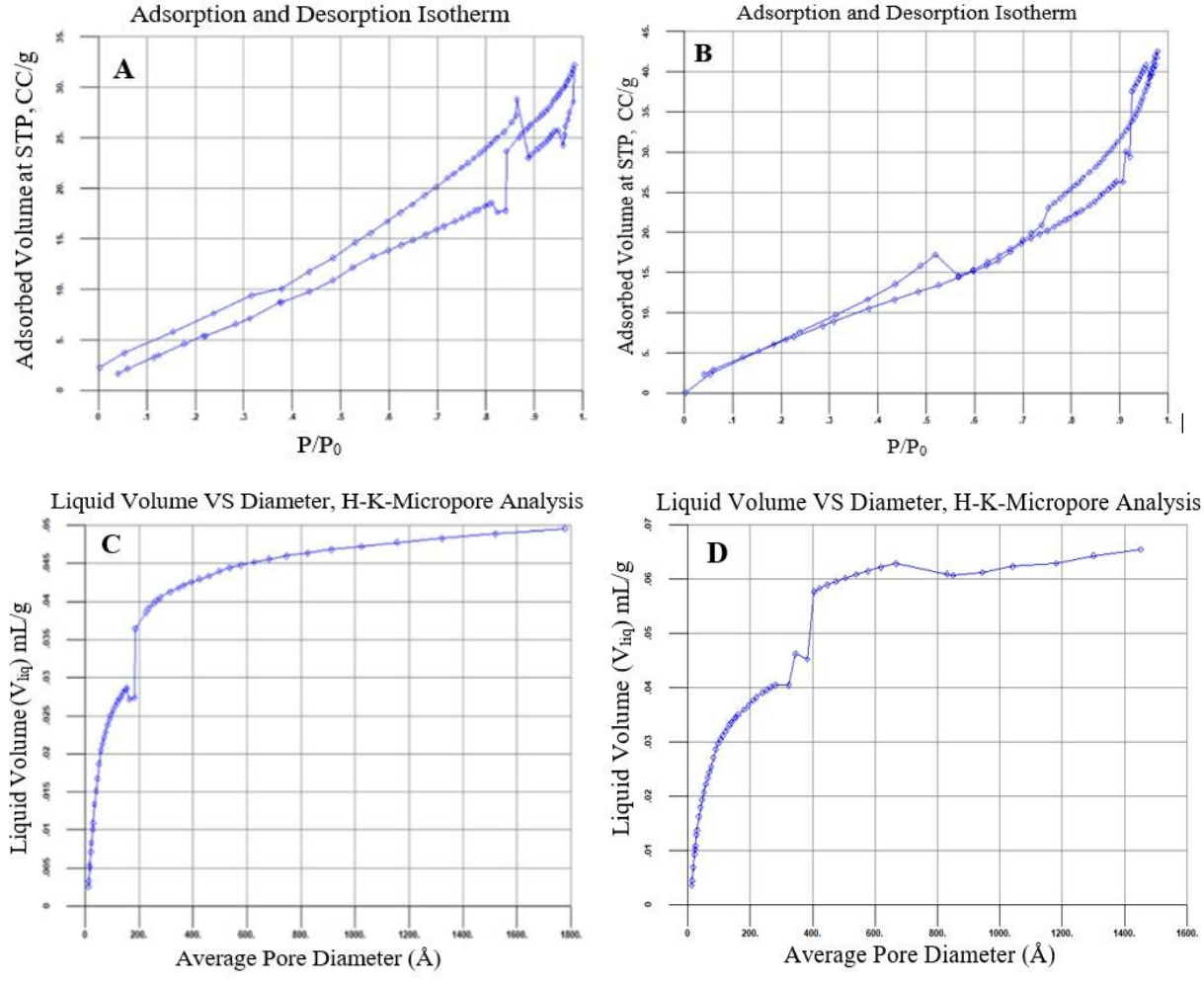

Figure-3.15: Surface Area Analysis by BET Sorptometer analysis A) Adsorption desorption isotherm of rGO-K220, B) Adsorption desorption isotherm of rGO-KAA, C) Pore size distribution of rGO-K220, D) Pore size distribution of rGO-KAA.

BET surface area and Vm value

The BET surface area of rGO-KAA (32.60 m^2/g) exceeded that of rGO-K220 (27.14 m^2/g), indicating a more developed surface, potentially due to structural differences. The corresponding BET Vm values (rGO-KAA: 7.48 cm^3; rGO-K220: 6.23 cm^3) reflect the larger monolayer capacity of rGO-KAA.

BET C value and correlation

rGO-KAA's higher BET C value (8.996 vs. 7.343) suggests stronger nitrogen interactions and greater surface heterogeneity. Both samples exhibit high correlation coefficients (rGO-K220: 0.994; rGO-KAA: 0.996), confirming the reliability of the BET data.

Total pore volume and average pore diameter

rGO-KAA showed higher total pore volume (0.0654 cc/g vs. 0.0496 cc/g) and slightly larger average pore diameter (80.27 Å vs. 73.03 Å), enhancing mass transport and diffusion properties.

Pore type Barrett-Joyner-Halenda (BJH) method

The BET and BJH analyses reveal significant differences between rGO-K220 and rGO-KAA, highlighting rGO-KAA's superior properties for advanced applications. Both materials are classified as mesoporous, ideal for adsorption, catalysis, and energy storage due to their balance of accessibility and surface area (Gregg S. J., et. al., 1967), (Barrett E. P., et. al., 1951), (Ioni Y., et. al., 2023).

3.3.2.9. Reduction mechanism

The reduction of GO to rGO primarily occurs through the thermal cleavage of oxygen-containing functional groups, such as hydroxyl (OH), epoxy (C-O-C), ketone (C=O), and carboxyl (COOH) groups. In this study, the reduction was conducted at temperatures ranging from 180 °C to 250 °C in water and kerosene media, leading to the release of H_2O, CO_2, and CO. This thermal reduction restores the conjugated π-electron system of the graphene lattice, which significantly enhances its electrical conductivity and other functional properties. Due to its simplicity and high efficiency, this method remains a widely employed strategy for the large-scale production of graphene-based materials. (M. Acik, 2011), (Larciprete R., et. al., 2011), (Le G. T., et. al., 2018).

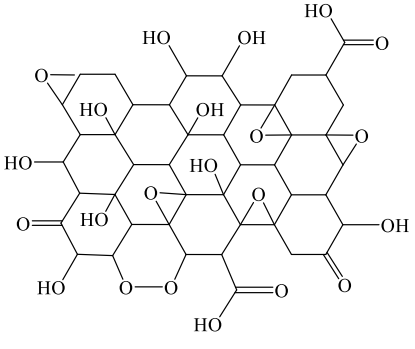

Figure 3.16: Different functional groups undergo cleavage during reduction process.

Figure 3.16 shows the versatile oxygen functional groups present in GO tend to break down during thermal degradation. The specific degradation mechanism involved in GO reduction is highly dependent on the reaction conditions, particularly the polarity of the reduction medium. In a kerosene medium, the reduction primarily follows a thermally influenced free radical mechanism, the details of which are presented in Figure 3.17, Figure 3.18 and Figure 3.19 (Acik M., et al., 2011).

3.3.2.9.1. Free radical mechanism

The free radical mechanism for the reduction of GOs to rGO was accomplished in three steps such as initiation, propagation and termination. The detailed description of the mechanism is explained bellow-

A. Initiation step

In this reaction system, the initiation phase is triggered by heating GOs at above 150 °C in a kerosene medium, which caused the thermal decomposition of trapped H_2O molecules into hydroxyl (•OH) and hydrogen (H•) free radicals. Simultaneously, the interaction between trapped H_2O and O_2 serves as an additional pathway for generating •OH radicals. These highly reactive primary species then underwent secondary reactions: the H• radical combines with another H_2O molecule to form a hydronium free radical H_3O•, while the •OH radical reacts with O_2 to produce a hydroperoxyl radical (HO_3•). The reactions involved in the initiation steps are follows:

$$H_2O \xrightarrow[\text{Heat}]{} HO\bullet + H\bullet \quad \text{[hydrogen and hydroxyl free radical]}$$

$$2H_2O + O_2 \xrightarrow[\text{Heat}]{} \text{[hydroxyl free radical]}$$

$$H\bullet + H_2O \xrightarrow[\text{Heat}]{} \text{ydronium free radical]}$$

$$HO\bullet + O_2 \quad HO_3\bullet \quad \text{[hy} \xrightarrow[\text{Heat}]{} \text{l radical]}$$

Figure 3.17: Initiation of the reduction process due to thermal reduction and cleavage of trapped water at higher temperature.

B. Propagation step

In this stage of the process, the free radicals generated during initiation attack the oxygenated sites on the GOs. The carboxylic acid groups are converted into carboxylic free radicals (COO•), while the ketonic groups are transformed into oxonium (O•) free radicals. The epoxy groups follow a more complex route, first converting into intermediate hydroxyl groups before being reduced further into carbon (C•) free radicals with the simultaneous release of H_2O molecule. This sequence is critical for the "deoxygenation" of GO, effectively restoring the carbon lattice. The reactions involved in propagation steps are as follows:

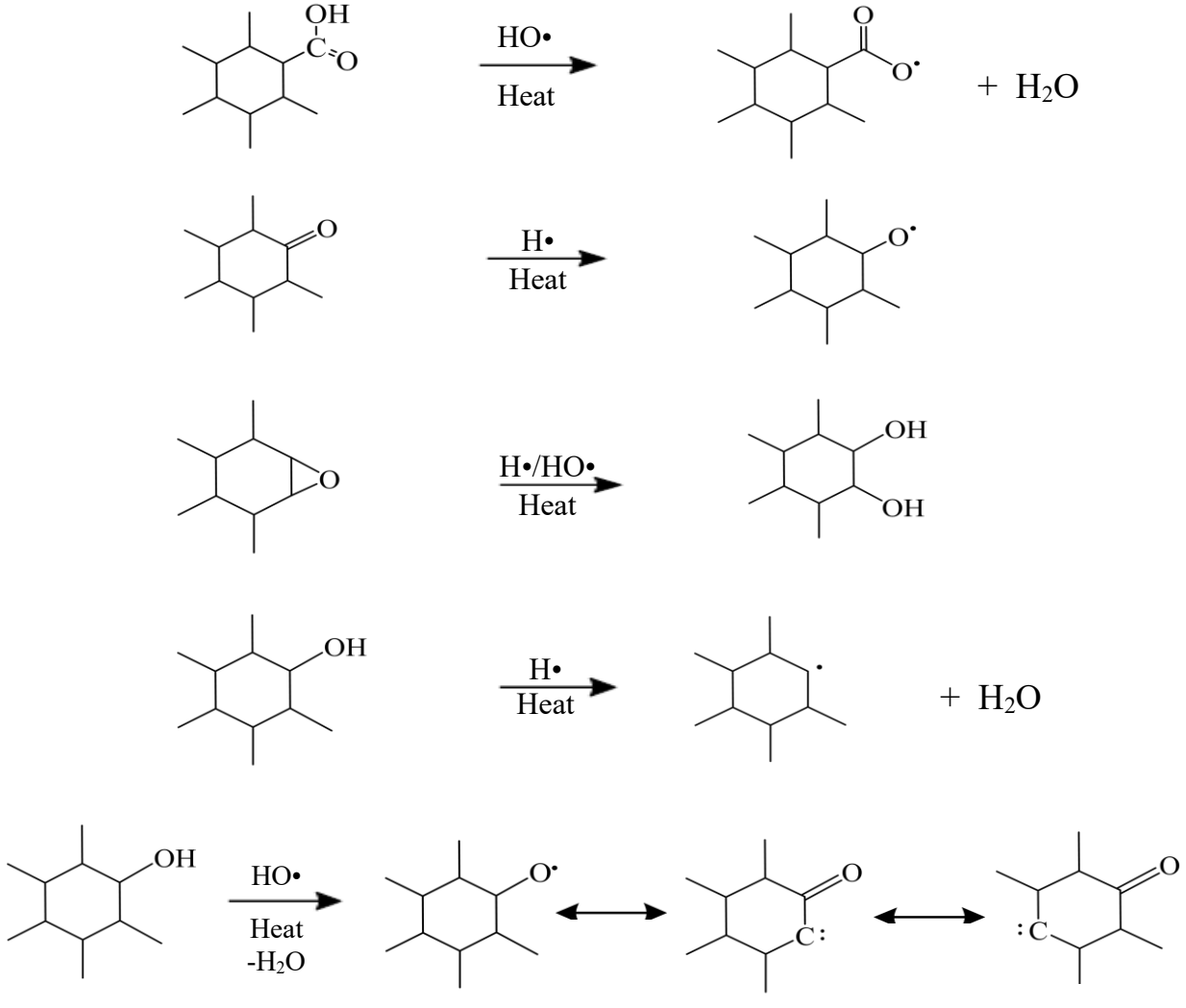

Figure 3.18: Propagation of the reduction process greatly accelerated with the thermal reduction at inert kerosene solvent medium at higher temperature.

C. Termination step

The process concluded with the termination step, where the unstable carbon free radicals across the graphene layers underwent recombination to restore the hexagonal graphitic lattice. During this phase, carboxylic radicals often decarboxylate to release CO and CO_2, while other oxygen-rich species combine to form H_2O vapor. The kerosene medium serves a dual role by providing a stable environment for these high-temperature collisions and potentially acting as a capping agent. The result is a significant reduction in oxygen content and the transformation of GOs into reduced rGO. The reactions involved in termination steps are follows:

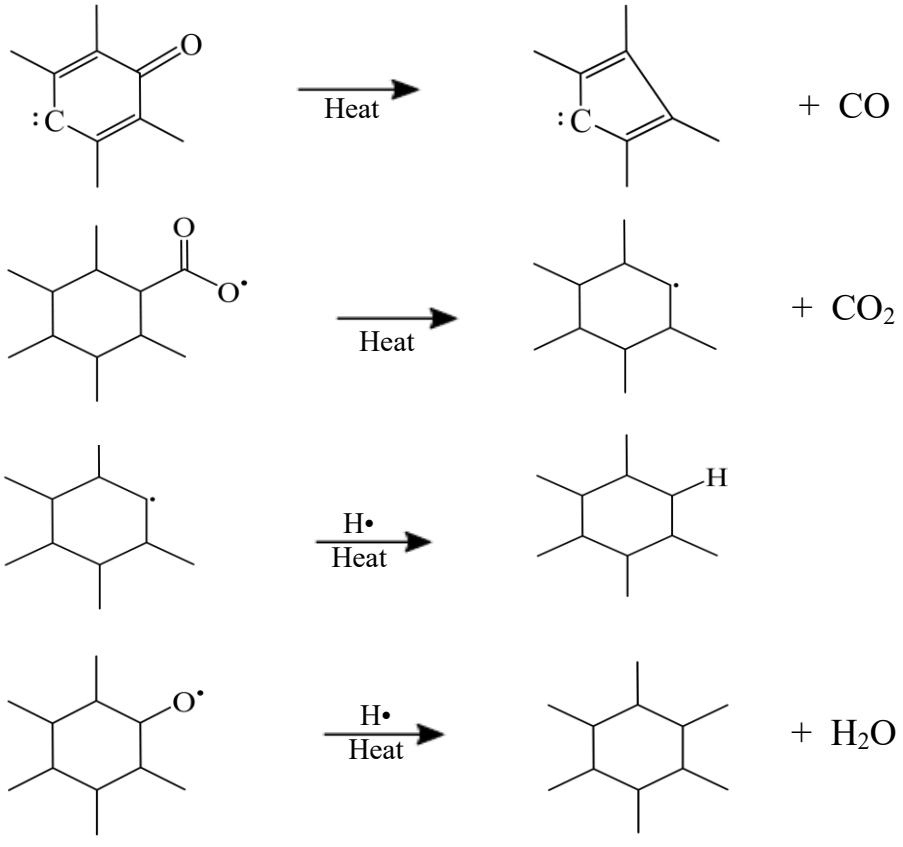

Figure-3.19: Termination of the free radicals generated in initiation and propagation steps by conjugation within themselves to end of the reduction process.

This mechanism is highly favorable for maintaining the structural integrity of the graphene lattice. The degradation mechanism further can be classified in to two major classes depending upon their disruption of the carbon backbone (Mohan V. B., et. al., 2020). Figure 3.20 showd the destructive degradation where the disruption or loss of carbon atom was occured and also the non-destructive degradation where there were no lows of carbon atom due to disruption in the carbon skeleton occured. In order to maximize the yield and to obtain good quality defect

free nano film non-destructive degradation is favorable, because by minimizing damage to the carbon framework, non-destructive degradation results in a higher quality rGO product with fewer defects.

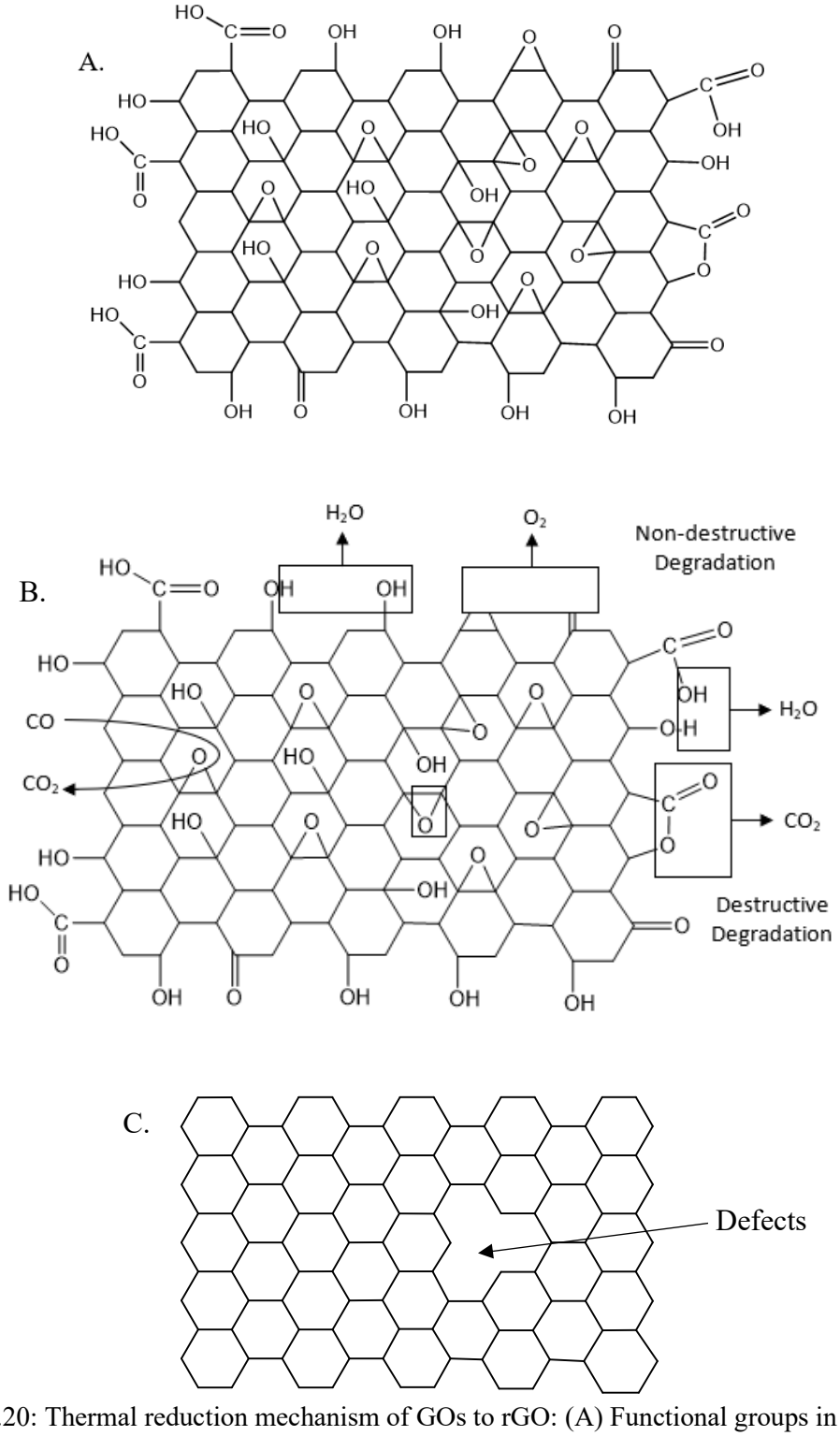

Figure-3.20: Thermal reduction mechanism of GOs to rGO: (A) Functional groups in GOs, (B) Reduced Mechanism, (C) Defects in rGOs.

3.3.2.9.2. Non-destructive degradation

Non-destructive degradation occured through the interactions between oxygen and hydrogen atoms in hydroxyl groups located on the surface of graphene. In this process, the reduction was initiated by different free radicals, as depicted in Figures 3.20 and 3.21. Under thermal treatment, these free radicals became increasingly excited and unstable, leading to their reaction with other oxygen-containing functional groups and it resulted formation of water, oxygen molecules, and carbondioxide were released without significantly disrupting the carbon backbone of the graphene structure. This free radical becomes more excited and unstable through thermal treatment, and reacted with other oxygen-containing functional groups to propagate and release water and oxygen molecules.

Reaction-1: Release of water

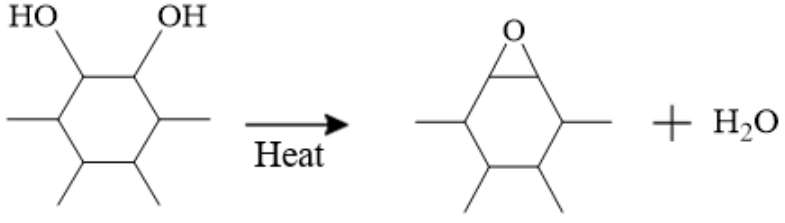

Reaction-2: Release of water

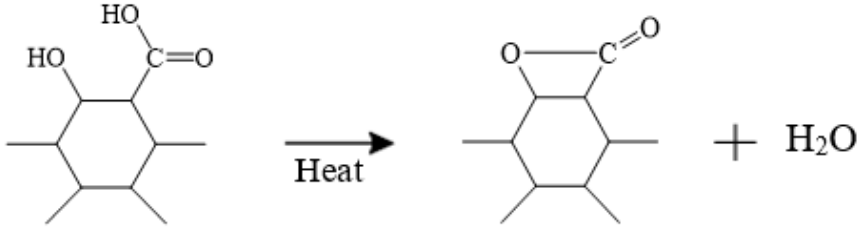

Reaction-3: Release of carbon monoxide

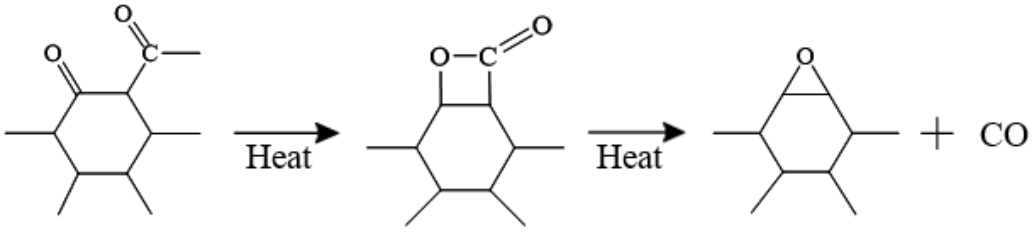

Reaction-4: Release of carbon dioxide

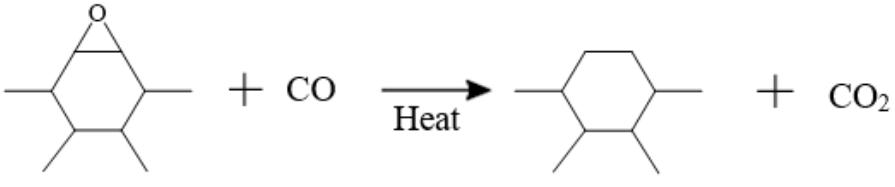

Figure-3.21: Non-destructive degradation reduction mechanisms (Reaction-1, 2, 3, and 4).

3.3.2.9.2. Destructive degradation mechanism

Unlike non-destructive degradation, this pathway compromises the structural integrity of the graphene lattice. The release of carbon dioxide results in the disruption of carbon backbone, introducing defects into the rGO. The extent of these defects depends on the degree of destructive degradation, which can be influenced by factors such as temperature and environment of the reaction.

Reaction-5: Release of carbon monoxide

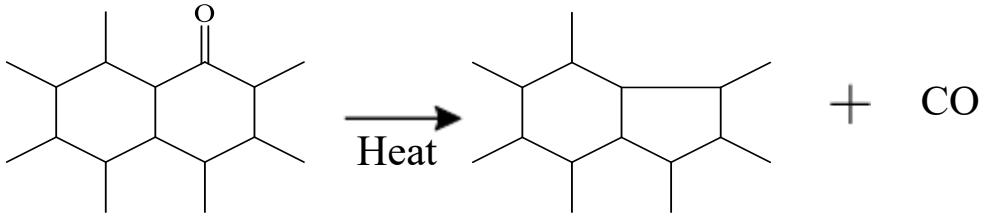

Reaction-6: Release of carbon dioxide

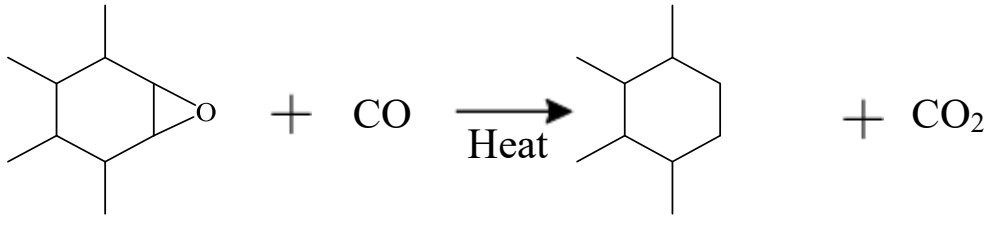

Figure-3.22: Destructive degradation reduction mechanisms.

The epoxy group along with other functional groups like carbonyl group, was also thermally reduced over 200-400 ^{o}C and yield carbon monoxide (CO). This liberated CO is a very strong reducing agent, which reduced almost all kinds of oxygen-containing functional groups present in GO, and partly reduced GO (Acik M., et. al., 2011). Defects in rGO are detrimental to its performance, as they negatively affect its electrical conductivity, mechanical strength, and chemical stability. Therefore, controlling the extent of destructive degradation is critical to achieving high-quality rGO.

The Kerosene medium showed a great advantage in degradation process that the inert medium accelerates the free radical formation and forces the radicals to leave the medium by showing a repulsive force at a high temperature. So, the kerosene as a reduction medium provides a high rGO yields with continuous defect free sheets and the higher temperature favored by the shortening of the reduction time.

3.3.3. Application of synthesized rGOs for antimicrobial activity study

The synthesized GOs and Different rGOs were applied for the Antimicrobial Activity of GOs and Different rGOs (Mann R., et. al., 2021), (Afrin S., et. al., 2022), (Liu S., et. al., 2011).

The antibacterial properties of Sample-1 (rGO-K220, Powder) and Sample-2 (rGO-KAA, Powder) were evaluated in this study. The results indicated that both samples effectively suppressed the growth of pathogenic bacteria, albeit with varying potency. As shown in Table 3.9 and Figure 3.19, the 5.0 mg/ml concentration of Sample-1 produced the largest zone of inhibition against Bacillus subtilis (19.5 ± 0.25 mm), while the smallest zone of inhibition was observed against Escherichia coli (8.0 ± 0.50 mm). Similarly, the 5.0 mg/ml extract of Sample-2 demonstrated the highest inhibitory effect against B. subtilis (13.0 ± 0.50 mm) but showed no inhibitory effect against any Gram-negative bacteria. The positive control exhibited significant inhibitory zones against all bacterial strains, while the negative control displayed no antibacterial activity.

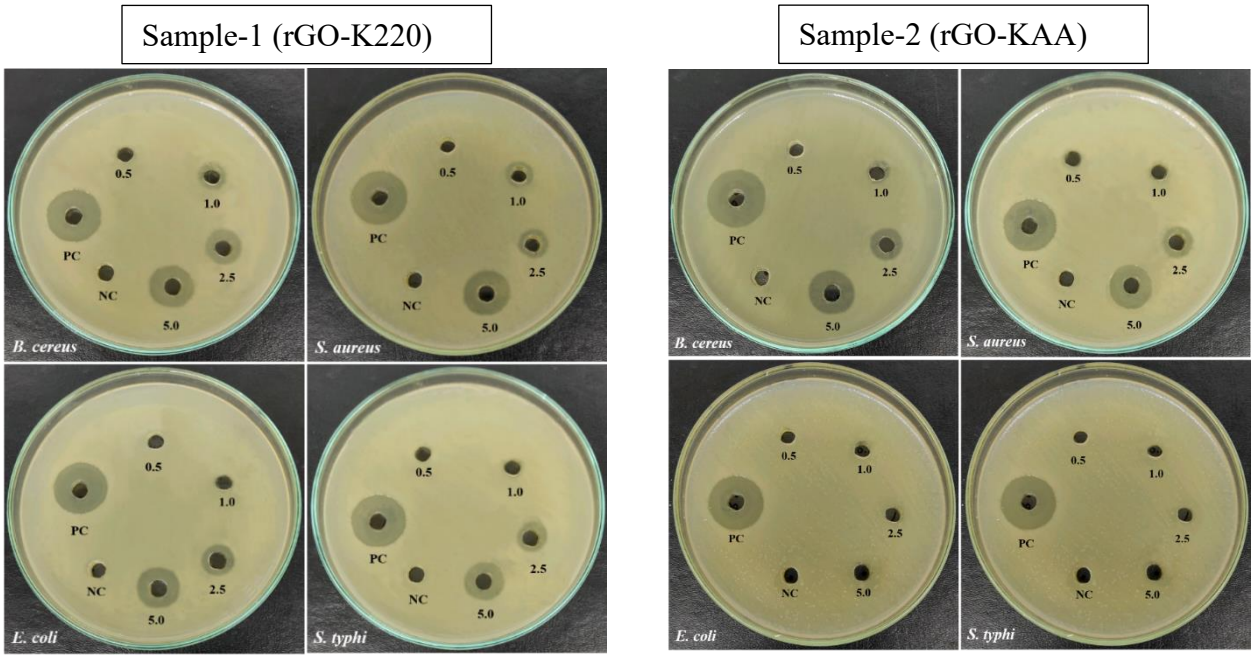

Figure-3.23: Antibacterial activity of rGO Samples- A) rGO-K220, B) rGO-KAA. 'PC' denotes tetracycline as the positive control, while 'NC' indicates 10% DMSO as the negative control.

This study highlights that the antibacterial activity of the yellow pigments correlates positively with the concentration of both extracts and the corresponding zones of inhibition.

These findings align with previous research (CLSI, 2019) (CLSI, 2019) (Barry A. L., 2007). (Ramamoorthy H., et. al., 2021). In recent years, the increase in microbial resistance and the adverse effects associated with antibiotics have led to significant interest in natural antimicrobial substances. These compounds offer promising alternatives for controlling bacterial infections with minimal cost and side effects. Consequently, the present study focuses on the antibacterial activity of these natural products.

Table-3.9: Evaluation of the antibacterial activity of different concentrations of Sample-1 and Sample-2 was performed using the agar well diffusion assay.

Sample (mg/ml)	**Gram-positive bacteria**		**Gram-negative bacteria**	
	***B. subtilis* ATCC 11774**	***S. aureus* ATCC 9144**	***E. coli* ATCC 11303**	***S. typhi* ATCC 13311**
rGO-220	Zone of Inhibition in mm			
0.5 mg/ml	-	-	-	-
1.0 mg/ml	6.20±0.00	6.00±0.35	-	-
2.5 mg/ml	11.0±0.21	8.50±0.31	6.50±0.00	6.50±0.00
5.0 mg/ml	19.5±0.25	17.0±0.50	8.5±0.50	10.3±0.15
rGO-KAA				
0.5 mg/ml	-	-	-	-
1.0 mg/ml	-	-	-	-
2.5 mg/ml	8.00±0.00	8.00±0.00	-	-
5.0 mg/ml	13.0±0.50	11.5±0.29	-	-
Positive control	27.5±0.21	27.0±0.00	23.0±0.50	22.5±0.50
Negative control	-	-	-	-

"-" indicates No Zone of inhibition.

3.4. Conclusions

GOs were synthesized using the acid liquor recycling technique in order to lower the production costs, and the product consistency can be maintained with product quality. The GOs with 66.75% oxygen to carbon were obtained. The synthesized GOs were softly and hardly thermally treated under polar and nonpolar solvent media to get thermally treated rGO. The degree of reduction of GOs in water at 98 ^{o}C for 48 hours was reduced to 45.39% oxygen content, and 96 hours was reduced to 32.68% oxygen content were achieved. The reduction method could reduce hydroxyl (-OH), more than carbonyl (>C=O) and epoxy (C-O-C) groups. The degree of reduction of GOs in nonpolar medium kerosene at 180 ^{o}C for 1 hour were reduced to 17.77% oxygen content and at 220 ^{o}C for 1 hour was reduced to 8.86% oxygen content was achieved. The reduction method could reduce all of the hydroxyl (-OH) groups and most of the carbonyl (>C=O) and epoxy (C-O-C) groups, and only very few (>C=O) and (C-O-C) groups remain. The double reduction process of rGO converts to extremely rGO with an oxygen content of less than 2.49% according to XPS analysis. The XRD analysis also confirms the degree of reduction by the various thermal treatments, with the formation of heterogeneous nanocrystalline and amorphous rGO. SEM and TEM images show the formation of a few-layer graphene. This nonpolar and extremely rGO shows very significant resistance against some gram-positive and gram-negative bacteria as *B. subtilis, S. aureus, E. coli,* and *S. typhi,* but kerosene-reduced rGO does not show any antimicrobial activities against gram-negative bacteria.

CHAPTER-4

Microwave Assisted Rapid Exfoliation of Graphite to Graphene and Its Application for the Removal of Acid Blue Dye from Aqueous Solution

Abstract

This study investigates a very fast, cost-effective, and eco-friendly method for synthesizing few-layer graphene (FLG) via microwave-assisted exfoliation of graphite, aiming to address water pollution caused by synthetic dyes like Acid Blue-25. Using ammonium bicarbonate as an exfoliating agent, the method employs solvent-free microwave irradiation and high pressure generated from NH_4HCO_3 decomposition to exfoliate graphite into high-quality graphene sheets with minimal defects. The graphene products were characterized using FT-IR, FT-Raman, and UV-Vis spectroscopy, XRD, FE-SEM, and XPS analysis, confirming their structural and functional properties suitable for adsorption applications. Four graphene samples were synthesized using varying NH_4HCO_3 ratios (1:1, 1:2, 1:3, and 1:4). Batch adsorption experiments demonstrated that graphene achieved 98–100% dye removal efficiency within 3 hours, outperforming activated carbon (89%) and graphite (95%) at 100 ppm dye concentration and pH 2.0. The process adhered to the Langmuir isotherm model, indicating monolayer adsorption with a maximum capacity of 180 mg/g, and followed a pseudo-second-order kinetic model, suggesting chemisorption as the primary mechanism. Thermodynamic analysis confirmed the process was spontaneous and endothermic, and demonstrated excellent reusability, retaining over 85% efficiency after five cycles. The findings highlight graphene's superior adsorption efficiency, rapid equilibrium, and scalability for industrial wastewater treatment. This study establishes microwave-exfoliated graphene as a promising material for sustainable dye remediation, with potential applications in treating industrial effluents and contaminated water systems.

Objectives

According to the literature review, although all the exfoliation processes involving the chemical process are widely used, they have several disadvantages, including the use of hazardous chemicals, production of toxic by-products, and the potential for incomplete removal of oxygen-containing functional groups, which may compromise the material's quality. Additionally, the process often requires lengthy reaction times and complex post-treatment steps, making it less environmentally friendly and time-efficient. In contrast, microwave-assisted synthesis of graphene offers significant advantages, such as rapid processing, uniform heating, and energy efficiency. This method facilitates the reduction of GOs to high-quality rGO without extensive use of harmful chemicals, aligning with sustainable and eco-friendly practices. So, the objectives are-

i. Synthesis of graphene by microwave-assisted rapid and direct exfoliation method to evaluate the effect of variation of intercalating agent.
ii. Searching for a suitable microwave irradiation and exfoliation arc-tolerant dish for graphene synthesis.
iii. Characterization of synthesized microwave graphene.
iv. Application of MG for the removal of acid blue dye from aqueous solution and studies on the isotherm and kinetics of the adsorption process.

4.1. Introduction

Graphene, a two-dimensional carbon allotrope discovered in 2004 and became highly renowned for its exceptional mechanical strength, superior thermal and electrical conductivity, and near-total transparency, attributes stemming from its sp^2-hybridized atomic structure (Dedkov Y., et. al., 2015), (Ares P., et. al., 2022), (Novoselov, et al., 2004), (Ono T., et al., 2017). Its semi-metallic nature facilitated ballistic charge transportation and established it as a cornerstone of two-dimensional materials with diverse applications. Beyond its utilization in electronics and materials science, its versatility extended to energy storage, supercapacitors (Dedkov Y., et. al., 2015), (Geim A. K., et. al., 2007), pollutant adsorption, and flexible alternatives to metals. It also became pivotal in nanocomposites and sensor technologies. Advancements in synthesis methods have further broadened its applicability, cementing graphene's role as a transformative material across scientific and industrial domains as electronics and materials science (Geim A. K., et. al., 2007), (Yu X., et al., 2017) energy storage, supercapacitors and effectively adsorbs pollutants and flexible alternative to metals (Kogan E., 2022), sensors to nanocomposites (Luan D., 2023), (Zou L., et al., 2018), (Farjadian F., et al., 2020), (Kogan E., et. al., 2022), (Singh J., et. al., 2018).

The graphene formulation already included both top-down and bottom-up approaches (Jilani A. I., et al., 2018), (Biliak R., 2023), (Zhang T., et. al., 2012). Electrochemical exfoliation also involved breaking down graphite into graphene sheets (Priyanka A., et. al., 2024), (Kornilov D. Y., et. al., 2020). Mechanical exfoliation incorporated high-quality graphene (Norman J., et. al., 2023), (Yip T. M., et. al., 2023), composite development enhances properties (Priyanka A., et. al., 2024), (Norman J., et. al., 2023), laser addition in pyrolysis (Kumara K. J., et. al., 2021), (Mahmood F., et al., 2023). Achievement of cost-effective, large-scale production of high-quality graphene has also been developed (Priyanka A., et. al., 2024), (Mahmood F., et al., 2023), along with many approaches including simplicity, scalability, and cost-effectiveness. Microwave-assisted methods offered a rapid, uniform, and controlled approach to graphene production, yielding larger sheets with fewer defects compared to conventional techniques (Shang J., et al., 2012), like chemical oxidation-reduction, chemical vapor deposition (CVD), and mechanical exfoliation (Perreault F., et. al., 2015), (Kumar P. V., et al., 2014). Techniques such as the microwave-assisted exfoliation method emerged as efficient than chemical oxidation reduction and cost-effective alternatives. A study comprehensively examined the principles of microwave technology, the mechanisms involved in graphene exfoliation, and the

benefits and challenges associated with highlighting its potential to overcome the limitations of traditional graphene synthesis methods (Zhu Y., et al., 2010). However, as mentioned earlier, the main challenges in producing graphene were limited in scalability, cost-effectiveness, and producing high-quality sheets without introducing too many defects and contaminants (Balandin A. A., et al., 2008), (Stankovich S., et al., 2006).

Traditional methods such as chemical vapor deposition (CVD) and mechanical exfoliation are highly effective in producing high-quality graphene, but they were not claimed as easily scalable for industrial applications (Li X., et al., 2009). Chemical oxidation-reduction of GOs was claimed to be another popular method used for graphene synthesis, but it often resulted in reduced graphene with significant defects and limited conductivity. Thus, the microwave-assisted method emerged as a promising alternative (Stankovich, et al., 2007), (Su C., et. al., 2013). Microwave radiation evolved as an electromagnetic radiation with wavelengths ranging from one millimeter to one meter, corresponding to frequencies between 300 MHz and 300 GHz.

In practical applications, microwaves are most commonly encountered in the range of 2.45 GHz, which is used in household microwave ovens and many industrial microwave systems (Meredith R. J., 1998). Unlike conventional heating methods, which rely on the conduction of heat from an external source, microwave heating works by directly interacting with the material at the molecular level (Metaxas A. A., et. al., 1983), (Thostenson E. T., et. al., 2001).

Microwaves interact with polar molecules in a material, causing them to rapidly oscillate and produce heat through dielectric loss. This mechanism allows microwaves to penetrate deeply and evenly into the materials, providing volumetric heating rather than surface heating (Kuhlmann J., et. al., 2021), (Gawande M. B., et. al., 2014), (Anis H., et. al., 2021), (Chandrasekaran S., et. al., 2012). This rapid, uniform heating is the key reason why microwave-assisted processes are highly attractive for material synthesis and modification, including the production of graphene (Rojas C. C., et. al., 2022), (Grewal A. S., et. al., 2013). The ability of microwave to rapidly heat the materials to high temperatures in short periods of time without excessive energy loss makes microwave-assisted methods particularly well-suited for graphene exfoliation. Additionally, microwave processing can be precisely controlled by adjusting the power and frequency, which is important for achieving desired material properties

in graphene (Zhang Y., et. al., 2022), (Jiang F., et. al., 2017), (Gao C., et. al., 2023), (Chen X., et. al., 2019), (Zhang Y., et. al., 2023), (Jakhar R., et. al., 2020). The key to producing graphene from graphite involves breaking its weak forces to separate the individual graphene layers, and this process is known as exfoliation (Mouni A., et. al., 2023), (Sumdani M. G., et. al., 2021), (Liu Z., et. al., 2022), (Moosa A., et. al., 2021).

Microwave-assisted exfoliation of graphite was achieved by the exfoliation due to the rapid heating capability of microwaves. In many cases, the exfoliation process was facilitated by the presence of certain compounds that decomposed under microwave irradiation and released as gases that generate high internal pressure between the graphite layers (Wang Y., et. al., 2022), (Dubey A., et. al., 2024), (Cheng J., et. al., 2023), (Jiang F., et. al., 2017). One such compound is ammonium bicarbonate (NH_4HCO_3), which decomposes into water vapor (H_2O), carbon dioxide (CO_2), and ammonia (NH_3) when heated by microwaves (Raj R. S., et. al., 2023), (Lin J., et. al., 2017). The decomposition of NH_4HCO_3 within the interlayer spaces of graphite, which generates high-pressure gases that act as a driving force to overcome the van der Waals forces, resulting in the separation of individual graphene layers (Liu Z., et. al., 2022), (Lin J., et. al., 2017), (Zhang Y., et. al., 2023). This rapid exfoliation process can occur within a matter of minutes, compared to hours or even days in some conventional methods (Liu X., et. al., 2023), (Ramezani M. J., et. al., 2024). Moreover, the use of microwaves allows for the exfoliation process to occur without the need for harsh chemicals or excessive mechanical force, which can introduce defects or contaminants into the graphene. This makes microwave-assisted exfoliation an attractive method for producing graphene with fewer defects and higher purity (Gao Y., et. al., 2023), (Wu W., et al., 2020), (Kumar R., et. al., 2022), (Kumar A., et. al., 2020), (Zhou Y., et. al., 2023), (Jiang F., et. al., 2017).

Microwave-assisted graphene manufacturing is increasingly popular for large-scale applications due to its numerous advantages over traditional methods. It completes the exfoliation process in minutes and reduces energy waste through efficient volumetric heating. The simplicity of the microwave process allows for easier scalability compared to complex techniques like CVD (Gao Y., et. al., 2023), (Liu X., et al., 2013), (Ghorbani M., et. al., 2022), (Kumar A., et. al., 2020). Additionally, it minimizes structural defects, producing higher-quality graphene. This method is also more sustainable, requiring fewer harmful chemicals and less mechanical processing, while being more cost-effective overall (Zhou Y., et. al., 2023), (Wang

J., et. al., 2022). The uniformity and effectiveness of graphene sheets in certain applications can be affected by the difficulty of managing their size and thickness, even though microwaves can exfoliate materials quickly (Ghorbani M., et. al., 2022), (Kumar R., et. al., 2022). It can take a lot of effort and experimentation to optimize variables like microwave power, irradiation duration, and precursor materials for successful microwave-assisted manufacturing. It can be difficult to maintain uniform quality over large quantities because of problems, including incomplete exfoliation and residual contaminants, even though these techniques usually produce graphene with fewer flaws. Microwave techniques provide a practical and economical way to create graphene for these various large-scale uses, advancing several industries (Kumar R., et. al., 2022), (Chang D. W., et. al., 2016). Despite its advantages, microwave-assisted graphene production faces limitations, such as difficulty in controlling the size and thickness of graphene sheets, which can affect uniformity and performance (Liu Z., et. al., 2023), (Xie X., et. al., 2019). Additionally, optimizing parameters like microwave energy and irradiation time requires extensive experimentation, the need for optimization, and the potential issues with impurities and inconsistent quality (Kumar R., et. al., 2022), (Chang D. W., et. al., 2016). Challenges remain in ensuring consistent quality across large batches, as residual impurities and incomplete exfoliation can still occur during the synthesis process (Zhang Y., et. al., 2023), (Sun J., et al., 2023).

The removal of two cationic dyes, methylene blue (MB) and rhodamine B (RhB), using GOs, fluorinated-GOs, and interconnected rGO (IC-rGO) was investigated from the aqueous solution (Mao B., et. al., 2020). The effect of the initial concentrations of MB and RhB was examined, and the maximum adsorption capacities of 403.3 mg/g and 686.6 mg/g were obtained. The adsorption kinetics study demonstrated that GO was found to be a very promising adsorbent for wastewater treatment and that GOs can effectively separate cationic species from anionic compounds.

In this experiment, we evaluate the effect of the quantity of intercalating agent in the yield and properties of graphene. On the other hand, we tried to minimize the environmental issues by modifying the microwave oven by absorbing the ammonia gas evolved in a mineral acid solution during exfoliation. Several experiments were done to control the degree of exfoliation and the particle sizes.

4.2. Materials and methods

4.2.1. Materials

4.2.1.1. Raw materials used for microwave exfoliation

The chemicals used to perform this experiment were collected from the following sources: Extra pure graphite fine powder of purity 98% with particle size 60 mesh was collected from Loba Chemie Pvt. Ltd., Mumbai, India; reagent grade ammonium bicarbonate (NH_4HCO_3) with purity 98.5% and reagent grade hydrochloric acid with purity 37% were from Merck, Darmstadt, Germany; Industrial grade Acid blue dyes (ABD), trade name Acid blue-119, were collected from Dycin Chem Pvt. Ltd. Dhaka, Bangladesh and were used directly.

4.2.2. Methodology

4.2.2.a. Instrumental methodology

The instruments were used for the microwave exfoliation and characterization of the MG and its application for the removal of Arsenic (III) from water are described below-

4.2.2.1. Microwave oven

A microwave oven (LG, Taiwan, 2450 MHz, 800 W) is an electric oven that is used for heating by electromagnetic irradiation in the microwave frequency range. This microwave frequency induces polar molecules in it to rotate and produce thermal energy in a process known as dielectric heating. Microwave oven heats materials quickly and efficiently because excitation is fairly uniform in the outer 25–38 mm (1–1.5 inches) of a homogeneous, high-water-content or polar material.

4.2.2.2. Measurements of thermal properties by thermogravimetric analyzer (TGA)

The detailed description of this instrument, including the operating conditions of the MG samples are same as the instrumental method described in chapter 3 (section 3.2.2.1.2).

4.2.2.3. FT-IR spectroscopic analysis

The detailed description of this instrument, including operating conditions of the MG samples are same as the instrumental method described in chapter 2 (section 2.2.2.4)

4.2.2.4. FT-Raman spectroscopic analysis

The detailed description of this instrument, including operating conditions of the MG samples are same as the instrumental method described in Chapter 2 (section 2.2.2.5).

4.2.2.5. X-Ray diffraction (XRD) analysis

The detailed description of this instrument, including operating conditions of the MG samples are same as the instrumental method described in Chapter 2 (section 3.2.2.1.5).

4.2.2.6. UV-Vis. spectroscopic analysis

The detailed description of this instrument, including operating conditions of the synthesized rGO samples are same as the instrumental method described in Chapter 2 (section 2.2.2.6).

4.2.2.7. Image analysis using SEM-EDX

The detailed description of this instrument, including the operating condition of the synthesized MG samples are same as the instrumental method described in Chapter 2 (section 2.2.2.8).

4.2.2.8. Roller milling intercalator

Roller Milling Grinders are a very commonly used laboratory milling machine. The rubber-coated parallel rollers rotate horizontally in the same direction, helping to rotate the intercalation jar at a desired rpm. This rotation creates friction between spherical balls and cylinders. It was used for the intercalation of the purified graphite powder. Sufficient friction forced the intercalating agents to intercalate graphite powder. The raw materials were charged into a cylindrical container with zirconia balls of different diameters and rotated at 120 rpm for several hours.

4.2.2.9. Muffle furnace

A muffle furnace is a very common laboratory instrument used to heat materials to extremely high temperatures whilst isolating them from the fuel. A muffle furnace (Carbolite-1100, Germany) can be operated at various temperatures for removing combustible organic or inorganic compounds at a definite temperature. It was used for the isolation of a selective material from the combustible part with specific properties. The microwave-exfoliated graphene was purified using a muffle furnace at 500 ^{o}C for 20 minutes by dissociating the intercalating agents.

4.2.3. Experimental procedure

The microwave exfoliated graphene preparation can be done using the following steps-

4.2.3.1. Purification of graphite powder by 5% HCl acid wash

At first, the graphite powders (50.0 g) were purified using acid wash, where 5% HCl solution (250 mL) was utilized for the washing. The mixture was heated at 98 ^{o}C for 2 hrs. with a hotplate magnetic stirrer. Then the slurry was filtered and washed with sufficient DI water to obtain a pH of 7.0. Then it was dried in a fridge dryer and stored as a feed material.

4.2.3.2. Preparation of intercalated graphene

The purified graphite sample (5.0 g) was measured and taken in an intercalation jar. A fixed ratio of intercalating agent was mixed in it. The ratio of NH_4HCO_3 intercalating agent to graphene was maintained at graphene : intercalator ratios of 1:1, 1:2, 1:3, and 1:4. Zirconia ceramic ball beads of varying diameters (3 mm, 5 mm, 8 mm, and 10 mm) were placed into the Jar to ensure optimal grinding and mixing. The jar was then agitated in a roller milling machine at a speed of 120 rpm for 2 hours to promote efficient intercalation of NH_4HCO_3 into the graphite matrix (Skorupska M., et. al., 2021).

4.2.3.3. Vacuum drying of intercalated graphene

Vacuum drying is essential for the microwave exfoliation of graphene. After the intercalation process, carefully transferred to a drying container to prepare it for moisture removal. The mixture was subsequently placed in a vacuum oven, where it was heated at a controlled temperature between 60 °C and 70 °C under a vacuum pressure of 50 mm Hg. This drying phase lasted for 30–40 minutes, allowing any absorbed moisture or residual solvent to be efficiently removed. The vacuum environment, coupled with moderate heating, ensured that the delicate structure of the intercalated graphite was preserved while achieving thorough dehydration.

4.2.3.4. Microwave exfoliation of intercalated graphene

Once the drying process was complete, the mixture was gradually cooled to room temperature. This cooling phase ensured that the NH_4HCO_3-intercalated graphite was sufficiently dried and ready for further characterization or use in subsequent applications, with minimal risk of moisture interference in its performance. The entire process was designed to maintain material

integrity while optimizing the intercalation and drying conditions. The intercalated graphite was then exposed to microwave irradiation (MWI) for 60 seconds, resulting in rapid exfoliation accompanied by intense light and arcing (Voiry D., et al., 2016). This exfoliation was triggered by the thermal decomposition of NH_4HCO_3, which dissociated into ammonia, water, and carbon dioxide, releasing heat. The generated heat was sufficient to separate the graphite layers, producing bursts of light and arcs.

4.2.3.5. Purification of MG

Upon completion of the reaction, the exfoliated product was collected, containing some residual, undissociated NH_4HCO_3. To ensure complete decomposition of NH_4HCO_3, the sample was subsequently heated in a muffle furnace at 500 °C for 15–20 minutes, effectively removing any remaining NH_4HCO_3 and yielding a purified exfoliated graphite product. This final product was then prepared for characterization. The product yields were calculated based on the raw graphite powder and were listed in Table 4.1.

Table-4.1: Yield of purified MG product after purification

Exp. No.	Amount of Graphite (g)	NH_4HCO_3 (g)	Feed ratio	MG (g)	Yield (%)
MG-1	10.0033	0.00	1:0	9.9915	99.99
MG-2	10.0012	10.0026	1:1	9.9882	99.87
MG-3	10.0008	20.0031	1:2	9.9904	99.84
MG-4	10.0025	30.0014	1:3	9.9832	99.89
MG-5	10.0018	40.0022	1:4	9.9812	99.79

4.2.4. Application of MG for the removal of textile dyes

Application of the microwave graphene for the removal of acid blue-25 (AB-25) dye from the aqueous solution involves the following steps-

4.2.4.1. Preparation of stock solution of acid blue-25 dye

At first, the stock solution of AB-25 dye was prepared by dissolving 2.0 g of dye in 10.0 Lt. DI water in order to obtain a 200-ppm solution concentration to use as a feed material throughout the measurement. The adsorption efficiencies and adsorption kinetics experiments were carried out with the solution. The solution was diluted to 100 and 50 ppm to observe the effect of the initial concentration. Figure 4.12 shows the 100-ppm AB-25 dye solution in water. Determination of the calibration curve using the stock solution from the aqueous solution.

4.2.4.2. Determination of calibration curve using the stock solution

Acid blue dye is an anthraquinone-based aromatic amine functional sodium sulfonate structural compound. It absorbs Visible light at the maximum absorption wavelength (λ_{max}) at 602 nm. An ABD solution of different concentrations of 2 ppm, 5 ppm, 10 ppm, 20 ppm, 50 ppm, and 100 ppm was prepared from the stock solution by serial dilution in water. The solutions were measured UV-Visible light absorption spectrum in the range 400 nm – 800 nm. The UV-Vis light absorption spectrum is shown in Figures 4.1 and 4.2 and Table 4.2.

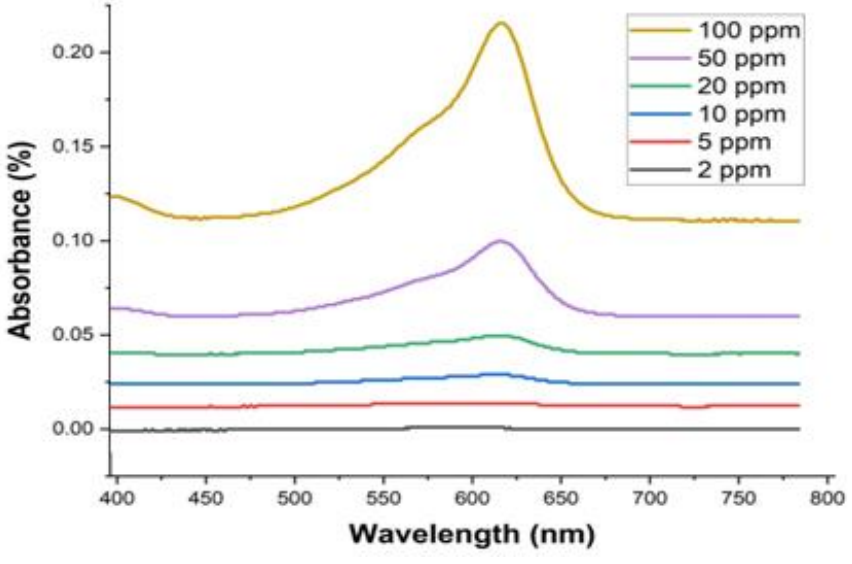

Figure-4.1: UV-Visible light absorption spectrum of ABD solution in concentration ranges of 2 ppm, 5 ppm, 10 ppm, 20 ppm, 50 ppm, and 100 ppm at 602 nm wavelength.

The maximum absorption % data were arranged against the dye concentration to obtain the calibration curve. Figure 4.5 shows the linearity and R^2 value of the calibration curve, which is 0.999.

Table-4.2: UV-Visible light absorbance % of Acid blue dye solution at wavelength (λ_{max}) at 602 nm for Calibration curve-

Sample no.	Wavelength (nm)	Concentration (ppm)	Absorbance (%)
1	602	2	0.002
2		5	0.005
3		10	0.009
4		20	0.020
5		50	0.048
6		100	0.102

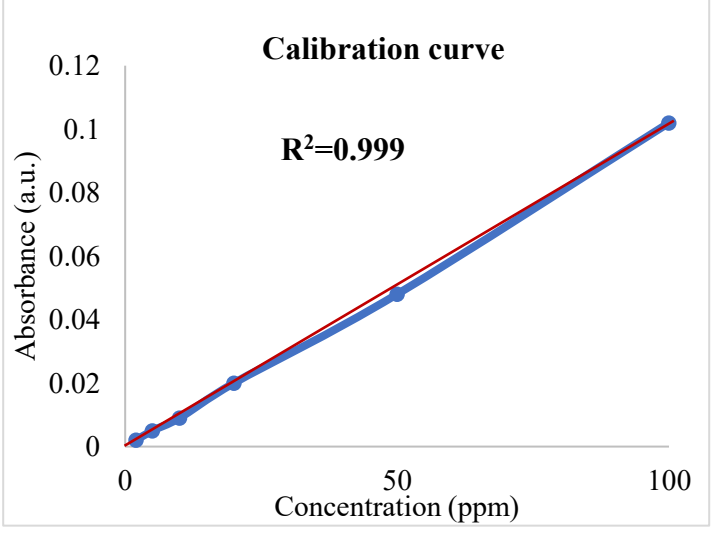

Figure-4.2: Calibration curve of the acid blue dye, obtained by plotting absorbance % against concentration of dye samples.

From the calibration curve, it can be observed that the absorbance plots form a linear straight line, which lies in the equation-

$$y = m.x + c \text{----------(14)}$$

Where Y is the absorbance % of the Acid blue dyes, X is the concentration of the Acid blue dyes, and m is the slope of the calibration line.

The linearity of the curve is good, and its recreation value $R^2 = 0.998$. For this dye in a water medium, m is constant, and its value is 0.001. As the equation goes through the origin, C is 0. So, the equation stands-

$$y = 0.001x \text{ ----------(15)}$$

From this equation, if we have the absorbance % of any unknown solution, we can have the concentration value.

4.2.4.3. Adsorption of AB-25 dye by MG from the aqueous solution

For the adsorption experiments, the stock solution was diluted to three initial concentrations of 50 ppm, 100 ppm, and 200 ppm. The dosage of microwave graphene adsorbents (MG-1, MG-2, MG-3, and MG-4) was measured in amount of 0.1 g for the 500 mL 100 ppm solutions of ABD samples. The experiments were designed for three initial concentrations of 50 ppm, 100 ppm, and 200 ppm. The 500 mL solution for each initial concentration was taken in different beakers and their pH was adjusted to 2.0 using HCl and NaOH solutions. Then 0.05 g, 0.1 g, and 0.2 g of MG of each type were added to the beaker and stirred at 90 rpm. Then, 5 mL solutions from each beaker were collected after each 30 minutes and filtered immediately using a 0.2-micron nylon syringe filter and preserved in a separate tube. The samplings were continued for 12 hours, and their concentration was measured using UV-Vis. spectrophotometer. The data were recorded in Table 4.9 % Removal was calculated by

$$\% \text{ Removal} = \frac{Co - Ce}{Co} \times 100 \text{ ----------(16)}$$

Where C_o = Initial dye concentration

C_e = Dye concentration at equilibrium

The equilibrium concentration (C_e) of the dye solutions was determined by referring to the corresponding calibration curve. The equilibrium sorption capacity (q_e) was calculated by:

$$q_e = \frac{Co - Ce}{m} \times V \text{ ----------(17)}$$

Where C_o = Initial concentration

C_e = Concentration at equilibrium

m = Amount of adsorbent

V = Volume of solution

4.2.4.4. Removal of the AB-25 dye using MG in a column method

A 0.5 g sample of microwave-exfoliated graphene was utilized as a fixed bed in a burette column to evaluate its dye removal capacity. A 100 ppm Acid Blue-25 Dye (ABD) solution was passed through the graphene bed at a controlled flow rate of 20 drops per minute. The process continued until the effluent solution reached a clarity corresponding to a dye concentration of 2 ppm. The total volume of the treated solution was recorded to determine the dye removal capacity of the graphene sample. This setup enables a continuous flow adsorption study, providing a practical assessment of the graphene's performance under dynamic conditions. The amount of the ABD solution decolorized by the graphene samples was quantified and presented in Table 4.8.

4.2.4.5. Determination of the AB-25 dye-removing efficiency using the different MG

The removal efficiency of Acid blue dye by different microwave-exfoliated graphene samples can be determined through batch adsorption experiments under controlled conditions. First, a 500-ppm concentration of the AB-25 dye solution of 500 mL is placed in a beaker. Then, different graphene samples of 0.1 g each are placed in separate containers containing dye solution. The mixtures are agitated at 90 rpm with a magnetic stirrer for 24 hours to ensure uniform contact between the dye molecules and the adsorbents. Then the concentration of the remaining solution was evaluated to measure the adsorption performance under consistent conditions. After the adsorption process, the solutions are filtered or centrifuged to separate the graphene adsorbents. The residual dye concentration in the supernatant is measured using UV-Vis spectrophotometry at the dye's maximum absorbance wavelength. Removal efficiency is calculated using the equation:

$$\text{Removal Efficiency (\%)} = \frac{Ci - Ce}{Ci} \times 100 \text{----------(18)}$$

Where Ci and Ce are the initial and equilibrium dye concentrations, respectively. This method allows comparative assessment of graphene samples for dye removal. The results thus obtained are listed in Table 4.3.

Table-4.3: The concentration of the solution after absorption for 24 hours by 0.1 g of different exfoliated graphene.

Graphene	Amount of MG (g)	Concentration of final dye solution (ppm)	dye removing ability (mg/g)
MG-0	0.2	268.6	231.4
MG-1	0.2	224.5	275.5
MG-2	0.2	181.3	318.7
MG-3	0.2	117.9	382.1
MG-4	0.2	27.2	472.8

4.3. Results and discussion

4.3.1. Synthesis of MG

The synthesis procedure involves several sensitive steps

4.3.1.1. Purification of graphite powder

As the Graphite powder was used as a feed raw material, it must be purified before use. Because it contains a lot of contaminants, especially metal salts, which may affect the exfoliation process.

Table-4.4: Purification of Graphite powder by 5% hydrochloric acid solution.

Exp. No.	Graphite powder (g)	5% Hydrochloric acid solution (mL)	Time (hrs.)	Purified Graphite powder (g)	Yield (%)
01.	50.0	250	2.0	49.91	99.83
02.	50.0	250	2.0	49.92	99.84

4.3.1.2. Exfoliation procedure

A microwave-assisted rapid exfoliation technique was applied for the preparation of the graphene. The process involves huge irradiation energy that dissociates the NH_4HCO_3 intercalator from the arc. Figure 4.3 shows the light and arc liberation in the microwave during

exfoliation. This release of energy was powerful enough to damage materials like glass, ceramics, and concrete, necessitating the search for a suitable, durable container for the reaction. Since metallic containers were unsuitable due to their interaction with microwaves, identifying a compatible material for this process became a focus of the research.

Figure-4.3: Microwave exfoliation of Graphene using microwave arc radiation

4.3.1.3. Intercalation process

The production procedure of microwave-assisted rapid exfoliation of graphene is shown in Figure 4.4. It is the fastest of all the production processes to produce single-crystalline pristine graphene produced directly from graphite. The stepwise production process is described with precautions. This method is highly suitable for production in bulk (Wu J., et al., 2020). The time of intercalation is very important. It takes about 2-4 hours for the intercalation process to complete, depending upon the amount of intercalating agent. The other important factors are the amount and size of the rotating ball compared to the feed, and the rotation/minute of the jar. It is better to maintain 90-120 rpm with 3, 5, 8, 10 mm mixture diameter balls in the jar.

4.3.1.4. Vacuum drying

Drying is a critical step in the preparation of graphite powder, whether natural or synthesized, to ensure the removal of impurities such as soil, catalysts, or other foreign particles. These impurities, if not removed, can adversely impact the subsequent intercalation process and compromise the quality of the final product. Proper drying is particularly essential before the exfoliation process, which involves microwave irradiation that interacts with NH_4HCO_3, producing electromagnetic irradiation. This interaction is sensitive to the presence of moisture, as even trace amounts can significantly affect the efficiency of exfoliation or the quality of the exfoliated graphene. During exfoliation, the presence of moisture in intercalated graphite

powder can result in arc generation that disrupts the reaction dynamics. As NH_4HCO_3 chemicals readily absorb atmospheric moisture, intercalated graphite must be thoroughly dried to minimize adverse effects on the exfoliation process. Traditional heating methods, such as oven drying, are not suitable due to the heat sensitivity of NH_4HCO_3, which dissociates rapidly at elevated temperatures. To address this challenge, vacuum drying was employed as an effective method for moisture removal, ensuring the stability of NH_4HCO_3 while achieving sufficient drying.

The vacuum drying process is conducted at a pressure of 30–50 mmHg and a temperature of 60 °C, conditions optimized to remove moisture without causing dissociation of NH_4HCO_3. By applying vacuum drying for a short duration, the trace amounts of moisture can be eliminated, preserving the integrity of the intercalated graphite and enhancing the efficiency of the exfoliation process. This step is crucial for obtaining high-quality exfoliated graphene, as it ensures a consistent and controlled reaction environment during exfoliation. Proper drying not only protects the chemical properties of NH_4HCO_3 but also contributes to the overall reliability and reproducibility of the synthesis process.

4.3.1.5. Microwave irradiation process

The exfoliation process is very easy and spontaneous. No trouble occurs if all the conditions are maintained properly, e.g., plate type, plate thickness, moisture content in plate, cooling of plate, thickness of feed materials, time of exfoliation, etc. No loss of materials occurs during the procedure except for NH_4HCO_3 dissociation.

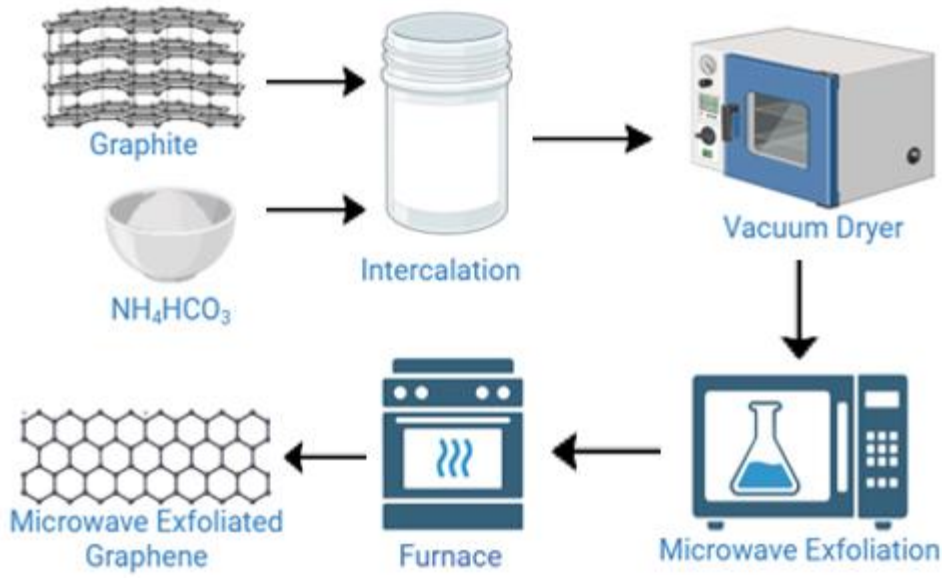

Figure-4.4: Flow diagram for the production of microwave-assisted rapid exfoliation of graphene.

For the investigation of the effect of NH_4HCO_3 ratios with graphite, a series of products was prepared, and their properties were evaluated in comparison. The controlled experiments were conducted using the same procedure without adding NH_4HCO_3 to observe the effects of NH_4HCO_3 on the exfoliation process. Additionally, experiments were conducted by varying the feed weight ratio of graphite to NH_4HCO_3 (1:1, 1:2, 1:3, and 1:4) to optimize reaction conditions and assess the impact of NH_4HCO_3 concentration on the exfoliation outcome. The entire process, illustrated in Figure 4.4, demonstrates the potential of MWI in producing exfoliated graphite with the controlled decomposition of intercalants in a carefully designed, stable environment. The product at different feed ratios and the yields were recorded in Table 4.1.

The purification of exfoliated graphene is another important step because some of the NH_4HCO_3 remain undissociated, and this impacts the graphene properties. As the NH_4HCO_3 dissociated around 60 ^oC and the MG product dissociated over 650 ^oC. So, it is better to heat the product graphene at 500 ^oC for 20 minutes to dissociate completely.

4.3.1.6. Selection of microwave irradiation and exfoliation arc-tolerant specimen (Dish)

The exfoliation process generates significant arc and heat energy, leading to intense thermal shocks that can damage the exfoliation dish used to hold the intercalated graphite within the microwave oven. This damage occurs almost instantaneously due to the rapid energy release. Additionally, certain materials are unsuitable for the exfoliation process as they either fail under

the irradiation-induced thermal shock or do not exfoliate effectively due to the influence of electric field effects on their conductivity. A comprehensive list of materials destroyed during exfoliation or rendered ineffective due to electric field interactions is presented in Table 4.5, highlighting the challenges of material selection.

Table-4.5: List of Microwave and arc-proofing failed material that was destroyed during exfoliation due to irradiation shock or not exfoliated due to the electric field effects of conductance.

Sl. No.	Name of the dish	Sl. No.	Name of the dish
01.	Microwave Oven glass plate (thickness 5 mm)	02.	Ceramic plate (thickness, 3 mm)
03.	PP Plastic sheet (thickness 5 mm)	04.	Ceramic plate (thickness 7 mm)
05.	PVC Plastic sheet (thickness 5 mm)	06.	Glass plate (thickness, 3 mm)
07.	Melamine Plate (thickness 3 mm)	08.	Glass plate (thickness, 7 mm)
09.	Bricks (thickness 10-20 mm)	10.	Ceramic Tiles (thickness, 7 mm)
11.	Aluminum Plate (thickness 1 mm)	12.	Roof top tiles (thickness 30 mm)
13.	Iron sheet (thickness 5 mm)		

After various trials, refractory non-glazed decorative tiles with a minimum depth of 30 mm were selected as suitable containers, capable of withstanding the reaction conditions. Another critical parameter for successful exfoliation was the initial temperature of the container. The reaction proceeded best when the container was warm to the touch, as temperatures that were either too high or at room temperature inhibited the process. To achieve this, the tile was pre-warmed, and a thin layer of dried intercalated graphite powder was spread over it before being placed in the microwave oven for irradiation. The microwave exfoliation process was successfully conducted using 20 mm thick insulator-type wall-decorated ceramic tiles, as shown in Figure 4.5, ensuring stability and resistance to thermal shock during exfoliation.

For successful and efficient exfoliation, both the choice of material and the temperature control of the exfoliation dish are critical factors. During the exfoliation process, the dish experiences a significant, sudden rise in temperature after each cycle. Excessively high temperatures are detrimental, as they can hinder the exfoliation process and may lead to the premature decomposition of NH_4HCO_3 before arc generation occurs. Therefore, it is essential to ensure

that the dish is adequately cooled between exfoliation cycles to maintain an optimal temperature. A properly cooled dish should remain safe to touch with bare hands, preventing overheating and preserving the integrity of the process.

These considerations are essential for maintaining the stability of the process and achieving high-quality exfoliated graphene with reproducible results.

Figure-4.5. The ceramic tiles that were used for the exfoliation of intercalated graphite

So, for the successful exfoliation process, all the criteria discussed above must be maintained.

4.3.1.7. Microwave exfoliation

Another crucial factor for achieving spontaneous and uniform exfoliation is the even distribution of intercalated graphite across the dish. The layer of material should be carefully spread to maintain a thickness of approximately 1–2 mm. Uneven or lumpy layers can lead to localized heat accumulation, increasing the risk of material destruction or the decomposition of NH_4HCO_3. Proper layer uniformity ensures consistent thermal and electrical field interactions during the exfoliation process, maximizing efficiency and reducing the likelihood of defects.

4.3.1.8. Purification of exfoliated graphene

Following the exfoliation of intercalated graphite, most of the NH_4HCO_3 decomposed during the process; however, a small proportion remains undecomposed and must be eliminated to achieve a purified graphene product. Complete removal of residual NH_4HCO_3 was accomplished through thermal degradation, conducted in a controlled furnace environment at a temperature of 500 °C.

To initiate the purification process, the furnace is preheated to the target temperature of 500 °C before the sample is introduced. The exfoliated material is then heated for a precise duration of 20 minutes to ensure complete decomposition of the remaining NH_4HCO_3. This controlled thermal treatment converts residual chemicals into gaseous by-products, effectively removing them from the sample. It is critical to maintain the specified temperature and time parameters, as exceeding these conditions may lead to partial combustion of the exfoliated graphene, compromising its structural and functional integrity. The optimized purification process ensures the removal of all NH_4HCO_3 while preserving the quality of the exfoliated graphene. The resulting graphene product is free from chemical residues, making it suitable for subsequent characterization and applications. This method provides a reliable approach to obtaining high-purity graphene through precise thermal control and adherence to defined processing conditions.

Refractory ceramic tiles possess a structure similar to that of ceramic insulators, making them resistant to conductivity and unaffected by stray currents. An additional advantage of these ceramic tiles is their minimal moisture adsorption from the atmosphere. Before initiating the exfoliation process, the ceramic dish is preheated in a microwave to remove any residual moisture. It is then allowed to cool to a warm state before reuse. This preconditioning ensures optimal conditions for the exfoliation process, enabling it to proceed smoothly and spontaneously. The combination of low moisture adsorption and the preheating procedure enhances the efficiency and reliability of the exfoliation process, making refractory ceramic tiles an ideal choice for applications requiring thermal and electrical insulation.

A critical criterion for successful microwave exfoliation is the precise control of the exfoliation time. The process is typically sustained until the occurrence of arc sparking ceases, indicating completion. The standard duration for complete exfoliation is approximately 90 seconds.

However, variations are observed based on specific parameters such as the quantity of the intercalating agent, the duration of intercalation, drying conditions, and the thickness of the macerals on the ceramic dish. In some cases, sparking concludes in as little as 45 seconds, while in others, it may persist for up to 120 seconds. For instances where sparking continues beyond the standard duration, a staged approach is employed to ensure safety and process efficiency. The microwave is initially operated for 60 seconds, after which the door is briefly opened to release accumulated gases such as NH_3, H_2O, and CO_2 and to dissipate excess heat. This step prevents overheating and mitigates the risks associated with gas buildup. The microwave is then restarted and run in periodic intervals, typically for 30 seconds each, until the exfoliation process is complete. This systematic approach ensures optimal exfoliation while maintaining operational safety and accommodating variations in sample characteristics.

According to the production procedure explained above, the product yield was about 99.85% based on the feed graphite only (Table 4.1). The overall yield of the MG does not greatly depend on the amount of feed charged. It slightly depends on the quantity of intercalating agents, and it was less than 0.01% based on each feed ratio.

4.3.2. Characterization

4.3.2.1. FT-IR spectroscopic analysis

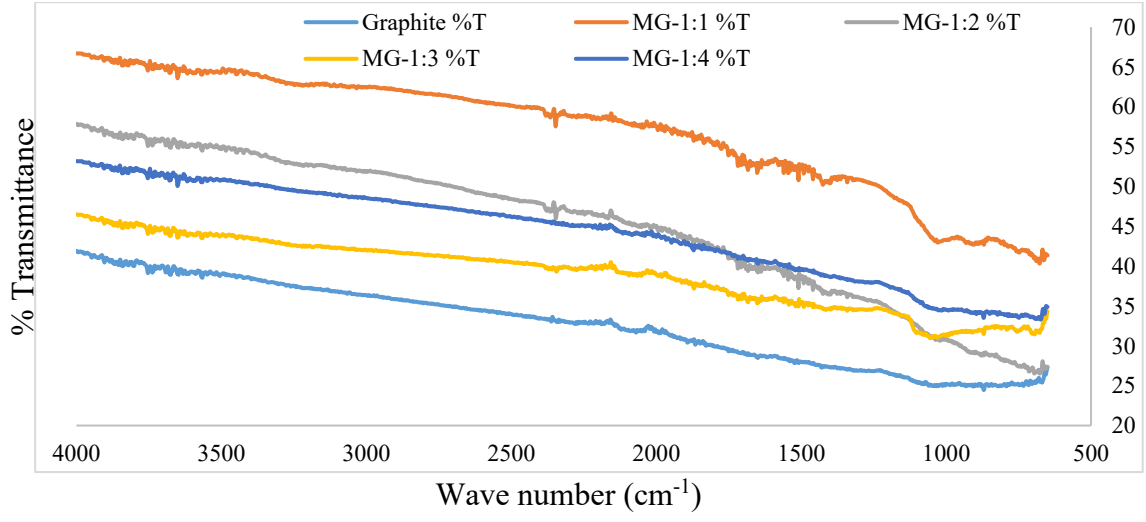

Figure-4.6: FT-IR spectrum of pure Graphite and synthesized Graphene.

FT-IR deals with the infrared region of the electromagnetic spectrum, and it works by measuring how much light is absorbed by the bonds of vibrating molecules to provide a molecular fingerprint. FT-IR spectroscopy was carried out to investigate the surface chemical nature of graphite and exfoliated graphene. FT-IR spectra of graphite and exfoliated graphene are shown in Figure 4.6. The data obtained from the FT-IR machine was used directly without tuning to express the real scenarios.

The microwave graphene exfoliation process did not incorporate any significant interaction between graphite and NH_4HCO_3, which might result in minimal chemical alteration of its structure. However, after tuning the original data twice, very minor interactions were observed at wavenumbers 3651 cm^{-1} and 3218 cm^{-1} O-H stretching, 2347 cm^{-1} C-H stretch, 1652 cm^{-1} C=O stretching vibration, 1509 cm^{-1} and 1400 cm^{-1} aromatic C=C, and 1100 - 1000 cm^{-1} bending of C-H (Zubair M., et. al., 2014). These peaks, however, exhibited neither significant height nor broadness, indicating weak or negligible chemical interactions. The microwave exfoliation process primarily facilitates the physical separation of graphene layers without inducing substantial chemical reactions. As a result, the graphene retains its original chemical structure while being effectively exfoliated. This means the microwave exfoliation method is predominantly a physical process, maintaining the chemical integrity of the graphene material.

4.3.2.2. FT-Raman spectroscopic analysis

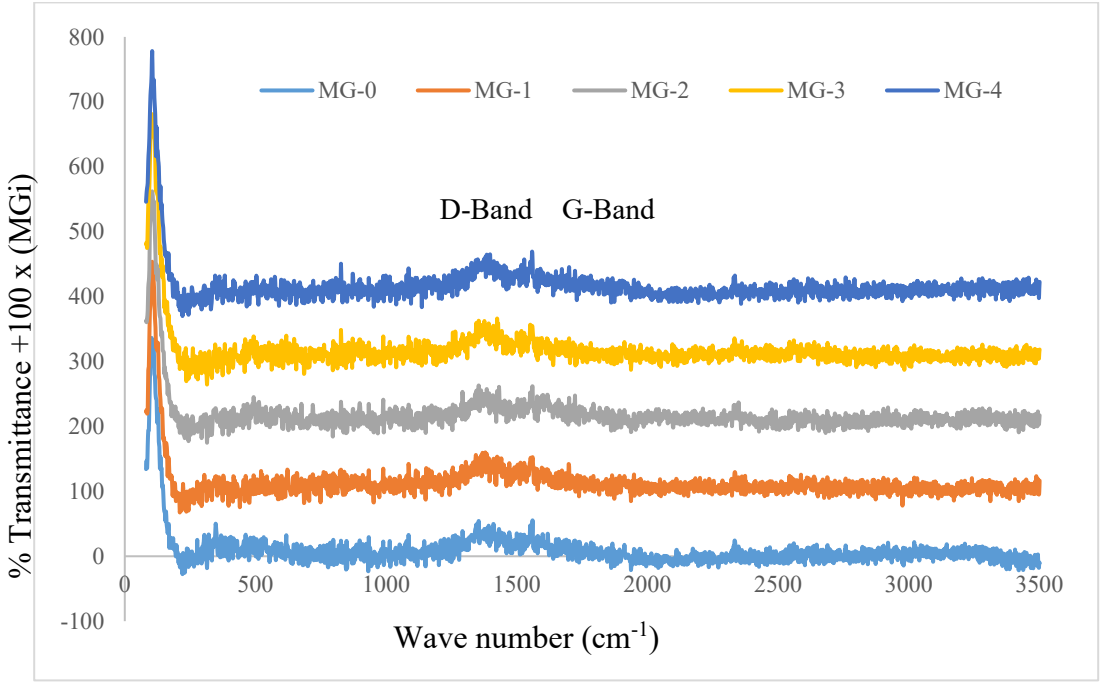

Figure-4.7: FT-Raman spectrum of pure Graphite and synthesized Graphene.

Figure 4.7 shows the FT-Raman spectrum of microwave graphene (MG) samples were characterized, revealing two prominent bands in the spectra, located at approximately 1385 cm^{-1} and 1585 cm^{-1}. The band at ~1385 cm^{-1}, referred to as the D band, originates from structural defects and imperfections, including graphitic edges and disordered carbon structures. Conversely, the band at ~1585 cm^{-1}, known as the G band, is associated with the in-plane vibrational modes of sp^2-hybridized carbon atoms within the graphite lattice. Together, these bands serve as critical indicators of the structural integrity and composition of the material. The intensity ratio of the G band to the D band (I_G/I_D) provides valuable insights into the degree of structural order in the rGO samples. This ratio varies substantially with the extent of reduction, offering a measure of changes in defect density and the re-establishment of graphitic domains. Specifically, higher (I_G/I_D) values indicate an enhanced graphitic order, which is typically attributed to the removal of oxygen-containing functional groups and the repair of structural defects during the exfoliation process.

4.3.2.3. XRD analysis

X-ray Diffraction (XRD) has been used extensively for the examination of materials and thin films. Its effective use depends upon the crystallinity of materials. The technique is a bulk-sensitive analytical method, but can be used to provide information relevant to surface changes in suitable circumstances. For example, XRD can provide useful information on the extent to which surface treatment of a carbon system has affected the bulk of the material. X-ray diffraction (XRD) is used for the primary characterization of material properties like crystal structure, crystallite size, and strain (Chilingarov N. S., et al., 2021), (Chamoli P., et. al., 2017), (Canever N., et al., 2022).

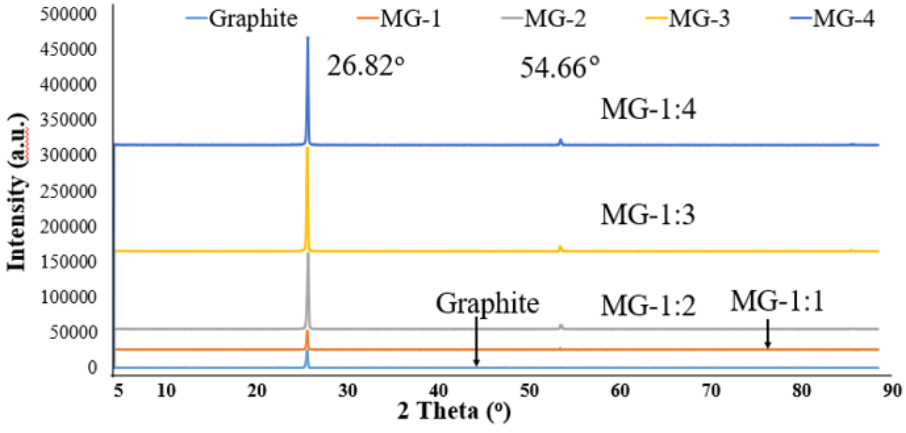

Figure-4.8: XRD spectrum of pure Graphite and Exfoliated Graphene.

Table-4.6: XRD analysis data obtained from the different MG samples.

Sl. No.	Sample Name	Major peak 100%				Secondary peak				
		(°) 2θ	Height [cts]	FWHM Left [°2θ]	d-spacing [Å]	(°) 2θ	Height [cts]	FWHM Left [°2θ]	d-spacing [Å]	% of Major peak
01.	Graphite	26.5011	24260.30	0.1791	3.36067	54.5773	805.10	0.2047	1.68014	3.32
02.	MG-1	26.5020	26126.58	0.1279	3.36056	54.6155	1213.21	0.1023	1.67905	4.64
03.	MG-2	26.6119	106911.80	0.2047	3.34694	54.7267	5927.43	0.1023	1.67591	5.54
04.	MG-3	26.5061	145276.60	0.1535	3.36006	54.6295	6647.13	0.2558	1.67866	4.58
05.	MG-4	26.5668	148992.50	0.1791	3.35251	54.6723	7930.87	0.1535	1.67744	5.32

Figure 4.8 shows the XRD patterns of the pure graphite and microwave exfoliated graphene, it is certain that the graphite sample shows a significant appearance of a sharp and strong diffraction peak at plane (002) at around 26.5011° of in XRD spectrum corresponding to the height 24260.30 cts, with full width at half maximum (FWHM) = 0.1791° 2θ and it corresponding to the layer spacing (d) is 3.36067 Å. Another significant secondary short peak at plane (004) at around 54.5773° with the area 3.32% of the major peak appears corresponding to the height 805.10 cts with FWHM = 0.2047° at 2θ, and it corresponds to the layer spacing (d) is 1.68014 Å. (Chilingarov N. S., et al., 2021).

The microwave graphene samples of MG-1, MG-2, MG-3 and MG-4 samples showed the significant appearance of same sharper and stronger diffraction peak at plane (002) at around 26.5020°, 26.6119°, 26.5061° and 26.5668° of in XRD spectrum corresponding to the height 26126.58 cts, 106911.80 cts, 145276.60 cts and 148992.50 cts, with full width at half maximum (FWHM) = 0.1279° 2θ, 0.2047° 2θ, 0.1535° 2θ and 0.1791° 2θ and it corresponding to the layer spacing (d) is 3.36056 Å, 3.34694 Å, 3.36006 Å and 3.35251 Å respectively.

Another significant secondary short peak at plane (004) with the area of MG-1, MG-2, MG-3 and MG-4 samples were 4.64%, 5.54%, 4.58% and 5.32% of the major peak appears at around 2θ = 54.6155°, 54.7267°, 54.6295° and 54.6723°, which corresponding to the height 1213.21 cts, 5927.43 cts 6647.13 cts and 7930.87 cts with FWHM = 0.1023° 2θ, 0.1023° 2θ, 0.2558° 2θ and 0.1535° 2θ and which corresponding to the layer spacing (d) is 1.67905 Å, 1.67591 Å, 1.67866 Å and 1.67744 Å respectively. So, from the XRD data, it can be concluded that the microwave exfoliation did not change the graphite chemically or morphologically; only the layer thicknesses were reduced, i.e., the successful exfoliations were performed.

Figure 4.9 shows the TGA analysis data of pure graphite and four MG samples. From the thermogravimetric analysis, acquired data of pure graphite it was observed that the sample was stable up to 600 ^{o}C. Beyond this temperature, the degradation started, and over 700 ^{o}C, the degradation rate increases significantly and steadily up to 850 ^{o}C. At this temperature, the residual mass was 52.79%.

4.3.2.4. Thermogravimetric analysis (TGA)

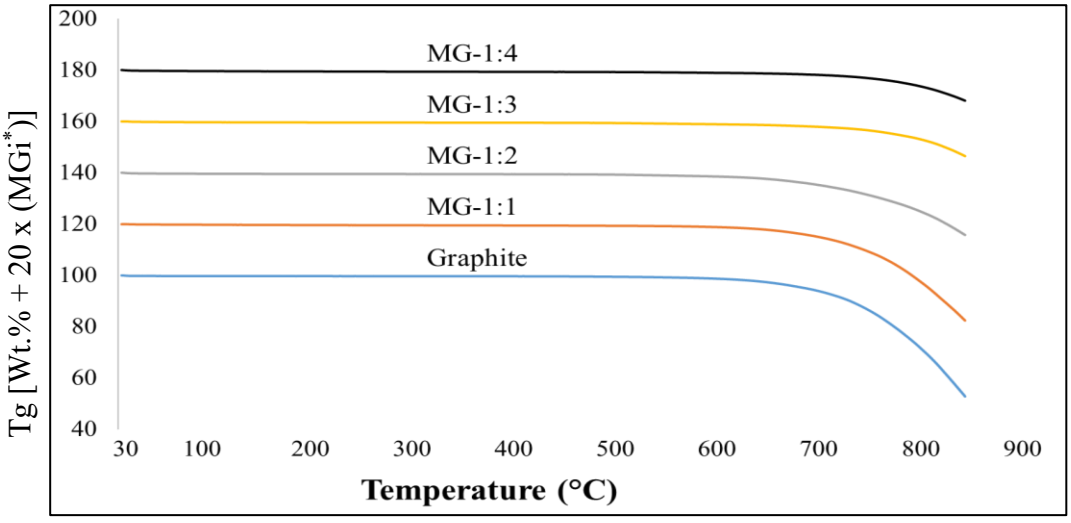

* MGi= Microwave Graphene of Run-i (where i= 1, 2, 3 and 4)

Figure-4.9: Thermogravimetric (TGA) analysis data of pure Graphite and microwave exfoliated Graphene samples.

The thermogravimetric analysis acquired data of microwave exfoliated graphene samples MG-1, MG-2, MG-3, and MG-4. It was found that the samples were stable up to 625 ºC, 650 ºC, 675 ºC, and 700 ºC, respectively. Beyond this temperature, the degradation started, and over 725 ºC, 750 ºC, 775 ºC, and 800 ºC, respectively, the degradation rate increases significantly and steadily up to 850 ºC. At this temperature, the residual mass was 62.39%, 75.74% 86.49% and 88.10% respectively. So, it can be concluded from the thermogravimetric analysis acquired data of microwave exfoliated graphene that the degree of exfoliation increases the thermal stability of graphene significantly and steadily.

4.3.2.5. FE-SEM image analysis

Figure 4.10 shows the Field Emission Scanning Electron Microscope (FE-SEM) Image analysis data of pure Graphite and four microwave exfoliated Graphene samples.

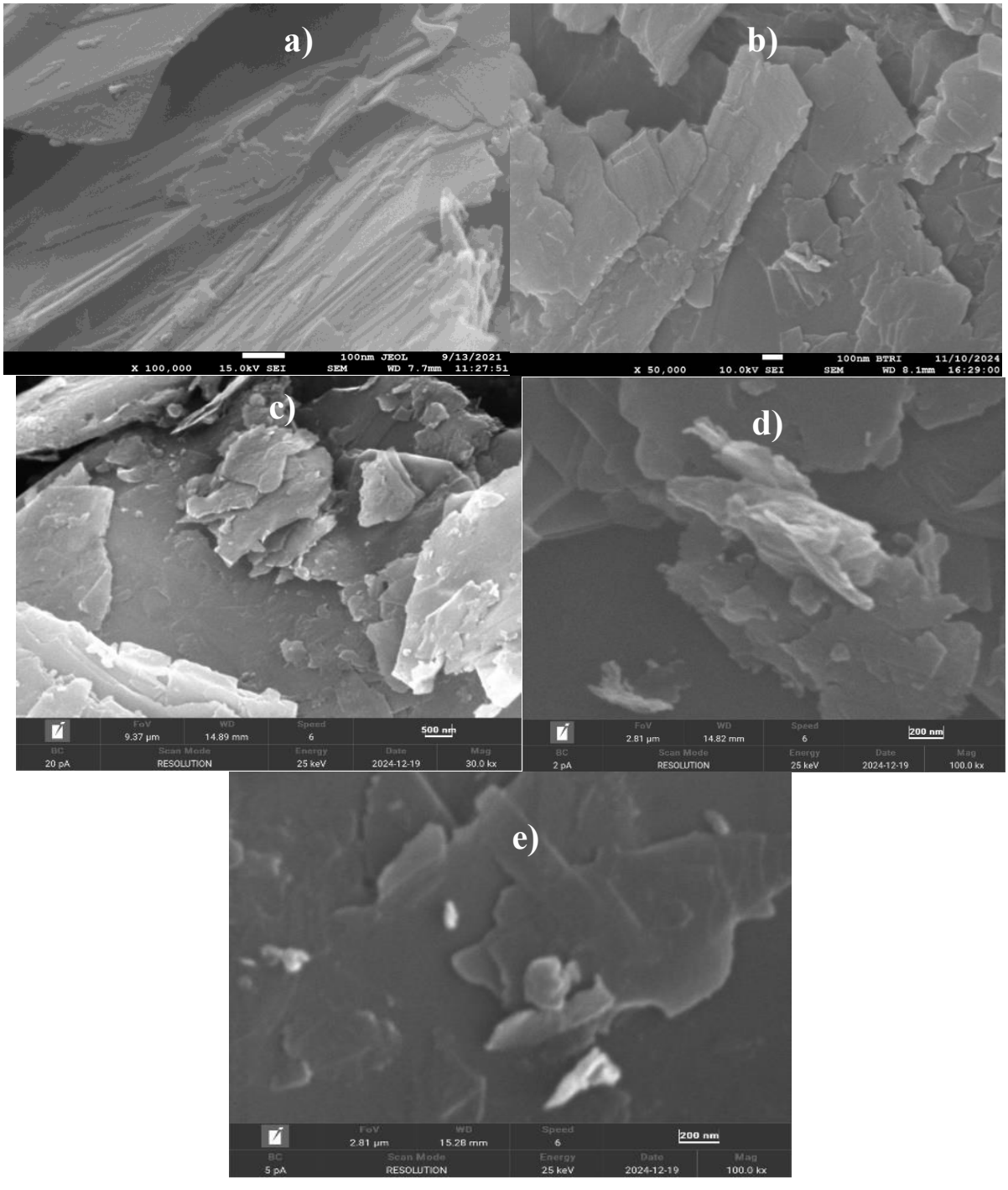

Figure-4.10: FE-SEM Image analysis of a) pure graphite and b) MG-1, c) MG-2, d) MG-3, and e) MG-4 samples.

Table-4.7: Thickness and diameter of microwave graphene samples determined by the ImageJ software analysis of SEM images.

Graphene	Average thickness of 30 measurements (nm)	Average grain size in diameter of 30 measurements (nm)
MG-0	83.05	1827.162
MG-1	16.201	142.157
MG-2	14.959	141.961
MG-3	13.572	141.465
MG-4	12.935	139.567

The FE-SEM images of graphene exfoliated from the graphite flakes by microwave synthesis using NH_4HCO_3 are presented in Figures 4 .10 (a)–(e). Figure 10 (a) revealed that the graphene reduced from graphite flakes consists of randomly aggregated, thin, crumbled sheets closely associated with each other and forming a disordered solid of average thickness about 83 nm and a grain size of average diameter 1827 nm. After exfoliation, the average diameter of graphene sheets was up to 142 nm, and the sheet's thickness was 16-12 nm. It can be noticed that it has a laminated structure in which a large number of sheets are stacked together. In Figure 4.10 (b), the graphene sheets break into pieces that are smaller than the graphite sheets in Figure 4.10 (a) and Figure 4.10 (b)-(e). All these samples show the morphology of graphene with slightly folded edges created during the ultrasonication of the colloidal dispersion.

4.4. Application of MG in acid blue-25 removal from aqueous solution

Application of Microwave Graphene for the removal of textile Acid blue dyes from water was studied

4.4.1. Removal principal

Acid Blue 25, a synthetic anthraquinone dye widely used in the textile, paper, and leather industries, poses significant environmental threats due to its persistence and toxicity. As a water-soluble amphoteric dye, it resists natural degradation processes, allowing it to persist in aquatic environments and cause long-term pollution. The discharge of Acid blue 25 into water bodies leads to pronounced coloration, reducing light penetration and disrupting photosynthesis, thereby impairing aquatic ecosystems and destabilizing food chains (Gadong B. D., 2016).

The chemical structure of Acid blue 25 is shown in Figure 4.11 (Wikipedia.org). Under anaerobic conditions, the dye degrades into toxic by-products, such as aromatic amines, which are carcinogenic and mutagenic. These compounds pose severe health risks to aquatic organisms, including genotoxicity and bioaccumulation, and may cause skin irritation, respiratory issues, and carcinogenic effects in humans. Acid blue 25 also increases chemical oxygen demand (COD) and biological oxygen demand (BOD), depleting oxygen levels essential for aquatic life. Its high stability and resistance to conventional treatment methods highlight the urgent need for advanced remediation technologies, including adsorption techniques, advanced oxidation processes, and stringent regulatory measures, to mitigate its environmental impact.

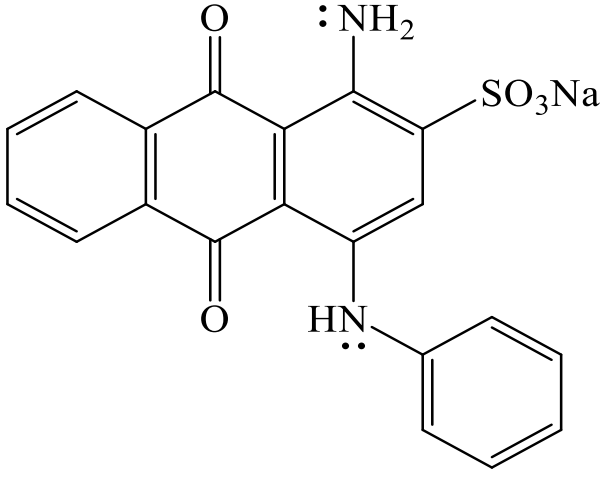

Figure-4.11: Chemical structure of Acid Blue 25 dye contains a lone pair of electrons.

So, removal of ABD is very important for a clean, safe, and sustainable environment. Microwave-assisted exfoliated graphene can be utilized for the removal of ABD from water. The π-π resonance interaction among the graphene molecules showed a strong attraction force to the lone pair electron available in the two Nitrogen atoms in the ABD.

Microwave exfoliated graphene showed promising adsorption efficiency for removing Acid blue-25 dye (ABD) from water. This approach leverages graphene's large surface area and enhanced surface charges, lads to increasing adsorption rates and efficiency while minimizing chemical additives and secondary pollutants. The method also allows graphene regeneration, making it environmentally friendly, cost-effective, and scalable for industries managing large volumes of dye-contaminated water.

Figure-4.12: Stock solution of acid blue-25 dyes in water.

4.4.2. Application of microwave graphene for the removal of textile acid blue dye

Microwave-synthesized graphene has proven to be a highly efficient material for the removal of textile dyes, such as AB-25, from water, with optimal performance observed at a pH of 2.0 (Gadong, 2016). At this acidic pH, the protonation of the dye molecules enhances their interaction with the negatively charged functional groups present on the graphene surface, facilitating efficient adsorption. The superior physicochemical properties of microwave graphene, including its high specific surface area, defect-rich structure, and abundant oxygen-containing functional groups, contribute to its exceptional dye removal capabilities. These properties enable strong electrostatic attractions and π–π stacking interactions between the dye molecules and the graphene surface, ensuring high adsorption efficiency.

The material's high adsorption capacity and fast adsorption kinetics allow for the efficient removal of large quantities of Acid blue dye in a short time, which is particularly beneficial for industrial-scale wastewater treatment.

Table-4.8: Amount of solution passed through 0.5 g of different exfoliated graphene.

Graphene	Amount of MG (g)	Amount of 100 ppm dye solution (L)	dye removing ability (mg/g)
Graphite	0.5	1.178	230.89
MG-1	0.5	1.698	332.81
MG-2	0.5	2.118	415.13
MG-3	0.5	2.422	458.63
MG-4	0.5	2.438	472.80

Calculation of dye removal ability by different MG samples in Table 4.8:

From the equation of dye removal efficiency,

$$\% \text{ of dye removal } q_{max} = \frac{C1-C2}{g} \times V_e$$

Where C_1 is the initial concentration of the dye = 500 ppm

C_2 = the final concentrations of the dye after the adsorption process = 2 ppm

g = weight in grams if graphene 0.5 g

V_e = the final volume of dye solution after the adsorption process = 5372.8

So, % of dye removal ability q_{max} = 472.80 mg/g

4.4.3. Effect of the degree of exfoliation of microwave graphene on the removal efficiency

Microwave-exfoliated graphene (MG) demonstrates high efficiency in the removal of ABD from aqueous solutions, with adsorption capacities ranging between 300–400 mg/g. However, the removal efficiency of MG is influenced by several factors, including pH, initial dye concentration, contact time, and the quality of MG. Among these, the quality of MG, which is determined by the degree of exfoliation, plays the most critical role in adsorption performance. Raw graphite exhibits an adsorption capacity of 231.4 mg/g of ABD at equilibrium after 24 hours. Following exfoliation, the adsorption efficiency significantly improves due to the enhanced surface area and active sites available for adsorption. For instance, MG-1 showed an increased adsorption capacity of 275.5 mg/g. Further improvements were observed with higher

degrees of exfoliation, e.g., MG-2, MG-3, and MG-4 demonstrated adsorption capacities of 318.7 mg/g, 382.1 mg/g, and 472.8 mg/g, respectively. These results highlight a strong correlation between the degree of exfoliation and the adsorption efficiency of MG.

The findings suggest that optimizing the exfoliation process is essential for maximizing the adsorption performance of MG. The increased adsorption efficiency with higher exfoliation ratios can be attributed to the greater availability of functional groups and surface area, which facilitate enhanced interaction with ABD molecules. This study underscores the pivotal role of MG quality in determining its potential as an effective adsorbent for water treatment applications.

Table-4.9: Removal of AB-25 dye from water solution at an initial concentration of 500 ppm using synthesized MG-0, MG-1, MG-2, MG-3, and MG-4 at pH = 2.

Adsorbent (Graphene)	Amount of Adsorbent (g)	Concentration of final dye solution (ppm)	Dye removing ability (mg/g)	% Removal
MG-0	0.2	268.6	231.4	46.28
MG-1	0.2	224.5	275.5	55.10
MG-2	0.2	181.3	318.7	63.74
MG-3	0.2	117.9	382.1	76.42
MG-4	0.2	27.2	472.8	94.56

Calculation of dye removal efficiency in percentage by different MG sample in Table-4.9:

From the equation of dye removal efficiency,

$$\% \text{ of dye removal} = \frac{C1-C2}{C1} \times 100\ \%.$$

Where C1 is the initial concentration of the dye = 500 ppm.
C2 = the final concentrations of the dye after the adsorption process = 27.2 ppm.

So, $\% \text{ of dye removal} = \frac{500\ \text{ppm}-27.2\ \text{ppm}}{500\ \text{ppm}} \times 100\ \%$

$= 94.56\%$

4.4.4. Effect of initial dye concentration on the removal efficiency

One of the most important parameters for the removal of Acid Blue dye from water is the initial dye concentration. The contact time of adsorption also depends on the initial dye concentration.

Table-4.10: Adsorption of Acid Blue dye from 500 mL water solution using MG-1, MG-2, MG-3, and MG-4 at pH 2.0 in various initial concentrations: A) at 50 ppm, B) at 100 ppm, and C) at 200 ppm.

Time (hrs.)	Concentration (ppm)				Concentration (ppm)				Concentration (ppm)			
	MWG-1	MWG-2	MWG-3	MWG-4	MWG-1	MWG-2	MWG-3	MWG-4	MWG-1	MWG-2	MWG-3	MWG-4
0.0	50.0	50.0	50.0	50.0	100.0	100.0	100.0	100.0	200.0	200.0	200.0	200.0
0.5	43.2	41.2	37.2	35.5	89.5	83.5	81.5	78.5	186.1	182.2	172.7	162.0
1.0	38.5	34.0	28.5	24.5	80.6	72.6	69.9	65.2	175.6	169.4	153.4	142.0
1.5	34.6	28.5	22.8	17.6	72.6	65.6	61.6	55.1	166.9	154.8	139.9	125.0
2.0	31.8	25.1	17.8	12.6	65.8	57.8	52.8	46.1	158.2	143.2	127.4	112.7
2.5	28.6	21.5	13.6	9.4	58.6	52.6	46.6	40.6	151.5	133.9	116.7	103.1
3.0	26.1	18.6	11.1	6.6	52.2	46.2	41.2	35.2	145.1	126.4	108.0	94.4
3.5	24.2	15.9	8.5	5.1	47.2	41.2	37.2	31.2	138.9	118.9	100.6	85.9
4.0	21.7	13.7	6.9	3.5	43.6	37.6	33.6	27.6	134.7	113.5	95.8	78.6
4.5	19.2	11.6	5.9	2.3	40.1	35.1	31.1	24.1	130.3	108.7	91.1	72.2
5.0	16.7	10.2	4.6	1.6	38.3	32.3	27.9	20.7	125.9	103.5	85.4	65.8
5.5	14.9	8.8	3.7	1.2	36.0	30.8	26.5	18.8	120.7	99.1	80.9	60.6
6.0	13.2	7.1	2.9	1.0	34.2	28.7	24.2	17.2	116.3	95.2	77.4	56.1
6.5	11.5	5.6	2.4	0.8	32.3	27.8	22.3	16.1	113.7	90.5	73.7	53.3
7.0	9.7	4.7	1.8	0.6	30.2	26.2	21.7	14.9	110.2	87.5	71.6	50.5
7.5	8.2	3.5	1.5	0.5	29.3	25.3	21.3	14.5	107.5	85.0	69.9	48.5
8.0	6.8	2.9	1.2	0.5	28.9	24.9	20.9	14.2	104.1	82.5	67.2	47.8
8.5	5.7	2.2	1.0	0.4	28.7	23.3	19.7	13.9	101.4	80.2	66.5	47.5
9.0	4.6	1.9	0.8	0.4	28.5	22.5	18.9	13.7	99.1	78.1	65.9	47.1
9.5	4.1	1.6	0.7	0.3	28.3	22.3	18.6	13.6	97.3	76.3	65.1	46.8
10.0	3.6	1.4	0.6	0.3	28.1	22.1	18.3	13.6	95.5	75.7	64.5	46.6
10.5	3.2	1.3	0.6	0.2	28.0	22.0	18.1	13.5	93.2	74.5	64.1	46.5
11.0	3.2	1.2	0.6	0.2	28.0	22.0	18.0	13.5	90.8	74.3	63.7	46.4
11.5	3.1	1.1	0.6	0.2	28.0	22.0	18.0	13.5	88.4	74.2	63.6	46.3
12.0	3.0	1.1	0.6	0.2	28.0	22.0	18.0	13.5	86.1	74.1	63.5	46.2

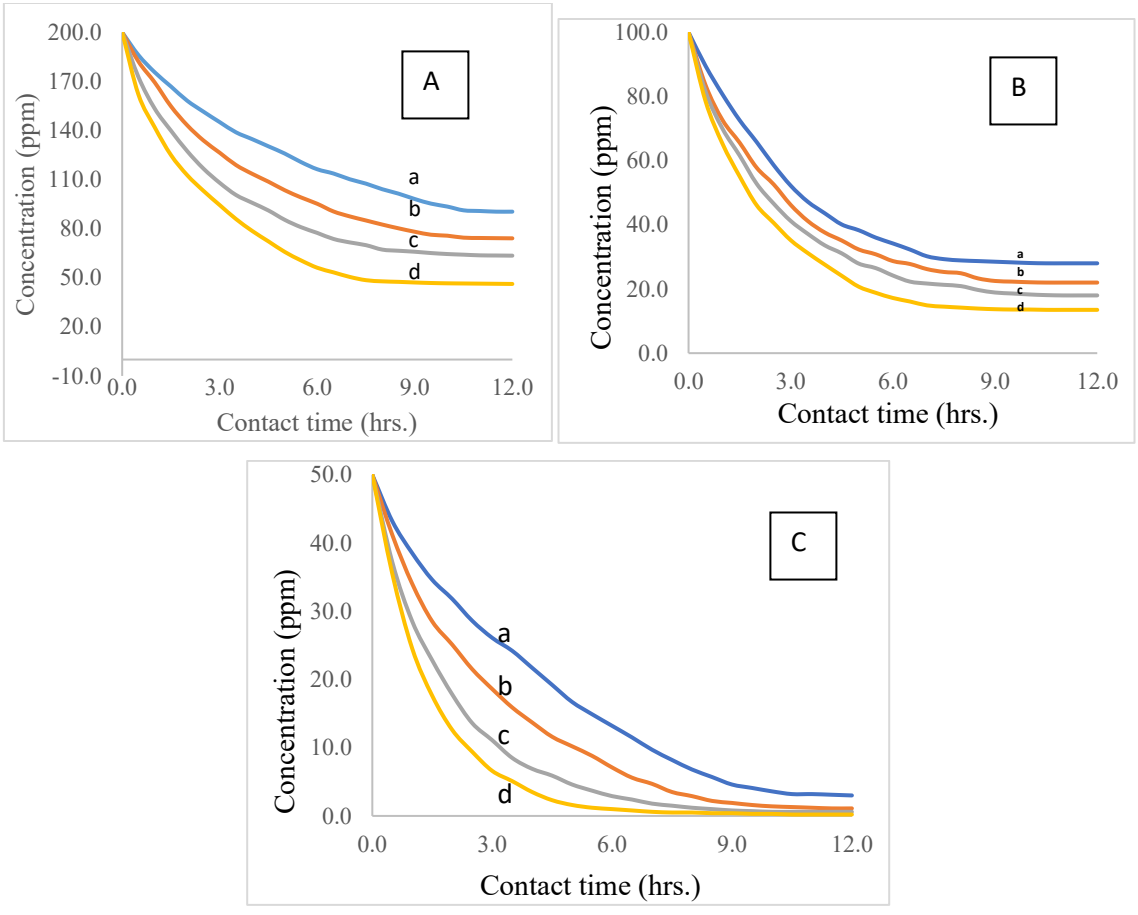

Figure-4.13: Adsorption of ABD from water solution using microwave graphene a) MG-1, b) MG-2, c) MG-3, and d) MG-4 at pH 2.0 in various initial concentrations of A) 200 ppm, B) 100 ppm, and C) 50 ppm, respectively.

Table 4.10 and Figure 4.13 illustrate the relationship between the initial dye concentration and adsorption time during the removal of ABD from aqueous solutions. The experiment was conducted with initial concentrations of 200 ppm, 100 ppm, and 50 ppm in 500 mL ABD solutions, using 0.5 g of microwave-exfoliated graphene (MG) samples: MG-1, MG-2, MG-3, and MG-4. The total contact time for the adsorption process was set to 12 hours.

The results indicate that for both the highest and lowest initial concentrations, 200 ppm and 50 ppm, MG-1 reached equilibrium at a longer time of approximately 10.0 hours. However, the equilibrium time decreased with an increasing degree of exfoliation. Specifically, MG-2, MG-3, and MG-4 reached equilibrium at 9.0, 7.5, and 6.5 hours, respectively, demonstrating a significant improvement in adsorption kinetics with better exfoliation quality. Interestingly, at a medium initial concentration of 100 ppm, the adsorption rate appears to be nearly constant

across all MG samples, with equilibrium times around 8.0 hours. This behavior can be attributed to the balance between the migration of dye molecules and the adsorption rate, which is influenced by both concentration and contact time. At lower and higher concentrations, the adsorption kinetics are more significantly affected by the degree of exfoliation, leading to variations in equilibrium time. These findings highlight the impact of both initial dye concentration and MG quality on adsorption efficiency and kinetics, providing valuable insights into optimizing conditions for effective Acid blue dye removal.

4.4.5. Recyclability of MG

Furthermore, microwave graphene exhibits excellent reusability, retaining a significant portion of its adsorption capacity after multiple regeneration cycles, which enhances its sustainability and economic viability. The optimal performance of microwave graphene at pH 2.0 underscores its suitability for treating acidic wastewater streams, commonly encountered in textile and dyeing industries. These attributes position microwave graphene as a promising material for sustainable and efficient dye removal in advanced water purification systems.

4.5. Conclusions

It can be concluded from the above discussion that the microwave-assisted rapid exfoliation technique is well-suited for the direct synthesis of pristine graphene. It is a fast and scalable method for exfoliation of graphite in the presence of ammonium bicarbonate as the intercalation agent, which can be removed thermally for purification. The microwave exfoliation irradiates a huge energy that can be tolerated by insulator-type refractory decorative tiles with 20-30 mm thickness. The graphene showed little change in FT-IR analysis, i.e., the synthesis process didn't incorporate any chemical reaction. It is also confirmed from the XRD analysis that both graphite and graphene samples showed a major diffraction pattern at the (002) plane and a minor diffraction pattern at the (004) plane at the same position. The exfoliation didn't affect interplanar distance, which was around 3.35 Å. They differ only in the response intensity, and the intensity increased with the degree of exfoliation. The thermogravimetric analysis of the microwave exfoliated graphene showed that the graphene products were very stable up to 600 °C temperature and beyond this temperature, a low degradation started at about 700 °C. After that, the degradation rate increased rapidly. At about 850 °C, the degradation of MG-1 graphene was only 38%. With the increase of the degree of exfoliation, the stability of MG increased significantly, and for the MG-4 graphene, the degradation at 850 °C reduced to 12% by mass. The FE-SEM study of the microwave exfoliated graphene was analyzed by ImageJ software and found that the average grain size of the graphite is around 600 nm, and with the increase of the degree of exfoliation, the grain size reduced to 200 nm, and the average thickness of the exfoliated graphene layer reduced from 18 nm to 12 nm.

The synthesized MG samples showed a very high removal efficiency of Acid blue dyes of 94.56% with the highest adsorption capacity was 472.8 mg/g in just a few hours, and the efficiency was measured by UV-VIS analyses at pH value 2.0.

General Conclusions

Hummer's method was used to synthesize GOs from graphite, achieving a maximum oxygen-to-carbon ratio of 66.7%. Optimal reaction conditions, with respect to yield and quality, were 60–70 ℃ for 14–18 hours, producing 65–70% GOs. Higher temperatures and shorter reaction times reduced oxidation and yield. Unreacted feed acid liquor (FAL) was successfully recycled and reused for five consecutive cycles, with 80–90% recovery in each cycle. Recycling increased the moisture content by 0.5% per cycle, affecting the acid concentration and GOs particle size, which grew from 900 to 1660 nm. Ion chromatography (IC) revealed SO_4^{2-} reacted more actively with K^+ and Mn^{2+} ions than PO_4^{3-}. Zeta potential of GOs increased with reaction temperatures up to 80–85 ℃. The study highlights how reaction parameters influence GOs properties and yield. The reaction temperature impacted the reaction rate negatively (-0.204 g/℃) and positively (+0.450 g/h) on reaction time. XPS analysis showed an oxygen-to-carbon atomic ratio of 66.7%, aligning with a 66.9% increase in product yield. Raman spectra confirmed the conversion of graphite to GOs with G and D bands at ~1355 cm^{-1} and ~1575 cm^{-1}, respectively. SEM images revealed a layered structure with a thickness of 200–260 nm. TGA indicated GOs' stability up to 75 ℃, with 75% decomposition at 193 ℃. Synthesized GOs effectively removed 343 mg/g of arsenic from aqueous solution with 98% efficiency. In this research, GOs were also synthesized using an acid liquor recycling technique to reduce production costs while maintaining product quality and consistency. GOs with an oxygen-to-carbon ratio of 66.75% were successfully obtained. rGOs were synthesized from these GOs through thermal reduction at 98 °C, 180 °C, and 200 °C in water and kerosene mediums for 48 and 96 hours. Hydrophobic rGO was produced in the kerosene medium. In the water medium, the oxygen content of GOs was reduced to 45.39% and 32.68% after 48 and 96 hours at 98 °C, respectively. In the reduction process, hydroxyl (-OH) groups were predominantly reduced compared to carbonyl (>C=O) and epoxy (C-O-C) groups. The degree of reduction of GOs in the nonpolar medium kerosene at 180 °C and 220 °C for 1 hour resulted in oxygen content reductions to 17.77% and 8.86%, respectively. This reduction method successfully eliminated all hydroxyl (-OH) groups and most carbonyl (>C=O) and epoxy (C-O-C) groups, leaving only trace amounts of (>C=O) and (C-O-C) groups. A double reduction process further converted rGO into extremely reduced rGO with an oxygen content of less than 2.49%, as confirmed by XPS analysis. XRD patterns validated the crystallinity of the synthesized rGO. The reduction of GOs was evidenced by the increased 2θ peaks at ~25° for the (002) plane in rGO, decreased

peaks at ~10–13° for the (001) plane in GOs, and unchanged peaks at ~43° (100). FE-SEM and TEM images revealed the formation of few-layer graphene. The compositional analysis of rGO was conducted using XPS analysis, and BET analysis indicated a mesoporous structure with a high surface area of 32.60 m^2/g for rGO-KAA. A reaction mechanism for the thermal reduction process of GOs was also proposed in this study. Antimicrobial tests showed that hydrophilic rGO had superior activity against B. subtilis, S. aureus, E. coli, and S. typhi compared to hydrophobic rGO, while GOs exhibited no activity. The highest zone of inhibition was 19.5 mm at 20 μg/mL after 24 hours, compared to 27.5 mm for standard tetracycline. This study utilized a microwave-assisted rapid exfoliation technique to synthesize pristine graphene using ammonium bicarbonate as an intercalation agent, which was thermally removed for purification. XRD confirmed no changes in interplanar distance (~3.35 Å), while thermogravimetric analysis showed stability up to 600 °C, with microwave graphene of MG-1:4 exhibiting only 12% degradation at 850 °C. FE-SEM revealed a reduction in grain size from 300 nm to 200 nm and layer thickness from 10 nm to 2 nm. The MG-4 sample showed the highest acid blue dyes (ABD) adsorption capacity of 472.8 mg/g (94.56%) at pH 2.0. This method is efficient, scalable, and chemical-free. Thus, GOs and rGO hold immense potential for wastewater treatment due to their high surface area, adsorption capacity, and functional tunability, offering sustainable solutions for industrial wastewater purification in the future.

REFERENCES

Abdelkader A. M., Cooper A. J., Dryfe R. A., Kinloch I. A.,. (2015). "How to get between the sheets: a review of recent works on the electrochemical exfoliation of graphene materials from bulk graphite." Nanoscale. 7: 6944-6956.

Abdolhosseinzadeh S. H., Asgharzadeh H., Kim S.,. (2015). "Fast and fully-scalable synthesis of reduced graphene oxide." Scientific reports. 5: 10160.

Abele C. D., Giesselmann F.,. (2022). "Dynamic light scattering analysis of size-selected graphene oxide 2D colloids fractioned via liquid crystal phase separation." Soft Matter. 18(35): 6607-6617.

Acik M., Lee G., Mattevi C., Pirkle A., Wallace R.M., Chhowalla M., Cho K., Chabal Y.,. (2011). "The Role of Oxygen during Thermal Reduction of Graphene Oxide Studied by Infrared Absorption Spectroscopy."The Journal of Physical Chemistry C. 115, 19761–19781.

Adar F.,. (2022). “Use of Raman spectroscopy to qualify carbon materials.”

Adel M., Ahmed M. A., Elabiad M. A., Mohamed A. A.,. (2022). "Removal of heavy metals and dyes from wastewater using graphene oxide-based nanomaterials: A critical review." Environmental Nanotechnology, Monitoring & Management. 18: 100719.

Afanas’ev V. P., Gryazev A. S., Bocharov G. S., Eletskii A. V.,. (2020). Studying Thermally Reduced Graphene Oxide by X-Ray Photoelectron Spectroscopy. Journal of Structural Chemistry. 61: 803-810.

Afrin S., Goswami B., Rahman S., Bhuiyan M. N. I, Shamima K. A. A.,. (2022). "Antimicrobial potential of Coriandrum sativum, Lactuca sativa and Mentha spicata against antibiotic resistant microorganisms." Journal of Herbs, Spices & Medicinal Plants. 28: 193-205.

Agarwal V., Zetterlund P. B.,. (2021). “Strategies for reduction of graphene oxide–A comprehensive review.” Chemical Engineering Journal. 405: 127018.

Ahmed S., Zohra F. T., Choudhury T. R., Nurnabi M., Alam Z.,. (2023). “Adsorption of Cu(II) and Cd(II) with graphene based adsorbent: adsorption kinetics, isotherm and thermodynamic studies.” Desalination and Water Treatment. 5: 167-179.

Ajay K., Potbhare S. K., Aziz T., Ayyub M. M., Kahate A., Madankar R., Wankar S., Dutta A., Abdala A., Mohmood S.H., Adhikari R., Chaudhary R. G.,. (2024). "Bioinspired graphene-based metal oxide nanocomposites for photocatalytic and electrochemical performances: an updated review." Nanoscale Advances. 6: 2539-2568.

Alanyalıoğlu M., Segura J. J., Oro-Sole J., Casañ-Pastor N.,. (2012). "The synthesis of graphene sheets with controlled thickness and order using surfactant-assisted electrochemical processes." Carbon. 50: 142-152.

Alayande A. B., Obaid M., Kim I. S.,. (2019). "Antimicrobial mechanism of reduced graphene oxide-copper oxide (rGO-CuO) nanocomposite films: The case of Pseudomonas aeruginosa PAO1." Materials Science and Engineering C. 109: 110596.

Aleksandrzak M., Urbas K., Onyszko M., Mijowska E.,. (2016) "Nanomedical applications of graphene and graphene oxide." Nanomaterials and regenerative medicine. Szczecin,. 582-610.

Al-Gaashani R., Najjar A., Zakaria Y., Mansour S.,. (2019). "XPS and structural studies of high-quality graphene oxide and reduced graphene oxide prepared by different chemical oxidation methods." Ceramics International. 45: 14439-14448.

Algamdi M. S., Alsohaimi I. H., Lawler J., Ali H. M., Aldawsari A. M., Hassan H. M.,. (2019). "Fabrication of graphene oxide incorporated polyethersulfone hybrid ultrafiltration membranes for humic acid removal." Separation and Purification Technology. 223: 17-23.

Ali I., Basheer A. A., Mbianda X.Y., Burakov A., Galunin E., Burakova I., Mkrtchyan E., Tkachev A., Grachev V.,. (2019). "Graphene based adsorbents for remediation of noxious pollutants from wastewater." Environment international. 127: 160-180.

Ali M. E., Hoque M. E., Hossain S. K., Biswas M. C.,. "Nanoadsorbents for wastewater treatment: next generation biotechnological solution." (2020). International Journal of Environmental Science and Technology. 17: 4095-4132.

Ali M. M., Sandhya K. Y.,. (2014). "Reduced graphene oxide as a highly efficient adsorbent for 1-naphthol and the mechanism thereof." RSC Advances. 4: 51624-51631.

Alimohammadzadeh E., John Hedley J.,. (2024). "Advances in Graphene Field Effect Transistors (FETs) for Amine Neurotransmitter Sensing" Applied Sciences. 14(22): 10109

Aliyev E., Filiz V., Khan M. M., Lee Y. J., Abetz C., Abetz V.,. (2019). "Structural characterization of graphene oxide: Surface functional groups and fractionated oxidative debris." Nanomaterials. 9: 1180.

Alkhouzaam A., Qiblawey H., Khraisheh M., Atieh M., Al-Ghouti M.,. (2020). "Synthesis of graphene oxides particle of high oxidation degree using a modified Hummers method." Ceramics International. 46: 23997-4007.

Al-Sherbini A., Al-Sayed, Mona B, Iman G., Mohamed S.,. (2017). "Exfoliation of graphene sheets via high energy wet milling of graphite in 2-ethylhexanol and kerosene." Journal of Advanced Research. 8: 209-215.

Al-Tohamy R., Ali S. S., Li F., Okasha K. M., Mahmoud Y. A. G., Elsamahy T., Jiao H., Fu Y., Sun J.,. (2022). "A critical review on the treatment of dye-containing wastewater: Ecotoxicological and health concerns of textile dyes and possible remediation approaches for environmental safety." Ecotoxicology and Environmental Safety. 231: 113160.

Amiri M., Konda S. K., Chen A.,. (2017). "Facile synthesis of a carbon nitride/reduced graphene oxide/nickel hydroxide nanocomposite for oxygen reduction in alkaline media." ChemElectroChem. 4: 997-1001.

Anaya I. O., Yuta N.,. (2023). "Unveiling the Reduction Process of Graphene Oxide by Ascorbic Acid: Grafting and Reduction Sequences for High Surface Area Graphene Materials." Chemistry Europe. 88: e202300328.

Andrijanto E., Shoelarta S, atot Subiyanto G., Rifki S.,. (2016). "Facile synthesis of graphene from graphite using ascorbic acid as reducing agent." AIP Confference Proceding Semarang, Indonesia: AIP Confference Proceding. 1725: 020003.

Anis H., Ghorbel E.,. (2021). "Microwave processing of materials: Mechanisms and applications." Materials Today: Proceedings. 46: 2884-2891.

Ansari M. Z., Johari R. Siddiqi W. A.,. (2019). "Novel and green synthesis of chemically reduced graphene sheets using Phyllanthus emblica (Indian Gooseberry) and its photovoltaic activity." Materials Research Express. 6: 055027.

Arefi-Rad M. R., Kafashan H.,. (2020). "Pb-doped SnS nano-powders: Comprehensive physical characterizations." Optical Materials. 105: 109887.

Ares P., Novoselov K. S.,. (2022). "Recent advances in graphene and other 2D materials." Nano Materials Science. 4: 3-9.

Arthi G., Pu B., Bd L.,. (2015). "A Simple Approach to Stepwise Synthesis of Graphene Oxide Nanomaterial" Journal of Nanomedicine & Nanotechnology. 6(1): 253-256.

Atta M. M., Habieb M. E., Mohamed M. A. E. H., Lotfy D. M., Taha E. O.,. (2022). "Radiation-assisted reduction of graphene oxide by aloe vera and ginger and their antioxidant and anti-inflammatory roles against male mice liver injury induced by gamma radiation." New Journal of Chemistry. 46: 4406-4420.

Aunkor M. T. H., Raihan T., Prodhan S. H., Metselaar H. S. C., Malik S. U. F., Azad A. K.,. (2020). "Antibacterial activity of graphene oxide nanosheet against multidrug resistant superbugs isolated from infected patients." Royal Society open science. 7(7): 200640.

Awad F., Zeid A. K., El-Maaty W., El-Wakil A., El-Shall M.,. (2017). "Efficient removal of heavy metals from polluted water with high selectivity for mercury(ii) by 2-imino-4-thiobiuret–partially reduced graphene oxide (it-prgo)." ACS Applied Materials & Interfaces. 9: 34230-34242.

Ayele D. W., Tarekegne A. H.,. (2019). "Synthesis and Characterization of Reduced Graphene Oxide (rGO) Started from Graphene Oxide (GO) Using the Tour Method with Different Parameters." Advances in Materials Science and Engineering. 2019(1): 5058163.

Balandin A. A., Ghosh S., Bao W., Calizo I., Teweldebrhan D., Miao F., Lau C. N.,. (2008). "Superior thermal conductivity of single-layer graphene." Nano Letters. 8(3): 902–907.

Banerjee A. N.,. (2018). "Graphene and its derivatives as biomedical materials: Future prospects and challenges." Interface focus. 8: 20170056.

Barik B., Yun Y., Kumar A., Bae H., Namgung Y., Park J. Y., Song S. J.,. (2023). "Highly enhanced proton conductivity of single-step-functionalized graphene oxide/nafion electrolyte membrane towards improved hydrogen fuel cell performance." International Journal of Hydrogen Energy. 48: 11029-11044.

Barrett E. P., Joyner L. G., Halenda P. P.,. (1951). "The determination of pore volume and area distributions in porous substances. I. Computations from nitrogen isotherms." Journal of the American Chemical Society. 73: 373-380.

Barry A. L.,. (2007). "An overview of the Clinical and Laboratory Standards Institute (CLSI) and its impact on antimicrobial susceptibility tests." Antimicrobial susceptibility testing protocols. 1.

Bautkinová T., Sifton A., Kutorglo E. M., Dendisová M., Kopecký D., Ulbrich P., Hassouna F.,. (2020). "New approach for the development of reduced graphene oxide/polyaniline nanocomposites via sacrificial surfactant-stabilized reduced graphene oxide." Colloids and Surfaces A: Physicochemical and Engineering Aspects. 589: 124415.

Benzait Z., Chen P., Trabzon L.,. (2021). "Enhanced synthesis method of graphene oxide." Nanoscale Advances. 3: 223-230.

Benzait Z., Lakhoua A.,. (2019). “Improving of 'Improved' Graphene Oxide Synthesis Method.” IEEE International Conference on Nanotechnology, Macau SAR." China 7: 978-991.

Biliak R.,. (2023). “Methods of obtaining graphene.” Computational Problems of Electrical Engineering. 1: 1–10.

Björk J., Hanke F., Palma C. A., Samori P., Cecchini M., Persson M.,. (2010). "Adsorption of aromatic and anti-aromatic systems on graphene through π-π stacking." The Journal of Physical Chemistry Letters. 1: 3407-3412.

Bolotin K. I., Sikes K. J., Jiang Z., Klima M., Fudenberg G., Hone J., Stormer H. L.,. (2008) "Ultrahigh electron mobility in suspended graphene." Solid state communications. 146: 351-355.

Bradder P., Ling S. K., Wang S., Liu S.,. (2011). "Dye adsorption on layered graphite oxide." Journal of Chemical & Engineering Data. 56: 138-141.

Brownson D. A., Kampouris D. K., Banks C. E.,. (2012). "Graphene electrochemistry: fundamental concepts through to prominent applications." Chemical Society Reviews. 41: 6944-6976.

Brunauer S., Emmett P. H., Teller E.,. (1938). “Adsorption of gases in multimolecular layers.” Journal of the American Chemical Society. 60(2): 309–319.

Butler A. J., Osborne L., El-Mohtadi M., Whitehead A. K.,. (2020). "Graphene derivatives potentiate the activity of antibiotics against Enterococcus faecium, Klebsiella pneumoniae and Escherichia coli." AIMS Bioengineering. 7(2), 106-113.

Canever N., Chen X., Wojcik M., Zhang H., Dai X., Dubois M., Nann T.,. (2022). “Graphite-mediated microwave-exfoliated graphene fluoride as supercapacitor electrodes.” Nanomaterials. 12(11): 1796.

Capaz R. B.,. (2022). "Grand challenges in graphene and graphite research." Frontiers in Carbon. 1: 1034557.

Ceniceros-Reyes M. A., Marín-Hernández K. S., Sierra U., Saucedo-Salazar E. M., Mendoza-Resendez R., Luna C., Hernández-Belmares P. J., Rodríguez-Fernández O. S., Fernández-Tavizón S., Hernández-Hernández E., Barriga-Castro E. D.,. (2022) "Reduction of graphene oxide by in-situ heating experiments in the transmission electron microscope." Surfaces and Interfaces. 1(35): 102448.

Chabot V., Higgins D., Yu A., Xiao X., Chen Z., Zhang J.,. (2014). "A review of graphene and graphene oxide sponge: material synthesis and applications to energy and the environment." Energy & Environmental Science. 7: 1564-1596.

Chamoli P., Das M. K., Kar K. K.,. (2017). “Structural, optical and electronic characteristics of N-doped graphene nanosheets synthesized using urea as reducing agent and nitrogen precursor.” Materials Research Express. 4(1): 015012.

Chandrasekaran S., Ramanathan S., Basak T.,. (2012). “Microwave material processing—a review.” AIChE Journal. 58(2): 330–363.

Chandu B., Kurmarayuni C. M., Kurapati S., Bollikolla H. B.,. (2020). Green and economical synthesis of graphene–silver nanocomposite exhibiting excellent photocatalytic efficiency. Carbon Letters. 30(2): 225-233.

Chang D. W., Baek J. B.,. (2016). "Eco-friendly synthesis of graphene nanoplatelets." Journal of Materials Chemistry. 4(40): 15281-15293.

Chen G., Seo J., Yang C., Prasad P. N.,. (2013). “Nanochemistry and nanomaterials for photovoltaics.” Chemical Society Reviews. 42(21): 8304–8338.

Chen J., Li Y., Huang L., Li C., Shi G.,. (2015). "High-yield preparation of graphene oxide from small graphite flakes via an improved Hummers method with a simple purification process." Carbon. 81: 826-834.

Chen J., Liu B., Gao X.,. (2020). “Thermal properties of graphene-based polymer composite materials: A molecular dynamics study.” Results in Physics. 16: 102974.

Chen J., Peng H., Wang X., Shao F., Yuan Z., Han H.,. (2013). "Graphene oxide exhibits broad-spectrum antimicrobial activity against bacterial phytopathogens and fungal conidia by intertwining and membrane perturbation." Nanoscale. 6: 1879-1889.

Chen J., Yao B., Li C., Shi G.,. (2013). "An improved Hummers method for eco-friendly synthesis of graphene oxide." Carbon. 64: 225-229.

Chen Q., Yin Q., Dong A., Gao Y., Qian Y., Wang D., Dong M., Shao Q., Liu H., ao. Hung B., H.,. Ding T., Bao-Hang H., Wang N.,. (2019). Metal complex hybrid composites based on fullerene-bearing porous polycarbazole for H2, CO2 and CH4 uptake and heterogeneous hydrogenation catalysis. Polymer. 169: 255-262.

Chen X., Bo X., Ren W., Chen S., Zhao C.,. (2019). "Microwave-assisted shock synthesis of diverse ultrathin graphene-derived materials." Materials Chemistry Frontiers. 3: 1433-1439.

Chen X., Qu Z., Liu Z., Ren G.,. (2022). "Mechanism of Oxidization of Graphite to Graphene Oxide by the Hummers Method." ACS Omega. 7(27): 23503–23510.

Cheng H., Huang Y., Shi G., Jiang L., Qu L.,. (2017) "Graphene-Based Functional Architectures: Sheets Regulation and Macrostructure Construction toward Actuators and Power Generators." Accounts of Chemical Research 50.7: 1663-1671.

Cheng J., Liu Z., Liu H., Zhang X.,. (2023). "Efficient production of graphene via microwave-assisted exfoliation of graphite with gas-evolving agents." Journal of Materials Science. 58(1): 74–83.

Chilingarov N. S., Knot'ko A. V., Skokan E. V., Khavrel P. A., Levanov A. V., Isaikina O. Y., Shulga Y. M.,. (2021). "Microwave exfoliated graphite oxide (MEGO) heat treatment: Transformation and stability." Diamond and Related Materials. 120: 108654.

Chronopoulos D., Bakandritsos A., Pykal M., Zbořil R., Otyepka M.,. (2017) "Chemistry, properties, and applications of fluorographene." Applied materials today. 9: 60-70.

Chua C. K., Pumera M.,. (2014) "Chemical reduction of graphene oxide: a synthetic chemistry viewpoint." Chemical Society Reviews. 43: 291-312.

Chuah R., Gopinath S. C., Anbu P., Salimi M. N., Yaakub A. R. W., Lakshmipriya T.,. (2020). Synthesis and characterization of reduced graphene oxide using the aqueous extract of Eclipta prostrata. 3 Biotech, 10(8), 364.

Çiplak Z., Yildiz N. and Çalimli A.,. (2015). "Investigation of graphene/Ag nanocomposites synthesis parameters for two different synthesis methods. Fullerenes." Nanotubes and Carbon Nanostructures. 23: 361-370.

Claramunt S., Varea A., Lopez-Diaz D., Velázquez M. M., Cornet A., Cirera A.,. (2015). "The importance of interbands on the interpretation of the Raman spectrum of graphene oxide." The Journal of Physical Chemistry C. 119(18): 10123–10129.

Cobos M., Fernández M. J., Fernández M. D.,. (2018). "Graphene based poly (Vinyl alcohol) nanocomposites prepared by in situ green reduction of graphene oxide by ascorbic acid: Influence of graphene content and glycerol plasticizer on properties." Nanomaterials. 8: 1013.

Coccato A., Jehlicka J., Moens L., Vandenabeele P.,. (2015). "Raman spectroscopy for the investigation of carbon-based black pigments." Journal of Raman Spectroscopy. 46(10), 1003-1015.

Coroş M., Pogăcean F., Măgeruşan L., Roşu M. C., Porav A. S., Socaci C., Pruneanu S.,. (2018). "Graphene-porphyrin composite synthesis through graphite exfoliation: the electrochemical sensing of catechol." Sensors and Actuators B: Chemical 256: 665-673.

Daniela C. M., Marcano, D. C., Kosynkin, D. V., Berlin, J. M., Sinitskii, A., Sun, Z., Slesarev, A., Tour, J. M.,. (2010). "Improved Synthesis of Graphene Oxide." ACS Nano. 4(8): 4806-4814.

Das P., Deoghare A. B., Maity S. R.,. (2021). "A novel approach to synthesize reduced graphene oxide (RGO) at low thermal conditions." Arabian Journal for Science and Engineering. 46: 5467-5475.

David L. D., Marta L. H., Mercedes V. M.,. (2017). "Evolution of the Raman spectrum with the chemical composition of graphene oxide." The Journal of Physical Chemistry C. 121(37): 20489-20497.

De Mendonça J. P. A., Lima A. H., Roldao J. C., Martins J. D. S., Junqueira G. M., Quirino W. G., Sato F.,. (2018). "The role of sulfate in the chemical synthesis of graphene oxide." Materials Chemistry and Physics. 215: 203-210.

De Silva K. K. H., Huang H. H., Yoshimura M.,. (2018). "Progress of reduction of graphene oxide by ascorbic acid." Applied Surface Science. 447: 338-346.

De Silva K. K., Huang H., Joshi R., Yoshimura M.,. (2017). "Chemical reduction of graphene oxide using green reductants." Carbon. 119: 190-199.

Dedkov Y. S., Voloshina E. N.,. (2015). “Graphene growth and properties on metal substrates.” Journal of Physics: Condensed Matter. 27(30): 303002.

De-Mendonça J. P., Lima A. H., Roldão J. C., Martins J. D., Junqueira G. M., Quirino W. G., Sato F.,. (2018). “The role of sulfate in the chemical synthesis of graphene oxide.” Materials Chemistry and Physics. 215: 203–210.

Dennison J. R., Holtz M., Swain G.,. (1996). "Raman spectroscopy of carbon materials." Spectroscopy, 11(8): 38-45.

Dimiev A. M., Tour J. M.,. (2014). “Mechanism of graphene oxide formation.” ACS Nano. 8(3): 3060–3068.

Dimiev A. M., Kosynkin D. V., Alemany L. B., Chaguine P., Tour J. M.,. (2012). "Pristine graphite oxide." Journal of the American Chemical Society. 134: 2815-2822.

Dreyer D. R., Park S., Bielawski C. W. Ruoff R. S.,. (2014). “Harnessing the chemistry of graphene oxide.” Chemical Society Reviews. 43(15): 5288–5301.

Dreyer D. R., Park S., Bielawski C. W., Ruoff R. S.,. (2010). "The chemistry of graphene oxide." Chemical Society Reviews. 39: 228-240.

Dubey A., Dube C. L.,. (2024). "Microwave processing of carbon-based materials: A review." Nano-Structures & Nano-Objects. 38:101136.

Eftekhari A., Shulga Y. M., Baskakov S. A., Gutsev G. L.,. (2018). "Graphene oxide membranes for electrochemical energy storage and conversion." International journal of hydrogen energy. 43: 2307-26.

Eigler S., Hirsch A.,. (2014). "Chemistry with Graphene and Graphene Oxide—Challenges for Synthetic Chemists." Angewandte Chemie International Edition. 53: 7720-7738.

Elhamid A. I., Aly H. F., Soliman H. A., El-Shanshory A. A.,. (2018). "Graphene oxide: Follow the oxidation mechanism and its application in water treatment." Journal of Molecular Liquids. 265: 226-37.

Elhamid A. I., Kamoun E. A., El-Shanshory A. A., Solima H. M., Aly H. F.,. (2019). "Evaluation of graphene oxide-activated carbon as effective composite adsorbent toward the removal of cationic dyes: Composite preparation, characterization and adsorption parameters." Journal of Molecular Liquids. 279: 530-9.

El-Khodary S. A., El-Enany G. M., El-Okr M., Ibrahim M.,. (2014). "Preparation and characterization of microwave reduced graphite oxide for high-performance supercapacitors." Electrochimica Acta. 150: 269-78.

Emiru T. F., Ayele D. W.,. (2016). "Controlled synthesis, characterization and reduction of graphene oxide: A convenient method for large scale production." Egyptian Journal of Basic and Applied Sciences. 4: 74-79.

Erickson K., Erni R., Lee Z., Alem N., Gannett W., Zettl A.,. (2010). "Determination of the local chemical structure of graphene oxide and reduced graphene oxide." Advanced materials. 22(40): 4467-4472.

Faisal S, Wasim J, Mohamed E. R., Sayed D. M., Ramashis E. B.,. (2023) "Mathematical modelling of graphene-oxide/kerosene oil nanofluid via radiative linear extendable surface." Alexandria Engineering Journal. 70: 395-410.

Faiz M. S., Azurahanim A., Che C. A., Raba'ah S. A., Ruzniza M. Z.,. (2020). "Low cost and green approach in the reduction of graphene oxide (GO) using palm oil leaves extract for potential in industrial applications." Results in Physics. 16: 102954.

Farah S., Farkas A., Madarász J., László K.,. (2020). "Comparison of thermally and chemically reduced graphene oxides by thermal analysis and Raman spectroscopy." Journal of Thermal Analysis and Calorimetry. 142: 331-337.

Farazas A. A. M., Chia D.,. (2018). “Ultrasound assisted green synthesis and characterization of graphene oxide.” International Journal of Nanoscience and Nanotechnology. 14(1): 11–17.

Farazas A., Mavropoulos A., Christofilos D., Tsiaousis I., Tsipas D.,. (2018). "Ultrasound assisted green synthesis and characterization of graphene oxide." International Journal of Nanoscience and Nanotechnology. 14(1): 11-17.

Farjadian F., Abbaspour S., Sadatlu M. A. A., Mirkiani S., Ghasemi A., Hoseini-Ghahfarokhi M., Hamblin M. R.,. (2020). "Recent developments in graphene and graphene oxide: Properties, synthesis, and modifications: A review." ChemistrySelect. 5(33): 10200-10219.

Felshia S. C., Gnanamani A.,. (2023). "Study on free and entangled binary metal nanocatalysts for removal of 2,4,6-trichlorophenol in aqueous phase: a comparative study." Nanotechnology. 34: 305702.

Feng H., Cheng R., Zhao X., Duan X., Li J.,. (2013). "A low-temperature method to produce highly reduced graphene oxide." Nature communications. 4(1): 1539.

Ferrari A. C., Robertson J.,. (2000). "Interpretation of Raman spectra of disordered and amorphous carbon." Physical review B. 61: 14095.

Foo K. Y., Hameed B. H.,. (2010). "An overview of dye removal via activated carbon adsorption process." Desalin Water Treat. 19: 255-274.

Forgacs E., Cserhati T., Oros G.,. (2004). "Removal of synthetic dyes from wastewaters: a review." Environment International. 30: 953-971.

Furchi M., Urich A., Pospischil A., Lilley G., Unterrainer K., Detz H., Mueller T.,. (2012). "Microcavity-integrated graphene photodetector." Nano Letters. 12: 2773-2777.

Gadong B. D. (2016).,. "Removal of acid blue 25 using cempedak durian peel from aqueous medium: Isotherm, kinetics and thermodynamics studies." International Food Research Journal. 23: 1154-1163.

Gan L., Li B., Chen Y., Yu B., Chen Z.,. (2019). "Green synthesis of reduced graphene oxide using bagasse and its application in dye removal: a waste-to-resource supply chain." Chemosphere. 219: 148-154.

Gao C., Xu Z., Ma J., Chen Y.,. (2023). “Advances in microwave-assisted synthesis of graphene and its derivatives.” Materials Today Advances. 16: 100287.

Gao Y., Xu J., Hu H., Zhang C.,. (2023). “Microwave-assisted exfoliation of graphite: A green and efficient method for producing high-quality graphene.” Journal of Cleaner Production. 386: 135674.

Gawande M. B., Shelke S. N., Zboril R., Varma R. S.,. (2014). "Microwave-assisted chemistry: synthetic applications for rapid assembly of nanomaterials and organics." Accounts of chemical research. 47(4), 1338-1348.

Geim A. K., Novoselov K. S.,. (2007). “The rise of graphene.” Nature Materials. 6(3): 183–191.

Gensheimer J., Broaddus J., Lin Y. C., Cao Y.,. (2014). "Scalable production of reduced graphene oxide (rGO) from graphite oxide (GO)." Young Scientist. 4: 39-42.

Georgakilas V., Perman J. A., Tucek J., Zboril R.,. (2015). "Broad family of carbon nanoallotropes: classification, chemistry, and applications of fullerenes, carbon dots, nanotubes, graphene, nanodiamonds, and combined superstructures." Chemical reviews. 115(11), 4744-4822.

Ghann W. E., Kang H., Uddin J., Chowdhury F. A., Khondaker S. I., Moniruzzaman M., Rahman M. M.,. (2019). "Synthesis and characterization of reduced graphene oxide and their application in dye-sensitized solar cells." ChemEngineering. 3(1): 7.

Ghorbani M., Abdizadeh H., Golobostanfard M. R.,. (2015). "Reduction of Graphene Oxide via Modified Hydrothermal Method." Procedia Materials Science: Procedia Materials Science. 11, 326-330.

Ghorbani M., Asl M. A., Shahraki A.,. (2022). “Microwave-assisted production of graphene: An overview of methods, advantages, and applications.” Nanomaterials. 12(20): 3298.

Ghulam A. N., Santos O. A. L., Hazeem L., Backx P. B., Bououdina M., Bellucci S.,. (2022). "Graphene Oxide (GO) Materials—Applications and Toxicity on Living Organisms and Environment." Journal of Functional Biomaterials. 13(2): 77.

Giang T. T., Lee G., Kim Y. A.,. (2018). “Divergent mechanisms for thermal reduction of graphene oxide and their highly different ion affinities.” Diamond and Related Materials. 89: 246–256.

Gisi D. S., Lofrano G., Grassi M., Notarnicola M.,. (2016). "Characteristics and adsorption capacities of low-cost sorbents for wastewater treatment: A review." Sustainable Materials and Technologies. 9: 10-40.

Gregg S. J., Sing K. S. W.,. (1967). “Adsorption, surface area, and porosity.” Academic Press.

Grewal A. S., Kumar K., Redhu S., Bhardwaj S.,. (2013). "Microwave assisted synthesis: a green chemistry approach." International Research Journal of Pharmaceutical and Applied Sciences. 3(5), 278-285.

Gu C., Zhang H., Wang X., Tu J.,. (2013). "Synthesis of reduced graphene oxide by an ionothermal method and electrochemical performance." RSC Advances. 3: 11807.

Guerrero-C. J., Caballero-Briones F.,. (2015). "Graphene oxide powders with different oxidation degree, prepared by synthesis variations of the Hummers method." Materials Chemistry and Physics. 153: 209-20.

Guex L. G., Sacchi B., Peuvot K. F., Andersson R. L., Pourrahimi A. M., Ström V., Farris S., Olsson R. T.,. (2017). "Experimental review: chemical reduction of graphene oxide (GO) to reduced graphene oxide (rGO) by aqueous chemistry." Nanoscale. 9: 9562-9571.

Guo T., Bulin C., Ma Z., Li B., Zhang Y., Zhang B., Ge X.,. (2021). "Mechanism of cd(ii) and cu(ii) adsorption onto few-layered magnetic graphene oxide as an efficient adsorbent." Acs Omega. 6: 16535-16545.

Guo, T.,. (2023). "Application of graphene technology in the removal of heavy metal ions in wastewater." Highlights in Science Engineering and Technology. 73: 464-470.

Gupta V. K., Suhas H.,. (2009). "Application of low-cost adsorbents for dye removal – A review." Environmental Management. 90: 2313-2342.

Gupta V., Sharma N., Singh U., Arif M., Singh A.,. (2017). "Higher oxidation level in graphene oxide." Optik. 143: 115-124.

Gurunathan S., Han J. W., Daye A. A., Eppakayala V. Kim J.,. (2012). "Oxidative stress-mediated antibacterial activity of graphene oxide and reduced graphene oxide in Pseudomonas aeruginosa." International Journal of Nanomedicine. 5901-5914.

Habte A. T., Ayele D. W.,. (2019). "Synthesis and characterization of reduced graphene oxide (rGO) started from graphene oxide (GO) using the tour method with different parameters." Advances in Materials Science and Engineering. 2019: 5058163.

Han R., Wang P., Zhang S.,. (2019). "High-performance graphene oxide nanofiltration membrane with continuous nanochannels prepared by the in-situ oxidation of MXene." Journal of Materials Chemistry A. 7(11): 6475–6481.

Hartono T., Wang S., Ma Q., Zhu Z.,. (2009). "Layer structured graphite oxide as a novel adsorbent for humic acid removal from aqueous solution." Journal of colloid and interface science. 333: 114-119.

Hassaan M. A., El Nemr A., Hassaan A.,. (2017). "Health and environmental impacts of dyes: mini review." American Journal of Environmental Science and Engineering. 1: 64-67.

Heidarizad M., Şengör S. S.,. (2016). "Synthesis of graphene oxide/magnesium oxide nanocomposites with high-rate adsorption of methylene blue." Journal of Molecular Liquids. 224: 607-17.

Hettler S., Sebastian D., Pelaez-Fernandez M., Benito A. M., Maser W. K., Arenal R.,. (2021). "In-situ reduction by Joule heating and measurement of electrical conductivity of graphene oxide in a transmission electron microscope." 2D Materials. 8(3): 031001.

Hidayah N. M., Liu W. W., Lai C. W., Noriman N. Z., Khe C. S., Hashim U., Lee H. C.,. (2017). "Comparison on graphite, graphene oxide and reduced graphene oxide: Synthesis and characterization." AIP Conference Proceedings. 1892: 150002.

Hofmann M., Chiang W., Nguyen T. D., Hsieh Y.,. (2015). "Controlling the properties of graphene produced by electrochemical exfoliation." Nanotechnology. 26: 335607.

Hoque M. A., Rahman A. M., Rahman M. M., Bhuiyan M. N. I., Jahan S. A., Shaikh M. A. A., Nurnabi M.,. (2024). "Effect of successive recycling and reuse of acid liquor for the synthesis of graphene oxides with higher oxygen-to-carbon ratios." Heliyon. 10(6): e27639.

Hossain M. N., Wen J., Konda S. K., Govindhan M., Chen A.,. (2017). "Electrochemical and FTIR spectroscopic study of CO2 reduction at a nanostructured Cu/reduced graphene oxide thin film." Electrochemistry Communications. 82: 16-20.

Hou D., Liu Q., Wang X., Quan Y., Qiao Z., Yu L., Ding S.,. (2018). "Facile synthesis of graphene via reduction of graphene oxide by artemisinin in ethanol." Journal of Materiomics. 4(3): 256-265.

Hou Y., Lv S., Liu L., Liu X.,. (2020). "High-quality preparation of graphene oxide via the Hummers' method: Understanding the roles of the intercalator, oxidant, and graphite particle size." Ceramics International. 46(2): 2392-2402.

Hua Y., Li F., Hu N., Fu S. Y.,. (2022). "Frictional characteristics of graphene oxide-modified continuous glass fiber reinforced epoxy composite." Composites Science and Technology. 223: 109446.

Huang X., Li S., Qi Z., Zhang W., Ye W., Fang Y.,. (2015). "Low defect concentration few-layer graphene using a two-step electrochemical exfoliation." Nanotechnology. 26(10): 105602.

Hui H. H., Silva K., De K. H., Yoshimura M., Kumara G. R. A.,. (2018). "Structural Evolution of Hydrothermally Derived Reduced Graphene Oxide." Scientific Reports. 8: 6849.

Hummer's Jr. W. S., Offeman R. E.,. (1958). "Preparation of graphitic oxide." Journal of the american chemical society. 80(6): 1339-1339.

Ickecan D., Sönmezoglu S.,. (2017). “Eco-friendly synthesis and characterization of reduced graphene oxide.” Journal of Physics: Conference Series. 902: 012027.

Ieggli C. V. S., Bohrer D., Do Nascimento P. C., De Carvalho L. M., Garcia S. C.,. (2010). "Determination of sodium, potassium, calcium, magnesium, zinc, and iron in emulsified egg samples by flame atomic absorption spectrometry." Talanta. 80(3), 1282-1286.

Ikram R., Jan B. M. Ahmad W.,. (2020). "An overview of industrial scalable production of graphene oxide and analytical approaches for synthesis and characterization." Journal of Materials Research and Technology. 9(5): 11587-11610.

Ioni Y., Sapkov I., Kirsanova M., Dimiev A. M.,. (2023). “Flame modified graphene oxide: Structure and sorption properties.” Carbon. 212: 118122.

Jadhav S. T., Dubal S. U., Jadhav L. D., Shaikh J. S., Chavana A. U., Jamale A. P., Kolekar S. S.,. (2013). "Behavior of graphene oxide in ionic liquid for supercapacitor application." AIP Conference Proceedings. 1183-1184.

Jakhar A., Sharma J., Sharma S., Sharma L. K.,. (2023). "Graphene-Based Nano Materials: Biomedical Applications." Chemistry Select. 8(37): e202302689.

Jakhar R., Yap J. E., Joshi R. K.,. (2020). “Microwave reduction of graphene oxide.” Carbon. 170: 277–293.

Jalagonia N., Bakradze N., Darakhvelidze N., Sanaia E., Bokuchava G., Kuchukhizdef T., Batako A.,. (2022). "Experimental investigation into a new method of scalable production of reduced graphene oxide for potential industrial graphene nanocomposite manufacture." Journal of Physics: Conference Series. 2198: 012054.

Jalili R., Esrafilzadeh D., Aboutalebi S. H., Sabri Y. M., Kandjani A. E., Bhargava S. K., Wallace G. G.,. (2018). "Silicon as a ubiquitous contaminant in graphene derivatives with significant impact on device performance." Nature Communications. 9(1): 5070.

Jankovský O., Nováček M., Luxa J., Sedmidubský D., Fila V., Pumera M., Sofer Z.,. (2016). “A new member of the graphene family: Graphene acid.” Chemistry – A European Journal. 22(48): 17416–17424.

Janowska I., Chizari K., Ersen O., Zafeiratos S., Soubane D., Costa V. D., Huu C. P.,. (2010). "Microwave synthesis of large few-layer graphene sheets in aqueous solution of ammonia." Nano Research. 3: 126-137.

Jeong H. K., Lee Y. P., Lahaye R. J., Park M. H., An K. H., Kim I. J., Lee Y. H.,. (2008). "Evidence of graphitic AB stacking order of graphite oxides." Journal of the American Chemical Society. 130: 1362-1366.

Jiang F., Yu Y., Wang Y., Feng A., Song L.,. (2017). A novel synthesis route of graphene via microwave assisted intercalation-exfoliation of graphite. Materials Letters. 200, 39-42.

Jiao X., Qin Y., Chen Y.,. (2017). "Comparison of the characteristic properties of reduced graphene oxides synthesized from natural graphites with different graphitization degrees." RSC Advances. 7(83): 52337–52344.

Jilani A. I., Othman M. H. D., Ansari M. O., Hussain S. Z., Ismail A. F., Khan I. U.,. (2018). "Graphene and its derivatives: Synthesis, modifications, and applications in wastewater treatment." Environmental Chemistry Letters. 16: 1301–1323.

Jin Y., Du Q., Li Y., Zhang Y., Chen B., Wang M., Jing Z.,. (2022). "Removal of methylene blue by crosslinked egg white protein/graphene oxide bionanocomposite aerogels." Nanomaterials. 12(5): 2659.

Jing S. N., Meng C. C., Lu C., Liu Z., Qiang K. Q., Rong C.,. (2014) "Thermally reduced graphene oxide films as flexible lateral heat spreaders." Journal of Materials Chemistry A. 2: 16563-16568.

Johra F. T., Lee J. W., Jung W. G.,. (2014). "Facile and safe graphene preparation on solution based platform." Journal of Industrial and Engineering Chemistry. 20(5): 2883-2887.

Kabir M. H., Hossain M. S., Rahman M. M., Ashrafuzzaman M., Hasan M., Pabel M. Y., Yasmin S.,. (2024). "Green Reduction of Waste-Battery-Derived Graphene Oxide by Jute Leaves and Its Application for the Removal of Tetracyclines from Aqueous Media." ACS Sustainable Resource Management. 1(8), 1812-1823.

Kafashan H., Baboukani A. R.,. (2024). "Electrochemically deposited nanostructured Cd-doped SnS thin films: Structural and optical characterizations." Ceramics International, 50(3), 5717-5727.

Kang J. H., Kim T., Choi J., Park J., Kim Y. S., Chang M. S., Jung H., Park K. T., Yang S. J., Park C. R.,. (2016). "Hidden second oxidation step of Hummers method." Chemistry of Materials. 28: 756-64.

Kar K. K.,. (2020). "Handbook of nanocomposite supercapacitor materials II (Vol. 302)." Cham: Springer International Publishing.

Karim M. R., Takehira H., Matsui T., Murashima Y., Ohtani R., Nakamura M., Hayami S.,. (2014). "Graphene and graphene oxide as super materials." Current Inorganic Chemistry (Discontinued). 4(3): 191–219.

Kaushal A., Dhawan S. K., Singh V. (2019). "Determination of crystallite size, number of graphene layers and defect density of graphene oxide (GO) and reduced graphene oxide (RGO). In AIP Conference Proceedings. 2115(1). AIP Publishing.

Kawabata A., Murakami T., Nihei M., Yokoyama N.,. (2013). "Growth of dense, vertical and horizontal graphene and its thermal properties." Japanese Journal of Applied Physics. 52(4S), 04CB06.

Kazuto G., Keisuke A., Michio K., Yoshiki S., Yukiya H., Yasumichi M.,. (2017). "Production of water-dispersible reduced graphene oxide without stabilizers using liquid-phase photoreduction." Soft Matter. 13: 8353-8356.

Khaliha S., Marforio T. D., Kovtun A., Mantovani S., Bianchi A., Navacchia M. L., Melucci M.,. (2021). "Defective graphene nanosheets for drinking water purification: Adsorption mechanism, performance, and recovery." FlatChem. 29: 100283.

Khan F. U., Mahmood S., Ahmad Z., Mahmood T., Nizami Z. A.,. (2019) "Graphene oxide synthesis by facile method and its characterization" Open Journal of Chemistry. 2(1): 11-15.

Khan J., Jaafar M.,. (2021). "Reduction efficiencies of natural substances for reduced graphene oxide synthesis." Journal of Materials Science. 56: 18477-18492.

Khan M. A., Kumar A., Zhang J., Kumar M.,. (2021). "Recent advances and prospects in reduced graphene oxide-based photodetectors." Journal of Materials Chemistry C. 9(26): 8129-8157.

Khan Q. A., Shaur A., Khan T. A., Joya Y. F., Awan M. S. (2017). Characterization of reduced graphene oxide produced through a modified Hoffman method. Cogent Chemistry. 3(1): 1298980.

Khanam, P. N., Al-Maadeed M. A., Ouederni M., Mayoral B., Hamilton A., Sun D.,. (2016). "Effect of two types of graphene nanoplatelets on the physico–mechanical properties of linear low–density polyethylene composites." Advanced Manufacturing: Polymer & Composites Science. 2(2): 67-73.

Kiew S. F., Kiew L. V., Lee H. B., Imae T., Chung L. Y.,. (2016). "Assessing biocompatibility of graphene oxide-based nanocarriers: A review." Journal of Controlled Release. 226: 217-228.

Kim J. M., Hong W. G., Lee S. M., Chang S. J., Jun Y., Kim B. H., Kim H. J.,. (2014). "Energy storage of thermally reduced graphene oxide." International Journal of Hydrogen Energy. 39: 3799-3804.

Kishor R., Purchase D., Saratale G. D., Saratale R. G., Ferreira L. F. R., Bilal M., Bharagava R. N.,. (2021). "Ecotoxicological and health concerns of persistent coloring pollutants of textile industry wastewater and treatment approaches for environmental safety." Journal of Environmental Chemical Engineering. 9: 105012.

Kogan E.,. (2022). "Graphene for electronics." Nanomaterials. 12: 4359.

Kong S., Lim M. Y., Shin H., Baik J. H., Lee J. C.,. (2020). "High-flux and antifouling polyethersulfone nanocomposite membranes incorporated with zwitterion-functionalized graphene oxide for ultrafiltration applications." Journal of Industrial and Engineering Chemistry. 84: 131-40.

Kornilov D. Y., Gubin S. P.,. (2020). "Graphene oxide: structure, properties, synthesis, and reduction (a review)." Russian Journal of Inorganic Chemistry. 65: 1965-1976.

Kostromin S. V., Podshivalov A., Asandulesa M., Bronnikov S.,. (2019). Electrical conductivity of polyazomethine/reduced graphene oxide nanocomposites." IOP Conference Series: Materials Science and Engineering. 634(1): 012005.

Kotsyubynsky V., Boychuk V., Budzulyak I. M., Rachiy B. I., Hodlevska M., Kachmar A., Hodlevsky M.,. (2021). "Graphene oxide synthesis using modified tour method." Advances in Natural Sciences: Nanoscience and Nanotechnology. 12: 035006.

Kovtun A., Treossi E., Mirotta N., Scidà A., Liscio A., Christian M., Palermo V.,. (2019). "Benchmarking of graphene-based materials: real commercial products versus ideal graphene." 2D Materials. 6: 025006.

Kudus M. H., Zakaria, M. R., Akil H. M., Ullah F., Javed F.,. (2020). "Oxidation of graphene via a simplified Hummers' method for graphene-diamine colloid production." Journal of King Saud University-Science. 32: 910-3.

Kuhlmann J., Schubert M.,. (2021). "Microwave-assisted methods for the production of nanomaterials: A review." Nanomaterials. 11: 2153.

Kumar A., Kuang Y., Liang Z., Sun X.,. (2020). "Microwave chemistry, recent advancements, and eco-friendly microwave-assisted synthesis of nanoarchitectures and their applications: a review." Materials Today Nano. 11: 100076.

Kumar D, Viprya P, Kowshik S.,. (2023). "Study of different properties of graphene oxide (GO) and reduced graphene oxide (rGO)." Engineering Proceedings. 59(1): 84.

Kumar P. V., Bardhan N. M., Tongay S., Wu J., Belcher A. M., Grossman J. C.,. (2014). "Scalable enhancement of graphene oxide properties by thermally driven phase transformation." Nature Chemistry. 6: 151–158.

Kumar P., Pos H.,. (2019). "Antibacterial properties of graphene-based nanomaterials." Nanomaterials. 9(5): 737.

Kumar R., Prasad A.,. (2022). "Eco-friendly microwave-assisted synthesis of graphene: An overview of its mechanisms, applications, and advantages." Materials Today: Proceedings. 64: 1806–1812.

Kumar R., Sahoo S., Joanni E., Singh R. K.,. (2022). "A review on the current research on microwave processing techniques applied to graphene-based supercapacitor electrodes: An emerging approach beyond conventional heating." Journal of Energy Chemistry. 74: 252-282.

Kumara K. J., Krishnamurthy G. N., Jinendra U., Bhat S.,. (2021). “Palladium metal embedded on mesoporous graphene oxide as an efficient heterogeneous catalyst for Suzuki coupling reaction.” Materials Today: Proceedings. 46: 2874–2879.

Kuo S., Liu W., Kuo C., Wu N., Wu H.,. (2013). "Lithium storage in reduced graphene oxides." Journal of Power Sources. 244: 552-556.

Kurapati R., Russier J., Squillaci M. A., Treossi E., Ménard-Moyon C., Del Rio-Castillo A. E., Bianco A.,. (2015). "Dispersibility-dependent biodegradation of graphene oxide by myeloperoxidase." Small. 11(32), 3985-3994.

Kurian M.,. (2021). “Recent progress in the chemical reduction of graphene oxide by green reductants: A mini review.” Carbon Trends. 5: 100120.

Lai Q., Zhu S., Luo X., Zou M., Huang S.,. (2012) "Ultraviolet-visible spectroscopy of graphene oxides." AIP advances. 2(3).

Larciprete R., Fabris S., Sun T., Lacovig P., Baraldi A., Lizzit S.,. (2011). "Dual path mechanism in the thermal reduction of graphene oxide." Journal of the American Chemical Society. 133(43), 17315-17321.

Le G. T., Manyam J., Opaprakasit P., Chanlek N., Grisdanurak N., Sreearunothai P.,. (2018). "Divergent mechanisms for thermal reduction of graphene oxide and their highly different ion affinities." Diamond and Related Materials. 89: 246-256.

Lee C., Wei X., Kysar J. W., Hone J.,. (2008). "Measurement of the elastic properties and intrinsic strength of monolayer graphene." Science. 321(5887), 385-388.

Lee S. H., Seo S. D., Jin Y. H., Shim H. W., Kim D. W.,. (2010) "A graphite foil electrode covered with electrochemically exfoliated graphene nanosheets." Electrochemistry communications. 12: 1419-1422.

Lellis B., Fávaro-Polonio C. Z., Pamphile J. A., Polonio J. C.,. (2019). "Effects of textile dyes on health and the environment and bioremediation potential of living organisms." Biotechnology Research and Innovation. 3(2): 275-290.

Leonardi A., Bish D. L.,. (2020). "Understanding powder X-ray diffraction profiles from layered minerals: The case of kaolinite nanocrystals." Inorganic Chemistry. 59: 5357-5367.

Leow C., Kreider P. B., Sommacal S., Kluth P., Compston P.,. (2023). “Electrical and thermal conductivity in graphene-enhanced carbon-fibre/PEEK: The effect of interlayer loading.” Carbon. 215: 118463.

Li B., Jin X., Lin J., Chen Z.,. (2018). "Green reduction of graphene oxide by sugarcane bagasse extract and its application for the removal of cadmium in aqueous solution." Journal of Cleaner Production. 189: 128-134.

Li C., Lu Y., Yan J., Yu W., Zhao R., Du S., Niu K.,. (2021). "Effect of long-term ageing on graphene oxide: structure and thermal decomposition." Royal Society Open Science. 8(12): 202309.

Li P., Wu W., Liu J., Shi B., Du Y., Li Y., Wang J.,. (2018). "Investigating the nanostructures and proton transfer properties of Nafion-GO hybrid membranes." Journal of Membrane Science. 555: 327-36.

Li X., Cai W., An J., Kim S., Nah J., Yang D., Ruoff R. S.,. (2009). "Large-area synthesis of high-quality and uniform graphene films on copper foils." Science. 324(5932): 1312-1314.

Li Y., Louarn G., Aubert P. H., Alain-Rizzo V., Galmiche L., Audebert P., Miomandre F.,. (2016). "Polypyrrole-modified graphene sheet nanocomposites as new efficient materials for supercapacitors." Carbon. 105: 510-520.

Li Z., Yao Y., Lin Z., Moon K. S., Lin W., Wong C.,. (2010). "Ultrafast, dry microwave synthesis of graphene sheets." Journal of Materials Chemistry. 20: 4781-4783.

Liang H., Bu Y., Zhang Y., Zhang J.,. (2014). "Graphene oxide as efficient high-concentration formaldehyde scavenger and reutilization in supercapacitor." Journal of Colloid and Interface Science. 444: 109-114.

Lim J. Y., Mubarak N.M., Abdullah E.C., Nizamuddin S., Khalid M.,. (2018) "Recent trends in the synthesis of graphene and graphene oxide based nanomaterials for removal of heavy metals-A review." Journal of Industrial and Engineering Chemistry. 66: 29-44.

Lin C., Wei W., Hu Y. H.,. (2016). "Catalytic behavior of graphene oxide for cement hydration process." Journal of Physics and Chemistry of Solids. 89: 128-33.

Lin J., Huang Y., Wang S., Chen G.,. (2017). "Microwave-assisted rapid exfoliation of graphite into graphene by using ammonium bicarbonate as the intercalation agent." Industrial & Engineering Chemistry Research. 56(33): 9341-9346.

Lin Z., Yao Y., Li Z., Liu Y., Li Z., Wong C. P.,. (2010). "Solvent-Assisted Thermal Reduction of Graphite Oxide." The Journal of Physical Chemistry C. 114: 14819-14825.

Liou Y. J., Tsai B. D., Huang W. J.,. (2015). "An economic route to mass production of graphene oxide solution for preparing graphene oxide papers." Materials Science and Engineering B. 193: 37-40.

Liu J., Poh C. K., Zhan D., Lai L., Lim S. H., Wang L., Lin J.,. (2013). "Improved synthesis of graphene flakes from the multiple electrochemical exfoliation of graphite rod." Nano Energy. 2: 377-386.

Liu L., Cheng Y., Zhang X., Shan Y., Zhang X., Wang W., Li D.,. (2017). "Graphene-based transparent conductive films with enhanced transmittance and conductivity by introducing antireflection nanostructure." Surface and Coatings Technology. 325: 611-616.

Liu N., Luo F., Wu H., Liu Y., Zhang C., Chen J.,. (2008). "One-step ionic-liquid-assisted electrochemical synthesis of ionic-liquid-functionalized graphene sheets directly from graphite." Advanced Functional Materials. 18: 1518-1525.

Liu S., Zeng T. H., Hofmann M., Burcombe E., Wei J., Jiang R., Chen Y.,. (2011). "Antibacterial activity of graphite, graphite oxide, graphene oxide, and reduced graphene oxide: membrane and oxidative stress." ACS nano. 5(9): 6971-6980..

Liu W., Speranza G.,. (2021). "Tuning the oxygen content of reduced graphene oxide and effects on its properties." ACS omega. 6(9): 6195-6205.

Liu W.W., Chai S.P., Mohamed A.R. Hashim U.,. (2014). "Synthesis and characterization of graphene and carbon nanotubes: A review on the past and recent developments." Journal of Industrial and Engineering Chemistry. 20: 1171-85.

Liu X., Liu J., Zhan D., Yan J., Wang J., Chao D., Lai L., Chen M., Yin J., Shen Z.,. (2013). "Repeated microwave-assisted exfoliation of expandable graphite for the preparation of large scale and high quality multi-layer graphene." RSC Advanced. 3(29): 11601-11606.

Liu X., Zhang X., Zhao Y.,. (2023). "Rapid microwave-assisted exfoliation of graphite facilitated by ammonium bicarbonate: A novel approach for producing high-quality graphene." Advanced Materials. 35: 2207552.

Liu Z., Xu J., Wang Y., Chen H.,. (2022). "Mechanisms of microwave-assisted exfoliation of graphite using ammonium bicarbonate for rapid graphene production." Journal of Materials Science 57: 6934–6947.

Lombardi L., Kovtun A., Mantovani S., Bertuzzi G., Favaretto L., Bettini C., Bandini M.,. (2022). "Visible-Light Assisted Covalent Surface Functionalization of Reduced Graphene Oxide Nanosheets with Arylazo Sulfones." Chemistry–A European Journal. 28: e202200333.

Long J., Fang M., Chen G.,. (2011). "Microwave-assisted rapid synthesis of water-soluble graphene." Journal of Materials Chemistry. 21: 10421-10425.

Long J., Xie X., Xu J., Gu Q., Chen L., Wang X.,. (2012). "Nitrogen-doped graphene nanosheets as metal-free catalysts for aerobic selective oxidation of benzylic alcohols." ACS Catalysis. 2: 622-631.

López-Díaz D., Lopez Holgado M., García-Fierro J. L., Velázquez M. M.,. (2017). "Evolution of the Raman spectrum with the chemical composition of graphene oxide." The Journal of Physical Chemistry C, 121(37), 20489-20497.

López-Garcıa I., Vinas P., Blanco C., Hernandez-Cordoba M.,. (1999). "Fast determination of calcium, magnesium and zinc in honey using continuous flow flame atomic absorption spectrometry." Talanta. 49(3): 597-602.

Low C. T. J., Walsh F. C., Chakrabarti M. H., Hashim M. A., Hussain M. A.,. (2013). "Electrochemical approaches to the production of graphene flakes and their potential applications." Carbon. 54: 1-21.

Luan D.,. (2023). "Applications of Graphene in Different Fields." In MATEC Web of Conferences, EDP Sciences. 386: 03015.

Lv S., Ma Y., Qiu C., Sun T., Liu J., Zhou Q. (2013) "Effect of graphene oxide nanosheets of microstructure and mechanical properties of cement composites." Construction and building materials 49: 121-7.

Machado B. F., Serp P.,. (2012) "Graphene-based materials for catalysis." Catalysis Science & Technology. 2(1): 54-75.

Machado P. B., Rocha M. C. G., de Andrade M. C., Junior F. L. S., Peripolli S. B., de Campos J. B.,. (2024). "Effect of reduced graphene oxide on thermal property of recycled textile polyamide." Journal of Materials Research and Technology. 30: 3941-3947.

Mahmood F., Ashraf S., Shahzad M., Li B., Asghar F., Amjad W., Omar M. M.,. (2023). "Graphene Synthesis from Organic Substrates: A Review." Industrial & Engineering Chemistry Research. 62(42): 17314-17327.

Mahmoudian M., Kochameshki M. G.,. (2021). "The performance of polyethersulfone nanocomposite membrane in the removal of industrial dyes." Polymer. 224: 123693.

Mahmudunnabi D. M., Alam M. Z., Nurnabi M.,. (2024). "Synthesis of Reduced Graphene Oxide and Its Application for the Removal of Anaionic dye TURQUOISE GN." Desalination and Water Treatment. 100459.

Majumdar B., Sarma D., Sarma., T. K.,. (2018) "Carbocatalytic activity of graphene oxide in organic synthesis." Graphene Oxide Application Opportunities. 25: 10.5772.25.

Malik P. K.,. (2004). "Dye removal from wastewater using activated carbon developed from sawdust: adsorption equilibrium and kinetics." Journal of Hazardous Materials. 113(1-3): 81-88.

Mann R., Mitsidis D., Xie Z., McNeilly O., Ng Y. H., Amal R., Gunawan C.,. (2021). "Antibacterial activity of reduced graphene oxide." Journal of Nanomaterials. 2021(1): 9941577.

Mantovani S., Khaliha S., Favaretto L., Bettini C., Bianchi A., Kovtun A., Melucci M. (2021) "Scalable synthesis and purification of functionalized graphene nanosheets for water remediation." Chemical Communications. 57: 3765-3768.

Mantovani S., Marforio T. D., Khaliha S., Pintus A., Kovtun A., Tunioli F., Melucci M.,. (2023) "Amino acid-driven adsorption of emerging contaminants in water by modified graphene oxide nanosheets." Environmental Science: Water Research & Technology. 9: 1030-1040.

Mao B., Sidhureddy B., Thiruppathi A. R., Wood P. C., Chen A.,. (2020). "Efficient dye removal and separation based on graphene oxide nanomaterials." New Journal of Chemistry. 44(11): 4519-4528.

Mao S., Yu K., Lu G., Chen J.,. (2011). "Highly sensitive protein sensor based on thermally-reduced graphene oxide field-effect transistor." Nano Research. 4 (2011): 921-930.

Marcano D. C., Kosynkin D. V., Berlin J. M., Sinitskii A., Sun Z., Slesarev A., Alemany L. B., Lu W., Tour J. M.,. (2010). "Improved synthesis of graphene oxide." ACS Nano. 4(8): 4806–4814.

Marcano D. C., Kosynkin D. V., Berlin J. M., Sinitskii A., Sun Z., Slesarev A. S., Tour J. M.,. (2018). “Correction to improved synthesis of graphene oxide.” ACS nano. 12(2): 2078-2078.

Markus O., Pierluigi B., Martin K., Jürgen S., Jiri D., Michael S. P., Peter L., Markus V.,. (2023) "L-Ascorbic Acid Treatment of Electrochemical Graphene Nanosheets: Reduction Optimization and Application for De-Icing, Water Uptake Prevention, and Corrosion Resistance." ACS Applied Material Interfaces. 15: 22471-22484.

Mashiath K., Pooja J., Manoj B.,. (2018). "Synthesis of Graphene Oxide Nano Structures from Kerosene Soot and its Impedance Analysis." Asian Journal of Chemistry. 30: 988-992.

Makhsin S. R., Zakaria M. H., Rani R. A., Gardner P., Scully P. J., Akashah M. H. N.,. (2023). “Enhancing Fibre Optic Sensor Signals Via Gold Nanoparticle-Decorated Agarose Hydrogels.” Optical Materials. 143: 114247.

Menezes I. R., Araújo N. R., Araújo B. C., Sakai T., Lago R. M., Sebastião R. C.,. (2023). “Shedding light on the mechanism of graphene oxide thermal decomposition: A kinetic study using isoconversional method and artificial neural network.” Thermochimica Acta. 721: 179454.

Meredith R. J.,. (1998). "Engineers' handbook of industrial microwave heating" (No. 25). IET.

Merino M. J. F., Guardia L., Paredes J. I., Rodil S. V., Fernández P. S., Alonso A. M., Tascón J. M. D.,. (2010). "Vitamin C Is an Ideal Substitute for Hydrazine in the Reduction of Graphene Oxide Suspensions." The Journal of Physical Chemistry C. 114: 6426-6432.

Metaxas A. A., Meredith R. J.,. (1983). "Industrial microwave heating" (No. 4). IET.

Mohan V. B., Jayaraman K., Bhattacharyya D.,. (2020). "Brunauer–Emmett–Teller (BET) specific surface area analysis of different graphene materials: a comparison to their structural regularity and electrical properties." Solid State Communications. 320: 114004.

Mokhtar M. M., Enein S. A., El A., Hassaan M. Y., Morsy M. S., Khalil M. H.,. (2017). "Thermally Reduced Graphene Oxide: Synthesis, Structuraland Electrical Properties." International Journal Nanoparticles Nanotech. 3: 1-9.

Moosa A., Abed M.,. (2021). "Graphene preparation and graphite exfoliation." Turkish journal of Chemistry. 45: 493-519.

Morales G. M., Schifani P., Ellis G., Ballesteros C., Martínez G., Barbero C., Salavagione H. J.,. (2011). "High-quality few layer graphene produced by electrochemical intercalation and microwave-assisted expansion of graphite." Carbon. 49: 2809-2816.

Mouni A., Hage-Ali H., Bouaziz M., Ammar S.,. (2023). “Recent advances in the exfoliation techniques for graphene production from graphite: A review.” Nanomaterials. 13: 433.

Munuera J. M., Paredes J. I., Enterría M., Pagán A., Rodil S. V., Pereira M. F. R., Tascón J. M. D.,. (2017). "Electrochemical exfoliation of graphite in aqueous sodium halide

electrolytes toward low oxygen content graphene for energy and environmental applications." ACS applied materials & interfaces. 9: 24085-24099.

Munuera J. M., Paredes J. I., Rodil S. V, Muñiz A. C., Alonso A. M., Tascón J. M. D.,. (2018). "High quality, low-oxidized graphene via anodic exfoliation with table salt as an efficient oxidation-preventing co-electrolyte for water/oil remediation and capacitive energy storage applications." Applied Materials Today. 11: 246-254.

Munuera J. M., Paredes J. I., Rodil S. V., Varela M. A., Pagán A., Cervantes S. D. A., Tascón J. M. D.,. (2015). "High quality, low oxygen content and biocompatible graphene nanosheets obtained by anodic exfoliation of different graphite types." Carbon. 94: 729-739.

Murugan A. V., Muraliganth T., Manthiram A.,. (2009). "Rapid, facile microwave-solvothermal synthesis of graphene nanosheets and their polyaniline nanocomposites for energy strorage." Chemistry of Materials. 21: 5004-5006.

Muzyka R., Kwoka M., Smędowski Ł., Díez N., Gryglewicz G.,. (2017). "Oxidation of graphite by different modified Hummers methods." New Carbon Materials. 32: 15-20.

Nair R. R., Blake P., Grigorenko A. N., Novoselov K. S., Booth T. J., Stauber T., Geim A. K.,. (2008). "Fine structure constant defines visual transparency of graphene." Science. 320: 1308-1308.

Nandakumar P., Sankar K. N. A., Ganesh A. S., Anandh B., Deepa R.,. (2022). "Electrochemical performance of carbon materials." Oriental Journal of Chemistry. 38: 604-609.

Narasimharao K., Venkata Ramana G., Sreedhar D., Vasudevarao V.,. (2016). "Synthesis of graphene oxide by modified hummers method and hydrothermal synthesis of graphene-NiO nano composite for supercapacitor application." Journal of Material Sciences & Engineering. 5: 2169-22.

Navarro G. C., Meyer J. C., Sundaram R. S., Chuvilin A., Kurasch S., Burghard M., Kaiser U.,. (2010). "Atomic structure of reduced graphene oxide." Nano letters. 10(4): 1144-1148.

Khanam N. P., AlMaadeed M. A., Ouederni M., Mayoral B., Hamilton A., Sun D.,. (2016). “Effect of two types of graphene nanoplatelets on the physico–mechanical properties of linear low–density polyethylene composites.” Advanced Manufacturing: Polymer & Composites Science. 2(2): 67-73.

Norman J., Goda W.,. (2023). “Fabrication routes of graphene.” Nanotechnology. 3.

Novoselov K. S., Colombo L., Gellert P. R., Schwab M. G., Kim K. A. J. N.,. (2012). "A roadmap for graphene." Nature. 490: 192-200.

Novoselov K. S., Geim A. K., Morozov S. V., Jiang D. E., Zhang Y., Dubonos S. V., GrigorievaI V., Firsov A. A.,. (2004) "Electric field effect in atomically thin carbon films." Science. 306: 666–669.

Novoselov K. S., Jiang D., Schedin F., Booth T. J., Khotkevich V. V., Morozov S. V., Geim A. K.,. (2005). "Two-dimensional atomic crystals." Proceedings of the National Academy of Sciences. 102: 10451-10453.

Offeman R. E., Hummers W. S.,. (1958). "Preparation of graphitic oxide." Journal of American Chemical Society. 80: 1339.

Olorunkosebi A. A., Eleruja M. A., Adedeji A. V., Olofinjana B., Fasakin O., Omotoso E., Oyedotun K. O., Ajayi E. O., Manyala N. (2021) "Optimization of graphene oxide through various Hummers' methods and comparative reduction using green approach." Diamond and Related Materials 117: 108456.

Ono T., Min Y., Shapira P., Zavan B., Kim S. O., Lammel T.,. (2017). "Advances in graphene." Advances in Graphene. 276.

Ovsiienko I., Len T., Matzui L., Lazarenko O., Normand F., Shames A.,. (2018). "Features of microstructure of chemically obtained graphene-like particles." Ukrainian Journal of Physics. 63(8): 759-771.

Pandey N., Tewari C., Dhali S., Bohra B. S., Rana S., Mehta S. P. S., Sahoo N. G.,. (2021). "Effect of graphene oxide on the mechanical and thermal properties of graphene oxide/hytrel nanocomposites." Journal of Thermoplastic Composite Materials 34.1: 55-67.

Panteleimonov R. A.,. (2022). "Ways of changing the structural-morphological, physico-chemical and elect¬rical properties of graphenes." Ukrainian Chemistry Journal. 88(7): 29-44.

Papaefthymiou G., Yi D., Nanda S. S.,. (2015). "Functionalization of Graphene Oxide and its Biomedical Applications." Critical Reviews in Solid State and Materials Sciences. 40: 291-315.

Paredes J. I., Munuera J. M.,. (2017). "Recent advances and energy-related applications of high quality/chemically doped graphenes obtained by electrochemical exfoliation methods." Journal of Materials Chemistry A. 5: 7228-7242.

Parmar S., Daki S., Bhattacharya S., Shrivastav A.,. (2022). "Microorganism: An ecofriendly tool for waste management and environmental safety." Development in wastewater treatment research and processes. Elsevier,. 175-193.

Parthipan P., Al-Dosary M. A., Al-Ghamdi A. A., Subramania A.,. (2021). "Eco-friendly synthesis of reduced graphene oxide as sustainable photocatalyst for removal of hazardous organic dyes." Journal of King Saud University-Science. 33(4): 101438.

Parvez K., Li R., Puniredd S. R., Hernandez Y., Hinkel F., Wang S., Mullen K.,. (2013). "Electrochemically exfoliated graphene as solution-processable, highly conductive electrodes for organic electronics." ACS nano. 7: 3598-3606.

Parvez K., Wu Z. S., Li R., Liu X., Graf R., Feng X., Müllen K.,. (2014). "Exfoliation of graphite into graphene in aqueous solutions of inorganic salts." Journal of the American Chemical Society. 136: 6083-6091.

Paulchamy B., Arthi G., Lignesh B. D.,. (2015). “A simple approach to stepwise synthesis of graphene oxide nanomaterial.” J Nanomed Nanotechnol. 6(1): 1.

Paull B.,. (2005). “ION EXCHANGE|” Ion Chromatography Applications.

Pei S., Wei Q., Huang K., Cheng H. M., Ren W.,. (2018). "Green synthesis of graphene oxide by seconds timescale water electrolytic oxidation." Nature communications. 9(1): 145.

Pelaez-Fernandez M., Bermejo A., Benito A. M., Maser W. K., Arenal R.,. (2021). “Detailed thermal reduction analyses of graphene oxide via in-situ TEM/EELS studies.” Carbon. 178: 477-487.

Peng C., Junghyun L., Eunhee H., Hyoyoung L.,. (2011). "One-pot reduction of graphene oxide at subzero temperatures." Chemical Communications. 47: 12370-12372.

Peng K. J., Lai J. Y., Liu Y. L.,. (2016). "Nanohybrids of graphene oxide chemically-bonded with Nafion: Preparation and application for proton exchange membrane fuel cells." Journal of Membrane Science. 514: 86-94.

Peng L., Xu Z., Liu Z., Wei Y., Sun H., Li Z., Gao C.,. (2015). "An iron-based green approach to 1-h production of single-layer graphene oxide." Nature communications. 6(1): 5716.

Perreault F., De Faria A. F., Elimelech M.,. (2015). "Environmental applications of graphene-based nanomaterials." Chemical Society Reviews. 44: 5861-5896.

Pirzado A., Dalmas G., Nguyen-Dinh L., Komissarov I., Le Normand F. Janowska I.,. (2016). "The electrical property of large few layer graphene flakes obtained by microwaves assisted exfoliation of expanded graphite." Current Microwave Chemistry. 3: 139-144.

Poh H. L., Šaněk F., Ambrosi A., Zhao G., Sofer Z., Pumera M.,. (2012). “Graphenes prepared by Staudenmaier, Hofmann and Hummers methods with consequent thermal exfoliation exhibit very different electrochemical properties.” Nanoscale. 4(11): 3515-3522.

Poulomi D., Sk I., Koushik C., Surajit G., Tanusri P.,. (2024). "Stepwise reduction of graphene oxide and studies on defect-controlled physical properties." Scientific Report. 14: 294.

Pourbeyram S.,. (2016). "Effective removal of heavy metals from aqueous solutions by graphene oxide–zirconium phosphate (GO–Zr-P) nanocomposite." Industrial & Engineering Chemistry Research. 55(19): 5608-5617.

Priante F., Salim M., Ottaviano L., Perrozzi F.,. (2018). "XPS study of graphene oxide reduction induced by (100) and (111)-oriented Si substrates." Nanotechnology. 29(7): 075704.

Priyadarshani M., Neha K., Rani R., Sharma R.,. (2024). a Systematic Investigation of the Structural Changes in Chemically and Thermally Reduced Graphene Oxide Using Raman and XRD. Surface Review and Letters, 32(1), 2450105.

Priyanka A., Haris V., Saeed A.,. (2024). “Recent advances in the synthesis of graphene and its derivative materials.” Unpublished.

Prodan D., Moldovan M., Furtos G., Saroși C., Filip M., Perhaița I., Popa D.,. (2021). “Synthesis and characterization of some graphene oxide powders used as additives in hydraulic mortars.” Applied Sciences. 11(23): 11330.

Pumera M., Sofer Z.,. (2017). “Towards stoichiometric analogues of graphene: Graphane, fluorographene, graphol, graphene acid, and others.” Chemical Society Reviews. 46(15): 4450–4463.

Qiu Y., Guo F., Hurt R., Külaots I.,. (2014). Explosive thermal reduction of graphene oxide-based materials: mechanism and safety implications. Carbon. 72: 215-223.

Quitain A. T., Sumigawa Y., Mission E. G., Sasaki M., Assabumrungrat S., Kida T.,. (2018). "Graphene oxide and microwave synergism for efficient esterification of fatty acids." Energy & Fuels. 32: 3599-607.

Rahayu E. F., Hamzah A.,. (2022). “Reduction of graphene oxide: Controlled synthesis by microwave irradiation.” Nanomaterials. 12(9): 56–62.

Rai S., Bhujel R., Swain B. P.,. (2018). "Electrochemical analysis of graphene oxide and reduced graphene oxide for super capacitor applications." IEEE electron devices Kolkata conference (EDKCON). 489-492.

Raj R. S., Sharma S., Patil K.,. (2023). “Enhanced microwave-assisted exfoliation of graphite using ammonium bicarbonate: Mechanisms and characterization.” Materials Today Communications. 34: 105366.

Ramamoorthy H., Buapan K., Chiawchan T., Thamkrongart K., Somphonsane R.,. (2021). "Exploration of the temperature-dependent correlations present in the structural, morphological and electrical properties of thermally reduced free-standing graphene oxide papers." Journal of Materials Science. 56: 15134-15150.

Ramesha G. V., Kumara A. B., Muralidhara H. S., Sampath K.,. (2011). "Graphene and graphene oxide as effective adsorbents toward anionic and cationic dyes." Journal of colloid and interface science. 361: 270-7.

Ramezani M. J., Rahmani O.,. (2024). "A review of recent progress in the graphene syntheses and its applications." Mechanics of Advanced Materials and Structures. 1-33.

Rathnayake R. M. N. M., Wijayasinghe H. W. M. A. C., Pitawala H. M. T. G. A., Yoshimura M., Huang H. H.,. (2017). "Synthesis of graphene oxide and reduced graphene oxide by needle platy natural vein graphite." Applied Surface Science. 393: 309-315.

Roberts M. W., Clemons C. B., Wilber J. P., Young G., Buldum A., Quinn D. D.,. (2010). "Continuum Plate Theory and Atomistic Modeling to Find the Flexural Rigidity of a Graphene Sheet Interacting with a Substrate." Journal of Nanotechnology. 2010(1), 868492.

Rojas C. C., Gómez A., Huerta A.,. (2022). “Microwave-assisted synthesis of materials: Principles and applications.” Materials Today: Proceedings. 63: 5172–5180.

Romero A., Lavin-Lopez M.P., Sanchez-Silva L., Valverde J.L. Paton-Carrero A.,. (2018). "Comparative study of different scalable routes to synthesize graphene oxide and reduced graphene oxide." Materials Chemistry and Physics. 203: 284-92.

Rosanna L., Ferrari S.,. (2011). “Dual path mechanism in the thermal reduction of graphene oxide.” Journal of the American Chemical Society. 133(43): 17315–17321.

Rouquerol J., Avnir D., Fairbridge C. W., Everett D. H., Haynes J. M., Pernicone N., Unger K. K.,. (1994). "Recommendations for the characterization of porous solids (Technical Report)." Pure and applied chemistry. 66(8): 1739-1758.

Rowley-Neale S. J., Randviir E. P., Dena A. S. A., Banks C. E.,. (2018). "An overview of recent applications of reduced graphene oxide as a basis of electroanalytical sensing platforms." Applied Materials Today. 10, 218-226.

Ruoff R.,. (2008). “Calling all chemists.” Nature Nanotechnology. 3(1): 10-11.

Rūta A., Justina G., Jurgis B.,. (2021). "Thermal reduction of graphene oxide in the presence of carbon suboxide." Journal of Solid-State Chemistry. 301: 122365.

Sabbaghan M.,. (2018). “Ultrasonic route synthesis, characterization, and electrochemical study of graphene oxide and reduced graphene oxide.” Research on Chemical Intermediates. 45(2): 487–505.

Sachdeva H.,. (2020). “Recent advances in the catalytic applications of GO/rGO for green organic synthesis.” Green Processing and Synthesis. 9: 515–537.

Sahoo P., Shubhadarshinee L., Jali B. R., Mohapatra P., Barick A. K.,. (2022). Synthesis and characterization of graphene oxide and graphene from coal. Materials Today: Proceedings. 56, 2421-2427.

Saini B., Raghavan K.,. (2021). “X-ray diffraction.” In Elsevier. 85–141.

Sali S., Mackey H. R., Abdala A. A.,. (2019). "Effect of graphene oxide synthesis method on properties and performance of polysulfone-graphene oxide mixed matrix membranes." Nanomaterials. 9(5): 769.

Sanchez V. C., Jachak A., Hurt R. H., Kane A. B.,. (2012). "Biological interactions of graphene-family nanomaterials: an interdisciplinary review.: Chemical research in toxicology. 1(25): 15-34.

Scholz E.,. (1984). “Karl Fischer titration. In Chemical Laboratory Practice.” Springer-Verlag.

Sengupta I., Chakraborty S., Talukdar M., Pal S. K., Chakraborty S.,. (2018). "Thermal reduction of graphene oxide: How temperature influences purity." Journal of Materials Research. 33(23): 4113-4122.

Sevilla M., Ferrero G. A., Fuertes A. B.,. (2016). "Aqueous dispersions of graphene from electrochemically exfoliated graphite." Chemistry–A European Journal. 22: 17351-17358.

Sha S. M., Anwar H., Musthafa F. N., Al-Lohedan H., Alfarwati S., Rajabathar J. R., Sadasivuni K. K.,. (2024). "Photocatalytic degradation of organic dyes using reduced graphene oxide (rGO)." Scientific Reports. 14: 3608.

Shang J., Ma L., Li J., Ai W., Yu T., Gurzadyan G. G.,. (2012). "The origin of fluorescence from graphene oxide." Scientific reports. 2(1): 792.

Shanmugaraj K., Vinoth V., Pugazhenthiran N., Valdés H., Salvo C., Sepúlveda E., Mangalaraja R.V.,. (2023) "Ferrihydrite − Graphene oxide foams as an efficient adsorbent for Arsenic(III) removal from an aqueous solution" Inorganic Chemistry Communications. 153(110892): 1-12.

Sharma T. K. A., Sharma M., Kumar A.,. (2021). "Synthesis of graphene oxide and its reduction by green reducing agent." Materials Today: Proceedings. 44: 3933-3938.

Shen J., Li T., Long Y., Shi M., Li N., Ye M.,. (2012). "One-step solid state preparation of reduced graphene oxide." Carbon. 50: 2134-2140.

Shi H., Chen X., Liu K., Ding X, Xu M.,. (2020). "Heterogeneous Fenton ferroferric oxide-reduced graphene oxide-based composite microjets for efficient organic dye degradation." Journal of Colloid and Interface Science. 572: 39-47.

Shirazi E. K., Metzger J. W., Fischer K., Hassani A. H.,. (2020). "Removal of textile dyes from single and binary component systems by Persian bentonite and a mixed adsorbent of bentonite/charred dolomite." Colloids and Surfaces A: Physicochemical and Engineering. 598: 124807.

Shubha P., Namratha K., Mithali K. C., Divya V., Thakur M. S., Byrappa K.,. (2018). Green technology enabled graphene oxide reduction using Justichia wynaadensis extract and assessment of in vitro antioxidant and antibacterial activity. Advanced Science Letters. 24(8): 5726-5730.

Siburian R., Sihotang H., Raja S. L., Supeno M., Simanjuntak C.,. (2018). "New route to synthesize of graphene nano sheets." Oriental Journal of Chemistry. 34(1): 182–187.

Singh J., Rathi A., Rawat M., Gupta M.,. (2018). "Graphene: from synthesis to engineering to biosensor applications." Frontiers of Materials Science. 12: 1-20.

Singh P. K.,. (2023). "Impact of high temperature thermal reduction on microstructure, crystallinity and surface topography of reduced graphene oxide." Materials Today: Proceedings,.

Skorupska M., Ilnicka A., Lukaszewicz J. P.,. (2021). "N-doped graphene foam obtained by microwave-assisted exfoliation of graphite." Scientific Reports. 11: 2044.

Smith R. E.,. (1987). "Ion chromatography applications." CRC Press,.

Sofer Z., Luxa J., Jankovský O., Sedmidubský D., Bystroň T., Pumera M.,. (2016). "Synthesis of graphene oxide by oxidation of graphite with ferrate (VI) compounds: Myth or reality." Angewandte Chemie International Edition. 55(39): 11965–11969.

Sohail M., Saleem M., Ullah S., Saeed N., Afridi A., Khan M., Arif M.,. (2017). Modified and improved Hummer's synthesis of graphene oxide for capacitors applications. Modern Electronic Materials. 3(3): 110-116.

Sokrates T., Pantelides N., Puzyrev Y., Tsetseris L., Wang B.,. (2012). "Defects and doping and their role in functionalizing graphene." MRS Bulletin. 37(12): 1187–1194.

Soldano C., Mahmood A., Dujardin E.,. (2010). "Production, properties and potential of graphene." Carbon. 48: 2127-2150.

Soltani T., Lee B. K.,. (2017). "A benign ultrasonic route to reduced graphene oxide from pristine graphite." Journal of Colloid and Interface Science. 486: 337-343.

Stankovich S., Dikin D. A., Dommett G. H., Kohlhaas K. M., Zimney E. J., Stach E. A., Ruoff R. S.,. (2006). "Graphene-based composite materials." Nature. 442: 282–286.

Stankovich S., Dikin D. A., Piner R. D., Kohlhaas K. A., Kleinhammes A., Jia Y., Ruoff R. S.,. (2007). "Synthesis of graphene-based nanosheets via chemical reduction of exfoliated graphite oxide." Carbon. 45(7): 1558-1565.

Stoller M. D., Park S. J., Zhu Y. W., An J. H., Ruoff R. S.,. (2008). "Graphene-Based Ultracapacitors." Nano Letters. 8: 3498-3502.

Su C. Y., Lu A. Y., Xu Y., Chen F. R., Khlobystov A. N., Li L. J.,. (2011). "High-quality thin graphene films from fast electrochemical exfoliation." ACS nano. 5: 2332-2339.

Su C., Loh K. P.,. (2013). "Carbocatalysts: graphene oxide and its derivatives." Accounts of chemical research. 46: 2275-2285.

Sumdani M. G., Islam M. R., Yahaya A. N. A., Safie S. I.,. (2021). "Recent advances of the graphite exfoliation processes and structural modification of graphene: a review." Journal of Nanoparticle Research. 23: 1-35.

Sun J., Chen W., Jia K., Li S., Jia P., Wang W., Chen S.,. (2023). "Progress on the microwave-assisted recycling of spent lithium battery graphite." Processes. 11: 1451.

Sun L., Fugetsu B.,. (2013). "Mass production of graphene oxide from expanded graphite." Materials Letters. 109: 207-10.

Sur U. K.,. (2012). "Graphene: a rising star on the horizon of materials science." International Journal of Electrochemistry. 2012: 237689.

Tamilselvi R., Ramesh M., Lekshmi G. S., Bazaka O., Levchenko I., Bazaka K., Mandhakini M.,. (2020). "Graphene oxide–Based supercapacitors from agricultural wastes: A step to mass production of highly efficient electrodes for electrical transportation systems." Renewable Energy. 151, 731-739.

Tarcan R., Todor-Boer O., Petrovai I., Leordean C., Astilean S., Botiz I.,. (2020). "Reduced graphene oxide today." Journal of Materials Chemistry C. 8(4), 1198-1224.

Tee J. Y., Ng F. L., Keng F. S. L., Lee C. W., Zhang B., Lin S., Phang S. M.,. (2024). "Green synthesis of reduced graphene oxide by using tropical microalgae and its application in biophotovoltaic devices." iScience. 27(4): 109564.

Tewatia K., Sharma A., Sharma M., Kumar A.,. (2021). "Synthesis of graphene oxide and its reduction by green reducing agent." Materials Today: Proceedings. 44: 3933-3938.

Thakur K., Kandasubramanian B.,. (2019). "Graphene and graphene oxide-based composites for removal of organic pollutants: a review." Journal of Chemical & Engineering Data. 64: 833-867.

Thostenson E. T., Ren Z., Chou T. W.,. (2001). "Advances in the science and technology of carbon nanotubes and their composites: a review." Composites science and technology. 61: 1899-1912.

Timochenco V., Caldas R. A.,. (2018). "Ultrasound-assisted green synthesis and characterization of graphene oxide." International Journal of Nano Science. 14(1): 11–17.

Torrisi L., Silipigni L., Cutroneo M., Torrisi A.,. (2023). "Mass spectrometry of graphene oxide thermal reduction in vacuum." Radiation Effects and Defects in Solids, 178(1-2): 28-39.

Trung T. Q., Tien N. T., Kim D., Jang M., Yoon O. J., Lee N. E.,. (2014). "A flexible reduced graphene oxide field-effect transistor for ultrasensitive strain sensing." Advanced Functional Materials. 24(1): 117–124.

Tsagkalias I. S., Vlachou A., Verros G. D., Achilias D. S. (2019) "Effect of graphene oxide or functionalized graphene oxide on the copolymerization kinetics of Styrene/n-butyl methacrylate." Polymers 11.6: 999.

Tuinstra F., Koenig J. L.,. (1970). "Raman spectrum of graphite." The Journal of Chemical Physics. 53(3): 1126–1130.

Tung T. T., Pereira A. L. C., Poloni E., Dang M. N., Wang J., Le T. S. D., Pho Q. H., Nine M. J., Shearer C. J., Hessel V., Losic D.,. (2023). "Irradiation methods for engineering of graphene related two-dimensional materials." Applied Physics Review. 10: 031309.

Uddin M. T., Islam M. A., Mahmud S., Rukanuzzaman M.,. (2009). "Adsorptive removal of methylene blue by tea waste." Journal of Hazardous Materials. 164: 53-60.

Vasilios G., Michal O., Athanasios B., Vimlesh C., Namdong K., Christian K., Pavel H., Radek Z., Kwang S. K.,. (2012). "Functionalization of Graphene: Covalent and Non-Covalent Approaches, Derivatives and Applications." Chemical Reviews. 112(11): 6156-6214.

Viswanathan A., Venugopal A.,. (2024). "Reduced graphene oxide from dead Li-ion batteries with β-Co(OH)2 as a potential electrode for enhanced charge storage capabilities." RSC Sustainability. 2(8): 2199–2212.

Voiry D., Yang J., Kupferberg J., Fullon R., Lee C., Jeong H. Y., Chhowalla M.,. (2016). "High-quality graphene via microwave reduction of solution-exfoliated graphene oxide." Science. 353(6306). 1413-1416.

Vorrada L., Krit T., Passakorn E., Wanchai B., Achanai B.,. (2013). "Preparation and Characterization of Reduced Graphene Oxide Sheets via Water-Based Exfoliation and Reduction Methods." Advances in Materials Science and Engineering. 2012: 923403.

Vu T. H. T., Tran T. T. T., Le T. H. N., Nguyen T. P. H., Bui N. Q., Essayem N.,. (2015). "A new green approach for the reduction of graphene oxide nanosheets using caffeine." Bulletin of Materials Science. 38, 667-671.

Wadekar P. H., Ahirrao D. J., Khose R. V., Pethsangave D. A., Jha N., Some S.,. (2018). "Synthesis of aqueous dispersible reduced graphene oxide by the reduction of graphene oxide in presence of carbonic acid." Chemistry Select. 3(20): 5630-5638.

Wanag A., Rokicka P., Nejman E. K., Kozar J. K., Wrobel R. J., Szczupak A. M., Morawski A. W.,. (2017). "Antibacterial properties of TiO2 modified with reduced graphene oxide." Ecotoxicology and Environmental Safety. 147: 788-793.

Wang B., Su D., Park J., Ahn H., Wang G.,. (2012). "Graphene-supported SNO2 nanoparticles prepared by a solvothermal approach for an enhanced electrochemical performance in lithium-ion batteries." Nanoscale Research Letters. 7.

Wang C., Sun X., Zhu X., Sun B.,. (2022). "Synthesis of graphene via in-liquid discharge plasma: a green, novel strategy and new insight.: Colloid and Interface Science Communications. 47: 100605.

Wang G., Yang J., Park J., Gou X., Wang B., Liu H., Yao J.,. (2008). “Facile synthesis and characterization of graphene nanosheets.” The Journal of Physical Chemistry C. 112: 8192–8195.

Wang H., Chen Y., Wei Y.,. (2016). "A novel magnetic calcium silicate/graphene oxide composite material for selective adsorption of acridine orange from aqueous solutions." RSC Advances. 6: 34770-34781.

Wang J. T., Chen C., Wang E.,. (2014). "A New Carbon Allotrope with Six-Fold Helical Chains in all-sp2 Bonding Networks." Science Report. 4: 4339.

Wang J., Manga K. K., Bao Q., Loh K. P.,. (2011). "High-yield synthesis of few-layer graphene flakes through electrochemical expansion of graphite in propylene carbonate electrolyte." Journal of the American Chemical Society. 133: 8888-8891.

Wang J., Song F., Ding Y., Shao M.,. (2020). "The incorporation of graphene to enhance mechanical properties of polypropylene self-reinforced polymer composites." Materials & Design. 195: 109073.

Wang J., Wu W., Kondo H., Fan T., Zhou H.,. (2022). “Recent progress in microwave-assisted preparations of 2D materials and catalysis applications.” Nanotechnology. 33: 342002.

Wang Y., Alsmeyer D. C. and McCreery R. L.,. (1990). "Raman spectroscopy of carbon materials: structural basis of observed spectra." Chemistry of Materials. 2: 557-563.

Wang Y., Xu J., Zhang C., Chen H.,. (2022). “Microwave-assisted exfoliation of graphite using ammonium bicarbonate as an expandable agent for graphene production.” Carbon. 191: 238–245.

Webb M. J., Palmgren P., Pal P., Karis O., Grennberg H. (2011). A simple method to produce almost perfect graphene on highly oriented pyrolytic graphite. Carbon, 49(10), 3242-3249..

Wei D., Grande L., Chundi V., White R., Bower C., Andrew P., Ryhänen T.,. (2012). "Graphene from electrochemical exfoliation and its direct applications in enhanced energy storage devices." Chemical communications. 48: 1239-1241.

Wikipedia: https://en.wikipedia.org/wiki/Acid_Blue_25

Wilson N. R., Pandey P. A., Beanland R., Young R. J., Kinloch I. A., Gong L., Liu Z., Suenaga K., Rourke J. P., York S. J., Sloan J.,. (2009). "Graphene oxide: structural analysis and application as a highly transparent support for electron microscopy." ACS Nano. 3: 2547-2556.

Wu J., Zhao J., Vaidhyanathan B., Zhang H., Anshuman A., Nare A., Saremi-Yarahmadi S.,. (2020). "Rapid microwave-assisted bulk production of high-quality reduced graphene oxide for lithium-ion batteries." Materialia. 13: 100833.

Wu L., Li W., Li P., Liao S., Qiu S., Chen M., Liu L.,. (2014). "Powder, paper and foam of few-layer graphene prepared in high yield by electrochemical intercalation exfoliation of expanded graphite." Small. 10: 1421-1429.

Wu T. T., Ting J. M.,. (2013). "Preparation and characteristics of graphene oxide and its thin films." Surface and coatings technology. 231: 487-491.

Wu W., Liu M., Gu Y., Guo B., Ma H., Wang P., Zhang R.,. (2020). "Fast chemical exfoliation of graphite to few-layer graphene with high quality and large size via a two-step microwave-assisted process." Chemical Engineering Journal. 381: 122592.

Xie X., Zhou Y., Huang K.,. (2019). "Advances in microwave-assisted production of reduced graphene oxide." Frontiers in chemistry. 7: 355.

Xing B., Yuan R., Zhang C., Huang G., Guo H., Chen Z., Yu J.,. (2017). "Facile synthesis of graphene nanosheets from humic acid for supercapacitors." Fuel Processing Technology. 165: 112–122.

Xiufeng M., Xiuqing M., Fengmin W.,. (2015). "Hydrothermal method for the production of reduced graphene oxide." Physica E: Low-dimensional Systems and Nanostructures. 68: 81-86.

Xu C., Shi X., Ji A., Shi L., Zhou C., Cui Y.,. (2015). "Fabrication and characteristics of reduced graphene oxide produced with different green reductants." PloS one. 10(12): e0144842.

Xu P., Liu X., Zhao Y., Lan D., Shin I.,. (2023). "Study of graphdiyne biomimetic nanomaterials as fluorescent sensors of ciprofloxacin hydrochloride in water environment." Desalin Water Treat. 302: 129-137.

Xu S., Liu J., Xue Y., Wu T., Zhang Z.,. (2017). "Appropriate conditions for preparing few-layered graphene oxide and reduced graphene oxide." Fullerenes, Nanotubes and Carbon Nanostructures. 25(1): 40-46.

Xu Y., Xu C., Wang Y., Liu Y.,. (2022). "A comprehensive review of graphite exfoliation and its applications in graphene production." Journal of Materials Science. 57: 3643–3664.

Xu Z., Li H., Li W., Cao G., Zhang Q., Li K., Wang J.,. (2011). "Large-scale production of graphene by microwave synthesis and rapid cooling." Chemical Communications. 47: 1166-1168.

Xu Z., Qin L., Xiaohua Z., Chunlan L., Maotian X.,. (2012). "Reduction of Graphene Oxide Via Ascorbic Acid and Its Application for Simultaneous Detection of Dopamine And Ascorbic Acid." International Journal of Electrochemical Science. 7: 5172-5184.

Yan J. X., Leng Y. C., Guo Y., Wang G., Gong H., Guo P., Tan H. P., Long Y. Z., Xuelu L., Han W. P.,. (2019). "Highly Conductive Graphene Paper with Vertically Aligned Reduced Graphene Oxide Sheets Fabricated by Improved Electrospray Deposition Technique." ACS applied materials & interfaces. 11(11): 10810-10817.

Yang D., Velamakanni A., Bozoklu G., Park S., Stoller M., Piner R. D., Stankovich S., Jung I., Field D. A., Ventrice J. C. A., Ruoff R. S.,. (2009). "Chemical analysis of graphene oxide films after heat and chemical treatments by X-ray photoelectron and Micro-Raman spectroscopy." Carbon. 47: 145-52.

Yang G., Li L., Lee W. B., Ng M. C.,. (2018). "Structure of graphene and its disorders: a review." Science and technology of advanced materials. 19: 613-648.

Yang S. T., Chen S., Chang Y., Cao A., Liu Y., Wang H.,. (2011). "Removal of methylene blue from aqueous solution by graphene oxide." Journal of colloid and interface science. 359: 24-29.

Yang S., Brüller S., Wu Z. S., Liu Z., Parvez K., Dong R., Müllen K.,. (2015) "Organic radical-assisted electrochemical exfoliation for the scalable production of high-quality graphene." Journal of the American Chemical Society. 137: 13927-13932.

Yang S., Lohe M. R., Müllen K., Feng X.,. (2016). "New-generation graphene from electrochemical approaches: production and applications." Advanced Materials. 28: 6213-6221.

Yankowitz M., Xue J., Cormode D., Yamagishi S. J., Watanabe K., Taniguchi T., LeRoy B.,. (2012). "Emergence of superlattice dirac points in graphene on hexagonal boron nitride." Nature Physics. 8: 382-386.

Ye W., Li X., Luo J., Wang X., Sun R.,. (2017). "Lignin as a green reductant and morphology directing agent in the fabrication of 3D graphene-based composites for high-performance supercapacitors." Industrial crops and products. 109, 410-419.

Ying Z., Diao J., Wang S., Cai X., Cai Y., Liu H., Wang N.,. (2021). "Thermal stability, ripening dynamics and coalescing microstructures of reduced graphene oxide-based platinum nanocatalysts: An in-situ TEM study." Diamond and Related Materials. 120: 108690.

Yip T. M., Tong G. B.,. (2023). "Fabrication Routes of Graphene." Graphene: Fabrication, Properties and Applications." Nature Singapore: Springer. 53-90.

You X., Chang J. H., Ju B. K., Pak J. J.,. (2011). "An electrochemical route to graphene oxide." Journal of nanoscience and nanotechnology. 11: 5965-5968.

Yu H., Zhang B., Bulin C., Li R., Xing R.,. (2016). "High-efficient synthesis of graphene oxide based on improved hummers method." Scientific reports. 6(1): 1-7.

Yu P., Lowe S. E., Simon G. P., Zhong Y. L.,. (2015). "Electrochemical exfoliation of graphite and production of functional graphene." Current opinion in colloid & interface science. 20(5-6): 329-338.

Yu X., Cheng H., Zhang M., Zhao Y., Qu L., Shi G.,. (2017). "Graphene-based smart materials." Nature Reviews Materials. 2(9): 1-13.

Yu Y., Wang Z., Sun R., Chen Z., Liu M., Zhou X., Wang G.,. (2020). "Self-supported reduced graphene oxide membrane and its Cu2+ adsorption capability." Materials. 14(1): 146.

Zaaba N. I., Foo K. L., Hashim U., Tan S. J., Liu W. W., Voon C. H.,. (2017). "Synthesis of graphene oxide using modified hummers method: solvent influence." Procedia engineering. 184: 469-477.

Zare P., Aleemardani M., Seifalian A., Bagher Z., Seifalian A. M.,. (2021). "Graphene oxide: opportunities and challenges in biomedicine." Nanomaterials. 11(5): 1083.

Zarrin H., Higgins D., Jun Y., Chen Z., Fowler M.,. (2011). "Functionalized graphene oxide nanocomposite membrane for low humidity and high temperature proton exchange membrane fuel cells." The Journal of Physical Chemistry C. 115: 20774-20781.

Zeng H., Yu Z., Shao L., Li X., Zhu M., Liu Y., Zhu X.,. (2020). "Ag2CO3@ UiO-66-NH2 embedding graphene oxide sheets photocatalytic membrane for enhancing the removal performance of Cr (VI) and dyes based on filtration." Desalination. 491: 114558.

Zhang B., Cao Y., Jiang S., Li Z., He G., Wu H.,. (2016). "Enhanced proton conductivity of Nafion nanohybrid membrane incorporated with phosphonic acid functionalized graphene oxide at elevated temperature and low humidity." Journal of Membrane Science. 518: 243-53.

Zhang C., Lv W., Xie X., Tang D., Liu C., Yang Q. H.,. (2013). "Towards low temperature thermal exfoliation of graphite oxide for graphene production." Carbon. 62, 11-24.

Zhang J., Yang H., Shen G., Cheng P., Zhang J., Guo S.,. (2010). "Reduction of graphene oxide vial-ascorbic acid." Chemical Communication. 46: 1112-1114.

Zhang Q., Zhon Y., Tong Y., Chi Y., Liu R., Dai C., Tan Y.,. (2023). "Reduced graphene oxide coating LiFePO4 composite cathodes for advanced lithium-ion battery applications." International Journal of Molecular Sciences. 24(24): 17549.

Zhang T., Xue Q., Zhang S., Dong M.,. (2012). "Theoretical approaches to graphene and graphene-based materials." Nano Today. 7(3): 180-200.

Zhang W., Xu H., Xie F., Ma X., Niu B., Chen M., Long D.,. (2022). "General synthesis of ultrafine metal oxide/reduced graphene oxide nanocomposites for ultrahigh-flux nanofiltration membrane." Nature Communications. 13(1): 471.

Zhang X., Tan Y.,. (2016). "A novel aluminum–graphite dual-ion battery." Advanced Energy Materials. 6(11): 1502588.

Zhang Y., Chen Y.,. (2023). “Review of microwave-assisted methods for the production of graphene: Mechanisms and applications.” Carbon. 208: 51–68.

Zhang Y., Chen Z., Li X., Xu C.,. (2023). “Optimization strategies for microwave-assisted exfoliation of graphite into graphene: Addressing challenges and limitations.” Journal of Materials Science. 58: 74–83.

Zhang Y., Zhang J., Huang X., Zhou X., Wu H., Guo S.,. (2011). "Assembly of graphene oxide–enzyme conjugates through hydrophobic interaction." Small. 8: 154-159.

Zhang Y., Zhang X., Chen H., Yang G.,. (2022). “Microwave-assisted exfoliation of graphite: A novel approach for preparing high-quality graphene.” Journal of Materials Science. 57: 2287–2300.

Zhao J., Pei S., Ren W., Gao L., Cheng H. M.,. (2010). "Efficient preparation of large-area graphene oxide sheets for transparent conductive films." ACS Nano. 4(9): 5245-5252.

Zhao S., Xie S., Zhao Z., Zhang J., Li L., Xin Z.,. (2018). "Green and high-efficiency production of graphene by tannic acid-assisted exfoliation of graphite in water." ACS Sustainable Chemistry & Engineering. 6(6): 7652-7661.

Zheng F., Xu W. L., Jin H. D. T., Hao X., Ghiggino K. P.,. (2015). "Charge transfer from poly (3-hexylthiophene) to graphene oxide and reduced graphene oxide." RSC Advances 5.109.

Zhi M., Liu Q., Chen H., Feng S., He Y.,. (2019). "Study on efficient and green reduction of graphene oxide by a one-step hydrothermal method." In Journal of Physics: Conference Series, IOP Publishing. 1213(5): 052047.

Zhou S., Bongiorno A.,. (2013). "Origin of the chemical and kinetic stability of graphene oxide." Scientific Reports. 3: 2484.

Zhou Y., Huang H., Chen Y.,. (2023). “A novel microwave-assisted method for exfoliating graphite into high-purity graphene without harmful chemicals.” Carbon. 221: 105–113.

Zhou Y., Xue C., Gan L., Owens G., Chen Z.,. (2023). "Antibacterial activity of reduced graphene oxide prepared by microbe." Materials Today Sustainability. 22: 100341.

Zhu C., Liu T., Qian F., Han T. Y. J., Duoss E. B., Kuntz J. D., Li Y.,. (2016). "Supercapacitors based on three-dimensional hierarchical graphene aerogels with periodic macropores." Nano letters. 16: 3448-3456.

Zhu Y., Murali S., Cai W., Li X., Suk J. W., Potts J. R., Ruoff R. S.,. (2010). “Graphene and graphene oxide: Synthesis, properties, and applications.” Advanced Materials. 22: 3906–3924.

Zhang Y., Zhang J., Huang X., Zhou X., Wu H., Guo S.,. (2011) “Assembly of graphene oxide–enzyme conjugates through hydrophobic interaction.” Small. 8: 154-159.

Zohra F. T., Ahmed S., Sultana R., Nurnabi M., Alam Z.,. (2022). “Removal of Cr(III) from tanning effluent using adsorbent prepared from peanut shell.” Desalination and Water Treatment. 7: 1-10.

Zou L., Wang L., Wu Y., Ma C., Yu S., Liu X.,. (2018). "Trends analysis of graphene research and development." Journal of Data and Information Science. 3(1): 82-100.

Zubair M., Jose J., Emwas A. H., Al-Harthi M. A.,. (2014). "Effect of modified graphene and microwave irradiation on the mechanical and thermal properties of poly (styrene-co-methyl methacrylate)/graphene nanocomposites." Surface and Interface Analysis. 46(9): 630-639.